



## UvA-DARE (Digital Academic Repository)

### Optimization of adaptive radiation therapy in cervical cancer: Solutions for photon and proton therapy

van de Schoot, A.J.A.J.

**Publication date**

2016

**Document Version**

Final published version

[Link to publication](#)

**Citation for published version (APA):**

van de Schoot, A. J. A. J. (2016). *Optimization of adaptive radiation therapy in cervical cancer: Solutions for photon and proton therapy*. [Thesis, fully internal, Universiteit van Amsterdam].

**General rights**

It is not permitted to download or to forward/distribute the text or part of it without the consent of the author(s) and/or copyright holder(s), other than for strictly personal, individual use, unless the work is under an open content license (like Creative Commons).

**Disclaimer/Complaints regulations**

If you believe that digital publication of certain material infringes any of your rights or (privacy) interests, please let the Library know, stating your reasons. In case of a legitimate complaint, the Library will make the material inaccessible and/or remove it from the website. Please Ask the Library: <https://uba.uva.nl/en/contact>, or a letter to: Library of the University of Amsterdam, Secretariat, P.O. Box 19185, 1000 GD Amsterdam, The Netherlands. You will be contacted as soon as possible.

# Optimization of adaptive radiation therapy in cervical cancer

*solutions for photon and proton therapy*

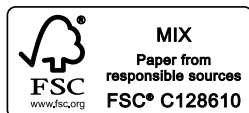


Stijn van de Schoot



# **Optimization of adaptive radiation therapy in cervical cancer**

*solutions for photon and proton therapy*



Layout: Legatron Electronic Publishing  
Infographic &  
cover illustration: Hans van de Schoot – [www.concepthans.com](http://www.concepthans.com)  
Production: Ipskamp Printing B.V., Enschede  
ISBN: 978-94-028-0148-4

The research described in this dissertation was carried out at the department of Radiation Oncology, Academic Medical Center, University of Amsterdam, Amsterdam, the Netherlands.

Copyright of the published articles in this dissertation has been transferred to the associated publishers.

Financial support for publication of this dissertation was kindly provided by Elekta B.V.

© A.J.A.J. van de Schoot, Amsterdam 2016

# **Optimization of adaptive radiation therapy in cervical cancer**

*solutions for photon and proton therapy*

ACADEMISCH PROEFSCHRIFT

ter verkrijging van de graad van doctor

aan de Universiteit van Amsterdam

op gezag van de Rector Magnificus

prof. dr. D.C. van den Boom

ten overstaan van een door het College voor Promoties ingestelde commissie,

in het openbaar te verdedigen in de Agnietenkapel

op dinsdag 5 juli 2016, te 12:00 uur

door

**Agustinus Jacobus Antonius Joannes van de Schoot**

geboren te Boxtel

## **Promotiecommissie:**

Promotor:	Prof. dr. C.R.N. Rasch	Universiteit van Amsterdam
Copromotores:	Dr. A. Bel Prof. dr. L.J.A. Stalpers	Academisch Medisch Centrum Universiteit van Amsterdam
Overige leden:	Prof. dr. G.G. Kenter Prof. dr. M.B. van Herk Dr. M.S. Hoogeman Prof. dr. D. Verellen Prof. dr. M.J. van de Vijver Dr. B. van Triest	Universiteit van Amsterdam Universiteit van Amsterdam Erasmus Medisch Centrum Vrije Universiteit Brussel Universiteit van Amsterdam Nederlands Kanker Instituut – Antoni van Leeuwenhoek

Faculteit der Geneeskunde





# Contents

<b>Chapter 1</b>	General introduction	<b>9</b>
<b>Chapter 2</b>	Dosimetric advantages of a clinical daily adaptive plan selection strategy compared with a non-adaptive strategy in cervical cancer radiation therapy	<b>23</b>
<b>Chapter 3</b>	Generic method for automatic bladder segmentation on cone beam CT using a patient-specific bladder shape model	<b>43</b>
<b>Chapter 4</b>	Beam configuration selection for robust intensity-modulated proton therapy in cervical cancer using Pareto front comparison	<b>61</b>
<b>Chapter 5</b>	Dosimetric advantages of proton therapy compared with photon therapy using an adaptive strategy in cervical cancer	<b>77</b>
<b>Chapter 6</b>	Quantification of delineation errors of the gross tumor volume on magnetic resonance imaging in uterine cervical cancer using pathology data and deformation correction	<b>95</b>
<b>Chapter 7</b>	Should excluding uninvaded uterine tissue be combined with proton therapy for cervical cancer?	<b>109</b>
<b>Chapter 8</b>	General discussion	<b>125</b>
<b>References</b>		<b>137</b>
<b>Summary</b>		<b>147</b>
<b>Nederlandse samenvatting</b>		<b>151</b>
<b>Addendum</b>		
	List of abbreviations	159
	List of publications	161
	PhD portfolio	165
	Curriculum vitae	169
	Infographic	170
	Dankwoord	179



# Chapter 1

General introduction

## 1.1 | Cervical cancer

The uterine cervix is the lower, narrow portion of the female uterus and is the connection between the uterine cavity and the lumen of the vagina. As part of the human female reproductive system, the cervix aids in sperm transportation after sexual intercourse to fertilize an egg cell during ovulation. As shown in Figure 1.1, the uterine cervix is located between the urinary bladder and the rectum.

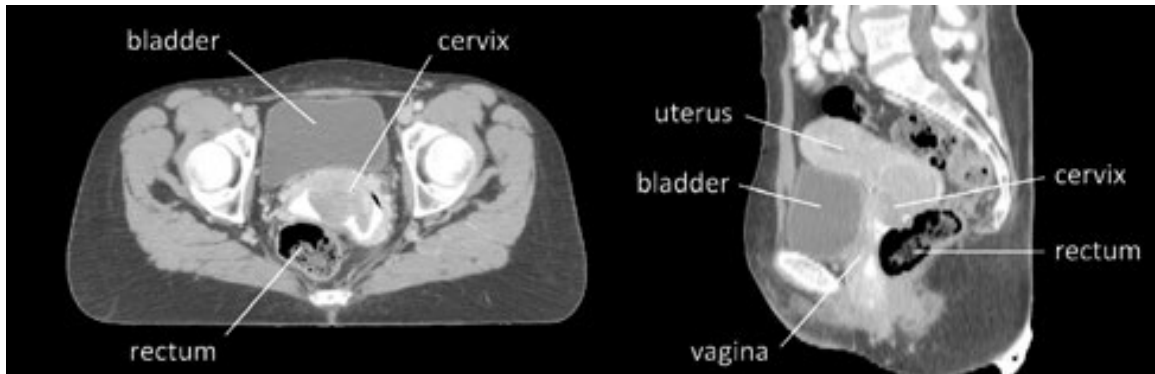


**Figure 1.1** | Transverse (left) and sagittal (right) CT slices showing the location of the cervix, uterus, vagina, bladder and rectum in the female pelvic area.

### Epidemiology

Cervical cancer is the fourth most common cancer in women worldwide, with an estimated incidence of 528,000 in 2012 [1]. The large majority of this estimated incidence occurs in the less developed regions, including Eastern Africa, Melanesia, Southern and Middle Africa. In Eastern and Middle Africa, cervical cancer is the most common female cancer. In 2012, an estimated 266,000 deaths from cervical cancer worldwide accounted for 7.5% of all female cancer deaths [1]. In the Netherlands, cervical cancer is the sixth most common cancer in women with 729 newly diagnosed cases and 198 cervical cancer-related deaths in 2014 (Figure 1.2). Current curative treatments in the Netherlands resulted in a three-year overall survival rate of 76% [2].

The major risk factor for cervical cancer is an infection with the human papillomavirus (HPV), especially with the high-risk oncogenic HPV types (HPV-16 and HPV-18). HPV infections are mainly transmitted through sexual contact. Although most infections with HPV are self-limiting and cause no symptoms of cervical cancer, HPV vaccination for young adolescent girls together with cervical screening is recommended by the World Health Organization (WHO). In the Netherlands, the national vaccination program includes HPV vaccination for young adolescent girls and female adults between 30 and 60 years old are screened once every five years. Other risk factors for cervical cancer include smoking, long-term use of oral contraceptives, sexual intercourse at a young age and multiple sexual partners.

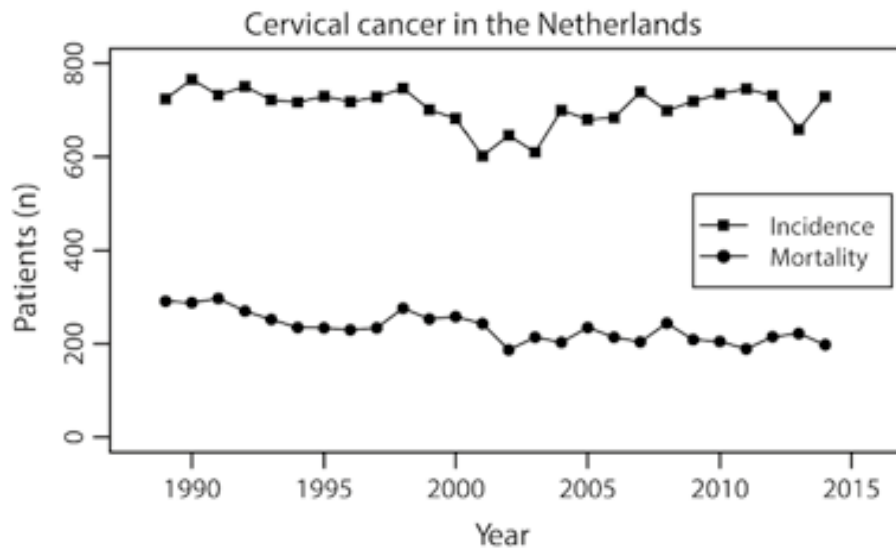


Figure 1.2 | Incidence and mortality of cervical cancer in the Netherlands from 1989 until 2014 [2].

## Tumor staging

Cervical tumors are staged by the International Federation of Gynecology and Obstetrics (FIGO) staging system based on clinical examination [3]. The use of imaging modalities to evaluate the tumor extension is recommended, however not mandatory [4,5]. Compared to other imaging modalities, magnetic resonance imaging (MRI) has been demonstrated to be superior in tumor extent evaluation including parametrial infiltration and vaginal extension [6-9]. For the evaluation of lymph nodes and distant disease,  $^{18}\text{F}$ -fluorodeoxyglucose ( $^{18}\text{F}$ FDG) positron emission tomography – computed tomography (PET-CT) is considered as the most useful modality [10,11]. Early-stage cervical tumors (FIGO stage IB1–IIA1) include clinically visible lesions limited to the cervix or carcinomas with a limited extension (<4 cm) beyond the cervix without parametrial invasion. Locally advanced cervical tumors (FIGO stage IB2, IIA2–IVA) include clinically visible lesions with a substantial extension (>4 cm) or an invasion in parametria, lower third of the vagina, pelvic wall or adjacent organs.

## 1.2 | Cervical cancer treatment

The standard curative treatment for women with early-stage cervical tumors (FIGO stage IB1–IIA1) is surgery and radiation therapy is reserved for women who are medically inoperable. Surgery usually consists of a radical hysterectomy including a pelvic lymph node dissection. Fertility preserving surgery is reserved for young women with very small tumors [12]. Adjuvant radiation therapy after surgery is offered to patients with early-stage cervical cancer who had pathological features associated with high risk or local recurrences [13].

Radiation therapy with concomitant chemotherapy is the cornerstone of treatment for women with locally advanced cervical tumors (FIGO stage IB2, IIB – IVA) [14-16]. The preferred alternative for cervical cancer patients with a contraindication for chemotherapy is radiation therapy with concomitant hyperthermia [17-20]. Hyperthermia is the artificial elevation of the tissue temperature (40°C – 44°C) to enhance radiation sensitivity of tumor cells resulting in an enlarged therapeutic efficacy of radiation therapy [17,19].

## **Radiation therapy**

Radiation therapy uses ionizing radiation to kill malignant cells and is generally applied with a curative intent. To restrain uncontrolled cell growth, the cell deoxyribonucleic acid (DNA) is damaged by ionizing radiation in order to cause cellular death. Instead of delivering a single fraction of high radiation dose, the total amount of prescribed dose is divided into multiple fractions in order to maximize the effect of radiation on tumor cells. Fractionating the dose allows healthy cells to activate their self-repair mechanisms in between fractions which repair the DNA damage. The repair mechanisms in tumor cells are usually less efficient compared to healthy cells, resulting in cell death after irradiation. The difference between therapeutic effectiveness and toxicity defines the therapeutic window of radiation therapy and fractionated treatments are applied to enlarge this therapeutic window.

Radiation therapy can be delivered by addressing the radiation to the tumor from outside the body (i.e. external beam radiation therapy) or by directing the radiation from inside the body (i.e. brachytherapy). In cervical cancer, radiation therapy is offered in a combined strategy: external beam radiation therapy and subsequently brachytherapy.

Brachytherapy, also known as internal radiation therapy, aims to irradiate the tumor locally by using radioactive sources that are placed temporarily or permanently inside or close to the tumor. In brachytherapy for cervical cancer, an applicator is placed temporarily in the vaginal vault and uterine cavity (intracavitary brachytherapy) and the radiation sources are loaded into the applicator. Since the brachytherapy sources are placed near to the tumor, a very high radiation dose can be delivered to the tumor whilst minimizing radiation exposure to surrounding healthy tissue [21]. Brachytherapy can be applied using either low-dose rate (LDR) sessions or as a fractionated high-dose rate (HDR) session. Despite the absence of significant difference when considering overall survival, relapse-free survival, local control rate, recurrences, metastasis and treatment-related complications [22], the use of intracavitary HDR for all clinical stages of cervical cancer is currently more popular than LDR due to shorter treatment times and improved accuracy of source and applicator positioning. As an alternative, a pulsed-dose rate (PDR) scheme can be applied in which short pulses of radiation are given during the course of treatment, typically lasting 24 till 48 hours [23].

### 1.3 | External beam radiation therapy

External beam radiation therapy is the most common form of radiation therapy in which the radiation is directed at the tumor from outside the body. External beam radiation therapy can be applied using beams of energetic X-rays, protons, neutrons or positive ions. The most commonly applied form of external beam radiation therapy, photon therapy, utilizes beams of high-energy X-rays and is usually delivered using a linear accelerator (Figure 1.3). The gantry of the linear particle accelerator can rotate around the treatment table on which the patient is positioned and allows radiation delivery from different directions. The complete procedure of external beam radiation therapy consists of patient imaging and target definition, radiation therapy planning and actual dose delivery. Photon beams are characterized by a relatively short build-up region to maximize dose deposition and the depth of maximum dose deposition is determined by the beam energy. After the build-up region, the energy deposition is decreased exponentially with increasing tissue depth (Figure 1.4). To limit dose deposition outside the target volume, the radiation dose is generally focused to the target volume by using multiple beams from different directions.



Figure 1.3 | A linear accelerator with an integrated kV-CBCT system used for clinical radiation therapy.

In particle therapy, beams of energetic protons, neutrons or positive ions are used for cancer treatment. Proton therapy is the most commonly applied form of particle therapy in current clinical practice. Also in the Netherlands, proton therapy will become clinically available in the near future.

In proton therapy, beams of energetic protons are used to irradiate the tumor. Compared to radiation therapy using photons, the penetration depth of the charged particles in proton therapy is determined by the final energy of the emerging proton beam (Figure 1.4). The maximum energy deposition is near the end of the proton range and known as the Bragg peak, while beyond the Bragg peak the dose drops to zero for protons. Due to the energy deposition profile, radiation therapy using protons holds the promise to provide a highly conformal dose distribution including sharp dose fall-offs around the target volume. A complete utilization of the physical characteristics of protons will result an advantage of proton therapy over conventional radiation therapy using high-energy X-rays [24].

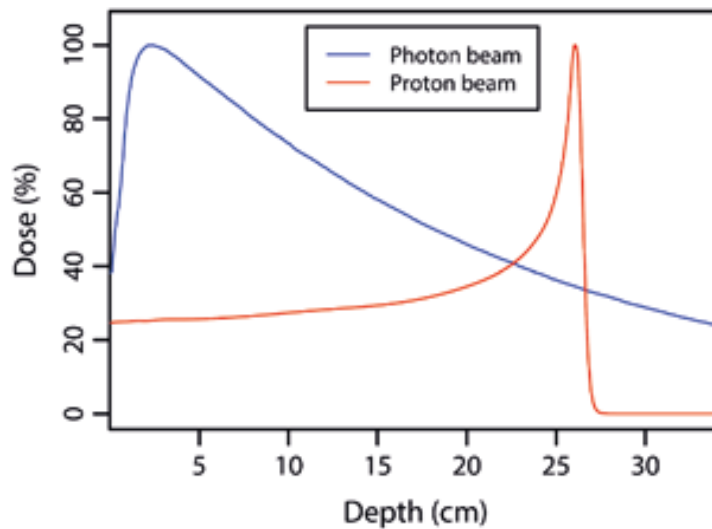


Figure 1.4 | Typical example of dose deposition as a function of depth below the body surface for a photon beam and a proton beam.

## Target definition

Computed tomography (CT) imaging of the patient is one of the first steps in the radiation therapy chain, whereby the patient body, inner organs and tumor are imaged in radiation treatment position. The patient must be in a position that is suitable for both CT acquisition and treatment delivery and reproducible in order to reduce systematic errors during treatment [25]. Cervical cancer patients are often treated in prone position using a belly board device to reduce bowel irradiation [26-28].

Next, the tumor is delineated on the CT imaging by the radiation oncologist. The gross tumor volume (GTV) represents the visible extent of malignant tumor growth. Although the GTV is generally delineated based on the visualized three-dimensional information on (PET-)CT imaging, additional MRI is increasingly used by the radiation oncologist to improve GTV definitions. The clinical target volume (CTV) is formed by expanding the GTV to include subclinical microscopic malignant cells. For cervical cancer radiation therapy, consensus guidelines recommend that the CTV should comprise the GTV, cervix, uterus, upper part of the vagina, parametria and pelvic

nodes [29]. To ensure a homogeneous dose to the CTV throughout the course of irradiation, the planning target volume (PTV) is formed by adding a site-specific (an)isotropic CTV-to-PTV margin. The PTV accounts for geometrical uncertainties and is used to ensure that the prescribed dose is actually delivered to the CTV. Next to the target volumes, also organ at risk (OAR) volumes are delineated on the CT imaging.

## Treatment planning

The pre-treatment acquired CT image including delineated target volumes and OARs delineations is used for external beam radiation therapy planning. Each pixel of the CT image is assigned a numerical value (i.e. CT number) and converted into relative electron densities to represent corresponding attenuation values, which are displayed using the Hounsfield unit (HU) scale. In radiation therapy planning, the HU information is used to predict the delivered dose along the beam path by calculating the attenuation of X-ray beams. Different dose calculation models are available, including pencil beam models, collapse cone convolution and Monte-Carlo algorithms, with precision versus computation time being the relevant trade-off [30,31]. The conventional forward treatment planning technique is increasingly replaced by the inverse treatment planning technique.

Forward planning is a technique in which the beams are added and adapted manually in order to deliver sufficient radiation dose to the target volume while minimizing the dose to healthy surrounding tissue. The process of forward planning involves the selection of the appropriate beam energy and the manual adaptation of the beams by defining field sizes, introducing attenuating wedges for non-uniform beam intensities and shaping individual leaves of the multileaf collimator (MLC). If the calculated dose distribution is not satisfactory, adaptations to the beams are applied until the determined dose distribution is satisfactory. In contrast to the forward planning technique, the inverse planning technique is designed to minimize the trial-and-error process while producing highly conformal dose distributions. The inverse problem defined by prescribed dose-volume objective functions for the target volume and OARs is solved in order to geometrically shape the beams.

Besides adaptations to the beam geometry, also the intensity of the beams can be modulated independently to produce the desired (non-)uniform dose distribution in the target volume. This advanced type of high-precision radiation therapy is known as intensity-modulated radiation therapy (IMRT). By modulating the intensity and the geometric shape of the beam, IMRT allows for a highly conformal dose distribution, even around concave target volumes. IMRT can be delivered with either a fixed gantry (i.e. static field IMRT) or a moving gantry (i.e. rotational IMRT). Compared to conventional static field IMRT, rotational IMRT techniques (e.g. volumetric modulated arc therapy (VMAT)) decreased treatment delivery time with the addition of further improved OAR sparing [32].

In proton therapy, the CT numbers are converted into proton stopping power values to approximate the loss of particle energy along the beam path. Proton therapy planning is performed using either a scattering technique or a scanning technique. In scattering techniques, proton beams are spread by placing scattering material in the beam path and custom-made collimators and compensators conform the dose to the target volume. Inside the gantry, range modulators or ridge filters are placed to obtain Bragg peaks at different depths. In beam scanning techniques (e.g. pencil beam scanning), a narrow mono-energetic beam is steered by magnets and the target volume is painted in successive layers. Since the depth of each pencil beam is controlled by varying the beam energy, scanning techniques do not require beam-modifying devices. The pencil beam scanning technique enables intensity-modulated proton therapy (IMPT) which is characterized by a highly conformal dose delivery to complex-shaped target volumes by combining heterogeneous contributions of individual beams [33].

Due to the highly localized dose deposition, IMPT has the potential to improve OAR sparing without compromising on target volume irradiation [34,35]. However, a major challenge in proton therapy is that dose deposition is very sensitive to treatment uncertainties [24]. Interfraction motion of the tumor and surrounding organs limit the targeting accuracy and affect the efficacy of IMPT. As a result, the actual delivered dose distribution is not necessarily similar to the high quality dose distribution obtained during treatment planning. In order to fully exploit the potential benefit of proton therapy, it is essential that IMPT plans are robust against treatment uncertainties.

### **Image-guided dose delivery**

External beam radiation therapy in cervical cancer is typically delivered in 23 fractions or 28 fractions when the para-aortic lymph nodes are included in the target volume. Prior to each irradiation fraction, patients are positioned on the treatment table identical to the position during pre-treatment CT imaging to be sure that the actual delivered dose matches the planned dose. Using the in-room laser systems, patients are aligned based on the pre-treatment applied skin marks. The internal patient anatomy relative to the skin marks can largely vary between treatment fractions and pre-fraction imaging is required for accurate dose delivery. Image-guided radiation therapy (IGRT) is a technique whereby frequent imaging is used during the radiation therapy course to improve the accuracy and precision of dose delivery [36,37]. Image guidance modalities commonly applied included portal imaging, planar kilovoltage (kV) or megavoltage (MV) imaging using digital reconstructed radiographs and cone-beam computed tomography (CBCT) imaging.

Portal imaging is the acquisition of patient images based on MV radiation beams used for radiation treatment by measuring the beam portion that passes through the patient. Although portal imaging was initially applied using radiographic films, advancements in digital imaging devices resulted in electronic portal imaging devices (EPID). Compared to film-based portal imaging, EPID allows to process the image directly and digitally and can be used for treatment

guidance [38,39]. However, the lack of volumetric information including soft-tissue information limits the use of EPID-based image guidance.

Volumetric imaging using kV-CBCT technology enables internal structure visualization and allows for treatment localization and verification based on three-dimensional images. Since CBCT imaging systems including a kV source and imaging panel have been integrated with linear accelerators (Figure 1.3), pre-fraction volumetric imaging using the CBCT system is increasingly used to guide irradiation. Two-dimensional projection images of the entire volume of interest are acquired by rotating the CBCT system around the patient and these projections are reconstructed into a three-dimensional volume analogous to the pre-treatment CT image. The reconstructed CBCT image is aligned with the pre-treatment CT image and the treatment table is shifted accordingly in order to minimize patient set-up errors. However, straightforward positional corrections are often not sufficient due to anatomical changes or tumor visibility is limited due to the poor soft-tissue contrast.

Even though the introduction of CBCT imaging has enabled soft-tissue visualization, tumor visibility on pre-fraction kV-CBCT images is often limited. To improve tumor localization on CBCT images, fiducial markers are often implanted in or near the tumor before the treatment course. For various tumor sites, different types of surrogates used for tumor localization are reported [40-44]. Also in cervical cancer, different types of tumor demarcations are investigated to improve daily tumor localization on pre-fraction CBCT images [44-46].

In proton therapy, dose delivery is very sensitive to geometric uncertainties and therefore image guidance during the course of treatment is essential. Since portal imaging is not feasible in proton therapy, orthogonal kV-based image-guided techniques have been used routinely [24]. However, target alignment based on two-dimensional imaging does not provide the variation in patient anatomy for accurate image guidance and high-precision dose delivery. Recently, volumetric imaging using kV-CBCT technology is introduced in proton therapy and modern proton therapy gantries are nowadays equipped with a CBCT imaging system.

## 1.4 | Adaptive radiation therapy

Adaptive radiation therapy (ART) aims to individualize radiation therapy based on patient-specific variations evaluated during the course of treatment. Originally, ART was developed as an offline strategy to correct for systematic errors by re-planning during the radiation therapy course [47-50]. However, this adaptive strategy increased the clinical workload during the course of radiation therapy without accounting for random day-to-day variations [50,51].

The introduction of pre-fraction volumetric imaging has enabled daily soft-tissue visualization and together with possible tumor demarcation by fiducial markers allows for treatment adaptations. In online ART, the dose delivery is adapted directly after imaging according to the observed interfraction anatomical changes. The obvious advantage of online adaptations is

that both systematic and random errors are corrected efficiently. Since adaptations can be applied using various approaches, different online adaptive strategies have been investigated [52-57]. The preferred online adaptive strategy includes daily radiation therapy re-optimization based on pre-fraction imaging. However, such an online adaptive strategy is not yet feasible in clinical practice due to technical and logistical limitations.

A frequently applied practical adaptive approach in radiation therapy for pelvic tumors is the plan-library based plan-of-the-day strategy [58-63]. Also in cervical cancer radiation therapy, this online adaptive strategy holds the promise to compensate for interfraction target motion. Next to daily adequate target coverage, each treatment fraction the dose to surrounding tissues may be reduced. Prior to treatment, several radiation therapy plans are generated corresponding to different target shapes and positions. Subsequently, each treatment fraction the plan best fitting the target shape is selected based on pre-fraction CBCT imaging.

### **Challenges in cervical cancer ART**

In cervical cancer radiation therapy, interfraction changes in target shape and position are largely influenced by variation in bladder volume [64-66]. Despite drinking instructions given to the patient, the day-to-day bladder volume may vary strongly during the course of treatment and consequently affects the target position [67,68]. Instead of using large CTV-to-PTV margins to account for target volume changes during cervical cancer radiation therapy, the plan-library based plan-of-the-day adaptive strategy is often selected as the standard treatment strategy. Also in the Academic Medical Center, cervical cancer patients selected for radiation therapy are treated according to the daily plan selection adaptive strategy. Based on multiple CT images acquired before treatment with variable bladder volumes, several target volumes are defined and corresponding radiation therapy plans are generated. Prior to irradiation, the library plan best fitting the target volume as observed on pre-fraction CBCT imaging is manually selected.

Additionally, the adaptive strategy can be applied using proton therapy in order to reduce the dose to healthy tissues. In cervical cancer radiation therapy, the potential benefit of proton therapy is only investigated in a limited number of studies without validating the actual delivered dose [69-71]. Based on planned dose distributions, proton therapy is compared to radiation therapy using photons in terms of dose to the target volume and OARs. Besides the lack of plan robustness assessment, none of the published studies reported on dose distribution recalculation to evaluate differences between both treatment modalities in terms of delivered dose.

Alternatively, the definition of target volumes in radiation therapy is currently based on (PET-)CT imaging. The addition of MRI in the process of target definition allows for improvements in target volume definitions and enables a more precise and efficient treatment procedure. However, little is known about the accuracy of target definition using MRI in cervical cancer and this knowledge is required before the actual benefits of target volume optimization can be assessed.

To improve treatment outcome in cervical cancer, adaptive radiation therapy needs to be optimized in terms of treatment precision and treatment efficiency. Besides improvements on daily target localization, the optimization of cervical cancer ART includes the reduction of radiation-associated toxicity without compromising on tumor control. Therefore, the goal of this thesis is to optimize adaptive radiation therapy in cervical cancer in order to improve the precision and accuracy of radiation therapy while minimizing radiation-induced toxicity.

## 1.5 | Outline of this thesis

In this thesis, optimization strategies for adaptive radiation therapy in cervical cancer are presented and solutions for both photon therapy and proton therapy will be addressed. The optimization strategies and potential advantages of adaptive radiation therapy in cervical cancer are the topics of research.

Adaptive radiation therapy is increasingly used to correct for anatomical changes during fractionated irradiation. Several adaptive strategies can be applied, dependent of the available pre-treatment imaging techniques and deformation types. A practical adaptive treatment approach often used in the pelvic area is the plan-library based plan-of-the-day strategy. Before treatment, a library of plans is generated based on pre-treatment imaging and each treatment fraction a library plan is selected based on pre-fraction imaging. Also in the Academic Medical Center, the daily plan selection adaptive strategy is introduced for curative radiation therapy in cervical cancer. The dosimetric evaluation of this clinically applied adaptive strategy is described in **chapter 2**. Compared to a non-adaptive approach, the advantages of adaptive radiation therapy using the daily plan selection adaptive strategy are presented in terms of target coverage and dose to healthy tissues.

The application of ART using the plan-of-the-day strategy requires daily plan selection. In current clinical practice, after accurate patient set-up the library plan best fitting the target volume as observed on the pre-fraction CBCT is selected manually. Plan selection based on automatic image segmentation holds the promise to reduce the time in the treatment room and decrease observer dependency. A generic method to automatically segment the bladder on pre-fraction CBCT images is proposed in **chapter 3**. This generic method is designed to segment bladder volumes independent of the treatment position while only available pre-treatment CT data is used to guide the segmentation. In addition, segmentation results are validated by comparing segmented and manually delineated bladder structures.

The challenges to further optimize cervical cancer radiation therapy by combining adaptive radiation therapy with the use of protons are addressed in the **chapters 4 and 5**. Rotational IMRT techniques are used for photon-based treatments in daily clinical practice, which are not applicable in proton-based radiation therapy. Given certain distinct advantages of protons over conventionally used X-rays, a fixed beam configuration based on a limited number of beams is preferred when

applying IMPT. To select an appropriate beam configuration in terms of plan robustness, target coverage and sparing of surrounding healthy tissues, different beam configuration candidates are objectively compared in **chapter 4** using an advanced method based on Pareto fronts.

The application of adaptive proton therapy and the actual dosimetric advantages of adaptive proton therapy in cervical cancer are investigated in **chapter 5**. Using the selected beam configuration for cervical cancer IMPT, the potential benefit of adaptive proton therapy compared with adaptive photon therapy in cervical cancer is demonstrated in terms of target coverage and dose to OARs.

Target definition for radiation therapy planning is generally performed based on pre-treatment CT imaging. In cervical cancer, the recommended clinical target volume encompasses the GTV, cervix, uterus and upper part of the vagina. The addition of safety margins to the CTV resulted in relatively large target volumes and consequently increased the volume of healthy tissue receiving a substantial amount of dose. Moreover, large target volumes including the entire uterus are prone to anatomical changes during the course of radiation therapy. In order to optimize the target volume, it has been suggested to only include the invaded part of the uterus in the clinical target volume. Since the GTV is poorly visible on CT images, MRI is considered for tumor extent assessment. In order to validate tumor definition accuracy using MRI, a method to correlate surgical specimen imaging and MRI including soft tissue deformations is demonstrated in **chapter 6**. In addition, discrepancies between MRI-based and pathological-based tumor definitions were quantified.

The consequences of excluding the non-invaded part of the uterine body from the target volume after tumor definition based on MRI is addressed in **chapter 7**. For both photon therapy and proton therapy, radiation therapy planning is performed based on conventional target volumes and MRI-based target volumes and plans are compared for target coverage and OAR dose. Also, the dosimetric advantages of the improved target volume definition strategy are presented in terms of OAR dose reductions as well as estimated complication probability differences.

In **chapter 8**, the most important findings presented in this thesis will be summarized. Furthermore, the presented results will be discussed and compared with other solutions to improve cervical cancer radiation therapy. Also, future perspectives on cervical cancer radiation therapy as well as alternative treatment options in cervical cancer will be addressed.





# Chapter 2

## Dosimetric advantages of a clinical daily adaptive plan selection strategy compared with a non-adaptive strategy in cervical cancer radiation therapy

A version of this chapter has been submitted to Acta Oncologica as:

*Dosimetric advantages of a clinical daily adaptive plan selection strategy compared with a non-adaptive strategy in cervical cancer radiation therapy*

A.J.A.J. van de Schoot, P. de Boer, J. Visser, L.J.A. Stalpers, C.R.N. Rasch and A. Bel

## Abstract

### Purpose

Radiation therapy (RT) using a daily plan selection adaptive strategy can be applied to account for interfraction organ motion while limiting organ at risk dose. The aim of this study was to quantify the dosimetric consequences of daily plan selection compared to the non-adaptive approach in cervical cancer RT.

### Material & Methods

Ten consecutive patients who received pelvic irradiation, planning CTs (full and empty bladder), weekly post-fraction CTs and pre-fraction CBCTs were included. Non-adaptive plans were generated based on the PTV defined using the full bladder planning CT. For the adaptive strategy, multiple PTVs were created based on both planning CTs by ITV of the primary CTVs (i.e. GTV, cervix, corpus-uterus and upper part of the vagina) and corresponding library plans were generated. Daily CBCTs were rigidly aligned to the full bladder planning CT and plans were selected. Post-fraction CTs were non-rigidly registered to CBCTs and used to recalculate the non-adaptive and selected library plans. Differences in target coverage ( $D_{98\%} > 95\%$ ) and in daily  $V_{0.5Gy}$ ,  $V_{1.5Gy}$ ,  $V_{2Gy}$ ,  $D_{50\%}$  and  $D_{2\%}$  for rectum, bladder and bowel were assessed.

### Results

The non-adaptive strategy showed inadequate primary CTV coverage in 17% of the fractions. Daily plan selection compensated for anatomical changes and improved primary CTV coverage significantly ( $p < 0.01$ ) to 98%. Compared to the non-adaptive approach, daily plan selection decreased the dose to rectum and bowel indicated by significant ( $p < 0.01$ ) improvements for daily  $V_{0.5Gy}$ ,  $V_{1.5Gy}$ ,  $V_{2Gy}$ ,  $D_{50\%}$  and  $D_{2\%}$ . However, daily plan selection significantly increased the bladder  $V_{1.5Gy}$ ,  $V_{2Gy}$ ,  $D_{50\%}$  and  $D_{2\%}$ .

### Conclusion

Cervical cancer RT using the non-adaptive strategy showed inadequate target coverage. Daily plan selection corrected for day-to-day anatomical variations and resulted in adequate target coverage in all fractions. The dose to bowel and rectum was decreased significantly when applying adaptive RT.

## 2.1 | Introduction

The primary treatment for locally advanced cervical cancer consists of external beam radiation therapy (EBRT) with concomitant chemotherapy and subsequently a brachytherapy boost [72]. For patients with a contra-indication for chemotherapy, radiation therapy with concurrent hyperthermia is the recommended treatment strategy [18]. Advanced EBRT techniques such as intensity-modulated radiation therapy (IMRT) or volumetric modulated arc therapy (VMAT) allow highly conformal dose distributions. These advanced techniques are most effective when combined with adequate image guidance. However, large interfraction anatomical changes limit the efficacy of these treatment techniques [73]. Despite drinking instructions, day-to-day bladder volume variations contribute to an increased risk of target under-dosing and consequently increase the dose to surrounding healthy tissue [73].

Adaptive radiation therapy (ART) has the potential to anticipate on anatomical changes during fractionated EBRT by adapting the radiation delivery during the treatment course based on pre-fraction imaging. Several adaptive strategies, both offline and online approaches, have been investigated [53,56]. The most widely reported approach for pelvic EBRT is the plan-library based plan-of-the-day strategy [58-60]. Prior to treatment, a patient-specific plan library is defined by generating multiple treatment plans corresponding to different target volumes. Each treatment day the library plan best fitting the anatomy as observed on pre-fraction cone-beam CT (CBCT) is selected in order to anticipate on interfraction anatomical changes.

Despite the use of large population-based margins added to the clinical target volume (CTV) to form the planning target volume (PTV), the interfraction anatomical changes in cervical cancer EBRT might still induce target under-dosing. Furthermore, these large safety margins increase the dose to surrounding healthy tissues, which results in the enhancement of radiation-induced toxicities. Recently, several adaptive strategies in cervical cancer were investigated to anticipate on anatomical changes during the course of radiation therapy [54,65]. Next to the description of a clinically implemented adaptive strategy [59], most studies reported on tools to support adaptive strategies [65,74-76]. However, the actual dosimetric improvements of an adaptive strategy compared with the non-adaptive approach in terms of target coverage and organ at risk (OAR) sparing are still unknown.

To investigate the dosimetric consequences of an adaptive strategy and determine the area of improvement, differences in dose delivery between an adaptive and non-adaptive strategy need to be assessed. Therefore, the purpose of this study was to quantify the potential dosimetric advantages of a daily adaptive plan selection treatment strategy compared with a non-adaptive treatment approach in cervical cancer radiation therapy.

## 2.2 | Material & Methods

### Patients and imaging

Ten consecutive cervical cancer patients who received pelvic irradiation and additional CT imaging were included. All patients, treated between January 2014 and August 2015, gave written informed consent after local medical ethical approval for additional CT imaging initially acquired for a study to investigate adaptive proton therapy [77]. Besides two planning CTs (i.e. full and empty bladder), all patients received pre-fraction CBCT imaging (Synergy platform, Elekta AB, Stockholm, Sweden) and weekly CT imaging in treatment position directly after irradiation. Due to the limited field of view of CBCT imaging, volumes of interest in patients who received para-aortic lymph nodes irradiation were not completely visualized on pre-fraction CBCTs and therefore unsuitable for analysis. For tumor localization on CBCT, fiducial markers (2–4 per patient, Visicoil, 0.35 mm diameter, IBA Dosimetry GmbH, Schwarzenbruck, Germany) were implanted in the cervix during the pre-treatment examination under anesthesia.

Six patients were treated in the recommended prone position using a belly board device and for four patients the supine position was applied since the prone position was not possible. Aiming at irradiations with a full bladder, patients were instructed to empty their bladder, to drink 0.5 liter of water, and to refrain from voiding 1.5 h prior to each treatment fraction. As a result of the clinical introduction of ART at our department in April 2015, two out of the ten included patients were actually treated according to the adaptive strategy (Table 2.1). Instead of the adaptive strategy, for these patients the non-adaptive approach was simulated.

### Target and OAR definition

According to clinical guidelines [29], the gross tumor volume (GTV), corpus-uterus, cervix, upper part of the vagina and lymph nodes were delineated on all CTs by an experienced radiation oncologist. Also, rectum, bowel cavity, as a surrogate for small bowel and bladder were delineated according to RTOG guidelines. The bladder wall was created using a 3 mm inwards expansion of the delineated bladder [52].

The library of target structures for the adaptive strategy was created based on the planning CTs acquired with an empty and a full bladder. After bony registration of both planning CTs, corresponding primary CTVs (pCTVs) which encompassed the GTV, cervix, corpus-uterus and upper part of the vagina were registered using a structure-based deformable image registration algorithm [78]. The patient-specific full-range primary internal target volume (ITV) was divided in pITV subranges by scaling the deformation vectors (Figure 2.1). According to our clinically applied adaptive strategy, the full-range pITV was divided into one (pITV<sub>0-100</sub>), two (pITV<sub>0-50</sub>, pITV<sub>50-100</sub>) or three (pITV<sub>0-33</sub>, pITV<sub>33-67</sub>, pITV<sub>67-100</sub>) subranges when the top of corpus-uterus displacement was below 10 mm, between 10–20 mm or above 20 mm, respectively. Corresponding to each pITV

subrange an ITV was constructed by including the lymph nodes and PTVs were generated by enlarging ITVs with an 8 mm isotropic margin. The part of the pITV including the cervix and vagina was enlarged with a margin of 8 mm, 8 mm and 13 mm in left-right, superior-inferior and anterior-posterior direction, respectively.

In the non-adaptive approach, target definition was based on only the full bladder planning CT using associated delineations. The pCTV, encompassing the GTV, cervix, corpus-uterus and upper part of the vagina was expanded with an isotropic margin of 10 mm. The expanded pCTV was combined with the lymph nodes and enlarged with an 8 mm isotropic margin to form the PTV.

**Table 2.1** | Patient characteristics.

Patient	FIGO stage	Clinical treatment strategy	Treatment position	No. of ITVs
1 *	IB2	non-ART	prone	1
2 **	IIB	non-ART	prone	3
3 *	IB2	non-ART	prone	3
4 **	IIA	non-ART	prone	3
5 **	IIB	non-ART	supine	3
6 *	IIA	non-ART	prone	2
7 **	IIB	non-ART	prone	3
8 **	IIB	non-ART	supine	3
9 *	IB1	ART	supine	2
10 *	IB1	ART	supine	3

*Abbreviations:* FIGO = International Federation of Gynecology and Obstetrics; CT = computed tomography; ITV = internal target volume; non-ART = non-adaptive radiation therapy; ART = adaptive radiation therapy.

\* Both planning CTs acquired with LightSpeed RT16, General Electric Company, Waukesha WI, USA.

\*\* Full bladder planning CT acquired with Gemini TF, Philips Medical Systems, Eindhoven, the Netherlands and empty bladder planning CT acquired with LightSpeed RT16, General Electric Company, Waukesha WI, USA.

## Treatment planning

In the adaptive strategy, plans based on the defined PTVs were created to form the plan library and for the non-adaptive approach a single treatment plan was generated based on the corresponding PTV. Dual-arc VMAT (356° per arc, fixed 20° collimator angle) treatment plans with 10 MV beam energy and a prescribed PTV dose of 46 Gy (23 x 2 Gy) were created (Oncentra, Elekta AB, Stockholm, Sweden). All plans were optimized on a uniform 3 mm dose grid with the beam isocenter set to the PTV center of mass using the full bladder planning CT. Plan optimizations were performed using the clinically used set of planning objectives in order to minimize OAR dose while maintaining ICRU-based PTV coverage ( $D_{98\%} > 95\%$ ,  $D_{2\%} < 107\%$ ).

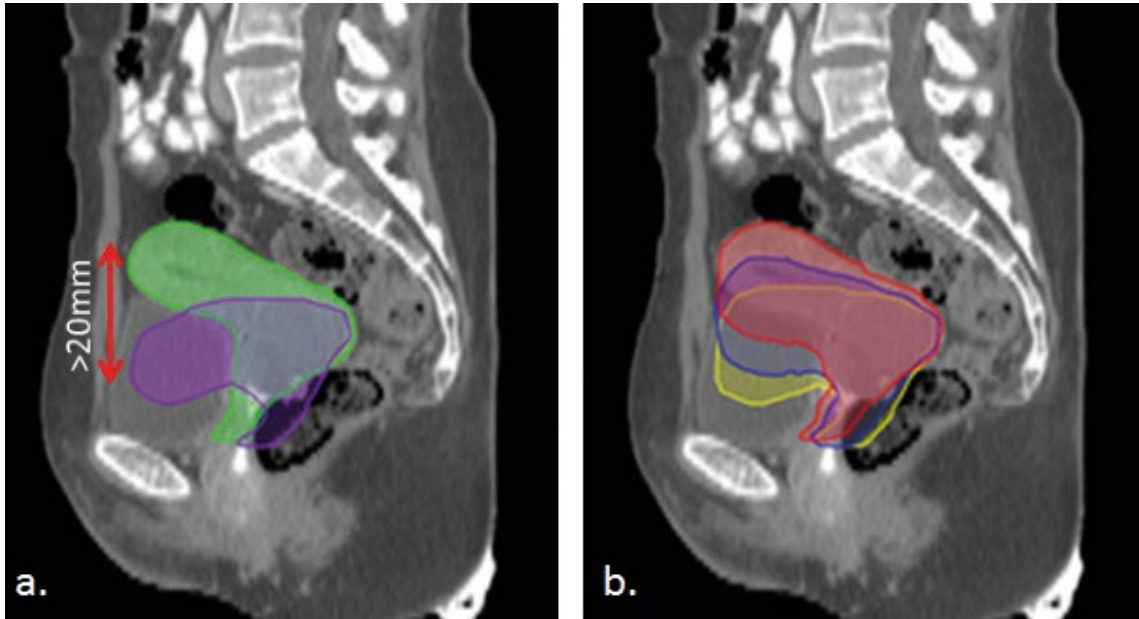


**Figure 2.1** | **a:** Sagittal view of the full bladder planning CT for patient 10 with in green the primary CTV corresponding to the full bladder planning CT and in purple the primary CTV corresponding to the empty bladder planning CT. The corpus-uterus top displacement is larger than 20 mm. **b:** Sagittal view of the full bladder planning CT for patient 10 with the primary ITV subranges (red, blue, yellow), obtained by dividing the full-range primary ITV based on linear scaling of the deformation vectors.

## Image analysis

Since CBCT grey values do not represent Hounsfield units (HU), CBCT images are not directly suitable for dose calculation. To enable daily dose distribution calculation, selected CTs were deformably registered to CBCT images (VelocityAI, version 3.1.0, Varian Medical Systems, Inc., Palo Alto, CA, USA) [79]. For each pre-fraction CBCT image, the CT best representing the daily pelvic anatomy (i.e. one of the planning CTs or weekly CTs) was selected to maximize deformable registration accuracy. After rigid alignment based on bony anatomy, selected CTs were deformed to represent CBCT images. Accordingly, delineations were deformed to match the deformed CT. Reported evaluations on deformable CT-to-CBCT registration performances in the pelvic area using the VelocityAI software showed accurate results and allowed for HU modification and structure deformation after deformable image registration [80,81]. Next to the reported evaluations, derived registration results in this study were also validated visually to verify plausible deformations.

For plan selection in the adaptive strategy, deformed CTs representing daily anatomy were aligned with the full bladder planning CT based on bony anatomy. Next, patient-specific PTVs were projected on the daily images and the PTV encompassing the target with the implanted fiducial markers inside the PTV was selected.

## Dosimetric analysis

The library plan corresponding to the selected ITV and the non-adaptive plan were recalculated to obtain daily dose distributions according to both treatment strategies. Dose-volume histograms (DVHs) of daily dose distributions were calculated for the pCTV, lymph nodes, CTV, bladder, bladder wall, bowel cavity and rectum. For the target structures, the fraction dose to 98%, 50% and 2% of the volume ( $D_{98\%}$ ,  $D_{50\%}$ ,  $D_{2\%}$ ) were calculated and differences between ICRU-based coverage ( $D_{98\%} > 95\%$ ) were tested pairwise for significance (McNemar chi-square test). Besides the median ( $D_{50\%}$ ) and near-maximum ( $D_{2\%}$ ) fraction dose, the  $V_{0.5\text{Gy}}$ ,  $V_{1.5\text{Gy}}$  and  $V_{2\text{Gy}}$  for OARs were extracted from daily DVHs and tested pairwise for significance using a non-parametric statistical test (Wilcoxon signed-rank test).

## 2.3 | Results

Since five fractions were excluded because CBCT quality was not suitable for analysis, in total 225 fractions were evaluated. Seven out of the ten patients showed pre-treatment displacements of the corpus-uterus top larger than 20 mm and resulted in plan libraries consisting of three plans. For two patients, the plan library consisted of two plans and a one-plan library was generated for one patient.

The selected library plans per patient for the adaptive strategy are presented (Figure 2.2). For most of the patients, in the majority of fractions the selected library plan corresponded to the target position related to a full bladder ( $PTV_{67-100}$ ,  $PTV_{50-100}$ ). However, despite drinking instructions, the preferred irradiation with a full bladder was not achieved for all fractions and library plans were selected corresponding to target positions related to low or intermediate bladder volumes. For patients with a three-plan library, the selection frequency of the library plan with the target position related to a full bladder ( $PTV_{67-100}$ ) was on average 50% and 57% for the prone and supine treatment position, respectively (Figure 2.2).

A typical example of fraction DVHs is shown for the target structures (Figure 2.3). In total, 24 (11%) and 38 (17%) fractions in the non-adaptive approach showed inadequate coverage ( $D_{98\%} < 95\%$ ) for the CTV and pCTV, respectively. Daily plan selection anticipated on day-to-day anatomical variations and resulted in adequate target coverage in 225 (100%) and 220 (98%) fractions for the CTV and pCTV, respectively. An adaptive strategy instead of a non-adaptive approach significantly ( $p < 0.01$ ) improved daily coverage ( $D_{98\%} > 95\%$ ) for the pCTV and CTV (Figure 2.4).

As an example, for one patient also fraction DVHs for OARs are shown (Figure 2.3). Figures 2.A.1–2.A.10 show fraction DVHs of target volumes and OARs for each patient. Compared to the non-adaptive approach, daily plan selection reduced the dose to rectum and bowel cavity indicated by significant improvements ( $p < 0.01$ ) of all DVH parameters of interest (Figure 2.5). However, the  $D_{50\%}$ ,  $V_{1.5\text{Gy}}$  and  $V_{2\text{Gy}}$  for bladder were increased significantly ( $p < 0.05$ ) when applying the adaptive strategy instead of the non-adaptive approach. Table 2.2 presents the mean parameter values for

the OARs and the absolute and relative differences between non-adaptive and adaptive radiation therapy.

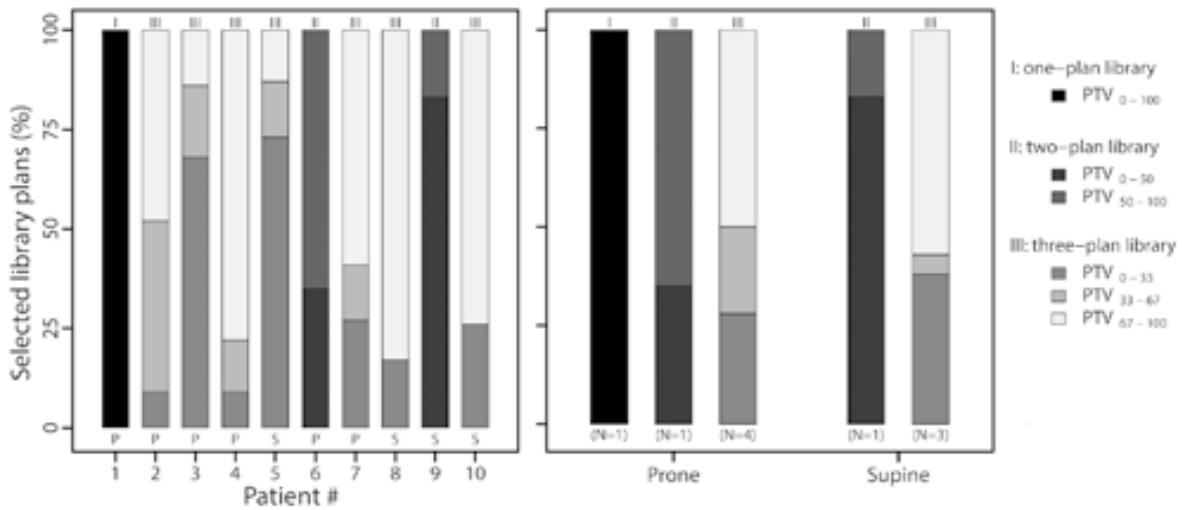


Figure 2.2 | Frequency of selected library plans during the course of treatment per patient (left) and average percentages per treatment position (right). The number on top of each bar represents the number of available library plans and the character in the left bar plot (*P*; *S*) represents the treatment position (*prone*; *supine*).

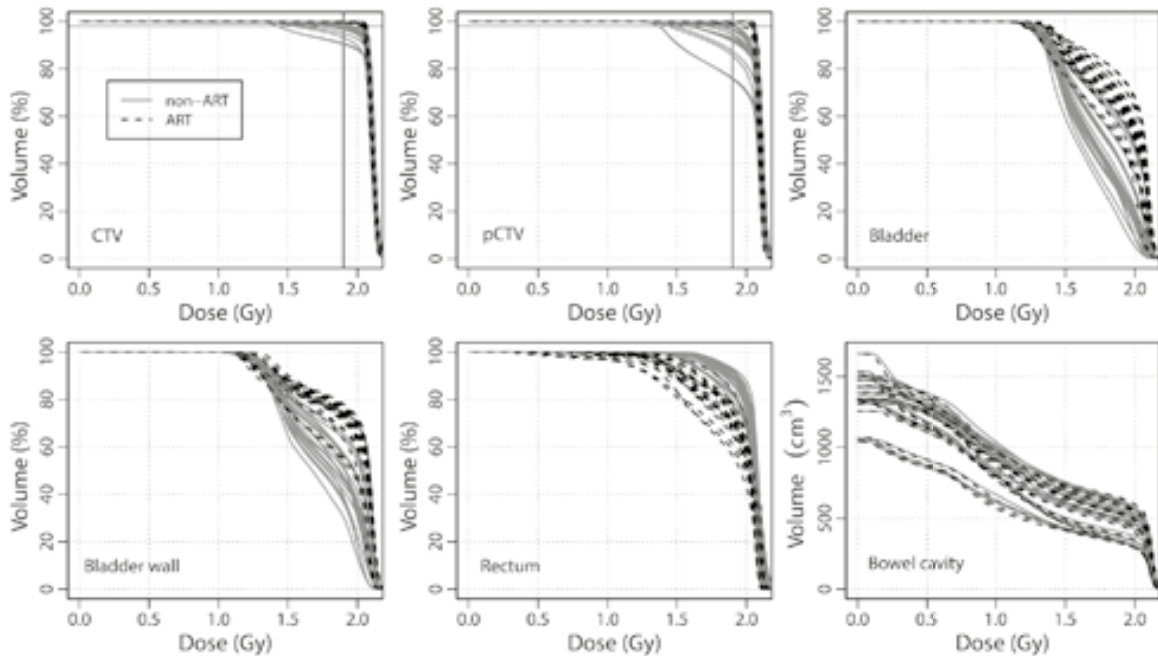
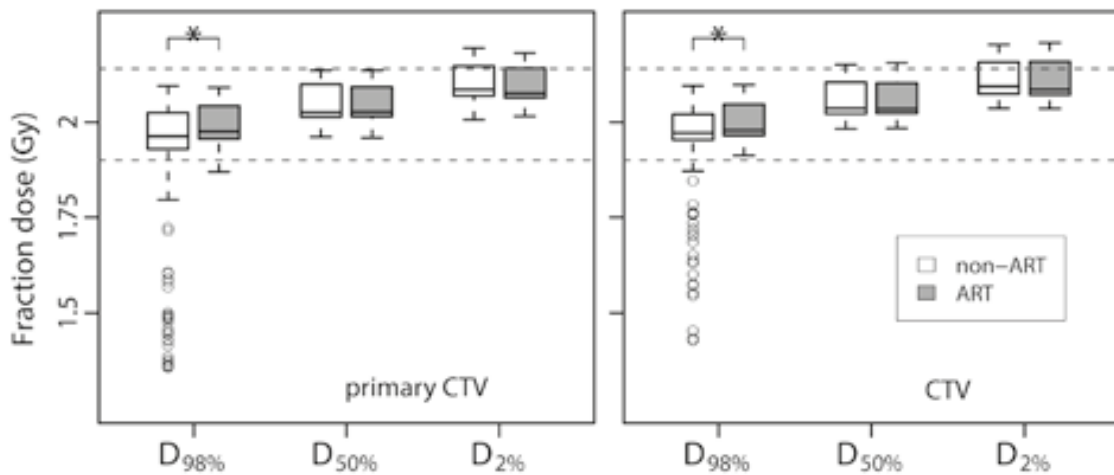


Figure 2.3 | For patient 3, DVHs of recalculated fraction dose distributions are shown for target volumes (CTV, pCTV) and OARs (bladder, bladder wall, rectum, bowel cavity) based on the non-adaptive (solid lines) and adaptive (dashed lines) treatment strategy. The intersection of the 2 solid black lines in the DVHs for target structures indicates  $V_{95\%}=98\%$ .

**Table 2.2** | Comparison of the mean DVH parameter values for the recalculated fractions of all patients.

	non-ART	ART	Absolute difference (non-ART – ART)	Relative difference (%)	p-Value
<b>Bladder</b>					
V <sub>0.5Gy</sub> (%)	99.9	99.9	0.0	0.0	0.4
V <sub>1.5Gy</sub> (%)	82.6	85.4	-2.8	-3.3	<0.01
V <sub>2Gy</sub> (%)	38.5	42.8	-4.3	-11.1	0.02
D <sub>50%</sub> (Gy)	1.9	1.9	0.0	-2.2	0.02
D <sub>2%</sub> (Gy)	2.0	2.0	0.0	-0.1	0.7
<b>Rectum</b>					
V <sub>0.5Gy</sub> (%)	99.9	99.9	0.1	0.1	<0.001
V <sub>1.5Gy</sub> (%)	93.5	91.4	2.1	2.3	<0.001
V <sub>2Gy</sub> (%)	36.1	28.8	7.3	20.2	<0.001
D <sub>50%</sub> (Gy)	1.9	1.9	0.0	1.0	<0.001
D <sub>2%</sub> (Gy)	2.0	2.0	0.0	0.4	<0.001
<b>Bowel cavity</b>					
V <sub>0.5Gy</sub> (cm <sup>3</sup> )	1490	1470.4	19.6	1.3	<0.001
V <sub>1.5Gy</sub> (cm <sup>3</sup> )	688.6	668.9	19.6	2.9	<0.001
V <sub>2Gy</sub> (cm <sup>3</sup> )	406.7	372.2	34.5	8.5	<0.001
D <sub>50%</sub> (Gy)	1.2	1.2	0.0	2.7	<0.001
D <sub>2%</sub> (Gy)	2.0	2.0	0.0	0.2	<0.001

Abbreviations: non-ART = non-adaptive radiation therapy; ART = adaptive radiation therapy.



**Figure 2.4** | For the recalculated fraction dose distributions based on the primary CTV (left) and the CTV (right), boxplots of daily dose parameters over all analyzed fractions of all included patients are shown for both the non-adaptive (non-ART) and the adaptive (ART) strategy. Boxes represent upper and lower quartiles (IQR), the band inside the box the median value and the whiskers the highest (lowest) value within 1.5 IQR of the upper (lower) quartile. Dashed gray horizontal lines indicate 95% and 107% of the prescribed fraction dose. Horizontal lines including an asterisk indicate statistical significant difference ( $p < 0.01$ ).

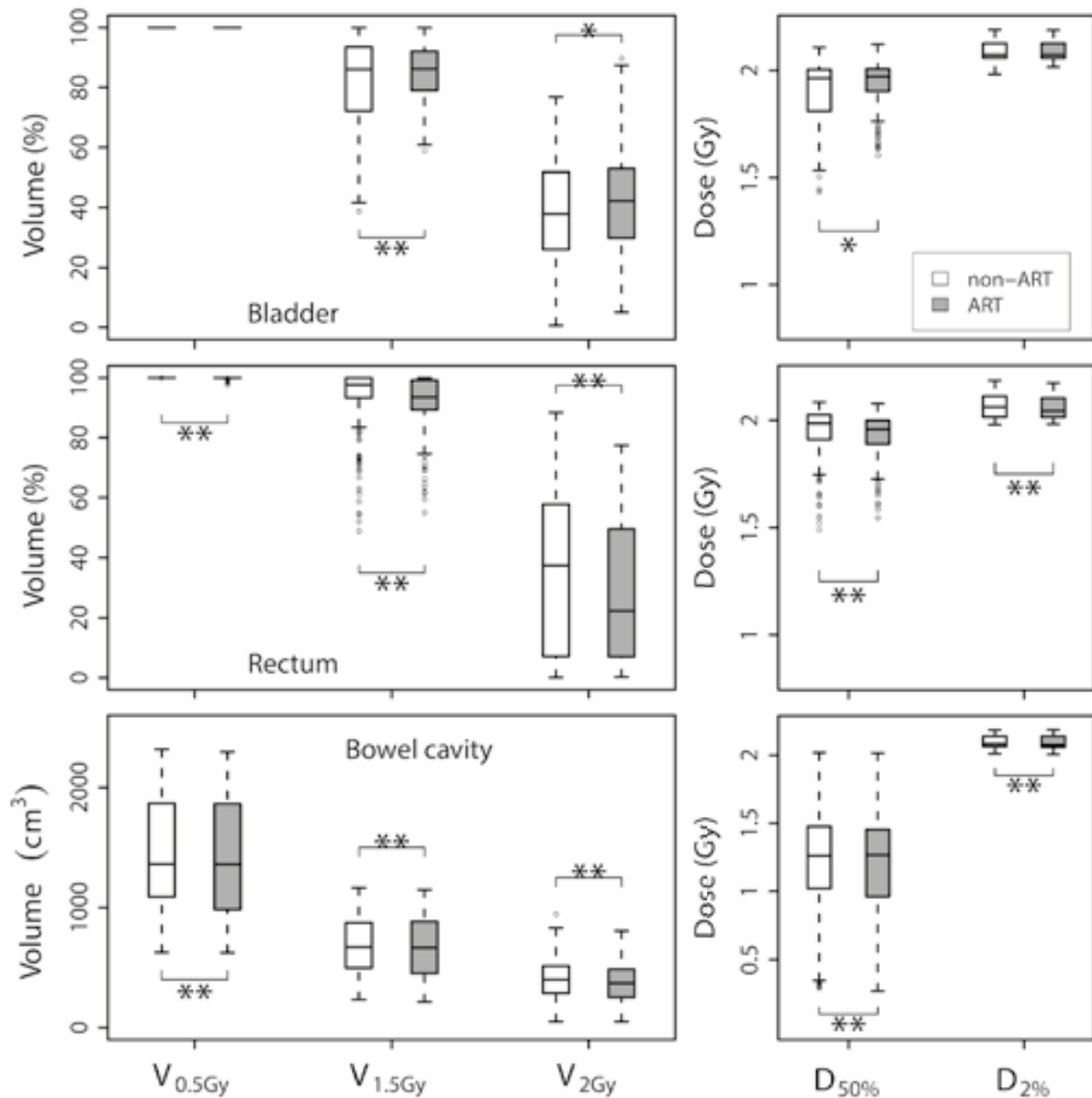


**Figure 2.5** | For the non-adaptive (non-ART) and adaptive (ART) strategy, boxplots of fraction DVH parameters over all analyzed fractions of all patients are shown for bladder (upper), rectum (middle) and bowel cavity (lower). For the meaning of box, whiskers and dots: see Figure 2.4. Horizontal lines including asterisks indicate statistical significant difference ( $*p < 0.05$ ;  $**p < 0.01$ ).

## 2.4 | Discussion

In this first realistic dosimetric analysis of an adaptive strategy in cervical cancer radiation therapy, we investigated the potential advantages of a daily plan selection strategy compared to a non-adaptive approach in cervical cancer radiation therapy. Using a plan-library based plan-of-the-day adaptive strategy to anticipate on day-to-day anatomical variations, daily dose distributions of both adaptive and non-adaptive treatments were calculated based on pre-fraction CBCT

imaging and compared for target coverage and OAR sparing. Compared to non-adaptive radiation therapy, a daily plan selection adaptive strategy allowed us to anticipate on anatomical changes and consequently improved daily target coverage significantly. Additionally, daily plan selection reduced the dose to rectum and bowel significantly, however the clinical relevance of the limited dose differences has to be investigated.

Previously conducted research on ART in cervical cancer focused either on the optimization of various adaptive strategies to correct for interfraction anatomical changes [54,65,82], tools to guide or automate adaptive strategies [75,76] or the clinical implementation of cervical cancer ART [59]. However, none of them validated the actual benefit of an adaptive strategy in terms of delivered dose while taking into account the day-to-day anatomical variations. Our recalculated daily dose distributions based on pre-fraction imaging for both a non-adaptive and adaptive strategy resulted in representative comparisons in terms of differences in target coverage and OAR sparing.

Our dosimetric analysis was performed based on a relatively small patient population. Because the majority of patients were treated using the non-adaptive approach, we simulated for these patients adaptive treatments according to the current clinical practice. For the two patients treated using the adaptive strategy, treatments were simulated according to the non-adaptive approach to fairly quantify the dosimetric consequences of the adaptive strategy. Although we quantified dosimetric differences, a prospective evaluation of clinically applied adaptive treatments is required to determine its actual dosimetric benefit. Furthermore, a larger number of patients will provide more information on target coverage improvement and maximum achievable OAR sparing.

Although the median and near-maximum target dose remained similar, we found a significant improvement on target coverage ( $D_{98\%} > 95\%$ ) when applying the adaptive strategy while the dose to rectum and bowel decreased significantly. However, the anticipation on anatomical changes by daily plan selection resulted in an increased dose to the adjacent bladder, indicated by the  $V_{2Gy}$ ,  $V_{1.5Gy}$  and  $D_{50\%}$  bladder parameters. Since adaptive target volumes were created based on bladder volume variations, bladder sparing in ART was expected to be less [83]. To avoid the increase of bladder dose when applying the adaptive strategy, reductions of CTV-to-PTV margins could be considered. Furthermore, target volume definitions could be optimized based on magnetic resonance imaging (MRI) by excluding the healthy corpus-uterus part from the target volume [6,84].

Instead of accumulated dose distributions, we compared recalculated fraction dose distributions. To reliably accumulate dose distributions within delineated organs, deformable image registration including accurate voxel-to-voxel correspondence is required. Due to the limited soft-tissue contrast in CBCT imaging, we decided to evaluate fraction dose distributions separately, but statistical tests were applied pairwise.

In this study, HU modification and structure warping was performed based on deformable image registration between CT and CBCT imaging using the implemented algorithm in VelocityAI. Deformable registrations between CT and CBCT imaging for pelvic anatomy using this algorithm

were previously evaluated in terms of registration errors and associated dose distribution uncertainties [80,81]. Compared to the average registration error (1.9 mm) across the whole pelvic area, the average registration error for bladder (4.6 mm) was relatively large due to initial large bladder volume differences [80]. Since we minimized the registration errors by selecting the CT best representing the daily pelvic anatomy, our deformable registrations used for HU modification and structure warping are considered accurate. In addition, all deformable registration results were validated by visual inspection for plausible deformations. Furthermore, Onozato *et al.* [81] evaluated the accuracy of dose calculation for pelvic anatomy after deformable registration between CT and CBCT imaging and reported dose uncertainties of on average 1.2%. The effect of residual deformation errors on our results was expected to be negligible, also because dose distributions for both the non-adaptive and adaptive strategy were calculated using identical deformed CT images including similar residual errors.

Intrafraction organ motion during cervical cancer irradiation can be considerable and might affect dose delivery [74]. In this study, CBCTs acquired prior to irradiation were used for both plan selection and dose recalculation. Possible consequences of intrafraction anatomical changes are therefore not represented by our calculated dose distributions. However, the reported intrafraction organ motion by Heijkoop *et al.* [74] is based on pre- and post-fraction CBCT imaging with a relatively large interval time of 20.8 minutes. According to our clinical experience, all operations between pre-fraction CBCT and the end of dose delivery, including patient position correction, library plan selection and VMAT dose delivery, is estimated to take up to 7 minutes. Consequently, the intrafraction organ motion present in our patients is assumed to be much smaller compared to the reported intrafraction displacements. Also, the use of ITVs in our adaptive strategy already compensates for possible intrafraction target motion induced by intrafraction bladder filling. Hence, dosimetric uncertainties induced by intrafraction anatomical changes in cervical cancer radiation therapy is assumed to be limited.

The presented adaptive strategy is designed to anticipate on day-to-day anatomical variations based on pre-treatment predicted deformations. However, anatomical changes not represented by the library plans (e.g. due to changing bowel or rectum volume) can limit the efficiency of this adaptive strategy. Heijkoop *et al.* [59] selected a motion-robust backup plan with very generous margins in 17.5% of all fractions to cover these unpredicted variations, however this will consequently limit OAR sparing.

In the future, our adaptive procedure will be optimized to reduce clinical workload and minimize OAR dose. Also, the use of online plan adaptations based on daily MRI will be implemented [85]. First of all, MRI guidance can be introduced to avoid plan selection difficulties due to limited CBCT image quality or to implement additional boost techniques based on tumor response. Moreover, the clinical introduction of MRI-guided radiation therapy allows online plan adaptations and could be the next step in online adaptive cervical cancer RT [85].

## 2.5 | Conclusion

An adaptive strategy using daily plan selection allows correcting for day-to-day anatomical variations in cervical cancer radiation therapy. Compared to a non-adaptive approach, significant improvements in target coverage were found when applying the adaptive strategy. Additionally, a significant reduction in dose to bowel cavity and rectum was observed with a yet unclear clinical relevance.

## Appendix 2.A

Patient 1 – plan library for adaptive radiation therapy consisted of 1 plan

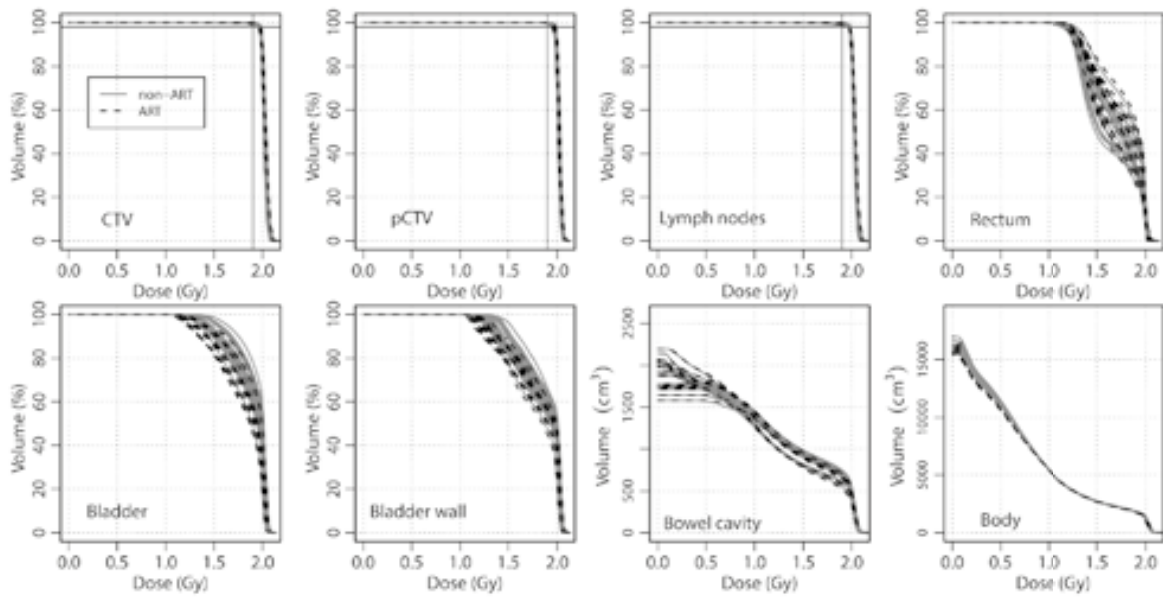


Figure 2.A.1 | Dose-volume histograms of the recalculated fraction dose distributions are shown based on the non-adaptive and the adaptive strategy for both the target volumes and OARs. The intersection of the two solid lines indicates  $D_{98\%}$ =95% of the prescribed fraction dose.

Patient 2 – plan library for adaptive radiation therapy consisted of 3 plans

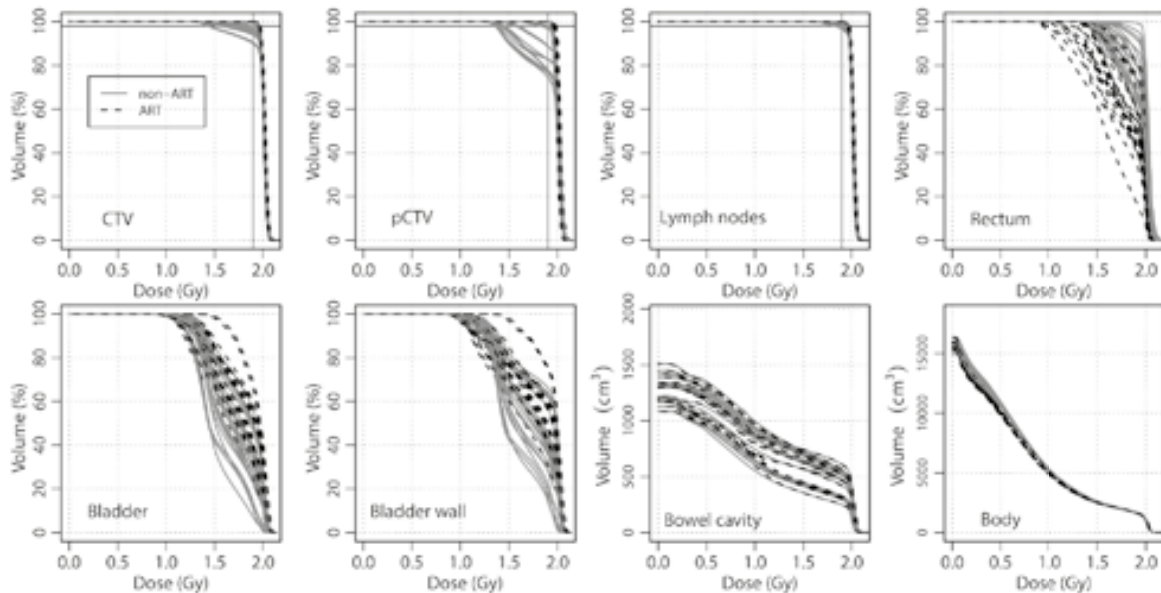


Figure 2.A.2 | Dose-volume histograms of the recalculated fraction dose distributions are shown based on the non-adaptive and the adaptive strategy for both the target volumes and OARs. The intersection of the two solid lines indicates  $D_{98\%}$ =95% of the prescribed fraction dose.

Patient 3 – plan library for adaptive radiation therapy consisted of 3 plans

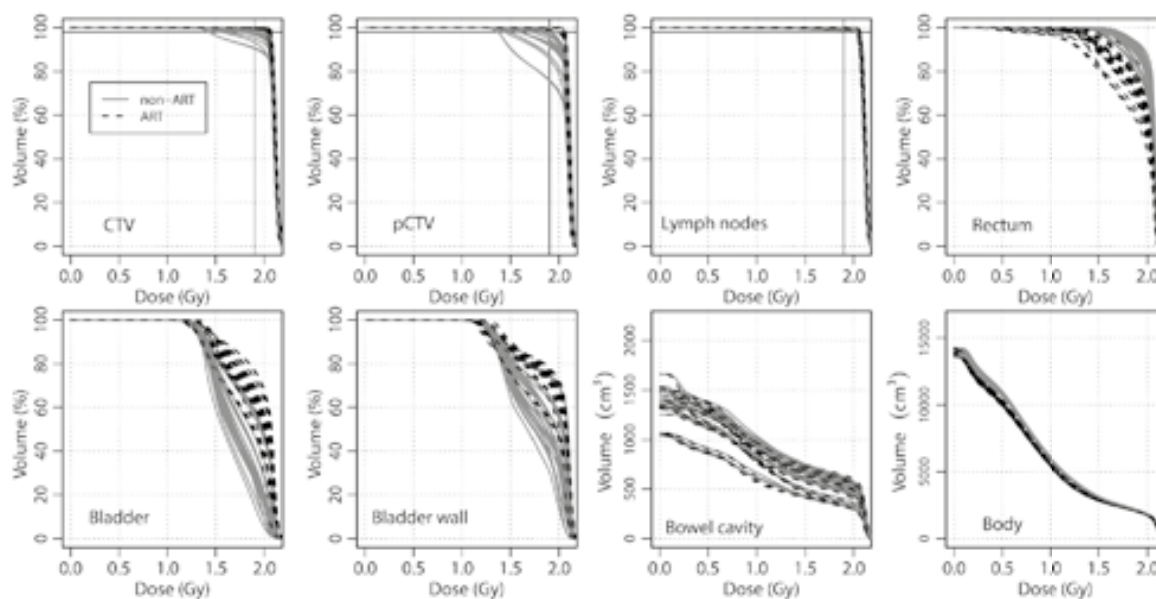


Figure 2.A.3 | Dose-volume histograms of the recalculated fraction dose distributions are shown based on the non-adaptive and the adaptive strategy for both the target volumes and OARs. The intersection of the two solid lines indicates  $D_{98\%}=95\%$  of the prescribed fraction dose.

Patient 4 – plan library for adaptive radiation therapy consisted of 3 plans

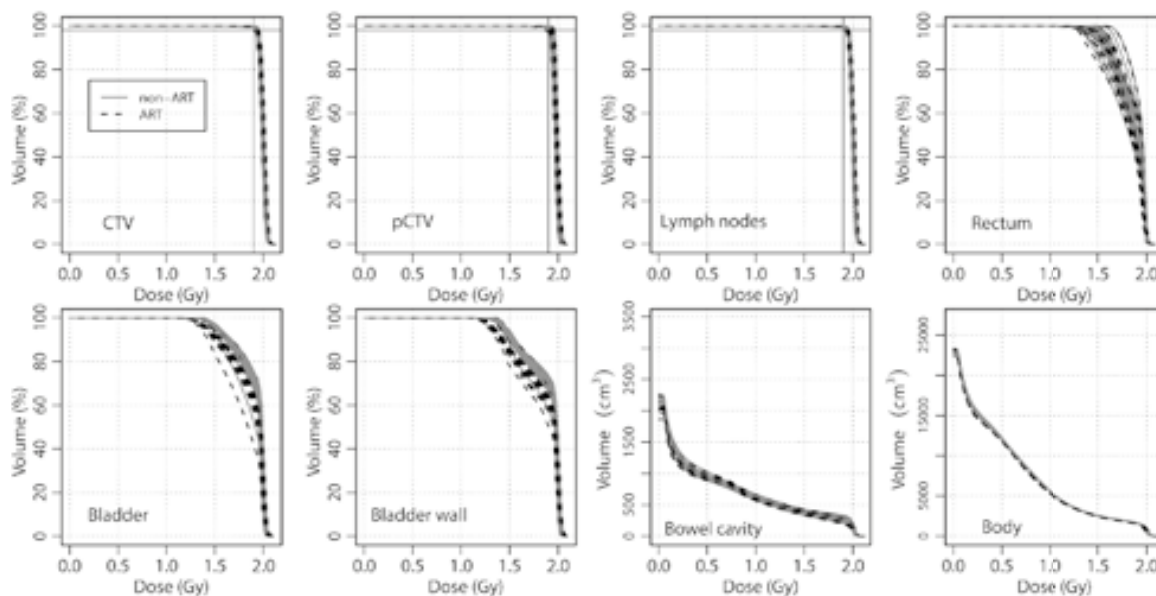


Figure 2.A.4 | Dose-volume histograms of the recalculated fraction dose distributions are shown based on the non-adaptive and the adaptive strategy for both the target volumes and OARs. The intersection of the two solid lines indicates  $D_{98\%}=95\%$  of the prescribed fraction dose.

Patient 5 – plan library for adaptive radiation therapy consisted of 3 plans

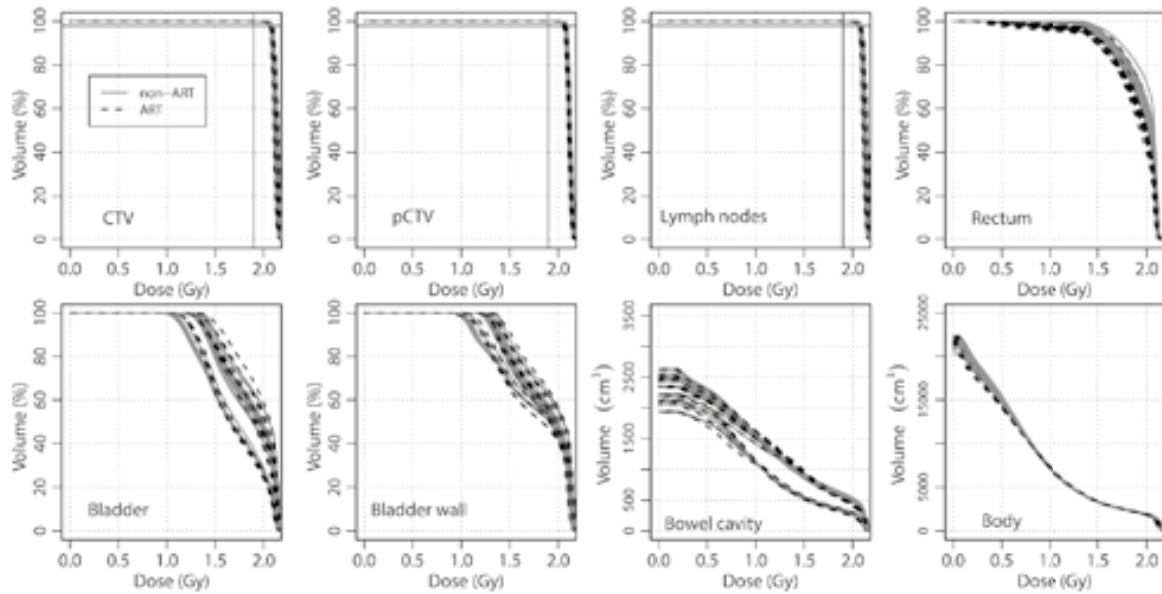


Figure 2.A.5 | Dose-volume histograms of the recalculated fraction dose distributions are shown based on the non-adaptive and the adaptive strategy for both the target volumes and OARs. The intersection of the two solid lines indicates  $D_{98\%} = 95\%$  of the prescribed fraction dose.

Patient 6 – plan library for adaptive radiation therapy consisted of 2 plans

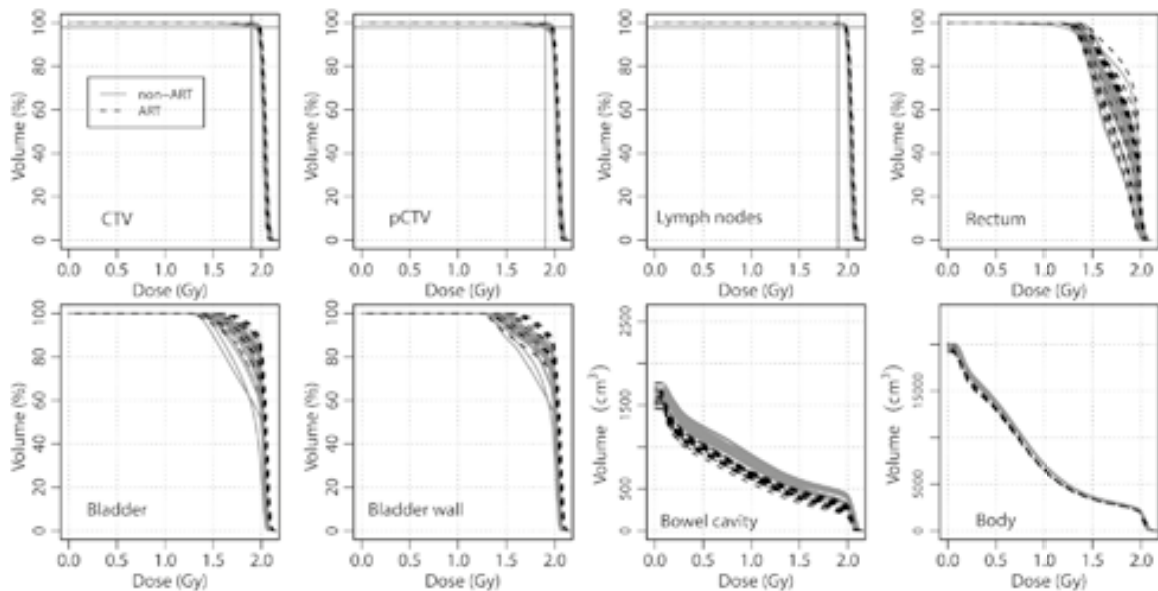


Figure 2.A.6 | Dose-volume histograms of the recalculated fraction dose distributions are shown based on the non-adaptive and the adaptive strategy for both the target volumes and OARs. The intersection of the two solid lines indicates  $D_{98\%} = 95\%$  of the prescribed fraction dose.

Patient 7 – plan library for adaptive radiation therapy consisted of 3 plans

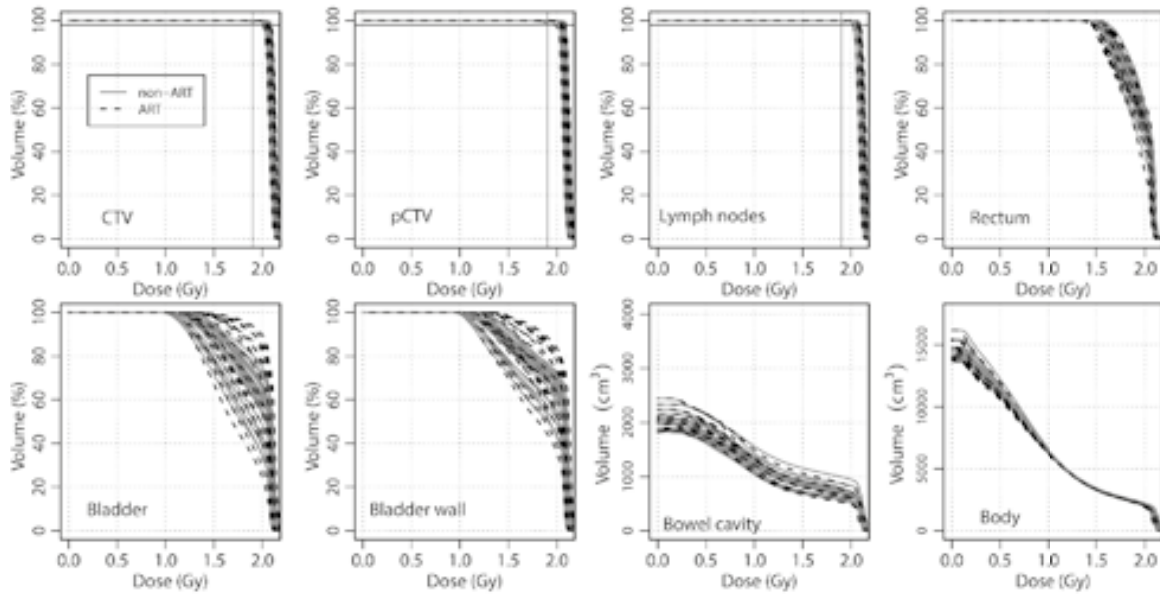


Figure 2.A.7 | Dose-volume histograms of the recalculated fraction dose distributions are shown based on the non-adaptive and the adaptive strategy for both the target volumes and OARs. The intersection of the two solid lines indicates  $D_{98\%}=95\%$  of the prescribed fraction dose.

Patient 8 – plan library for adaptive radiation therapy consisted of 3 plans

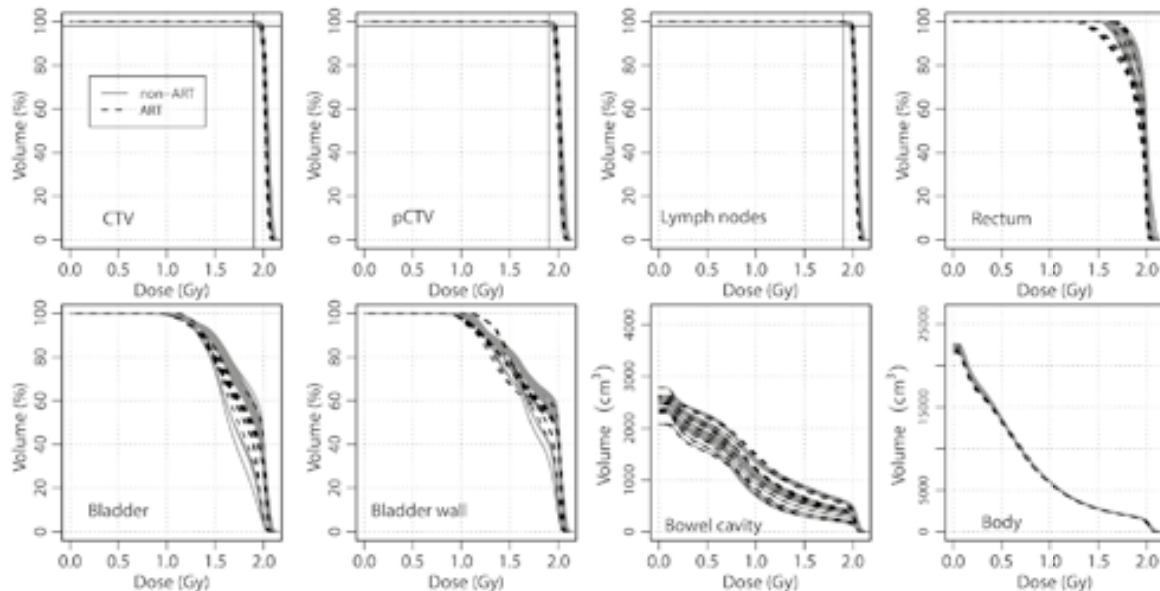


Figure 2.A.8 | Dose-volume histograms of the recalculated fraction dose distributions are shown based on the non-adaptive and the adaptive strategy for both the target volumes and OARs. The intersection of the two solid lines indicates  $D_{98\%}=95\%$  of the prescribed fraction dose.

Patient 9 – plan library for adaptive radiation therapy consisted of 2 plans

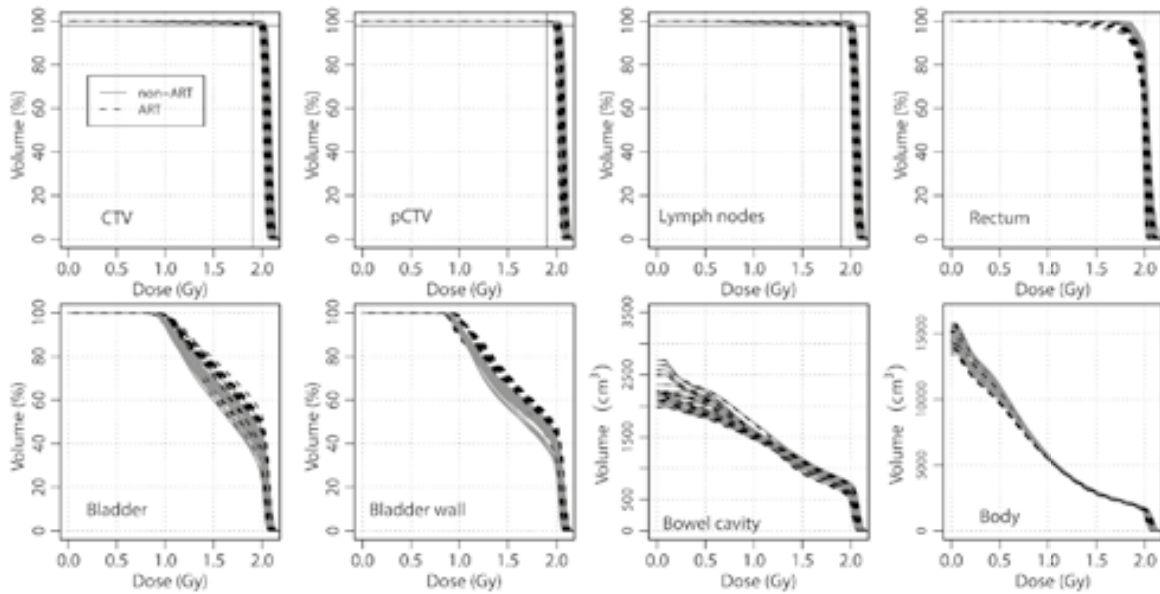


Figure 2.A.9 | Dose-volume histograms of the recalculated fraction dose distributions are shown based on the non-adaptive and the adaptive strategy for both the target volumes and OARs. The intersection of the two solid lines indicates  $D_{98\%}$ =95% of the prescribed fraction dose.

Patient 10 – plan library for adaptive radiation therapy consisted of 3 plans

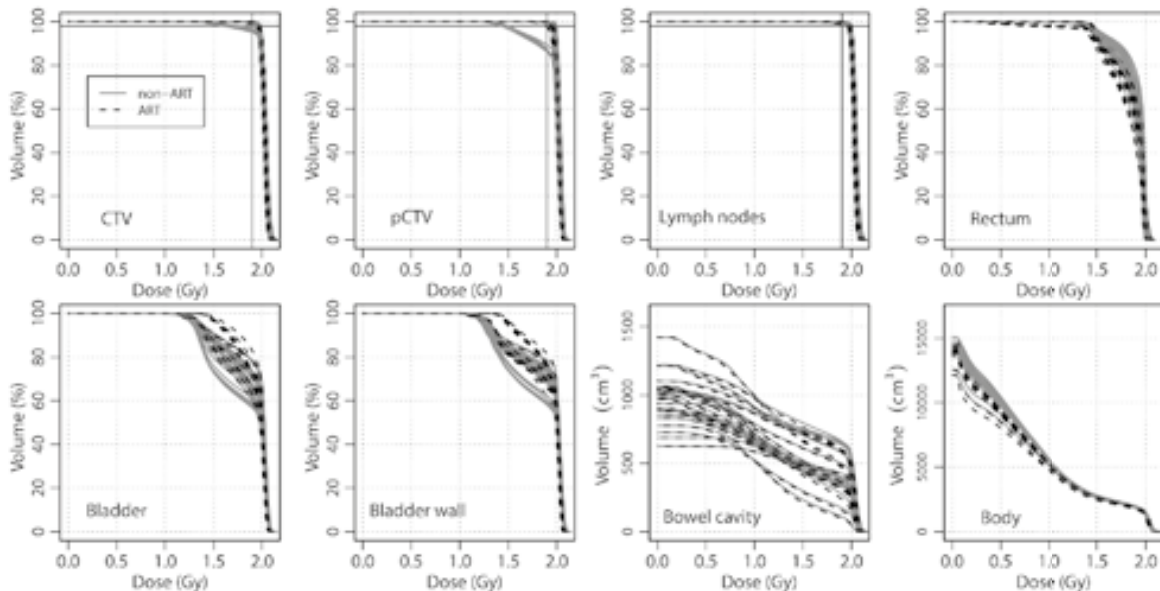


Figure 2.A.10 | Dose-volume histograms of the recalculated fraction dose distributions are shown based on the non-adaptive and the adaptive strategy for both the target volumes and OARs. The intersection of the two solid lines indicates  $D_{98\%}$ =95% of the prescribed fraction dose.





# Chapter 3

Generic method for automatic bladder segmentation on cone beam CT using a patient-specific bladder shape model

A version of this chapter has been published as:

*Generic method for automatic bladder segmentation on cone beam CT using a patient-specific bladder shape model*

A.J.A.J. van de Schoot, G. Schooneveldt, S. Wognum, M.S. Hoogeman, X. Chai, L.J.A. Stalpers, C.R.N. Rasch and A. Bel

*Medical Physics* 2014; 41(3): 031707.

<http://dx.doi.org/10.1118/1.4865762>

## **Abstract**

### **Purpose**

The aim of this study is to develop and validate a generic method for automatic bladder segmentation on CBCT, independent of gender and treatment position (prone or supine), using only pre-treatment imaging data.

### **Material & Methods**

Data of twenty patients, treated for tumors in the pelvic region with the entire bladder visible on CT and CBCT, were divided into four equally sized groups based on gender and treatment position. The full and empty bladder contour, that can be acquired with pre-treatment CT imaging, were used to generate a patient-specific bladder shape model. This model was used to guide the segmentation process on CBCT. To obtain the bladder segmentation, the reference bladder contour was deformed iteratively by maximizing the cross-correlation between directional grey value gradients over the reference and CBCT bladder edge. To overcome incorrect segmentations caused by CBCT image artifacts, automatic adaptations were implemented. Moreover, locally incorrect segmentations could be adapted manually. After each adapted segmentation, the bladder shape model was expanded and new shape patterns were calculated for following segmentations. All available CBCTs were used to validate the segmentation algorithm. The bladder segmentations were validated by comparison with the manual delineations and the segmentation performance was quantified using the Dice similarity coefficient (DSC), surface distance error (SDE) and SD of contour-to-contour distances. Also, bladder volumes obtained by manual delineations and segmentations were compared using a Bland-Altman error analysis.

### **Results**

The mean DSC, mean SDE and mean SD of contour-to-contour distances between segmentations and manual delineations were 0.87, 0.27 cm and 0.22 cm (female, prone), 0.85, 0.28 cm and 0.22 cm (female, supine), 0.89, 0.21 cm and 0.17 cm (male, supine) and 0.88, 0.23 cm and 0.17 cm (male, prone), respectively. Manual local adaptations improved the segmentation results significantly ( $p < 0.01$ ) based on DSC (6.72%) and SD of contour-to-contour distances (0.08 cm) and decreased the 95% confidence intervals of the bladder volume differences. Moreover, expanding the shape model improved the segmentation results significantly ( $p < 0.01$ ) based on DSC and SD of contour-to-contour distances.

### **Conclusion**

This patient-specific shape model based automatic bladder segmentation method on CBCT is accurate and generic. Our segmentation method only needs two pre-treatment imaging data sets as prior knowledge, is independent of patient gender and patient treatment position and has the possibility to manually adapt the segmentation locally.

### 3.1 | Introduction

Image-guided radiation therapy (IGRT) using daily cone beam computed tomography (CBCT) aims to safeguard the delivery of the planned dose to the patient [86,87]. However, anatomical deformations in patients limit the benefits of IGRT, since a straightforward positional correction is often not possible. The pelvic region contains several organs, e.g. bladder, rectum and cervix-uterus or prostate, with large daily variation in size and position during fractionated radiation therapy (RT) [64,88–91]. To compensate for these geometrical uncertainties, large safety margins around the target volume have to be applied [92,93]. However, these margins result in a high dose to surrounding healthy tissue and are in some cases even insufficient [94,95].

Adaptive radiation therapy (ART) is increasingly used to correct for these large interfraction deformations during fractionated RT and can be applied using several strategies, dependent on the size of deformations and position verification possibilities [53,96–98]. Originally, ART was developed as an offline strategy to correct for systematic errors by re-planning during the course of RT [47,48]. However, this adaptive strategy induces additional clinical workload during RT [56]. More recently, an alternative practical approach of ART using a multiple-plan strategy has been applied more frequently [60,63,83,98,99]. Several treatment plans are designed in advance based on pre-treatment imaging with substantial target variation in size and position. Each treatment day the plan corresponding best with the target position, the plan-of-the-day, will be selected while the patient is positioned correctly on the treatment table. This online plan selection procedure is based on daily CBCT imaging and will lead to less irradiated healthy tissue without reducing CTV coverage [60,99]. Consequently, this can lead to the use of smaller CTV-to-PTV margins in future. In this plan-of-the-day approach for tumors in the pelvic region the bladder plays a crucial role, either as a deforming target organ in the case of bladder tumors [60,98,99] or as an organ at risk (OAR) influencing the target position for cervix-uterus tumors [64,83] or prostate tumors [97]. Therefore, daily quantification of the size and position of the bladder will be of interest in those adaptive strategies.

Automatic organ segmentation on daily CBCT images is challenging due to the poor soft tissue contrast and the various reconstruction artifacts [100], but it is required for online recalculation of the dose [101] or adequate image guidance [102,103]. Furthermore, automatic segmentation of the bladder on daily CBCT images will facilitate multiple-plan ART in different ways. To accumulate the delivered dose to the bladder correctly, the daily size and position of the bladder need to be determined [104,105]. Moreover, automatic bladder segmentation can facilitate plan-of-the-day selection from a library of plans by decreasing the observer dependency and decision time in the treatment room [63,106,107].

Previously, two automatic bladder segmentation methods on CBCT were developed in our group [106,107]. However, both methods have limitations in their application for multiple-plan ART. The first proposed segmentation method was based on a training set acquired with the first five CBCTs and is hampering the application from the start of the adaptive treatment

[106]. The second proposed method used a population-based bladder shape model to guide the segmentation [107]. However, this population-based model needed a sufficient number of bladder shapes to describe all patient-specific shape variations and for each gender and treatment position a population-based bladder shape model would have to be created. Also, both proposed methods have only been applied and tested on male patients treated in supine position.

In this study, we added a number of improvements to the earlier automatic bladder segmentation methods on CBCT and validated this method for different patient groups. To enable the segmentation for the various patient groups, independent of gender and position on the treatment table (prone or supine), only patient-specific bladder shape information based on pre-treatment imaging data was used. For each patient, a model was built to estimate the patient-specific bladder shape variation from the start of treatment and this model was expanded during treatment. The aim of this study is to present a generic method for automatic bladder segmentation on CBCT for each gender and treatment position using only patient-specific pre-treatment imaging data.

## 3.2 | Material & Methods

### Patient data

Imaging data (CT and CBCT) of 20 patients were selected, who were treated for tumors in the pelvic region with the entire bladder visible on CT and CBCT. The CT images (LightSpeed RT16 system, General Electric Company, Waukesha WI, USA) were acquired with a pixel size of  $1.0 \times 1.0 \text{ mm}^2$  and a slice thickness of 2.5 mm. The resolution of the CBCT images (Synergy, Elekta Oncology systems, Crawley, UK) were either  $410 \times 410 \times 264$  or  $410 \times 410 \times 120$ , with a pixel size of  $1.0 \times 1.0 \text{ mm}^2$  and a slice thickness of 1.0 mm. The acquisition parameters of the CBCT projection images were either 120 kV, 40 mA, 40 ms per projection or 120 kV, 32 mA, 40 ms per projection.

Since the bladder position, bladder shape and the bladder deformation vary between both the gender of the patient and its treatment position [26,91,106], the data of these patients were divided into four equally sized subgroups based on gender and treatment position (Table 3.1). Each patient had a median of 7 (range, 5–9) CBCT images, all acquired for position verification purposes. As part of the clinical routine for treatment planning purposes, the outer boundary of the bladder on CT images were manually delineated slice-by-slice by a radiation oncologist. The outer boundary of the bladder on all CBCT images were manually delineated slice-by-slice by one observer and revised by an experienced radiation therapy technologist (RTT).

Since we used retrospective patient data, only one pre-treatment CT was available for each included patient. According to the clinical protocol, this CT was acquired with a full bladder. Due to the absence of an empty bladder CT for these patients, the CBCT image with the emptiest bladder was used as a surrogate. All other CBCT images were used to validate the segmentation algorithm.

**Table 3.1** | Characteristics of the different patient groups, with five patients in each group. All patients were treated with IMRT. Patients treated in prone position were lying on a belly board [26].

Group	Gender	Treatment position	Treatment site	Fractionation scheme (Gy)	Total CBCTs	Bladder volume range (ml)				
						Patient 1	Patient 2	Patient 3	Patient 4	Patient 5
A	Female	Prone	Cervix-Uterus	23 x 2.00	36	122–487	77–381	90–502	165–359	86–506
B	Female	Supine	Cervix-Uterus	23 x 2.00	29	60–200	98–311	141–403	187–356	48–114
C	Male	Supine	Bladder (1–4) Prostate (5)	20 x 2.75 35 x 2.20	37	145–189	158–216	53–375	82–106	91–406
D	Male	Prone	Rectum	28 x 1.80	37	78–335	114–199	100–446	173–259	94–332

*Abbreviations:* CBCT = cone-beam computed tomography; Gy = gray.

## Bladder segmentation

This novel method of automatic bladder segmentation on CBCT images consisted of three main parts. First, for each patient a principal component analysis (PCA) based statistical model was built to estimate the patient-specific bladder shape variation from the full bladder contour and the empty bladder contour. Second, this patient-specific bladder shape model was used in an online 3D segmentation process to segment the bladder on CBCT images. Finally, the resulting segmentation can be improved locally by manual adaptations and this adapted bladder segmentation was included in the model for ensuing segmentations.

### *Patient-specific bladder shape model*

For each patient, a unique patient-specific bladder shape model was built prior to treatment using only the manually delineated full and empty reference bladder contours. To create this shape model, both contours were aligned by registering the image with the full bladder to the image with the empty bladder based on bony anatomy. Next, the contours were transformed to 3D triangular surface meshes. To eliminate unnatural shape differences, both 3D triangular surfaces were smoothed using a non-shrinkage smoothing method [108].

The smoothed bladder surfaces were described with an equal number of points and triangular connections. To do so, a uniform 3D sphere surface was created with an arbitrary chosen and evenly distributed number of vertices ( $M=2091$ ). The central point of this sphere ( $O_{\text{sphere}}$ ) was automatically positioned at the center of the empty bladder contour and consequently inside both bladder surfaces. The smoothed bladder surfaces were resampled in 3D at the intersection of the spherical radial lines passing through the central point and bladder surface. These 2091 lines in radial direction were assumed to be dense enough to fully capture the feature points of bladder surfaces.

The resampled bladder surface shape vectors in Cartesian coordinates were represented in spherical coordinates using  $O_{\text{sphere}}$  as origin. Next, we applied a spherical harmonic transformation to both bladder surfaces, as described by Chai *et al.* [107] and Brechbühler *et al.* [109]. The bladder

surfaces were described using vectors consisting of spherical harmonic coefficients up to degree  $K$ , representing spatial variation of the bladder surface. Spatial variation was defined as the mean distance between corresponding points on the original bladder surface and the bladder surface described using  $K$  degrees. In this study, the degree  $K=7$  was used as upper limit to model spatial variation of bladder surfaces, as that was sufficient to achieve a mean distance error smaller than 0.10 cm for all bladder surfaces.

After resampling and spherical harmonic transformation, the full and empty bladder surface were described by a unique shape parameter vector ( $\omega_i$ ) consisting of  $3(K+1)^2=192$  spherical harmonic coefficients [107]. It was assumed that the set of shape parameter vectors could be seen as samples from a random process. For anatomical reasons, displacements of vertices and bladder deformation are highly correlated. This implies that the underlying dimensionality of this multivariate statistical problem is much smaller than the number of vertices and thus the correlated displacements of the surface points can be described using PCA [110]. This method reduces the dimensionality of the shape parameter vector by computing the major modes of shape variation.

First, the mean shape parameter vector ( $\bar{\omega}$ ) was calculated from the shape parameter vectors ( $\omega_i$ ) (Equation 3.1) and the mean shape vector was used to determine the covariance matrix ( $C$ ) (Equation 3.2). Next, the eigenvector ( $v$ ) and associated eigenvalue ( $\lambda$ ) were determined by eigendecomposition of the covariance matrix (Equation 3.3). The determined eigenvectors of this covariance matrix represented the bladder deformation pattern based on the full and empty bladder contours.

$$\bar{\omega} = \frac{1}{N} \sum_{i=1}^N \omega_i \quad (3.1)$$

$$C = \frac{1}{N-1} \sum_{i=1}^N (\omega_i - \bar{\omega}) \cdot (\omega_i - \bar{\omega})^T \quad (3.2)$$

$$C\lambda = \lambda \lambda \quad (3.3)$$

### *Segmentation process*

The input of the segmentation algorithm was the CBCT image to be segmented, a reference image with delineated bladder contour and the patient-specific bladder shape model. In order to suppress noise, the grey values of both the reference image and the CBCT image were smoothed by an isotropic 3D Gaussian smoothing filter with a standard deviation (SD) of 0.3 cm. This value was optimized in a previous study and based on a different patient population [106]. Next, the images were registered based on bony anatomy by using the clinically obtained translation vector after CT image and CBCT image alignment.

The process of segmentation was similar to the segmentation process described in detail by Chai *et al.* [107]. The process started with a delineated bladder contour from pre-treatment imaging as initial segmentation and this contour was deformed iteratively according to the deformation patterns calculated from the patient-specific bladder shape model. The segmentation

was obtained by minimizing a cost function (CF) (Equation 3.4), based on the cross-correlation between directional internal and external grey value gradients over the reference bladder contour ( $G_R$ ) and the segmented bladder contour ( $G_S$ ) (Equation 3.5). To find the bladder shape that best corresponds with the reference bladder contour within the interval  $[-3, 3]$ , a simplex optimizer was used for cost function minimization [111]. The process of optimization was completed when the cost function value difference between two consecutive iterations was below  $5.0e^{-5}$ .

$$CF=2-(CC(G_R^{int}, G_S^{int}) + CC(G_R^{ext}, G_S^{ext})) \quad (3.4)$$

$$CC(G_R, G_S) = \frac{\sum_{i=1}^M (G_R(i) - \bar{G}_R)(G_S(i) - \bar{G}_S)}{\sqrt{\sum_{i=1}^M (G_R(i) - \bar{G}_R)^2} \sqrt{\sum_{i=1}^M (G_S(i) - \bar{G}_S)^2}} \quad (3.5)$$

### Automatic adaptations

As observed by Chai *et al.* [107], the algorithm could produce an incorrect bladder segmentation after regular cost function minimization due to various causes. Image artifacts on CBCT could produce fictitious bladder edges, the cost function optimization could end in a local minimum or large anatomical differences between reference structure and the structure on CBCT could cause different grey value gradient fields. To avoid segmentation failure caused by these artifacts, several automatic fine-tuning mechanisms were implemented that were not present in the approach by Chai *et al.* [107].

The first automatic fine-tuning mechanism is the implementation of different starting points and different reference contours. The contours of the full and empty bladder were both used as initial contour at the start of the segmentation. In addition, both contours were used as reference contours, combined with their associated imaging data. Consequently, the process of segmentation was done four times: two different initial contours and two different reference contours. The segmentation with the lowest cost function result was considered the best segmentation and therefore selected as final bladder segmentation.

Another fine-tuning mechanism was introduced to overcome incorrect segmentations caused by dominating inconsistent grey value gradients. For example, if a part of the bladder edge in the reference image was located next to bony structure, the directional grey value gradients became large and dominated the cost function. To decrease the influence of vertices with large gradient values (i.e. grey value gradients  $>125$ ) to the cost function, its contribution was weighted with a factor ( $\alpha$ ) (Equation 3.6). This factor is defined as the number of vertices corresponding to large gradient values divided by the total number of vertices.

$$CC(G_R, G_S) = \frac{\sum_{i=1}^M (\alpha G_R(i) - \bar{G}_{R,\alpha})(\alpha G_S(i) - \bar{G}_{S,\alpha})}{\sqrt{\sum_{i=1}^M (\alpha G_R(i) - \bar{G}_{R,\alpha})^2} \sqrt{\sum_{i=1}^M (\alpha G_S(i) - \bar{G}_{S,\alpha})^2}} \quad (3.6)$$

Finally, inconsistent gradient values between the bladder edge on the reference image and bladder edge on the CBCT image could result in segmentations with unrealistic large bladder volumes. These bladder volume explosions were prevented by adding a volume dependent value to the cost function (Equation 3.7). If the segmented volume ( $V_s$ ) was above 125% of the full reference bladder volume ( $V_T$ ) or below 75% of the empty reference bladder volume ( $V_T$ ), the cost function value was increased with an additional volume dependent value.

$$CF^* = CF + \frac{|V_s - V_T|}{50} \quad (3.7)$$

### *Manual adaptations and model expansion*

At the start of treatment, the patient-specific bladder shape model described the major bladder deformation pattern based on the full and empty bladder shape information. The use of this model assumed a bladder deformation during the course of treatment according to this deformation pattern. However, additional deformations during the course of treatment would not be taken into account. For example, the bladder could be locally deformed due to bowel filling during treatment which was not included in the model. As a consequence, the model was not able to segment the bladder correctly and manual local adaptations were needed to improve the bladder segmentation. This additional bladder shape information, obtained after manual adaptations, was used for optimizing the patient-specific bladder shape model during treatment.

If, after visual inspection of the result, the fully automatic segmentation strategy using the shape model proved insufficient, the observer could directly improve the segmentation by manually selecting correction points on the bladder edge. For each correction point the shortest distance to the segmented bladder surface mesh ( $P_{dist}$ ) and its associated point of mesh intersection ( $P_{cp}$ ) were determined (Figure 3.1). Next, mesh vertices of the bladder segmentation closest to  $P_{cp}$  (one if  $P_{cp}$  was a vertex point, two if  $P_{cp}$  was on an edge of a triangle or three if  $P_{cp}$  was on the face of a triangle) were shifted, parallel to the displacement vector from  $P_{cp}$  to the manually selected correction point, towards the manually selected correction point by the distance  $P_{dist}$ . Consequently, mesh vertices could be displaced in all three dimensions.

To prevent irregular bladder shapes or peaks in the bladder surface, vertices of connected triangular faces to  $P_{cp}$  vertices were also shifted using a scaled distance. If the distance  $P_{dist}$  was below 1.0 cm, the 1<sup>st</sup>, 2<sup>nd</sup> and 3<sup>rd</sup> order of connected vertices were shifted by scaling the distance  $P_{dist}$  by a factor 0.80, 0.50 and 0.20, respectively. If the distance  $P_{dist}$  was above 1.0 cm, the 1<sup>st</sup>, 2<sup>nd</sup>, 3<sup>rd</sup> and 4<sup>th</sup> order of connected vertices were shifted by scaling the distance  $P_{dist}$  by a factor 0.85, 0.60, 0.30, 0.10, respectively. After manual adaptation of the segmentation the entire bladder surface was smoothed using the previous described smoothing method to prevent unnatural shapes.

After segmentation using manual local adaptations, the resulting bladder shape described by spherical harmonic coefficients was added to the existing bladder shape model in order to optimize the patient-specific shape model. Consequently, new major modes of shape variation were calculated by determining new dominating eigenvectors. It was assumed that the sum of

all eigenvalues described 100% of the bladder shape variation. The dominating eigenvectors, determined by its eigenvalues describing 95% of the bladder shape variation, were used to build the expanded model. The new bladder deformation patterns were used to segment the bladder on the following CBCT images during treatment.



**Figure 3.1** | Schematic overview of the manual local adaptation procedure (A) and an example of this procedure applied to improve the bladder segmentation, with the segmentation result obtained using the FA strategy in red (B) and the segmentation result obtained using the MAE strategy in yellow (C). From the manually defined correction point the closest point on the bladder surface mesh ( $P_{cp}$ ) was determined and the associated distance ( $P_{dist}$ ) was calculated. Mesh vertices closest to  $P_{cp}$  were shifted, parallel to the red dashed line, towards the manually selected correction point by the distance  $P_{dist}$ . Also, the 1<sup>st</sup>, 2<sup>nd</sup> and 3<sup>rd</sup> order vertices were shifted, indicated by the green ( $\alpha$ ), yellow ( $\beta$ ) and orange ( $\gamma$ ) arrow, respectively.

## Segmentation validation

In this study, two segmentation strategies were performed and compared. The first strategy, the fully automatic (FA) strategy, consistently used only the shape model based on the full and empty bladder surfaces for segmentation without the use of manual adaptations. The second strategy, the manual adaptation and expanded (MAE) strategy, allowed manual local adaptations and the expanded shape model was used for the following segmentation.

To validate the segmentation results using the manual bladder delineations, all manual delineations were resampled in 3D using the previous defined sphere with 2091 evenly distributed vertices that was also used to resample the reference contours. After resampling, all manual delineations and segmentations consisted of an equal number of vertices and triangles.

We used the Dice similarity coefficient (DSC) to determine the volume overlap between the bladder segmentation and the manual bladder delineation. Given the manually delineated bladder structure ( $Bladder_{Del}$ ) and the segmented bladder structure ( $Bladder_{Seg}$ ), the DSC was defined as the volume of intersection divided by the average of both volumes (Equation 3.8).

$$DSC(Bladder_{Del}, Bladder_{Seg}) = 2 \frac{(Bladder_{Del} \cap Bladder_{Seg})}{(Bladder_{Del} + Bladder_{Seg})} \quad (3.8)$$

The contour-to-contour distances, i.e. the shortest distances between segmentation and manual delineation, were determined by calculating the shortest distance between each vertex of one mesh to an intersection with the other mesh. For each segmentation obtained using the FA strategy and the MAE strategy, the surface distance error (SDE) was defined as the mean of contour-to-contour distances.

The improvement of segmentation using manual adaptations and model expansion was studied by testing (Wilcoxon signed-rank test) the difference in segmentation results obtained using the FA strategy and the MAE strategy for the SDE, the DSC and the SD of contour-to-contour distances.

Besides the volume- and distance-based conformity test, the bladder volume determined by manual delineation was compared with the bladder volume determined by segmentation using the two strategies. For each patient group, a Bland-Altman error analysis was performed to determine the agreement between bladder volumes obtained by manual delineation and segmentation. The difference between obtained bladder volumes by manual delineation and segmentation was plotted against the average of obtained bladder volumes for both segmentation strategies and the 95% confidence interval of the error distribution was reported. In addition, the time needed to segment the bladder using the FA strategy and the MAE strategy was recorded.

To establish the efficacy of the expanded model on the segmentation results, an additional fully automatic with expanded model (FAE) segmentation strategy was performed. This FAE strategy was comparable to the FA strategy, but using the expanded shape model obtained during the MAE strategy instead of the shape model based on only the full and empty bladder surfaces. The improvement in segmentation results obtained using the FAE strategy compared to the FA strategy was tested (Wilcoxon signed-rank test) for both the DSC and SD of contour-to-contour distances.

### 3.3 | Results

For each patient, a unique patient-specific bladder shape model was built using surface meshes, described by 192 ( $K=7$ ) spherical harmonic coefficients. One PCA mode was used to represent the bladder shape deformation in the model, which is associated with bladder volume change. After expanding the model with manually adapted surfaces, one to four PCA modes were used to represent bladder shape deformations. The second and third PCA mode modeled mainly translations and rotations of the bladder and higher order PCA modes modeled other deformation patterns.

In total, 119 CBCT images were used to validate the segmentation algorithm. Initialization of the segmentation procedure took 18 seconds on average and the computer needed 29 seconds on average to segment the bladder using the FA strategy. Bladder segmentation using the MAE strategy took 36 seconds on average and manual adaptation added 21 seconds on average to this

segmentation time. All segmentations were performed on a personal computer with a quad core, CPU of 3.20 GHz and 6.0 GB of RAM.

The DSC and the SD of the contour-to-contour distances between the segmentation and manual delineation, for the FA strategy as well as the MAE strategy, were plotted (Figure 3.2). The manual local adaptations yielded an increased agreement with the manually delineated volumes, as can be seen by the increased median DSC and decreased median SD of contour-to-contour distances. Although the mean SDE between the segmentation and manual delineation using the FA strategy was accurate, the use of the MAE strategy increased the agreement between the segmentation and manual delineation significantly ( $p < 0.01$ ) for each group, indicated by a decreased mean SDE (Table 3.2). Moreover, the results obtained with the use of manual local adaptations (MAE strategy) were improved significantly for both the DSC ( $p < 0.01$ ) (Figure 3.3a) and the SD of contour-to-contour distances ( $p < 0.01$ ) (Figure 3.3b).

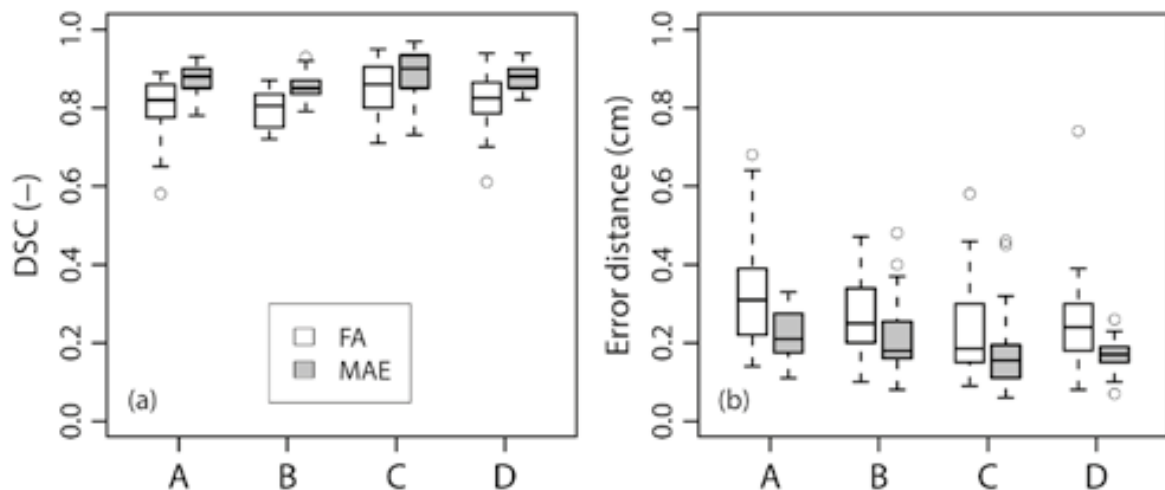


**Figure 3.2** | Box-and-whisker plots of the DSC (a) and SD of contour-to-contour distances (i.e. error distance) (b) between manual delineations and segmentations, acquired according to the FA strategy and the MAE strategy, for each patient group defined on the x-axis. The box represents the upper and lower quartiles (IQR) and the band inside the box the median value. The whisker represents the largest (lowest) value still within 1.5 IQR of the upper (lower) quartile. Dots above or below the whiskers are considered as outliers.

The Bland-Altman error analysis between bladder volume obtained by manual delineation and bladder volume obtained using automatic segmentation is shown (Figure 3.4). The mean (SD) difference in bladder volume obtained by manual delineation and segmentation was 23 (90) ml and 11 (38) ml (female, prone), 15 (48) ml and -4 (23) ml (female, supine), 9 (27) ml and -1 (21) ml (male, supine) and 0 (35) ml and 1 (19) ml (male, prone) using the FA strategy and the MAE strategy respectively. The results showed that the 95% confidence interval of the error distribution decreased for all groups using the MAE strategy instead of using the FA strategy.

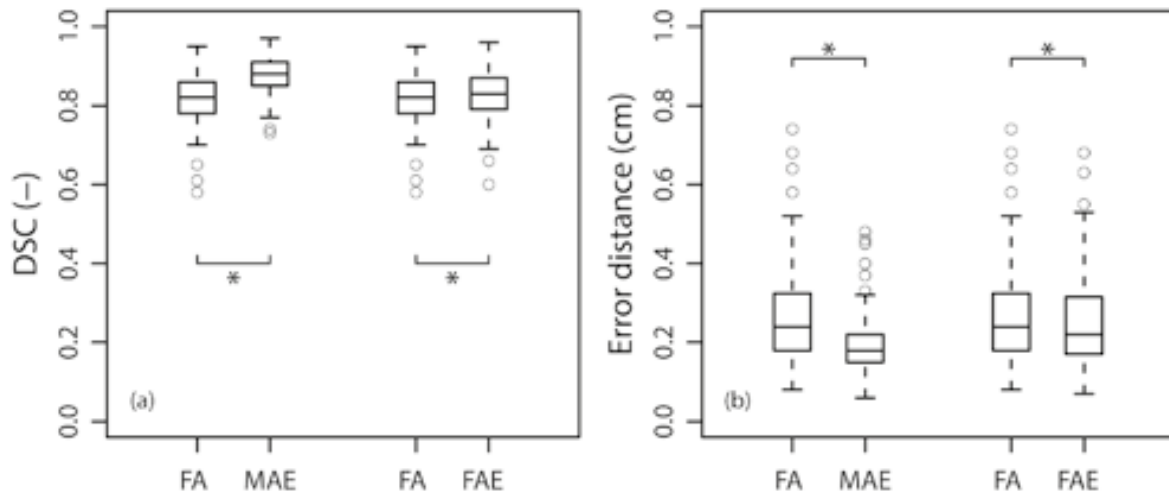


**Figure 3.3** | Box-and-whisker plots of the DSC (a) and SD of contour-to-contour distances (i.e. error distance) (b) between manual delineations and segmentations for the FA strategy versus the MAE strategy and the FA strategy versus the FAE strategy. For the meaning of box, whiskers and dots: see Figure 3.2. Horizontal lines including an asterisks indicate statistical significant difference ( $p < 0.01$ ).

Regarding the DSC (Figure 3.3a) and the SD of contour-to-contour distances (Figure 3.3b), the segmentations obtained using the FAE strategy instead of using the FA strategy were improved significantly ( $p < 0.01$ ). Although an overall significant improvement was observed, the segmentation accuracy in 11% of the individual cases was improved substantially (i.e. increase of DSC  $> 0.05$  or decrease of SD of contour-to-contour distances  $> 0.1$  cm) to possibly be clinically beneficial (Figure 3.5). Using these criteria, the segmentation results obtained using the FAE strategy were worse compared to the segmentation results obtained using the FA strategy in only 2% of the cases.

**Table 3.2** | Mean (range) surface distance error for each patient group using the FA segmentation strategy and the MAE segmentation strategy. Asterisks indicate a statistical significant difference ( $p < 0.01$ ) between SDE obtained using the FA strategy and using the MAE strategy.

SDE (cm)	Group A *	Group B *	Group C *	Group D *
FA strategy	0.38 (0.15–0.76)	0.35 (0.12–0.70)	0.26 (0.10–0.58)	0.33 (0.10–0.78)
MAE strategy	0.27 (0.14–0.40)	0.28 (0.11–0.58)	0.21 (0.08–0.42)	0.23 (0.09–0.35)

*Abbreviations:* SDE = surface distance error; FA = fully automatic; MAE = manual adaptation and expanded.

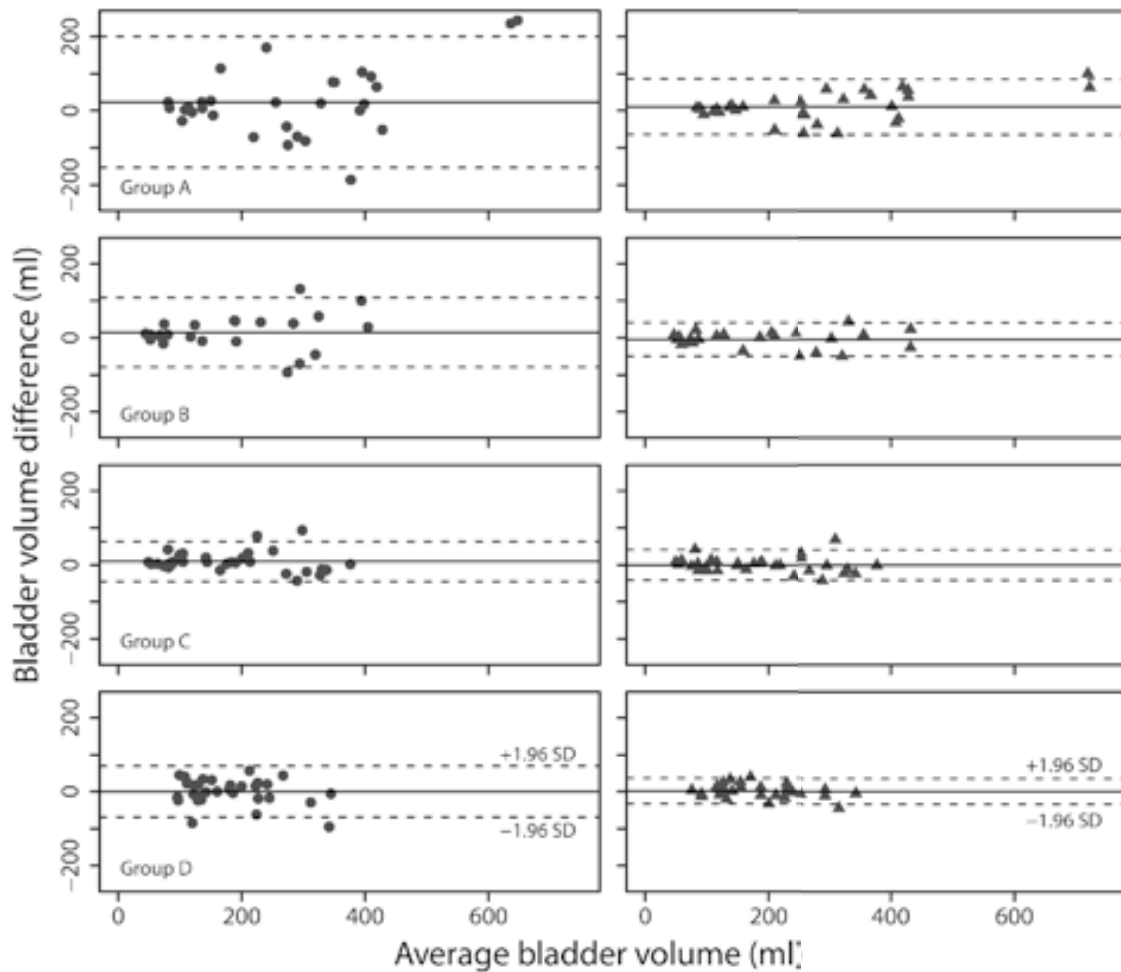


Figure 3.4 | Bland-Altman error analysis for bladder volumes obtained by manual delineation vs. bladder volumes obtained by segmentation using the FA strategy (dots; left column) and using the MAE strategy (triangles; right column) for each patient group separately. The horizontal solid line indicates the mean bladder volume difference and the horizontal dashed lines indicate the 95% confidence interval.

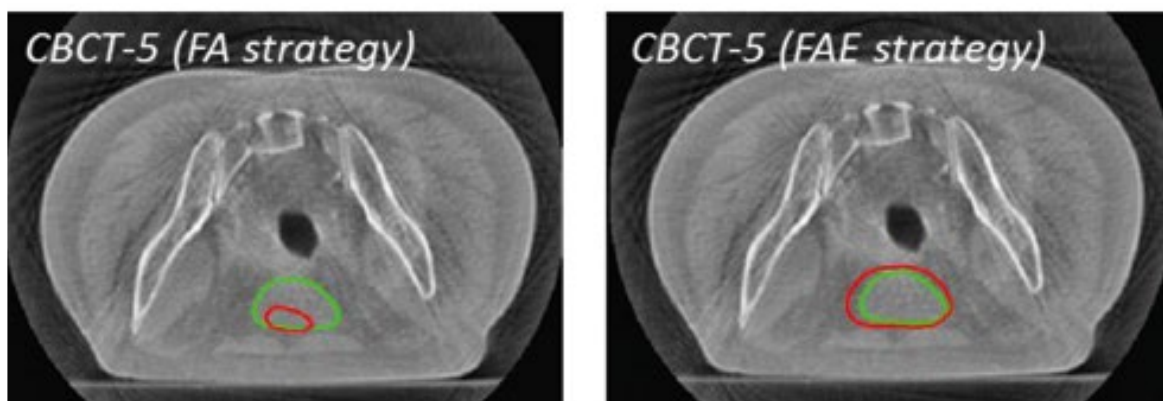


Figure 3.5 | An example of the difference in segmentation result for the fifth treatment fraction, obtained using the FA strategy (left) and using the FAE strategy (right) with the segmentation result (red) and manual delineation (green). Since this was the fifth CBCT to be analyzed for this patient, the model used in the FAE strategy also included shape information from manually adapted bladder segmentations of previous CBCT images of this patient.

### 3.4 | Discussion

We presented a method for automatic bladder segmentation on CBCT, independent of gender and the treatment position (prone or supine). Using a patient-specific bladder shape model based on a full and empty bladder structure, this method automatically produced an accurate bladder segmentation in a short time. Provided CT sets with a full and empty bladder are available, this segmentation strategy can be used from the first CBCT image during an adaptive radiation therapy treatment. This novel segmentation method contained several automatic correction strategies to avoid segmentation failure caused by the moderate CBCT image quality. In cases with less adequate results, the segmentation can be locally adapted by quick manual corrections. In addition, after manual adaptations the patient-specific bladder shape model can be expanded with the adapted segmentation to better optimize the patient-specific bladder shape model in subsequent CBCTs.

The bladder segmentation method presented in this study produced more accurate segmentations compared to previous reported results of bladder segmentation on CBCT by Chai *et al.* [106,107]: a higher mean DSC of 0.87 (0.79 and 0.78, respectively) and smaller SD of contour-to-contour distances of 0.19 cm (0.24 cm and 0.30 cm, respectively). Moreover, our mean DSC of bladder segmentation using the fully automatic strategy (0.82) was similar to the inter-observer bladder delineation variation on CBCT reported by Lütgendorf-Caucig *et al.* [112] (0.82) and Foroudi *et al.* [113] (0.75). Besides these accurate segmentations compared to previous reported studies on bladder segmentation on CBCT, this method is applicable from the start of ART with a plan-of-the-day approach without the need for a large training set. Furthermore, it was successfully applied and tested on male and female patients treated in both supine and prone position.

Since retrospective data were used in this study, the CBCT with the emptiest bladder was used as a surrogate to compensate for the absence of a second pre-treatment CT with empty bladder. Using this strategy, the patient-specific shape model included also possible rectum and bowel filling variability influencing the bladder shape. This additional information of shape deformation will not be included in the model when using two pre-treatment CTs. However, rectum and bowel filling variability influencing the bladder shape will also be present using two pre-treatment CTs for model building due to intrafraction motion of bowel and rectum [114]. Nevertheless, the bladder shape variation caused by rectum and bowel filling variability in the used strategy was probably increased due to the large time between scans used for shape modeling. Therefore, the results in this study contained a possible small bias in favor of our method due to the use of a CBCT scan as a surrogate.

Our patient population consisted of twenty patients, divided in four groups based on gender and the treatment position. A substantial number of patients was analyzed and the robustness of our method was verified by a large number of CBCTs. The data analyzed in this study were sufficient to show the efficacy of our proposed method for each patient group. However, for bladder cancer patients with the bladder being the target area instead of an OAR, the difference in flexibility between the bladder wall and tumor can influence the bladder deformation pattern [115].

Since the delineated bladder contours on CT images, used for model building, were all used clinically for treatment planning purposes, these CT-based bladder contours were of high quality. Due to the low inter-observer delineation variation of the bladder on CT [116], the input used for model building will not become more accurate when provided by different observers. Consequently, model input provided by different observers will have a very limited impact on segmentation results.

To acquire accurate bladder contours on CBCT images for validation purposes, delineations were performed by one observer and revised by a second observer. Although the inter-observer bladder delineation variation on CBCT is relatively low and revision by a second observer increased the delineation accuracy even more, the influence of inter-observer bladder delineation variability on our proposed automatic segmentation algorithm is of interest [112]. However, to fully determine this influence on our outcome would require a complete delineation study and was out of the scope of this study.

The manually delineated bladder contours on CBCT images were resampled using the uniform 3D sphere surface with its evenly distributed 2091 vertices for validation purposes. The determination of the central point ( $O_{\text{sphere}}$ ) was performed automatically by calculating the center of the empty bladder contour. As observed by Chai *et al.* [106], the segmentation was not sensitive to this position if every point on the bladder surface was visible from  $O_{\text{sphere}}$ . Moreover, for a number of segmentations several positions of  $O_{\text{sphere}}$  were tested and minimal differences in segmentation results were observed. The number of evenly distributed vertices used to resample the manually delineated bladder contours on CBCT were assumed to be dense enough to fully describe the bladder surfaces. To verify this assumption, a 3D sphere with known radius was created and its volume was compared with the volume of this sphere obtained after our resampling strategy. Only 1% volume difference was observed between the volume of the sphere (114 ml) and the volume determined after resampling. Given this very small volume difference, the number of evenly distributed vertices is sufficient and the validation accuracy will not increase when using the original manually delineated bladder contours instead of the resampled manual delineations for validation purposes.

Incorrect bladder segmentations caused by image artefacts on CBCT were already observed by Chai *et al.* [107] and a failure rate (i.e. a very low similarity with the manually delineated bladder:  $\text{DSC} < 0.65$ ) of 32% was reported. To avoid this relatively high failure rate caused by image artefacts on CBCT, automatic adaptations were implemented in our segmentation algorithm. The use of these automatic adaptations resulted in an overall failure rate of only 3%.

To locally improve bladder segmentations using manual adaptations, mesh vertices closest to the selected point and connected vertices were shifted towards this selected point, parallel to the displacement vector between  $P_{\text{cp}}$  and the manually selected correction point. The scaling factors used to shift connected vertices were tested and optimized on four randomly selected patients. Since these scaling factor values worked for our purpose, these values were not optimized and tested

on all patients. Moreover, after local manual adaptation the entire bladder surface was smoothed to prevent unnatural shapes which decreased the influence of these factors on segmentation outcome.

After each locally improved segmentation using manual adaptations, the patient-specific bladder shape model was expanded. The advantage of this strategy is the use of all available information of the patient instead of only the pre-treatment defined bladder shape information. Although the use of the expanded patient-specific shape model did improve the segmentation results significantly in terms of DSC (Figure 3.3a) and SD of contour-to-contour distances (Figure 3.3b), substantial improvement of the segmentation accuracy was observed only for some individual cases (Figure 3.5). This is probably caused by the use of only a relatively small number of CBCT images per patient. In the case of ART, daily CBCT images are acquired and the effect of model expansion will probably increase.

Our automatic procedure performed within the range of human observer variability, being the best standard presently available. This delineation variability should be accounted for in the planning margin around target volumes. In addition, automatic bladder segmentation can be applied to select the plan-of-the-day, as demonstrated for multiple-plan bladder ART by Chai *et al.* [107]. Whether our procedure also supports plan-of-the-day selection during multiple-plan ART for cervical cancer patients will have to be studied. For dose calculation and dose accumulation purposes, more accurate segmentations might be needed and therefore the CBCT image quality need to be improved or MRI can be considered for image guidance.

An alternative approach for automatic organ segmentation is the use of an atlas-based segmentation algorithm. A large number of successful studies reported on automatic segmentation on CT images using an atlas-based approach. Only one study reported about the application of such a method for bladder on CBCT [117]. They showed a mean DSC of 0.54, indicating a weak performance of atlas-based segmentation on CBCT. The main reason for failure using this atlas-based strategy is the relatively poor image quality of CBCT. However, our segmentation method is much better able to handle this relatively poor image quality.

The proposed automatic bladder segmentation method is especially applicable during multiple-plan bladder ART [60,99], because a library of bladder contours for designing multiple plans is already available and can also be used for bladder shape modeling. Moreover, the proposed segmentation method will be extremely suitable for online position verification purposes or online plan selection purposes during multiple-plan bladder ART. However, the total time of the segmentation process currently limits the online application and therefore the implementation of our segmentation method will be improved to speed up the process of segmentation.

Furthermore, our proposed automatic bladder segmentation method is also applicable during multiple-plan ART of the cervix-uterus for both supine and prone treatment position. Several studies reported on the correlation between bladder volume differences and the position of the cervix-uterus [64,83]. Given this correlation, daily size and position of the bladder determined by automatic segmentation can predict the position of the cervix-uterus and can be used for online

plan-of-the-day selection. In addition, the pre-treatment imaging acquired for cervix-uterus ART is also suitable to create a bladder shape model needed for segmentation on CBCT [83].

### 3.5 | Conclusion

The presented patient-specific bladder shape model, based on only pre-treatment imaging information, was suitable for automatic bladder segmentation on CBCT images. This method was independent of gender and treatment position and allowed for accurate automatic segmentation of the bladder on CBCT. Bladder segmentations can be improved locally using manual adaptations, which was easily incorporated into the workflow.



# Chapter 4

## Beam configuration selection for robust intensity-modulated proton therapy in cervical cancer using Pareto front comparison

A version of this chapter has been published as:

*Beam configuration selection for robust intensity-modulated proton therapy in cervical cancer using Pareto front comparison*

A.J.A.J. van de Schoot, J. Visser, Z. van Kesteren, T.M. Janssen, C.R.N. Rasch and A. Bel

*Physics in Medicine and Biology* 2016; 61(4): 1780–1794.

<http://dx.doi.org/10.1088/0031-9155/61/4/1780>

## Abstract

### Purpose

The Pareto front reflects the optimal trade-offs between conflicting objectives and can be used to quantify the effect of different beam configurations on plan robustness and dose-volume histogram parameters. Therefore, our aim was to develop and implement a method to automatically approach the Pareto front in robust intensity-modulated proton therapy (IMPT) planning. Additionally, clinically relevant Pareto fronts based on different beam configurations will be derived and compared to enable beam configuration selection in cervical cancer proton therapy.

### Material & Methods

A method to iteratively approach the Pareto front by automatically generating robustly optimized IMPT plans was developed. To verify plan quality, IMPT plans were evaluated on robustness by simulating range and position errors and recalculating the dose. For five retrospectively selected cervical cancer patients, this method was applied for IMPT plans with three different beam configurations using two, three and four beams. Three-dimensional Pareto fronts were optimized on target coverage (CTV  $D_{99\%}$ ) and OAR doses (rectum  $V_{30\text{Gy}}$ ; bladder  $V_{40\text{Gy}}$ ). Per patient, proportions of non-approved IMPT plans were determined and differences between patient-specific Pareto fronts were quantified in terms of CTV  $D_{99\%}$ , rectum  $V_{30\text{Gy}}$  and bladder  $V_{40\text{Gy}}$  to perform beam configuration selection.

### Results

Per patient and beam configuration, Pareto fronts were successfully sampled based on 200 IMPT plans of which on average 29% were non-approved plans. In all patients, IMPT plans based on the 2-beam set-up were completely dominated by plans with the 3-beam and 4-beam configuration. Compared to the 3-beam set-up, the 4-beam set-up increased the median CTV  $D_{99\%}$  on average by 0.2 Gy and decreased the median rectum  $V_{30\text{Gy}}$  and median bladder  $V_{40\text{Gy}}$  on average by 3.6% and 1.3%, respectively.

### Conclusion

This study demonstrates a method to automatically derive Pareto fronts in robust IMPT planning. For all patients, the defined four-beam configuration was found optimal in terms of plan robustness, target coverage and OAR sparing.

## 4.1 | Introduction

The primary treatment for patients with locally advanced uterine cervical cancer consists of photon-based external-beam radiation therapy (RT) with concurrent chemotherapy or hyperthermia [18,72], often followed by brachytherapy [118]. The introduction of intensity-modulated RT (IMRT), which enables highly conformal target doses with steep dose fall-offs, decreased organ at risk (OAR) doses [119,120], but also required adequate patient set-up using image guidance in order to fully exploit the potential advantage. Besides the reduction of positioning errors and the quantification of geometric uncertainties induced by interfraction anatomical changes of pelvic organs [89,92], image-guided RT (IGRT) including daily soft-tissue visualization offers possibilities for online adaptive RT. Moreover, the implementation of rotational IMRT techniques further improved OAR sparing with the addition of decreased treatment delivery time [32]. Despite all improvements, healthy surrounding tissue still receives a substantial amount of dose which causes serious toxicity and significantly reduces quality of life [121].

Because of its characteristic Bragg peak, protons have certain distinct advantages over conventionally used X-rays. Among others, uterine cervical cancer patients may also benefit from proton therapy (PT) and interest in the application of PT has increased recently [24,70,71,122]. Intensity-modulated PT (IMPT) using pencil beam scanning technology paints dose to target volumes while minimizing surrounding dose, enabling adequate dose delivery to complex-shaped target volumes and limited OAR doses. However, proton-based RT is sensitive to range and position uncertainties and therefore IMPT plan robustness is necessary to guarantee target coverage and OAR sparing.

Although several studies investigated PT for uterine cervical cancer patients [70,71,123,124], none of them used treatment plans that are robust against possible position and range uncertainties. Besides the lack of plan robustness, no agreement between beam configurations was observed and the effect of beam configurations on dose-volume histogram (DVH) parameters was not considered. Therefore, the optimal beam configuration and the influence of uncertainties on dose distributions in cervical cancer PT are still unknown. In order to obtain patient-specific optimal dose distributions in addition to robustness, the number of beams and associated gantry angles should be included in the process of optimization. Although some studies demonstrated gantry angle optimization algorithms in photon-based RT [125-127], complete beam configuration optimization is currently not implemented in the process of plan optimization.

To objectively investigate the use of different beam configurations in IMPT planning without the arbitrariness of individual planning decisions, the set of Pareto optimal plans that reflects the optimal trade-offs between conflicting objectives (i.e. the Pareto front) are compared. The feasibility of using Pareto fronts as an evaluative and comparative tool has been shown [128]. Along these lines, we aim to investigate the influence of beam configuration on plan robustness and DVH parameters by comparing Pareto fronts obtained with various sets of gantry angles. The purpose of this study was therefore to develop and implement a method to derive the Pareto front based

on robust IMPT planning to be used in clinical practice. In addition, Pareto fronts with a potential clinical relevance derived using different beam configurations will be compared to enable beam configuration selection for cervical cancer PT.

## 4.2 | Material & Methods

### Patient data

Data of five patients with a cervical carcinoma and treated with photon-based RT were included retrospectively. These patients were treated in prone treatment position using a belly board device for bowel dose minimization [26]. CT images (LightSpeed RT16 system, General Electric Company, Waukesha WI, USA) with a slice thickness of 2.5 mm acquired for photon-based RT treatment planning were also used for IMPT treatment planning. Relevant regions of interest for IMPT treatment planning include the delineated OARs (body, rectum, bladder and bowel cavity) and the clinical target volume (CTV), encompassing the cervix, gross tumor volume (GTV), corpus uterus, upper part of the vagina and elective lymph nodes [29].

### IMPT treatment planning

IMPT treatment plans were generated with RayStation (version 4.4, RaySearch Laboratories AB, Stockholm, Sweden). High-density CT values due to contrast agents used for vagina and bladder visualization were corrected to muscle ( $1.05 \text{ g/cm}^3$ ) and water ( $1.0 \text{ g/cm}^3$ ) density, respectively. For each patient, three initial IMPT plans based on different fixed beam configurations were created with the beam isocenter set to the GTV center of mass (Table 4.1). The prescribed physical CTV dose of 46 Gy ( $23 \times 2 \text{ Gy}$ ) was planned using a pencil beam scanning technique on a uniform 4 mm dose grid. The planning objectives used for initial IMPT planning consisted of an extended set of planning objectives applied clinically for photon-based RT in order to also penalize intermediate doses to rectum ( $V_{30\text{Gy}}$ ) and bladder ( $V_{40\text{Gy}}$ ) (Table 4.1).

### *Robust plan optimization*

IMPT plans were robustly optimized by minimizing the penalty of the worst-case scenario within the interval of pre-defined range and position errors [129]. Besides the nominal scenario, six position error scenarios were included during optimization by shifting the isocenter position (left, right, inferior, superior, posterior, anterior). In photon-based RT, margins to expand the CTV to form the planning target volume (PTV) are not solely used to correct for geometric uncertainties. However, in this study the clinically used CTV-to-PTV margin in photon-based cervical cancer RT of 8 mm was used as position error for robust optimization. Also, three range error scenarios

were included (-3%, 0%, 3%) per position error scenario [24], resulting in a total of 21 scenarios consisting of both position and range errors considered during optimization.

### *IMPT plan approval*

After robust optimization, IMPT plan quality was first assessed by verifying if the obtained nominal dose distribution fulfilled all pre-defined evaluation objectives (Table 4.1). Next, robustly optimized IMPT plans were evaluated on robustness by applying range and position errors and recalculating the dose. Because robust optimization only included position errors in the main directions, the evaluation on robustness was applied based on an extended set of position errors. Next to the six isocenter position shifts used during optimization (i.e. 8 mm isocenter position shifts in the main directions), eight additional isocenter position shifts of 8 mm along the diagonal of each octant in three-dimensional space were added. Also, minimum (-3%) and maximum (3%) range errors used during optimization were included for evaluation to consider in total 28 perturbed dose scenarios. Robustly optimized IMPT plans were approved when the nominal dose scenario as well as at least 27 out of all 28 perturbed dose scenarios fulfilled all pre-defined evaluation objectives (Table 4.1).

**Table 4.1** | Beam configurations with associated gantry angles, initial planning objectives and evaluation objectives used.

Configuration	Gantry angles (°)
2-beam	90, 270
3-beam	0, 90, 270
4-beam	30, 90, 270, 330
Planning objectives	
CTV	Minimum dose 46 Gy ( $w=120$ ) Maximum dose 46.8 Gy ( $w=80$ ; $\sigma=50$ )
Body	Dose fall-off: 46–30 Gy over 1.2 cm ( $\sigma=0.6$ cm) ( $w=50$ ; $\sigma=30$ )
Bladder	Maximum 40 Gy to 20% ( $\sigma=10\%$ ) of the volume ( $w=10$ ; $\sigma=10$ )
Rectum	Maximum 30 Gy to 30% ( $\sigma=10\%$ ) of the volume ( $w=10$ ; $\sigma=10$ )
Evaluation objectives	
CTV	At least 40 Gy received by 99% of the volume * At most 50.4 Gy received by 2% of the volume
Body	At most 1800 cm <sup>3</sup> receiving 43.7 Gy
Rectum	At most 90% of the volume receiving 30 Gy *
Bowel	At most 600 cm <sup>3</sup> receiving 45 Gy
Bladder	At most 80% of the volume receiving 40 Gy *

*Abbreviations:* CTV = clinical target volume;  $w$  = weight;  $\sigma$  = standard deviation.

*Note:* Asterisks indicate evaluation objectives used for Pareto front generation.

## Pareto front approximation

The scripting facilities in RayStation were used to automatically approximate the Pareto front in robust IMPT planning (Figure 4.1). To start the automatic Pareto front approximation, an initially created IMPT plan with a fixed beam configuration and a set of planning objectives was required and assigned as base plan for the first iteration. Given the IMPT base plan, per iteration multiple IMPT plans were automatically generated with new planning objective values drawn from a Gaussian distribution with the value of the base plan as mean and pre-defined standard deviations. All generated plans were robustly optimized and plan approval was assessed by evaluating the nominal dose scenario as well as the 28 perturbed dose scenarios. When the pre-defined number of IMPT plans per iteration were generated, the dominating plans were derived using all approved IMPT plans from completed iterations. Dominating plans are plans for which one selected evaluation objective for Pareto front generation cannot be improved without deteriorating other selected evaluation objectives for Pareto front generation.

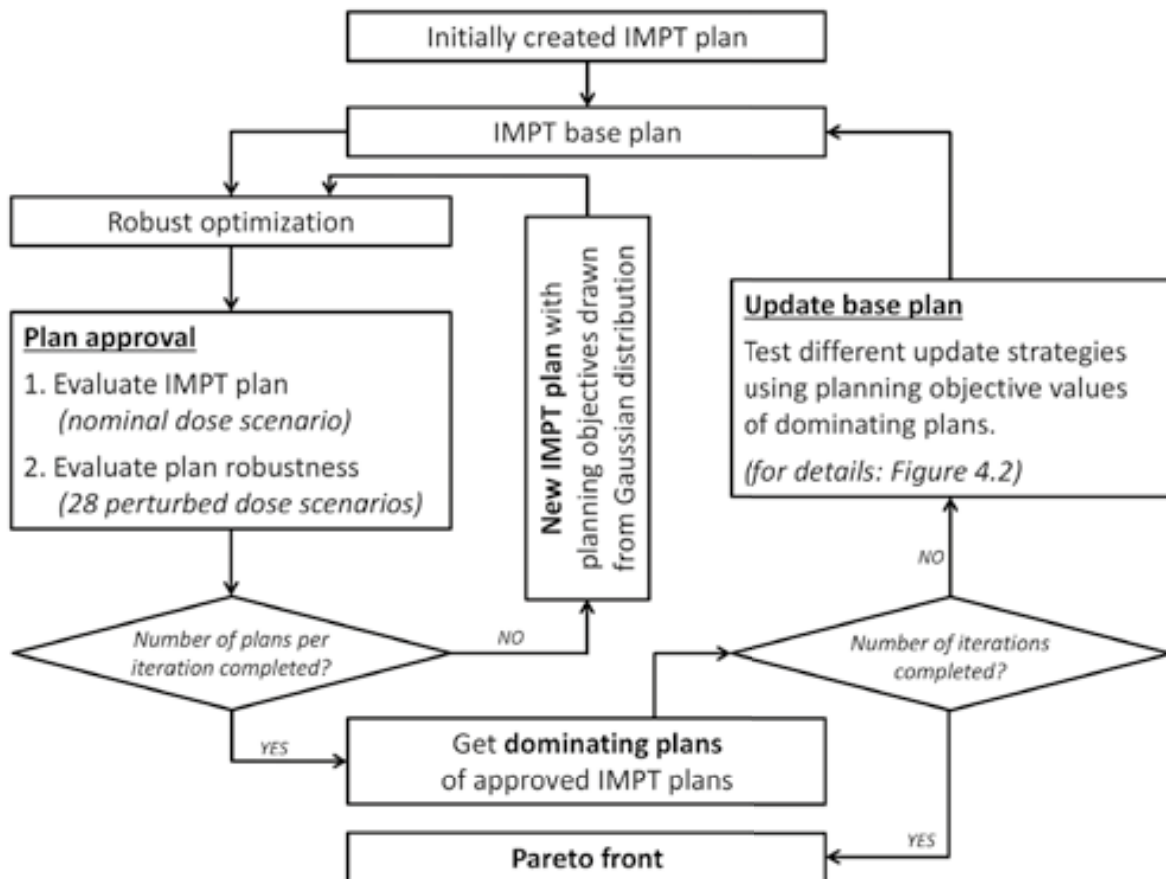
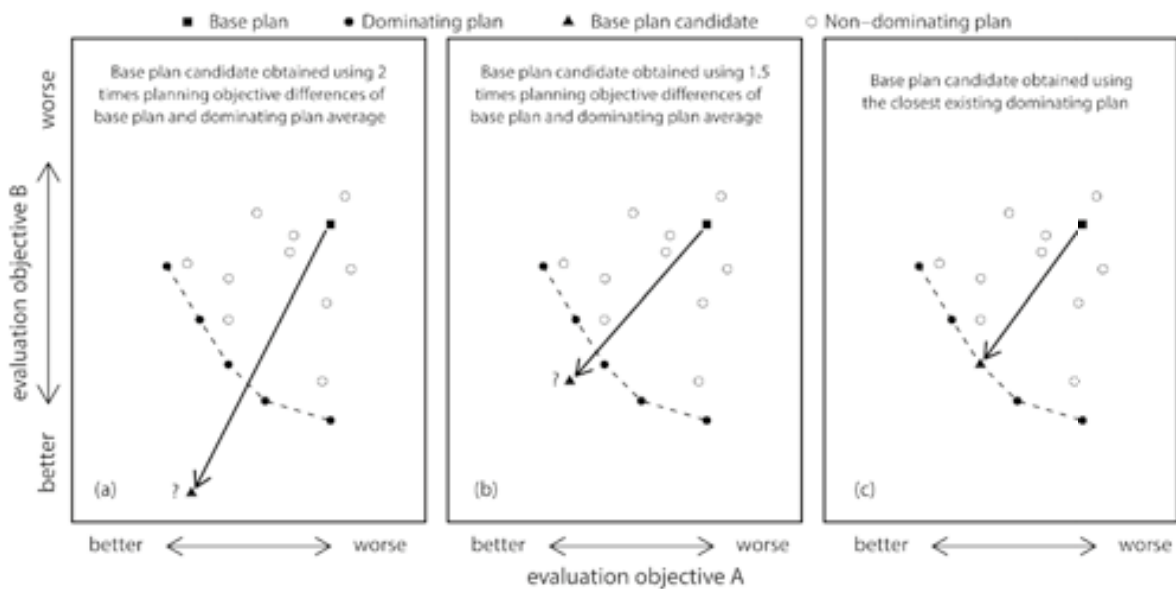


Figure 4.1 | Flowchart of the scripted method to approximate the Pareto front by automatically generating and evaluating multiple IMPT plans, including an update of the base plan after each iteration. The different scenarios tested to update the base plan are illustrated in more detail in Figure 4.2.

A new iteration was started with an updated IMPT base plan to approximate the Pareto front in a more efficient way. To update the base plan, planning objective values of the current base plan were adapted using dominating plans of all completed iterations. For all planning objectives, differences between the value of the current base plan and the average of all dominating plan values ( $PO_{diff}$ ) were calculated and used to test different update strategies. As a first approach, planning objective values of the current base plan were adapted by subtracting doubled  $PO_{diff}$  values and proposed as updated base plan candidate. After robust optimization and assessment of plan approval, this base plan candidate was considered suitable when both the plan was approved and the plan was a dominating plan within the set of approved plans. Alternatively, the described strategy was repeated using 1.5 times  $PO_{diff}$ . When both base plan candidates were not suitable, an existing dominating plan close to the current base plan (i.e. minimum sum of squared relative objective differences) was set as updated base plan. Compared to the current base plan, for all strategies the updated base plan should be shifted towards the Pareto front. Figure 4.2 shows a schematic 2D representation of the concept for the different update strategies.



**Figure 4.2** | Schematic 2D illustration of the three different strategies tested when updating the base plan. Each example shows the base plan together with approved IMPT plans including the dominating plans for the objectives of interest. First, planning objective value differences between the current base plan and averages of dominating plans were doubled and subtracted from planning objective values of the current base plan (a). This updated base plan candidate is only used when the plan is approved and a dominating plan within the set of generated plans. If strategy A is not suitable, 1.5 times planning objective value differences between the current base plan and averages of dominating plans were subtracted from planning objective values of the current base plan (b). This updated base plan candidate is only used when the plan is approved and a dominating plan within the set of generated plans. When both base plan candidates were not suitable, an existing dominating plan close to the current base plan was set as updated base plan (c).

When the pre-defined number of iterations were completed, the dominating plans of approved IMPT plans from all iterations were derived based on the selected evaluation objectives for Pareto front generation. This derived set of dominating IMPT plans was defined as the Pareto front.

## Data analysis

For each included patient, three Pareto fronts corresponding to three pre-defined beam configurations with identical gantry angles were generated. Each Pareto front was approximated using 5 iterations consisting of 40 IMPT plans per iteration. Given all pre-defined evaluation objectives, three evaluation objectives considered clinically most relevant and consistent with planning objectives were selected to span the three-dimensional Pareto front. Table 4.1 presents standard deviations used to automatically generate new planning objective values as well as the subset of evaluation objectives selected for Pareto front generation. The time needed to optimize and approve all IMPT plans on a personal computer with a 8-core, CPU of 2.40 GHz and 48 GB of RAM was recorded.

Per patient and beam configuration, the proportion of non-approved IMPT plans ( $NA_{\text{IMPT}}$ ) was calculated to investigate the effect of beam configuration on plan robustness. Also, from the 200 generated IMPT plans per defined beam configuration the proportion of dominating plans ( $DP_{\text{IMPT}}$ ) that described the Pareto front was assessed. To determine which beam configuration dominates, corresponding Pareto fronts were compared by calculating the proportion of approved IMPT plans contributing to the overall Pareto front. Given sets of approved IMPT plans based on different beam configurations, the overall Pareto front was defined by plans dominating this set of plans.

Differences between Pareto fronts were quantified according to a previously described method [130,131]. For each objective, the distribution of differences was calculated between linearly interpolated surfaces spanned by all other objectives (Figure 4.3). Pareto front differences were represented by the distribution quartiles and only considered appropriate when the overlap between surfaces spanned by all other objectives (i.e. the surface shared by both Pareto fronts divided by the average surface of both Pareto fronts) was at least 10%. This threshold was selected to avoid quantifications based on minimal information without omitting valuable information. Either positive or negative distribution quartiles represented overall differences between Pareto fronts (i.e. one Pareto front is dominated by the other Pareto front) while both positive and negative distribution quartiles indicated a Pareto front crossing.

When a limited or no overlap was observed between linearly interpolated surfaces, the proposed method could not be performed and an alternative method to compare Pareto fronts was used (Figure 4.3). Without keeping all other objectives constant, objective differences between individual dominating plans of both Pareto fronts were determined. Based on the derived distribution of differences, Pareto front ranges for the given objective were compared without taking into account all other objectives. Objective ranges were considered similar when the interval

defined by the first and third distribution quartile ( $I_{Q1-Q3}$ ) contained both positive and negative difference values. A complete positive or negative interval represented a substantial objective range difference between Pareto fronts.

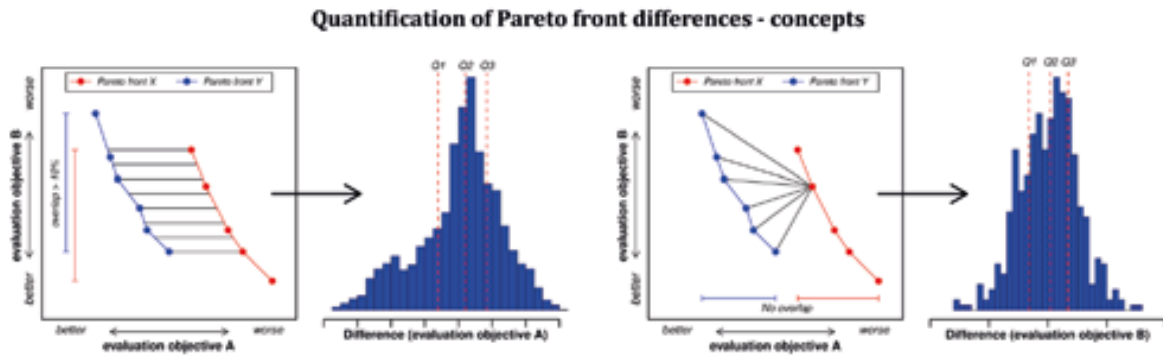


**Figure 4.3** | A 2D representation of the concepts to quantify the differences between Pareto fronts. The figure on the left side illustrates the quantification of Pareto front differences for evaluation objective A. Since the overlap between surfaces spanned by all other evaluation objectives (e.g. evaluation objective B) is substantial (>10%), the distribution of differences and associated quartiles between the linearly interpolated surfaces were calculated. The figure on the right side illustrates the quantification of Pareto front differences for evaluation objective B. Since no overlap between surfaces spanned by all other evaluation objectives (e.g. evaluation objective A) is observed, evaluation objective differences between dominating IMPT plans were calculated. Based on the interval defined by associated distribution quartiles, evaluation objective ranges were compared.

### 4.3 | Results

For each patient and pre-defined beam configuration, three-dimensional Pareto fronts were successfully sampled based on 200 IMPT plans. On average, robust optimization and consecutively plan approval of one IMPT plan took 40 minutes, 55 minutes and 75 minutes for the 2-beam, 3-beam and 4-beam set-up, respectively. As an example, Figure 4.4 shows a two-dimensional representation of the derived three-dimensional Pareto fronts of robust IMPT plans for one arbitrarily selected patient. Derived Pareto fronts of all patients can be found in the supplementary data available online<sup>1</sup>. In addition, an example representing dose distributions of dominating plans for the different beam configurations is shown (Figure 4.5).

Given all robustly optimized IMPT plans, the average proportion of non-approved IMPT plans was 32% (range, 12%–41%), 29% (range, 12%–43%) and 28% (range, 19%–45%) for the configuration using two beams, three beams and four beams, respectively. In all patients, IMPT plans based on the 2-beam set-up were completely dominated by plans with other beam configurations.

<sup>1</sup> [stacks.iop.org/PMB/61/1780/mmedia](https://stacks.iop.org/PMB/61/1780/mmedia)

For the 3-beam and 4-beam set-up, the average proportion of dominating plans contributing to the overall front was 28% (range, 12%–45%) and 72% (range, 55%–88%), respectively. Table 4.2 summarizes patient-specific proportions of  $NA_{IMPT}$  and  $DP_{IMPT}$  together with patient-specific proportions of dominating plans contributing to the overall Pareto front.

**Table 4.2** | Percentages of non-approved IMPT plans ( $NA_{IMPT}$ ) and dominating IMPT plans ( $DP_{IMPT}$ ) as well as percentages of dominating plans contributing to the overall patient-specific Pareto surface based on all approved IMPT plans per patient.

Patient	$NA_{IMPT}$ ( $DP_{IMPT}$ )			Overall Pareto front		
	2B	3B	4B	2B	3B	4B
1	38.0 (19.0)	11.7 (18.0)	22.9 (20.5)	0.0	12.5	87.5
2	40.5 (16.0)	29.5 (30.5)	33.0 (28.0)	0.0	21.7	78.3
3	30.5 (16.0)	39.5 (13.0)	21.5 (22.5)	0.0	24.5	75.5
4	40.0 (20.5)	43.0 (19.5)	45.0 (13.5)	0.0	45.5	54.5
5	12.0 (17.5)	23.5 (18.0)	18.5 (12.5)	0.0	33.3	66.7
Average	32.2 (17.8)	29.4 (19.8)	28.2 (19.4)	0.0	27.5	72.5

*Abbreviations:* 2B = 2-beam set-up; 3B = 3-beam set-up; 4B = 4-beam set-up.

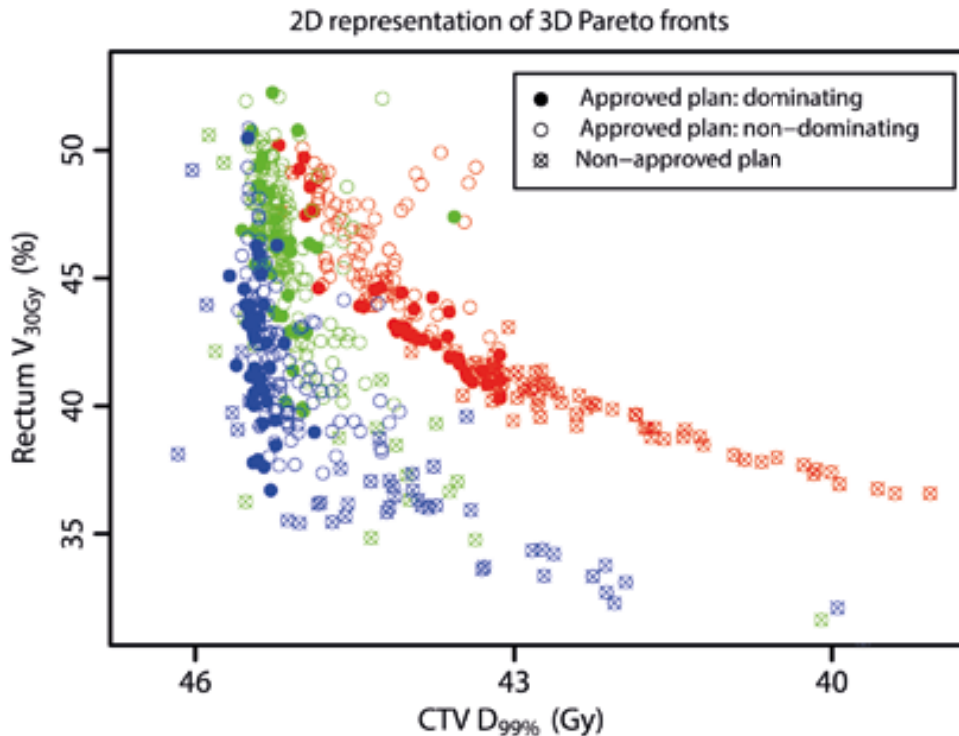


**Figure 4.4** | 2D representation of 3D Pareto fronts sampled using 200 generated IMPT plans and the nominal dose distribution is represented by dots for beam configurations using 2 beams (red), 3 beams (green) and 4 beams (blue). Per beam configuration, dominating plans are presented by filled dots and non-approved plans are represented by crossed dots.

**Table 4.3** | Results of the quantified differences between Pareto fronts per patient. For each evaluation objective, the quartiles of the difference distribution are presented. If no difference distribution could be determined while keeping all other objectives constant (indicated by a cross), results of the comparison between evaluation objective ranges and associated intervals ( $I_{Q1-Q3}$ ) are presented. Interpretation of results: Pareto front based on the first beam set-up compared to the Pareto front based on the second beam set-up (second column).

Patient	CTV D <sub>99%</sub> (Gy)		Rectum V <sub>30Gy</sub> (%)		Bladder V <sub>40Gy</sub> (%)	
	Q2 (Q1 - Q3)	objective range; ( $I_{Q1-Q3}$ )	Q2 (Q1 - Q3)	objective range; ( $I_{Q1-Q3}$ )	Q2 (Q1 - Q3)	objective range; ( $I_{Q1-Q3}$ )
1	3B-2B x	difference; (0.7-1.7)	x	similar; (-0.5-5.1)	-13.5 (-11.8- -14.8)	difference; (-12.7- -8.1)
	4B-2B x	difference; (1.0-1.8)	x	similar; (-4.1-0.8)	x	
	4B-3B 0.3 (0.2-0.3)		-6.5 (-7.8- -5.0)		-4.1 (-5.2- -2.9)	
2	3B-2B 1.4 (1.0-1.7)		-12.2 (-13.6- -10.4)		-10.3 (-12.4- -8.9)	
	4B-2B x	difference; (0.2-1.3)	x	difference; (-17.1- -9.2)	x	difference; (-7.1- -0.9)
	4B-3B 0.3 (0.1-0.5)		-5.9 (-8.2- -4.1)		-0.6 (-1.7-0.5)	
3	3B-2B 0.7 (0.6-0.8)		x	similar; (-7.5-0.1)	-7.8 (-8.6- -5.6)	
	4B-2B 0.5 (0.4-0.7)		-1.4 (-3.1-0.1)		-8.3 (-10.2- -6.3)	
	4B-3B 0.1 (0.0-0.1)		-2.4 (-5.5- -0.1)		-0.4 (-1.7-0.6)	
4	3B-2B 1.6 (1.3-1.8)		-11.1 (-12.0- -9.3)		-11.2 (-11.9- -10.3)	
	4B-2B 1.8 (1.7-1.8)		x	difference; (-7.8- -0.4)	x	difference; (-7.6- -2.5)
	4B-3B 0.1 (-0.1-0.3)		-1.4 (-2.4- -0.3)		-0.8 (-1.6- -0.1)	
5	3B-2B 0.5 (0.4-0.6)		x	difference; (-6.1- -2.1)	-3.2 (-3.5- -2.8)	
	4B-2B 0.5 (0.4-0.6)		x	difference; (-7.5- -2.6)	x	similar; (-1.5-1.0)
	4B-3B 0.1 (0.1-0.2)		-1.8 (-3.0- -0.7)		-0.7 (-1.1- -0.3)	

*Abbreviations:* Q1 = first quartile; Q2 = second quartile; Q3 = third quartile; 2B = 2-beam set-up; 3B = 3-beam set-up; 4B = 4-beam set-up.

Differences between Pareto fronts based on the 3-beam and 4-beam set-up in one objective were quantified for all patients using the surface spanned by the other two objectives. Compared to the 3-beam configuration, the median CTV  $D_{99\%}$  increased on average by 0.2 Gy when using the 4-beam configuration and the median rectum  $V_{30\text{Gy}}$  and bladder  $V_{40\text{Gy}}$  decreased on average by 3.6% and 1.3%, respectively. For the Pareto fronts based on the 2-beam configuration, differences with other Pareto fronts were quantified using the surface spanned by the other two objectives or individual dominating plans. Compared to the 2-beam configuration, evaluation objective range differences with positive interval values indicated improvements in CTV  $D_{99\%}$  for the 3-beam and 4-beam configuration, respectively. For both rectum  $V_{30\text{Gy}}$  and bladder  $V_{40\text{Gy}}$ , the 3-beam configuration as well as the 4-beam configuration resulted in similar or improved objective ranges. Table 4.3 summarizes the results of comparisons between obtained Pareto fronts for different beam configurations per patient.

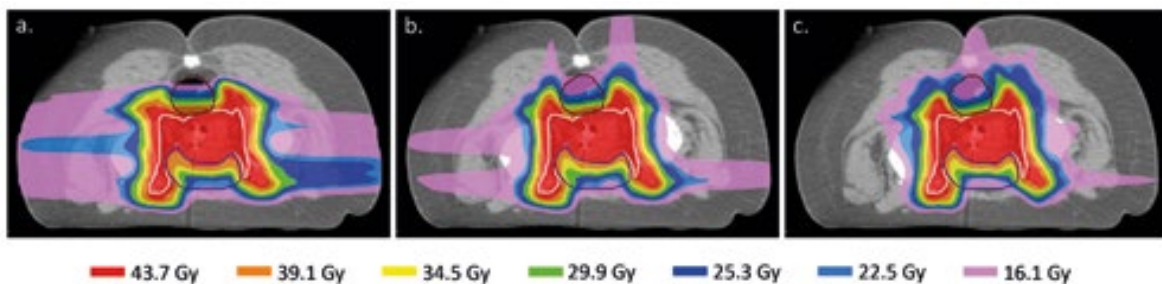


**Figure 4.5** | For one patient, color wash map examples of dose distributions corresponding to dominating plans are shown for the 2-beam (a), 3-beam (b) and 4-beam (c) configuration. All dose distributions indicated adequate CTV (white) coverage while differences in dose to rectum (brown) and bladder (purple) are observed.

## 4.4 | Discussion

We implemented a method to automatically approach the Pareto front of robust IMPT plans to enable beam configuration selection for cervical cancer PT. By comparing clinically relevant Pareto fronts of robust IMPT plans for different gantry angle sets, the most favourable beam configuration in terms of inspected parameters was selected. The presented study was the first to investigate the effect of beam configurations on robust IMPT planning, which included robust optimization followed by an evaluation of the actual robustness, and to compare Pareto fronts for beam configuration selection. A total of 200 robust IMPT plans per beam configuration per patient resulted in configuration-specific Pareto fronts, allowing us to objectively compare the effect of different beam set-ups on plan quality for beam configuration selection in cervical cancer PT. Our study showed that per beam configuration a substantial part of the robustly optimized IMPT plans (i.e. on average 29%) was not approved after robustness evaluation. For all patients, the defined

configuration using two beams was inferior compared to the other specified beam configurations in terms of robustness, target coverage and OARs sparing. Although differences with the specified 3-beam set-up are small, IMPT plans based on the defined 4-beam set-up largely dominated the overall Pareto fronts.

Unlike beam configurations used in previous studies on proton-based cervical cancer RT [70,71,123,124], we demonstrated the feasibility of beam configuration selection in cervical cancer PT by objectively comparing Pareto fronts based on different gantry angle sets. The optimal exploitation of proton therapy for specific tumor sites (e.g. cervical cancer) will only be achieved by determining the optimal beam configuration. Moreover, range and position uncertainties can largely affect IMPT dose distributions [122,132]. However, the effect of uncertainties on dose delivery in proton-based cervical cancer RT is not yet investigated. Together with the lack of beam configuration comparisons in cervical cancer, previously reported results on proton-based RT for cervical cancer might need to be interpreted with caution.

Even though the feasibility of using Pareto fronts as a comparative tool for treatment strategies and delivery techniques was proven [128], only a limited number of studies reported on the use of Pareto fronts for treatment technique comparison or treatment plan validation [130,131,133]. Along the lines of these studies, we implemented our method to automatically approach the Pareto front in robust IMPT planning. Besides the addition of robustness validation after robust optimization, we also added the efficiency of approaching the Pareto front by starting each iteration with an updated base plan [134].

Instead of Pareto front approximation based on random sampling used in this study, Pareto fronts could theoretically also be approached by using mathematically derived gradient directions to approximate towards the Pareto front [135]. However, for relatively simple multi-criteria optimization problems already a complex situation arises and implementation of this mathematical method is beyond the clinical purpose of our study.

In this study, we compared three pre-defined beam configurations for PT in the pelvic region using three-dimensional Pareto fronts based on robust IMPT planning. The pre-defined beam set-ups consisted of a limited number of beams, resulting in relatively short delivery times and limited inter-beam patient movement errors. Combined with the defined update strategy, three-dimensional Pareto fronts are approximated using a relatively large number of IMPT plans and therefore assumed to represent realistic trade-offs between target coverage and OAR sparing. Although three-dimensional Pareto fronts were sampled in this study based on the subset of evaluation objectives selected for Pareto front generation, the presented method can be used to sample and compare multidimensional Pareto fronts based on multiple selected evaluation objectives. However, an increased number of evaluation objectives used for Pareto front generation requires a larger number of IMPT plans to sufficiently sample multidimensional Pareto fronts.

Although the application of planning objectives used clinically for photon-based RT, initial IMPT treatment plans resulted already in relatively good IMPT plans. Therefore, only a limited number of iterations were needed to sample the clinically most relevant parts of the Pareto front.

However, the use of these initial plans also steered already towards specific parts of the Pareto front and approximated Pareto fronts could therefore not always be compared quantitatively. If the current calculation times can be largely reduced, sufficiently sampling the entire Pareto front by using multiple starting positions could solve this issue.

In this study, sets of dominating IMPT plans acquired with identical optimization conditions were compared and spot filtering using the machine-specific minimum monitor units (MU) was not included in the IMPT optimization process. However, the influence of spot filtering using the machine-specific MU minimum on optimized dose distributions was investigated. Because the contribution of spots with below minimum MU was expected to increase with the number of beams, a subset of dominating plans based on the 4-beam configuration was also optimized including spot filtering. The minor differences (<2%) found between dose distributions obtained with and without spot filtering indicated reliable results presented in this study.

For robust optimization and evaluation on robustness, the range error value was selected based on literature [24] and the clinically used CTV-to-PTV margin in photon-based RT for cervical cancer was used to define the position error. These values directly determine IMPT plan robustness, but whether the selected values are adequate to anticipate on patient-specific uncertainties during the course of treatment can only be validated using daily imaging. Although all plans were robustly optimized, on average 29% was not approved after evaluation using the same error values. Nevertheless, the error values were considered adequate and for the purpose of this study were kept constant to reliably compare Pareto fronts based on different beam configurations. Additional research is required to quantify individual error values and corresponding consequences for dose distributions obtained with specific beam configurations.

Compared to analytical dose calculation algorithms, a Monte Carlo algorithm might improve the accuracy of dose calculation in complex geometries [136]. In the pelvic area, as in this study, effects of inhomogeneities mainly due to air and bone are limited and dose distributions can be calculated accurately using an analytical algorithm. Therefore, the limitation induced by the dose calculation algorithm was assumed to be negligible.

Because of a limited overlap, the quantification of Pareto front differences based on linearly interpolated surfaces could not be performed for all objectives. The overlap threshold of 10% was selected to avoid quantifications based on minimal information while an increase of this threshold could omit valuable information. Although Pareto fronts with a limited overlap could also be extrapolated to enable quantification, Pareto front differences would strongly depend on only a few IMPT plans without representing realistic differences. As an alternative, differences between individual dominating plans were calculated without keeping all other objectives constant.

Although the limited number of patients included in this study, all patients showed similar results with respect to the optimal beam configuration in terms of DVH parameters. However, general conclusions on beam configuration selection in cervical cancer PT can only be drawn when more patients are included. Since the calculation time is the limiting factor, for one patient we explored the possible reduction in calculation time by using RayStation version 4.6.102.4 installed

on a personal computer with 2 CPUs of 12 physical cores each. The average calculation time reduction of 70% found for this patient opens the possibility to extend this study in future.

Besides the approximation of Pareto fronts based on robust IMPT planning in cervical cancer, our presented method to approach the Pareto front is generic and therefore can be applied for different treatment sites. Although our strategy is especially developed for proton-based RT by focusing on plan robustness, also Pareto fronts of photon-based plans can be derived to improve clinically obtained RT plans or compare RT treatment techniques.

To actually take advantage of the planned IMPT dose distributions acquired with the selected beam configuration, anticipation on interfraction anatomical changes during fractionated EBRT in cervical cancer is required. Pre-fraction imaging allows, besides verifying the patient position accurately, adapting the radiation delivery during the treatment course and automatic segmentation tools are developed to support these purposes [75,76]. Nevertheless, the dosimetric advantages of proton therapy compared with photon therapy for cervical cancer patients using the selected beam configuration combined with an adaptive strategy to compensate for interfraction anatomical changes are being investigated.

## 4.5 | Conclusion

This study demonstrated a method to automatically approach the Pareto front in robust IMPT treatment planning. For five cervical cancer patients, we derived and compared Pareto fronts based on robust IMPT plans for three different beam configurations. For all patients, the defined 4-beam configuration was found to be optimal in terms of robustness, target coverage and OAR sparing.



# Chapter 5

## Dosimetric advantages of proton therapy compared with photon therapy using an adaptive strategy in cervical cancer

A version of this chapter has been published as:

*Dosimetric advantages of proton therapy compared with photon therapy using an adaptive strategy in cervical cancer*

A.J.A.J. van de Schoot, P. de Boer, K.F. Crama, J. Visser, L.J.A. Stalpers,  
C.R.N. Rasch and A. Bel

*Acta Oncologica* 2016; DOI:10.3109/0284186X.2016.1139179.

<http://dx.doi.org/10.3109/0284186X.2016.1139179>

## Abstract

### Purpose

Image-guided adaptive proton therapy (IGAPT) can potentially be applied to take into account interfraction motion while limiting organ at risk (OAR) dose in cervical cancer radiation therapy (RT). In this study, the potential dosimetric advantages of IGAPT compared with photon-based image-guided adaptive RT (IGART) were investigated.

### Material & Methods

For thirteen cervical cancer patients, full and empty bladder planning computed tomography (CT) images and weekly CTs were acquired. Based on both primary clinical target volumes (pCTVs) (i.e. gross tumor volume (GTV), cervix, corpus-uterus and upper part of the vagina) on planning CTs, the pre-treatment observed full-range primary internal target volume (pITV) was interpolated to derive pITV subranges. Given corresponding ITV<sub>s</sub> (i.e. pITVs including lymph nodes), patient-specific photon and proton plan libraries were generated. Using all weekly CTs, IGART and IGAPT treatments were simulated by selecting library plans and recalculating the dose. For each recalculated IGART and IGAPT fraction, CTV (i.e. pCTV including lymph nodes) coverage was assessed and differences in fractionated substitutes of dose-volume histogram (DVH) parameters ( $V_{15\text{Gy}}$ ,  $V_{30\text{Gy}}$ ,  $V_{45\text{Gy}}$ ,  $D_{\text{mean}}$ ,  $D_{2\text{cc}}$ ) for bladder, bowel and rectum were tested for significance (Wilcoxon signed-rank test). Also, differences in toxicity-related DVH parameters (rectum  $V_{30\text{Gy}}$ , bowel  $V_{45\text{Gy}}$ ) were approximated based on accumulated dose distributions.

### Results

In 92% (96%) of all recalculated IGAPT (IGART) fractions adequate CTV coverage ( $V_{95\%} > 98\%$ ) was obtained. All dose parameters for bladder, bowel and rectum, except the fractionated substitute for rectum  $V_{45\text{Gy}}$ , were improved using IGAPT. Also, IGAPT reduced the mean dose to bowel, bladder and rectum significantly ( $p < 0.01$ ). In addition, an average decrease of rectum  $V_{30\text{Gy}}$  and bowel  $V_{45\text{Gy}}$  indicated reductions in toxicity probabilities when using IGAPT.

### Conclusion

This study demonstrates the feasibility of IGAPT in cervical cancer using a plan-library based plan-of-the-day approach. Compared to photon-based IGART, IGAPT maintains target coverage while significant dose reductions for the bladder, bowel and rectum can be achieved.

## 5.1 | Introduction

Radiation therapy (RT) for patients with locally advanced cervical cancer usually consists of external beam RT (EBRT) with concomitant chemotherapy or hyperthermia and subsequently brachytherapy [72]. Compared to conformal EBRT, intensity-modulated RT (IMRT) allows highly conformal dose distributions resulting in decreased organ at risk (OAR) dose [119]. To completely benefit from this potential advantage, adequate patient set-up based on daily image guidance is essential. However, despite drinking instructions, large bladder volume variations may induce interfraction target motion which increases the risk of target under-dosing and limits OAR sparing [73].

Pre-fraction cone-beam CT (CBCT) allows adapting the radiation delivery during the course of treatment. This is known as adaptive RT (ART) and several ART strategies have been investigated [53,56]. Similar to our current clinical practice, a practical approach frequently applied for pelvic EBRT is the plan-library based plan-of-the-day strategy [58,59]. Based on the pre-treatment acquired target motion range, treatment plans corresponding to different target shapes and positions are created and using pre-fraction CBCT the plan best fitting the target shape is selected. Also in cervical cancer, this online adaptive strategy has the potential to correct for most interfraction target motion to ensure daily target coverage. However, OARs still receive substantial dose during photon-based image-guided ART (IGART) [58,59].

Compared to photons, protons have certain distinct advantages due to their finite range and hold the promise of limited OAR toxicity [34,69]. Intensity-modulated proton therapy (IMPT) enables a highly conformal dose delivery to complex-shaped target volumes including steep dose fall-offs around the target. However, due to its sensitivity to range and position uncertainties, IMPT dose delivery requires appropriate online image guidance [24]. Moreover, anatomical changes can largely influence dose delivery and therefore IMPT can benefit from treatment adaptation based on pre-fraction imaging.

Previously, only a limited number of studies investigated the potential benefit of proton-based RT compared to photon-based RT in cervical cancer [69-71,123]. Even though the planning target volume (PTV) concept is less suitable for IMPT [24], those studies used the PTV concept to anticipate on uncertainties. Moreover, none of them recalculated planned dose distributions using additional imaging data in order to evaluate differences between photon-based and proton-based RT in terms of delivered dose.

To investigate the actual benefit of proton therapy in cervical cancer, differences in delivered dose between photon-based and proton-based RT treatments using an adaptive strategy need to be determined. Therefore, our aim was to investigate the dosimetric advantages of image-guided adaptive proton therapy (IGAPT) in cervical cancer compared to photon-based IGART. Using a plan-library based plan-of-the-day adaptive strategy, both IGAPT and IGART treatments were simulated by recalculating selected plans on weekly CTs. Differences were evaluated in terms of dose-volume histogram (DVH) parameters and normal tissue complication probability (NTCP).

## 5.2 | Material & Methods

### Patients and imaging

Thirteen cervical cancer patients treated with photon-based RT between January 2014 and August 2015 were included after obtaining written informed consent for additional CT imaging. These additional CTs were acquired solely for a pilot study to explore the potential benefit of ART and were approved by the local medical ethical committee. One patient was excluded because of image artifacts induced by a metal hip prosthesis. Patients were treated in prone position using a belly board device and in supine position when selected for para-aortic irradiation or when the prone position was not possible. In order to treat with a full bladder, patients were instructed to empty their bladder, to drink 0.5 liter of water, and to refrain from voiding 1.5 h prior to irradiation. Table 5.1 presents patient characteristics and clinical treatment details.

Besides the full bladder planning CT, an additional empty bladder planning CT prior to treatment and weekly CTs directly after RT delivery were acquired. All CT images with a slice thickness of 2.5 mm were obtained in RT treatment position. For two patients, the empty bladder planning CT was not acquired and the weekly CT with the smallest bladder volume was used as surrogate and excluded for treatment simulations. Three patients received four instead of five weekly CTs due to logistical issues and one patient received an additional sixth CT due to clinical issues regarding tumor response. The radiation oncologist delineated on all CTs the gross tumor volume (GTV), corpus-uterus, cervix, upper part of the vagina and elective lymph nodes. Also, the body, bowel cavity, as a surrogate for small bowel, rectum, kidneys and bladder were delineated using Radiation Therapy Oncology Group (RTOG) guidelines [137]. The primary CTV (pCTV) encompasses the GTV, cervix, corpus-uterus and upper part of the vagina. The CTV included the pCTV and elective lymph nodes.

### Library of structures

After bony registration of both planning CTs, the pCTV on the full bladder planning CT was registered to the pCTV on the empty bladder planning CT using a structure-based deformable image registration algorithm [78]. The obtained deformation vectors after registration represented the connection between corresponding points on both structures. By linear scaling of the deformation vectors, the patient-specific full-range primary internal target volume (pITV) was divided into three, one or two pITV subranges when the corpus-uterus tip displacement was above 20 mm, below 10 mm or in between, respectively (Table 5.1, Figure 5.1). Corresponding to each pITV subrange an ITV was constructed by including elective lymph nodes.

**Table 5.1** | Patient characteristics.

Patient	FIGO stage	Type of irradiation	Fractionation scheme	Clinical treatment		Treatment position	No. of CTs (repeat CTs)	No. of ITVs	
1	*	IB2	pelvic	23 x 2.0 Gy	5-field IMRT	non-ART	prone	6 (4)	1
2	**	IIB	pelvic	23 x 2.0 Gy	dual-arc VMAT	non-ART	prone	7 (5)	3
3	*	IB2	pelvic	23 x 2.0 Gy	dual-arc VMAT	non-ART	prone	8 (6)	3
4	**	IIA	pelvic	23 x 2.0 Gy	5-field IMRT	non-ART	prone	7 (5)	3
5	**	IIB	pelvic	23 x 2.0 Gy	5-field IMRT	non-ART	supine	6 (5)	3
6	*	IIA	pelvic	23 x 2.0 Gy	dual-arc VMAT	non-ART	prone	7 (5)	2
7	*	IIB	para-aortic	28 x 1.8 Gy	dual-arc VMAT	non-ART	supine	7 (5)	1
8	**	IIB	pelvic	23 x 2.0 Gy	dual-arc VMAT	non-ART	prone	5 (4)	3
9	*	IIIB	para-aortic	28 x 1.8 Gy	dual-arc VMAT	non-ART	supine	7 (5)	2
10	**	IIB	pelvic	23 x 2.0 Gy	dual-arc VMAT	non-ART	supine	7 (5)	3
11	*	IB1	pelvic	23 x 2.0 Gy	dual-arc VMAT	ART	supine	7 (5)	2
12	*	IB1	pelvic	23 x 2.0 Gy	dual-arc VMAT	ART	supine	6 (4)	3

*Abbreviations:* FIGO = International Federation of Gynecology and Obstetrics; CT = computed tomography; ITV = internal target volume; ART = adaptive radiation therapy; VMAT = volumetric modulated arc therapy; IMRT = intensity modulated radiation therapy.

\* All CTs acquired with LightSpeed RT16, General Electric Company, Waukesha WI, USA.

\*\* All CTs acquired with LightSpeed RT16, General Electric Company, Waukesha WI, USA. Only full bladder planning CT acquired with Gemini TF, Philips Medical Systems, Eindhoven, the Netherlands.

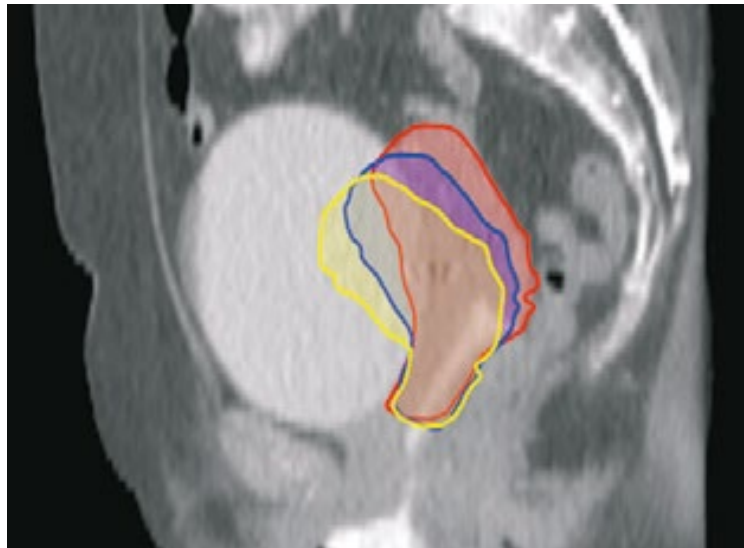


**Figure 5.1** | Sagittal view of the full bladder planning CT for a patient that showed large cervix-uterus motion (corpus-uterus tip displacement >2.0 cm) induced by bladder volume variation. The three illustrated primary ITV subranges (red, blue and yellow) are obtained by dividing the full-range primary ITV based on linear scaling of the obtained deformation vectors.

## Treatment planning

All treatment plans were generated with RayStation (version 4.4, RaySearch Laboratories AB, Stockholm, Sweden). Contrast agent induced high-density values on planning CTs used for vagina or bowel and bladder visualization were corrected to muscle ( $1.05 \text{ g/cm}^3$ ) and water ( $1.0 \text{ g/cm}^3$ ) density, respectively. Patient-specific plan libraries for both photons and protons were created based on a prescribed physical ITV dose of 46 Gy ( $23 \times 2 \text{ Gy}$ ) for pelvic irradiation or 50.4 Gy ( $28 \times 1.8 \text{ Gy}$ ) for para-aortic irradiation. Plans were robustly optimized on a uniform 3 mm dose grid with the beam isocenter set to the ITV center of mass using the full bladder planning CT [129]. Plan optimizations were started with the initial set of planning objectives for each plan (Table 5.2) and objective values were individually optimized to minimize OAR dose while maintaining International Commission on Radiation Units & Measurements (ICRU) based ITV coverage ( $D_{98\%} > 95\%$ ,  $D_{2\%} < 107\%$ ). Since the prescribed target dose is below OAR dose limits, only target coverage robustness was evaluated by applying errors and recalculating the dose. For all perturbed dose distributions adequate ITV coverage was required.

Photon plans were generated using a 10-MV dual-arc volumetric modulated arc therapy (VMAT) technique ( $356^\circ$  per arc, fixed  $20^\circ$  collimator angle). Besides the nominal isocenter position, six isocenter position shifts in each main direction (left, right, inferior, superior, posterior, anterior) were included to consider in total seven scenarios for robust optimization. Position shifts of 8 mm were applied, which equals the clinically used ITV-to-PTV margin in cervical cancer RT. For robustness evaluation, next to the six error scenarios used for optimization, eight additional error scenarios with 8 mm isocenter shifts along the diagonal of each octant in three-dimensional space were added. In total, 14 error scenarios were considered for ITV coverage robustness evaluation.

**Table 5.2** | Initial set of planning objectives used for pelvic (para-aortic) irradiation. An asterisk indicates planning objectives only used for para-aortic irradiation.

Planning objectives		
CTV	Minimum dose 46 (50.40) Gy	w=120
	Maximum dose 46.80 (51.40) Gy	w=80
Body	Dose fall-off: 46–30 (51.40–36) Gy over 1.20 cm	w=50
Rectum	Maximum dose 43.70 (47.88) Gy	w=10
	Maximum 30 Gy to 70% (80%) of the volume	w=5
Bladder	Maximum dose 43.70 (47.88) Gy	w=10
	Maximum 30 Gy to 70% (80%) of the volume	w=5
Bowel cavity	Maximum dose 43.70 (47.88) Gy	w=10
Kidney	* Maximum 18 Gy to 33% of the volume	w=25

*Abbreviations:* CTV = clinical target volume; w = weight.

IMPT plans were generated based on pencil beam scanning (spot size in air:  $\sigma=2.5$  mm – 7.0 mm (226.7 MeV – 70.0 MeV)) using four fixed posterior beams (30°, 90°, 270°, 330° (prone); 90°, 150°, 210°, 270° (supine)) [138]. Assuming a proton relative biological effectiveness of 1.1 [139], IMPT plans were created with a prescribed ITV dose of 46 Gy-equivalent or 50.4 Gy-equivalent. Besides the nominal isocenter position and the six isocenter position shifts of 8 mm in the main directions also three range errors (3%, 0%, -3%) were included to consider in total 21 scenarios for robust optimization. ITV coverage robustness was evaluated using 28 error scenarios, consisting of 14 position errors (8 mm) and 2 range errors (-3%, 3%). Similar to the VMAT plans, these position errors included isocenter position shifts in the six main directions and the eight diagonal directions of each octant in three-dimensional space.

### Planned dose distributions

To explore differences between VMAT and IMPT plans, dose distributions for bladder, rectum and bowel cavity were evaluated. Planned dose parameters for the volumes receiving 15 Gy ( $V_{15\text{Gy}}$ ), 30 Gy ( $V_{30\text{Gy}}$ ) and 45 Gy ( $V_{45\text{Gy}}$ ) were extracted [56,140]. Because we aim to treat with a full bladder to minimize bowel irradiation, only planned dose parameters of library plans representing the full bladder planning CT anatomy were evaluated.

### Recalculated fraction doses

Using all weekly CTs, IGART and IGAPT treatments were simulated by selecting plans from the created plan libraries and recalculating fraction dose distributions based on our clinical applied strategy. First, image-guided patient alignment was simulated by registering CTs to the full bladder planning CT based on bony anatomy using only translations. Patient-specific ITV structures were projected on the registered CT and the ITV encompassing the pCTV was selected. Both VMAT and IMPT library plans corresponding to the selected ITV were recalculated on the registered CTs to obtain fraction dose distributions.

IGART and IGAPT fraction dose distributions were verified on target coverage and compared for OAR doses. Target coverage was assessed by calculating the CTV volume receiving at least 95% of the prescribed fraction dose ( $V_{95\%}$ ). Differences in bladder, bowel cavity and rectum sparing were verified by calculating the mean ( $D_{\text{mean}}$ ) and maximum ( $D_{2\text{cc}}$ ) fraction dose and extracting fractionated substitutes of  $V_{15\text{Gy}}$ ,  $V_{30\text{Gy}}$  and  $V_{45\text{Gy}}$  (i.e.  $V_{15\text{Gy}}\text{-fx}$ ,  $V_{30\text{Gy}}\text{-fx}$  and  $V_{45\text{Gy}}\text{-fx}$ ). A fractionated substitute represents the volume receiving the corresponding fraction dose (i.e. the dose level divided by the number of fractions). Patient-specific DVHs were plotted and dose differences between IGART and IGAPT fractions were tested pairwise for significance using a non-parametric statistical test (Wilcoxon signed-rank test).

## OAR toxicity

In addition to the analysis based on recalculated fraction dose distributions, differences in toxicity probabilities for bowel and rectum were estimated. Differences between the DVH parameter associated with overall rectum toxicity ( $V_{30\text{Gy}}$ ) were derived [140]. For bowel, NTCP differences associated with at least grade 2 acute gastrointestinal toxicity were quantified using

$$NTCP = \frac{1}{1 + \left(\frac{V_{50}}{V_{45\text{Gy}}}\right)^k}$$

where  $V_{45\text{Gy}}$  represents the volume ( $\text{cm}^3$ ) receiving 45 Gy,  $V_{50}=410 \text{ cm}^3$  and  $k=3.2$  [141].

The toxicity-related DVH parameters (rectum  $V_{30\text{Gy}}$ , bowel cavity  $V_{45\text{Gy}}$ ) were estimated by scaling patient-specific averages of rectum  $V_{30\text{Gy}}$ -fx and bowel cavity  $V_{45\text{Gy}}$ -fx with the prescribed number of fractions. Alternatively, CTs were registered deformable to the full bladder planning CT using the hybrid deformable registration algorithm implemented in RayStation [142]. Based on these registrations, fraction dose distributions were warped and weighted accumulated to derive total delivered dose distributions. Toxicity-related DVH parameter values were extracted and differences were tested pairwise using a non-parametric statistical test (Wilcoxon-signed rank test). The explanation and validation of the algorithm can be found in Appendix 5.A.

## 5.3 | Results

Per patient, plan libraries consisting of clinically acceptable VMAT and IMPT plans were created (Figure 5.2). Adequate ITV coverage ( $D_{98\%} \geq 95\%$ ;  $D_{2\%} \leq 107\%$ ) was found for all perturbed dose distributions after robustness evaluation and resulted in a total number of 58 robust library plans. Planned dose distributions indicated improvements in OAR sparing using IGAPT. The average planned  $V_{15\text{Gy}}$ ,  $V_{30\text{Gy}}$  and  $V_{45\text{Gy}}$  decreased with 0.1%, 13.0% and 26.0%, 19.0%, 27.0% and 15.5%, and 43.2%, 26.9% and 10.7% for rectum, bladder and bowel cavity, respectively. Patient-specific DVHs of planned dose distributions are available online<sup>2</sup>.

After dose recalculation on the weekly CTs, six simulated fractions (10.7%) from four different patients showed inadequate CTV coverage for both the IGART and IGAPT strategy. Due to substantial deviating anatomy compared to the pre-treatment derived full-range pITV, library plans were inappropriate and these fractions were excluded from further analysis. For the remaining fractions, adequate target coverage ( $V_{95\%} > 98\%$ ) was obtained in 92% (96%) of the recalculated IGAPT (IGART) plans and results on planned and recalculated target dose ( $D_{98\%}$ ,  $D_{2\%}$ ) are presented (Figure 5.3). Although two (four) fractions resulted in CTV  $V_{95\%} < 98\%$  for the IGART (IGAPT) strategy while the IGAPT (IGART) strategy resulted in CTV  $V_{95\%} > 98\%$ , the average CTV coverage per patient was adequate for both strategies.

<sup>2</sup> <http://www.tandfonline.com/doi/suppl/10.3109/0284186X.2016.1139179>

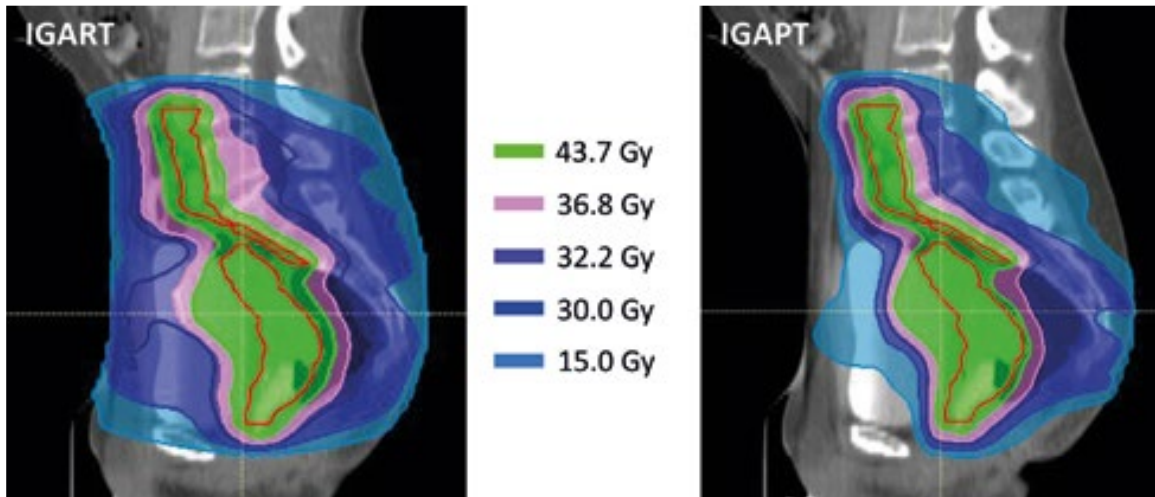


Figure 5.2 | Sagittal view of color wash map examples of dose distributions are shown for the IGART strategy (left) and the IGAPT strategy (right). Both dose distributions indicated adequate CTV (red) coverage while large differences in low and medium dose to surrounding healthy tissue are observed.

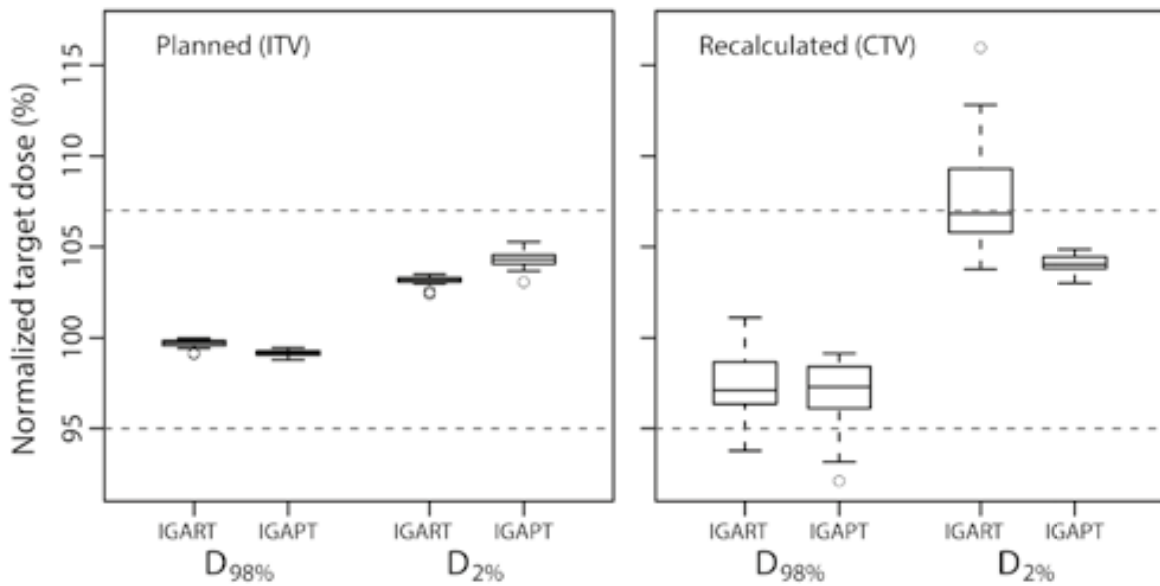


Figure 5.3 | For the planned dose distributions based on the ITV (left) and the recalculated dose distribution based on the CTV (right), boxplots of target dose parameters over all patients are shown as percentage of the prescribed dose for both the IGART and the IGAPT strategy. Boxes represent upper and lower quartiles (IQR), the band inside the box the median value and the whiskers the highest (lowest) value within 1.5 IQR of the upper (lower) quartile.

The simulated fractions indicated OAR dose reductions for  $V_{15Gy}$ -fx,  $V_{30Gy}$ -fx and  $V_{45Gy}$ -fx, similar to the OAR dose reductions represented by the planned dose distributions. As an example, Figure 5.4 shows DVHs of recalculated fraction dose distributions for two typical patients. Patient-specific DVHs of recalculated fraction dose distributions are available online<sup>2</sup>. All DVH parameters, except

rectum  $V_{45Gy}$ -fx, showed a relative improvement in OAR sparing when using IGAPT. Also, both  $D_{mean}$  and  $V_{30Gy}$ -fx for bladder, rectum and bowel cavity decreased significantly (Figure 5.5). Table 5.3 presents the mean dosimetric parameter values for the OAR evaluations and the absolute and relative differences between IGART and IGAPT.

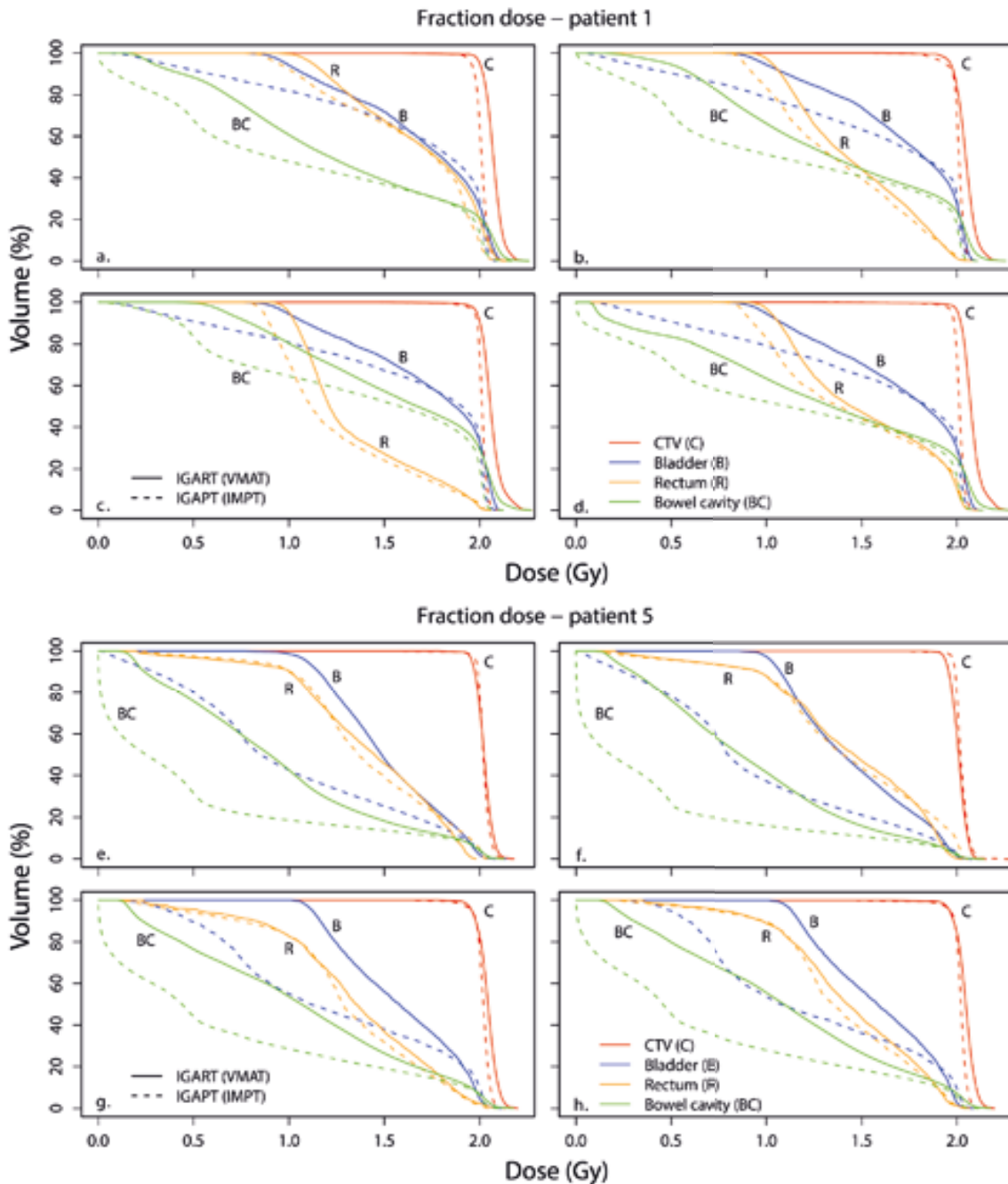


Figure 5.4 | For patient 1 (a-d) and patient 5 (e-h), DVHs of recalculated fraction dose distributions are shown for target and OARs based on VMAT plans for the IGART strategy (solid lines) and IMPT plans for the IGAPT strategy (dotted lines). The intersection of the 2 solid black lines indicates  $V_{95\%}=98\%$ . For one fraction of patient 1 (b), IGAPT resulted in inadequate CTV coverage while CTV coverage using IGART was adequate.

The scaled averages of DVH parameters indicated a reduction in rectum  $V_{30\text{Gy}}$  of 8% for IGAPT (average, 69%) compared to IGART (average, 77%). Also, a decrease in NTCP for bowel of 0.07 was estimated for IGAPT (average, 0.43) compared to IGART (average, 0.50). Dose accumulation based on deformable registration resulted in an average rectum  $V_{30\text{Gy}}$  difference of 7% between IGART (average, 81%) and IGAPT (average, 74%). For bowel, the NTCP decreased on average 0.15 when using IGAPT (average, 0.18) instead of IGART (average, 0.33). Moreover, IGAPT resulted in significant improvements ( $p < 0.01$ ) for rectum  $V_{30\text{Gy}}$  and bowel NTCP. However, two (one) patients showed a limited increase in rectum  $V_{30\text{Gy}}$  (bowel NTCP) for IGAPT compared to IGART.

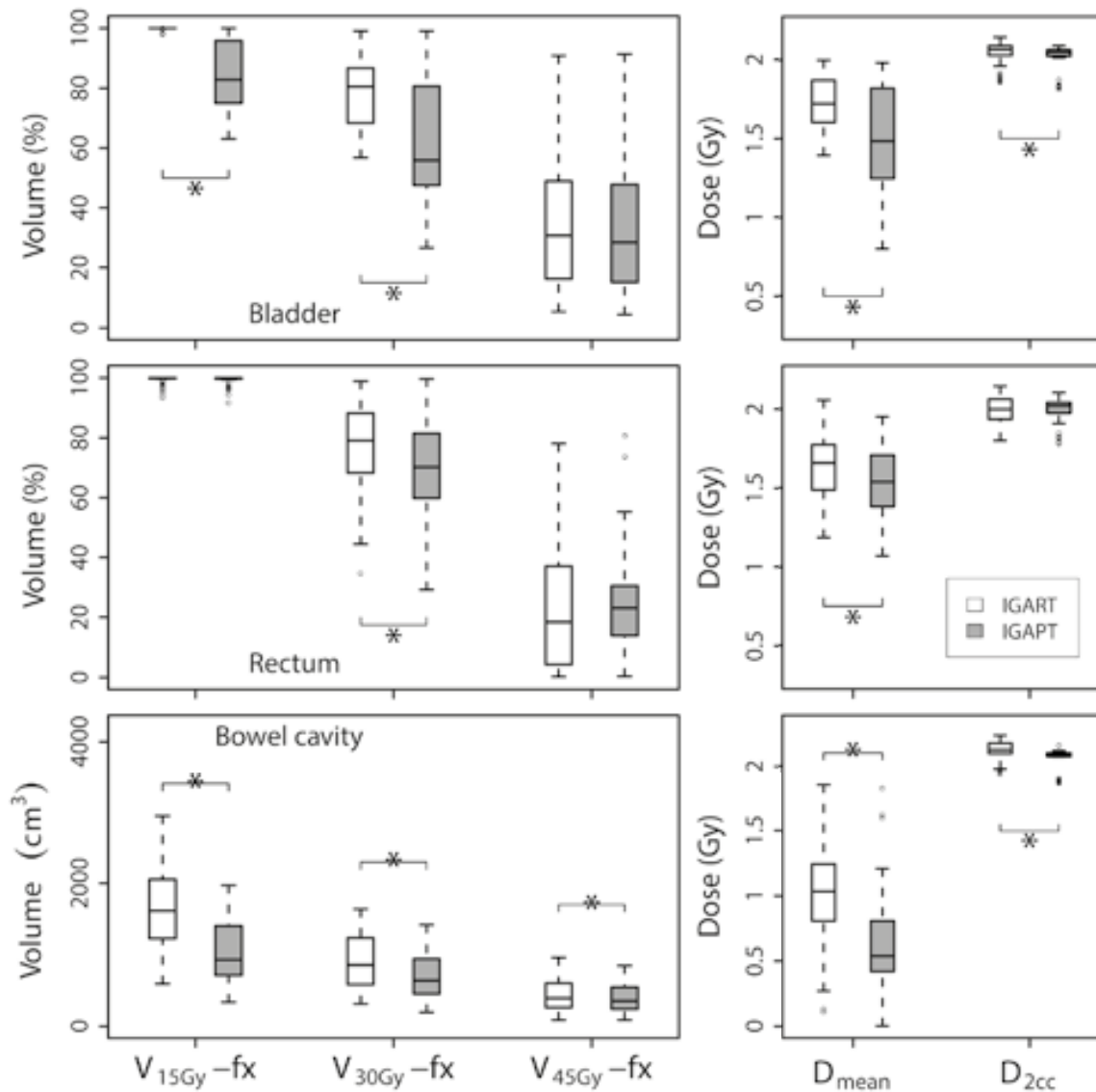


Figure 5.5 | For bladder (upper), rectum (middle) and bowel cavity (lower), boxplots of fraction DVH parameters over all analyzed fractions of all patients are shown. Boxes represent upper and lower quartiles (IQR), the band inside the box the median value and the whiskers the highest (lowest) value within 1.5 IQR of the upper (lower) quartile. Horizontal lines including an asterisk indicate statistical significant difference ( $p < 0.01$ ) based on a paired non-parametric statistical test.

**Table 5.3** | Comparison of the mean dosimetric parameters for the recalculated fractions of all patients.

	IGART	IGAPT	Absolute difference (IGART – IGAPT)	Relative difference (%)	<i>p</i> -Value
<b>Bladder</b>					
$V_{15\text{Gy}}\text{-fx}$ (%)	99.9	84	15.8	15.9	<.001
$V_{30\text{Gy}}\text{-fx}$ (%)	78.2	62.9	15.4	21.1	<.001
$V_{45\text{Gy}}\text{-fx}$ (%)	36.3	34.7	1.7	3.3	0.08
$D_{\text{mean}}$ (Gy)	1.7	1.5	0.2	13	<.001
$D_{2\text{cc}}$ (Gy)	2.0	2.0	0.0	1.4	<.001
<b>Rectum</b>					
$V_{15\text{Gy}}\text{-fx}$ (%)	99.3	99.2	0.1	0.1	0.3
$V_{30\text{Gy}}\text{-fx}$ (%)	77.6	70.3	7.3	10.0	<.001
$V_{45\text{Gy}}\text{-fx}$ (%)	23.6	24.5	-0.9	-12.7	0.46
$D_{\text{mean}}$ (Gy)	1.6	1.5	0.1	5.3	<.001
$D_{2\text{cc}}$ (Gy)	2.0	2.0	0.0	0.0	0.91
<b>Bowel cavity</b>					
$V_{15\text{Gy}}\text{-fx}$ (cm <sup>3</sup> )	1673.1	1012.8	660.3	37.8	<.001
$V_{30\text{Gy}}\text{-fx}$ (cm <sup>3</sup> )	887.2	693.8	193.5	22.4	<.001
$V_{45\text{Gy}}\text{-fx}$ (cm <sup>3</sup> )	428.0	387.0	41.1	7.8	<.001
$D_{\text{mean}}$ (Gy)	1.0	0.6	0.4	45.0	<.001
$D_{2\text{cc}}$ (Gy)	2.1	2.1	0.1	3.0	<.001

*Abbreviations:* IGART = image-guided adaptive radiation therapy; IGAPT = image-guided adaptive proton therapy; fx = fractionated substitute.

## 5.4 | Discussion

In this study, we investigated the feasibility and potential dosimetric advantages of adaptive proton therapy compared to adaptive photon therapy in cervical cancer. Using a plan-library based plan-of-the-day image-guided adaptive strategy to compensate for anatomical interfraction changes, IGART and IGAPT treatments were simulated using weekly CTs and compared for target coverage and OAR dose. Our study is the first to demonstrate the potential benefit of image-guided adaptive proton therapy in cervical cancer including a dosimetric analysis based on weekly CTs. Compared to photon-based IGART, IGAPT maintains adequate target coverage while significant dose reductions can be achieved for bladder, bowel cavity and rectum, which results in decreased toxicity.

Unlike previously reported studies on proton therapy in cervical cancer [69-71,123], our analysis included treatment simulations by recalculating dose distributions using additional imaging obtained during treatment. To anticipate on anatomical changes during the treatment

course and prevent incorrect dose delivery, we combined proton therapy with a state-of-the-art adaptive strategy. Consequently, our recalculated dose distributions are more representative in terms of target coverage and OAR sparing compared to the use of only planned proton dose distributions.

Besides the recalculation of dose distributions, the highly recommended robust optimization for proton therapy planning was applied using reported uncertainty values instead of using the photon-based PTV concept based on population-based margins [24,138]. However, uncertainty values reflecting the optimal trade-off between target coverage robustness and OAR sparing need to be derived. To compare IGART and IGAPT fairly, also VMAT plans were robustly optimized using reported uncertainty values thereby eliminating the influence of different optimization techniques. Consequently, IGART results derived in this study do not directly represent results of our clinically applied PTV-based IGART treatments. To complete the comparison between IGART and IGAPT, additional research is needed to investigate the dosimetric advantage of IGAPT compared to our clinical IGART results.

Except for the robust optimization, the applied adaptive strategy in this study is similar to our clinically implemented adaptive strategy for cervical cancer RT. Prior to treatment, the full-range pITV was derived based on two planning CTs with extreme bladder volumes and interpolated to obtain pITV subranges. The number of pITVs generated is based on our clinical experience and the pre-treatment predicted full-range pITV was sufficient for almost all included patients. However, 10.7% of all fractions showed substantial deviation from the pre-treatment derived full-range pITV which resulted in inappropriate library plans. Since additional shifts after bony registration are not permitted to ensure lymph node coverage, treatment fractions will be postponed in clinical practice and justified the exclusion of this limited amount of fractions from our analysis. Even when this percentage increases, the use of a motion-robust backup plan (i.e. single field uniform dose plan to the full-range ITV, including robust optimization using larger uncertainty values) can be considered.

Next to interfraction motion, intrafraction organ motion during cervical cancer radiation therapy can be considerable and might affect dose delivery [74]. Besides potentially prolonged delivery times, IGAPT is more sensitive to uncertainties compared to IGART and intrafraction motion should be taken into account. In this study, we anticipated on possible intrafraction motion by robust optimization using appropriate uncertainty values. Moreover, the use of ITVs in our proposed adaptive strategy already compensated for possible intrafraction target motion induced by intrafraction bladder filling. Hence, the combination of ITVs with robust optimization is assumed to limit dosimetric consequences of intrafraction motion.

Similar to our current clinical workflow, all library plans were optimized using the full bladder planning CT. Preferably, plan optimization would be performed using the CT representing the corresponding anatomy. However, since multiple library plans were created corresponding to targets obtained by interpolation, available planning CTs do not necessarily represent associated anatomy for all target volumes.

Similar to the plan selection procedure applied clinically, the library plan best fitting the target shape and position as seen on CT was selected visually after bony registration. In our study, plan selection was relatively easy since only CTs were used. CBCT-based plan selection is more challenging due to limited soft-tissue contrast, resulting in an additional observer variation. To minimize the effect of this variation, plan selection based on automatic organ segmentation could be applied [75]. However, disturbed CBCT quality could hinder automatic organ segmentation and still require manual selection. Alternatively, dose-guided plan selection could be beneficial and can be applied when online recalculation of library plans based on pre-fraction imaging will become available [143].

Although cervical cancer irradiation is generally delivered in 23 or 28 fractions, we only used a limited number of weekly CTs per patient to simulate adaptive treatments. Consequently, the complete range of anatomical deformations occurring during the course of treatment are not necessarily included. Even though the included anatomical changes can influence observed dose differences due to their weighted contribution, this influence is assumed to be limited due to the substantial number of included patients. To completely eliminate these possible overestimations or underestimations of dosimetric differences, daily anatomical variations preferably based on an increased number of patients need to be included. However, daily CBCT images are not directly suitable for dose calculations.

Our dosimetric analysis is mainly based on DVHs of recalculated fraction dose distributions, from which parameter values were extracted. DVH parameter differences between recalculated IGART and IGAPT fractions were analyzed and statistical tests were applied pairwise to allow different fractionation schemes. In addition to the analysis based on fraction DVH parameters, reductions in toxicity probabilities for rectum and bowel were estimated based on DVH parameters representing the complete treatment course. Because no spatial information is present in fraction DVHs, the scaled average fraction DVH parameter approximation not necessarily represents reliably accumulated OAR parameter values. Therefore, DVH parameters were also derived based on dose accumulation after deformable image registration. For rectum  $V_{30Gy}$ , both methods resulted in similar parameter values while an improvement for bowel  $V_{45Gy}$  was observed when using the dose accumulation method.

Although the deformable registration algorithm was validated previously for pelvic registrations [142], we validated our registrations by visual inspection and OAR similarity quantification to ensure plausible dose warping. However, an extensive validation of the complete anatomical correctness and the influence of possible incorrectness on dose accumulation is still an important challenge in RT [144] and beyond the scope of this study.

According to QUANTEC recommendations, differences in NTCP for grade 2 acute gastrointestinal toxicity were quantified using the associated DVH parameter (bowel  $V_{45Gy}$ ) [141]. However, the recommended lowest toxicity thresholds for rectum ( $V_{50Gy} < 50\%$ ) and bladder ( $V_{65Gy} < 50\%$ ) were in our study never reached. To differentiate between IGAPT and IGART, the reported DVH parameter associated with overall rectum toxicity ( $V_{30Gy}$ ) was used [140].

Even though the application of IGAPT in cervical cancer has been demonstrated, additional steps will have to be taken before implementing this technique clinically. Daily pre-fraction imaging, preferably using MRI or CT, will be required for plan selection. In addition, appropriate clinical protocols regarding plan selection need to be developed.

## 5.5 | Conclusion

Our study demonstrates the feasibility of adaptive proton therapy in cervical cancer. Compared to photon-based IGART, simulated IGAPT treatments result in adequate target coverage while the OAR dose decreases significantly. In addition, our results indicate toxicity probability reductions, but further analysis is needed to determine clinical outcome in terms of toxicity.

## Appendix 5.A

In this study, weekly acquired repeat CTs were deformable registered to the full bladder planning CT using the hybrid deformable registration algorithm implemented in RayStation (version 4.4, RaySearch Laboratories AB, Stockholm, Sweden). This algorithm combines image information (i.e. image intensities) with anatomical information as provided by delineated structures [142]. The objective function is a linear combination of four nonlinear terms: 1) image similarity term (to maintain image similarity), 2) grid regularization term (to keep the image grid smooth and invertible), 3) a shape based regularization term (to keep the deformation anatomically reasonable when regions of interest are present) and 4) a penalty term when controlling structures are used (to deform the selected structure in the reference image to the corresponding structure in the target image).

The deformable registrations performed between the repeat CTs and the full bladder planning CT were guided by contoured structures present in both image sets. By providing all anatomical information available in term of contoured structures, the optimization function is steered towards anatomical plausible registrations. For our analysis, the delineated bladder, rectum, pCTV, bowel cavity, left hip and right hip structures were included. Registration results were first visually verified by overlying the registered image sets. Due to the absence of a set of unique corresponding landmark for both image sets to validate deformable registrations, two commonly used similarity measures were used for validation [75,84,144]. First, the similarity of registered structures was quantified using the Dice similarity coefficient (DSC) for the structures of interest. Additionally, the surface distance error (SDE), i.e. the mean of distances between registered corresponding structures, was calculated to confirm structure similarity.

For all patients, the obtained deformable registrations between the full bladder planning CT and repeat CTs were considered accurate after visual inspection. Also, similarity between inspected structures after deformable registration was sufficient in terms of DSC and SDE. Table 5.A.1 represents average results of applied deformable registrations per patient for DSC as well as SDE.

**Table 5.A.1** | Results of deformable image registration per patient, represented by the mean DSC and SDE for contoured structures.

Patient	DSC (-)						SDE (cm)					
	bladder	rectum	bowel cavity	pCTV	left hip	right hip	bladder	rectum	bowel cavity	pCTV	left hip	right hip
1	0.96	0.93	0.94	0.92	0.98	0.98	0.05	0.10	0.15	0.17	0.01	0.01
2	0.88	0.91	0.88	0.84	0.98	0.98	0.15	0.17	0.27	0.19	0.02	0.02
3	0.91	0.94	0.90	0.91	0.98	0.98	0.11	0.08	0.24	0.16	0.02	0.02
4	0.91	0.92	0.89	0.89	0.95	0.96	0.14	0.12	0.46	0.19	0.05	0.04
5	0.87	0.91	0.93	0.87	0.98	0.98	0.18	0.08	0.26	0.13	0.02	0.02
6	0.82	0.90	0.89	0.91	0.97	0.97	0.22	0.16	0.30	0.23	0.03	0.03
7	0.97	0.93	0.93	0.94	0.98	0.98	0.03	0.14	0.23	0.06	0.02	0.02
8	0.96	0.89	0.97	0.97	0.98	0.98	0.04	0.34	0.12	0.05	0.01	0.02
9	0.69	0.73	0.83	0.81	0.95	0.96	0.23	0.30	0.58	0.37	0.06	0.05
10	0.98	0.92	0.96	0.91	0.98	0.98	0.03	0.12	0.20	0.13	0.02	0.02
11	0.96	0.93	0.88	0.93	0.98	0.98	0.04	0.12	0.67	0.13	0.02	0.02
12	0.92	0.93	0.89	0.90	0.97	0.98	0.10	0.09	0.28	0.14	0.03	0.03

*Abbreviations:* DSC = Dice similarity coefficient; SDE = surface distance error; pCTV = primary clinical target volume.



# Chapter 6

Quantification of delineation errors of the gross tumor volume on magnetic resonance imaging in uterine cervical cancer using pathology data and deformation correction

A version of this chapter has been published as:

*Quantification of delineation errors of the gross tumor volume on magnetic resonance imaging in uterine cervical cancer using pathology data and deformation correction*

A.J.A.J. van de Schoot, P. de Boer, M.R. Buist, J. Stoker, M.C.G. Bleeker, L.J.A. Stalpers, C.R.N. Rasch and A. Bel

*Acta Oncologica* 2015; 54(2): 224–231.

<http://dx.doi.org/10.3109/0284186X.2014.983655>

## **Abstract**

### **Purpose**

To safely optimize target volumes using magnetic resonance imaging (MRI) for uterine cervical cancer radiation therapy, MRI findings need to be validated. The aim of this study was to correlate pre-operatively acquired MRI and surgical specimen imaging for uterine cervical cancer patients using deformable image registration and quantify gross tumor volume (GTV) delineation discrepancies.

### **Material & Methods**

For sixteen retrospectively selected early-stage uterine cervical cancer patients, the cervix-uterus structure, uterine cavity and the GTV were delineated on 2D pathology photos after macroscopic intersection and corresponding pre-operatively acquired T2-weighted 2D sagittal MR images. Segmentations of pathology photos and MR images were simultaneously registered using a three-step multi-image registration strategy. The registration outcome was evaluated by the Dice similarity coefficient (DSC) and the surface distance error (SDE). In addition, GTV expansions within the cervix-uterus structure needed to obtain 95% GTV coverage were determined.

### **Results**

After three-step multi-image registration, the median DSC and median SDE were 0.98 and 0.4 mm (cervix-uterus) and 0.90 and 0.4 mm (uterine cavity), respectively. The average SDE around the GTV was 0.7 mm (range, 0.1 mm – 2.6 mm). An underestimation of MRI-based GTV delineations was found when no margin was applied, indicated by a mean GTV coverage of 61%. To obtain 95% GTV coverage for 90% of the patients, a minimum 12.0 mm margin around MRI-based GTVs was needed.

### **Conclusion**

The presented three-step multi-image registration strategy was suitable and accurate to correlate MRI and pathology data for uterine cervical cancer patients. To cover the pathology-based GTV, a margin of at least 12.0 mm around GTV delineations on T2-weighted MRI is needed.

## 6.1 | Introduction

The treatment policy in patients with uterine cervical cancer is mainly based on the stage of the tumor, indicated by the International Federation of Gynecology and Obstetrics (FIGO) staging system. Surgery is usually recommended for patients with early-stage uterine cervical cancer (FIGO stage IB–IIA). Radiation therapy (RT) with concurrent chemotherapy is the cornerstone of treatment for patients with locally advanced uterine cervical cancer (FIGO stage IIB–IVA) [72,121].

According to clinical guidelines for RT treatment of uterine cervical cancer, the clinical target volume (CTV) is defined as the gross tumor volume (GTV) together with the entire uterine cervix and body [145,146]. The planning target volume (PTV) is obtained by adding an additional margin around the CTV to account for uncertainties, such as uncertainties in daily set-up, delineation and organ motion [45,83,89,147]. Despite the limited local recurrence rate after RT, large treatment volumes cause serious late vaginal, bowel and bladder toxicity, which significantly reduces quality of life [121].

To substantially decrease the target volume and spare healthy tissue during uterine cervical cancer RT, it has been suggested to only include the invaded part of the uterine body in the CTV [6,29]. However, information of the exact tumor extent is necessary in order to optimize RT treatment volumes in uterine cervical cancer RT. Since the GTV is poorly visible on computed tomography (CT) images acquired for RT treatment planning [8,148,149], distinction between tumor and healthy tissue on CT is not reliable. Therefore, magnetic resonance imaging (MRI) is considered as an additional imaging modality for RT treatment planning to assess the exact tumor extent [150]. However, the accuracy of tumor delineation on MRI needs to be validated by comparing tumor extent visible on MRI with the corresponding pathology-proven tumor extension [6].

Previously, several studies have been performed to correlate MRI and pathology data in order to validate MRI findings. The majority of those reported studies were performed on the prostate gland, e.g. [151,152], but also a few studies on other organs were reported, e.g. [153]. For uterine cervical cancer imaging data, only a limited number of studies addressed the validation of MRI findings [154,155]. However, in none of these studies the potentially large deformation between the in-vivo structure on MRI and pathology specimen after surgical removal was corrected. In this study, pathology imaging will be used to validate GTV delineations on MRI using deformable image registration in uterine cervical cancer patients.

The aim of this study was to develop a method to correlate pre-operatively acquired MRI and surgical specimen imaging for early-stage uterine cervical cancer patients, including corrections for potential large shape deformations. In addition, the discrepancy between MRI-based and pathology-based GTV delineations after deformable image registration was quantified.

## 6.2 | Material & Methods

### Patient data

According to clinical guidelines, uterine cervical cancer patients who received a radical hysterectomy with pelvic lymphadenectomy underwent anatomical MRI prior to surgery. The standard MRI protocol consisted of sagittal, axial oblique and coronal oblique T2-weighted turbo spin-echo sequences (repetition time/echo time=2500/70 ms, field of view 300 x 300 mm<sup>2</sup>, acquisition matrix 512 x 384, slice thickness 4.0 mm and turbo factor 11) in supine position on a 1.5 Tesla whole-body MRI system (Siemens Avanto, Erlangen, Germany). After surgery, the pathologist routinely analyzed the fresh surgical specimen by making an anterior median incision to expose the internal os of the uterus. A digital photo of this macroscopic intersection was only made if the remaining tumor was still visible macroscopically after pre-operatively performed biopsies.

Patients who received a radical hysterectomy for cervical carcinoma between January 2012 and December 2013 were selected retrospectively based on the availability of pre-operative MRI data and a digital photo of the surgical specimen obtained during pathology analysis. After exclusion of three patients (GTV invisibility on either MRI or digital photo (n=2), presence of a large uterine fibroid (n=1)), sixteen uterine cervical cancer patients with FIGO stages IB1 (n=10), IB2 (n=5) and IIA1 (n=1) were included with MRI acquired on average 24 days (range, 14–48 days) prior to surgery. The pathology photos and the sagittal T2-weighted MRI data corresponding to the plane of the anterior median incision were used to correlate pathology findings with pre-operatively acquired MRI data.

### Delineation and segmentation

For each patient, two radiation oncologists independently delineated the cervix-uterus structure, i.e. uterus including the uterine cervix, the uterine cavity and the GTV, i.e. the macroscopically visible tumor extension, on the sagittal T2-weighted MRI (Figure 6.1b) according to clinical guidelines [145,146]. Also, for GTV delineation on MRI, access to the radiology report was available. With at least one week in between, one of these two radiation oncologists also delineated corresponding structures (cervix-uterus, uterine cavity and GTV) on all anonymized pathology photos. To obtain reliable and accurate pathology-based delineations and avoid bias, delineations on pathology photos were created independently without information of previously performed delineations and subsequently revised by an experienced pathologist (Figure 6.1a).

The mid-sagittal 2D MR image, representing the central part of the uterine body and corresponding to the plane of macroscopic intersection, was selected based on uterine cavity visibility. Since the uterine cavity is located in the central part of the uterine body, it was only visible in a limited number of sagittal 2D MR images; therefore, the uterine cavity was considered a reliable landmark for corresponding image selection. After selection, the delineated structures

were segmented from the background on pathology photos and from surrounding tissue on corresponding MR images (Figure 6.1c–6.1d). Also, all segmented grayscale images were transformed to binary images with pixel values inside the structures set to true and those outside the structures set to false. An examples is presented in the supplementary data available online<sup>3</sup>.

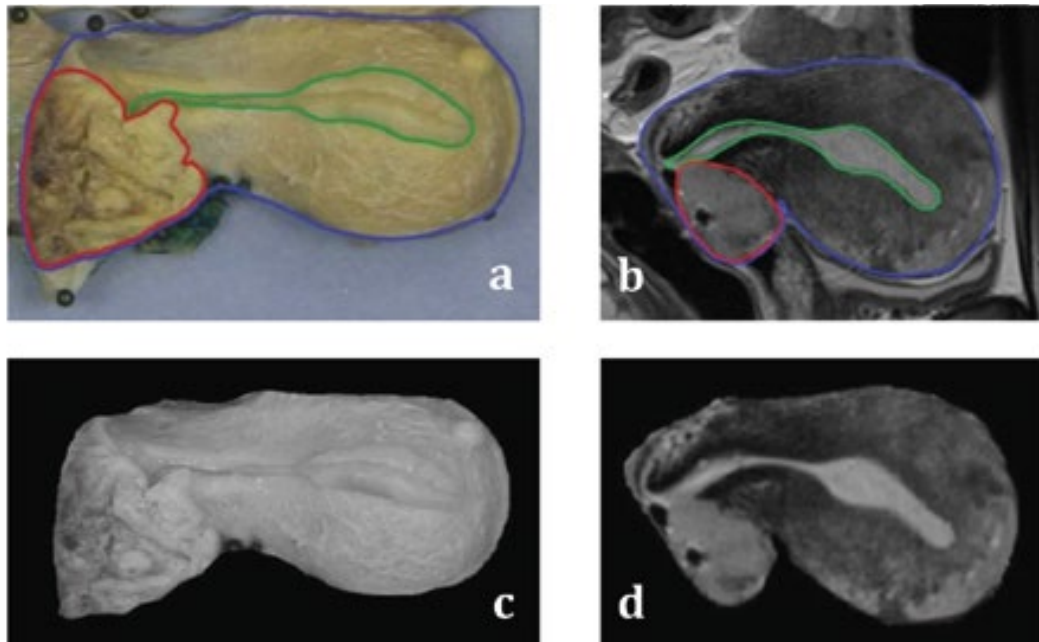


**Figure 6.1** | An example of a 2D digital photo of the macroscopic intersection (a) and the corresponding 2D sagittal MR image (b) with delineated structures (cervix-uterus (blue), uterine cavity (green), GTV (red)). The cervix-uterus structures were segmented from the background on the photo (c) and from surrounding tissue on MRI (d).

## MRI-pathology registration

Pathology data were registered to MRI data based on a three-step multi-image registration strategy using Elastix, a freely available image registration software package [156]. First, a rigid registration was performed between binary image pairs of the cervix-uterus based on translations and rotations. Next, affine multi-image registration was achieved using a weighted contribution of binary image pairs of the cervix-uterus and the uterine cavity based on translation, rotation, scaling and shearing. To finalize the three-step registration strategy and correct for deformations, a B-splines based deformable multi-image registration step was performed using a weighted contribution of segmented grayscale image pairs of the cervix-uterus and the uterine cavity<sup>3</sup>. The transformation ( $T$ ) between the pathology photo ( $I_{PAT}$ ) and its corresponding MR image ( $I_{MRI}$ ) using a multi-image registration process with a weighted contribution was determined by optimizing the registration cost function ( $C$ ) of multiple image pairs with its associated weight factor ( $\omega_i$ ) (Equation 6.1).

<sup>3</sup> <http://www.tandfonline.com/doi/suppl/10.3109/0284186X.2014.983655>

$$C(\mathbf{T}; I_{MRI}, I_{PAT}) = \frac{1}{\sum_{i=1}^N \omega_i} \sum_{i=1}^N \omega_i C(\mathbf{T}; I_{MRI}^i, I_{PAT}^i) \quad (6.1)$$

Optimal contributions of the cervix-uterus pair ( $\omega_{CU}$ ) and the uterine cavity image pair ( $\omega_{UCa}$ ) to the final registration result were determined for each patient and the results are presented in the supplementary data available online<sup>3</sup>. An equal contribution of both image pairs ( $\omega_{CU}=0.5$ ;  $\omega_{UCa}=0.5$ ) was used in nine patients and a larger (smaller) contribution of the cervix-uterus image pair compared to the uterine cavity image pair was used in three (four) patients. For each registration step, image registration was performed using B-spline interpolation, multi-resolution registration, normalized mutual information similarity measure and gradient descent optimization. The three-step multi-image registration process was performed twice with segmented MR images based on delineations of each radiation oncologist ( $REG_1$  and  $REG_2$ ).

## Registration evaluation

Given the delineations of both radiation oncologists on MRI, the inter-observer delineation variation was quantified by calculating the conformity index (CI). The CI was defined as the ratio of the overlapping and the encompassing delineated volumes and chosen as conformity metric to enable a comparison with published data [157]. After three-step multi-image registration, the registration result was first inspected visually by displaying the MR image together with the deformed pathology photo. Next, the outcome of image registration was evaluated by determination of the surface distance error (SDE) and the Dice similarity coefficient (DSC) for both the cervix-uterus and the uterine cavity structure [158]. Also, the SDE of the boundary points from the cervix-uterus structure around the GTV, the GTV-S, was calculated.

The SDE described the registration error and was defined as the mean of all minimum distances between boundary points of the reference structure and the corresponding deformed structure. The DSC is frequently used to describe the overlap between corresponding structures [156,158] and was defined as the number of pixels shared by the structure on MRI ( $PIX_{MRI}$ ) and the structure on the pathology photo ( $PIX_{PATH}$ ) divided by the average amount of pixels in both structures (Equation 6.2).

$$DSC = 2 \frac{(PIX_{MRI} \cap PIX_{PATH})}{(PIX_{MRI} + PIX_{PATH})} \quad (6.2)$$

Absolute pixel displacements, differences between pixel displacement vectors after the second and third registration step, were evaluated in order to indicate possible unrealistic displacements within the different structures. The improvement of registration accuracy was studied by testing (Wilcoxon signed-rank test) the difference in registration accuracy (DSC, SDE) obtained after each registration step for both the cervix-uterus and the uterine cavity. Moreover, the robustness of our proposed registration strategy was determined by calculating the registration accuracy for both

the cervix-uterus and the uterine cavity using the sagittal T2-weighted MR images adjacent to the corresponding MR image during three-step multi-image registration for REG<sub>1</sub>.

### GTV validation

Pathology-based GTV delineations, denoted as the reference GTV (GTV<sub>REF</sub>), were used to validate T2-weighted MRI-based GTV delineations (GTV<sub>MRI</sub>). The GTV<sub>REF</sub> was deformed according to the obtained transformation after three-step multi-image registration and the coverage of the deformed GTV<sub>REF</sub> with the GTV<sub>MRI</sub> was calculated (Equation 6.3).

$$GTV_{coverage} = \frac{GTV_{MRI} \cap GTV_{REF}}{GTV_{REF}} \times 100\% \quad (6.3)$$

Margins needed around MRI-based GTV delineations to obtain 95% GTV coverage for at least 90% of the patients were determined by uniformly expanding the GTV<sub>MRI</sub> using a 2.0 mm step size. The expansions were performed only within the cervix-uterus structure to mainly represent the GTV discrepancy along the axis of the uterine body<sup>3</sup>. For each applied margin, the coverage of the GTV<sub>REF</sub> with the expanded GTV<sub>MRI</sub> was calculated. To investigate the effect of inter-observer variation on obtained margins, coverage based on the GTV<sub>MRI</sub> from the first and the second radiation oncologist (GTV<sub>MRI-1</sub> and GTV<sub>MRI-2</sub>, respectively) was determined.

After margin determination needed to obtain 95% GTV coverage, correlations with the observed time interval between MRI and surgery and with the GTV<sub>MRI</sub> were tested (Pearson correlation coefficient (R)). To investigate the influence of deformable image registration in terms of GTV coverage, we also determined GTV coverage based on image registration results after only rigid registration.

## 6.3 | Results

A limited inter-observer delineation variation on MRI was observed, indicated by a median CI of 0.88, 0.63 and 0.80 for the cervix-uterus, uterine cavity and GTV, respectively. Box-and-whisker plots present the registration accuracy after REG<sub>1</sub>. The multi-image deformable registration step improved the correlation between the cervix-uterus as well as the uterine cavity significantly ( $p < 0.01$ ), indicated by the increased median DSC and decreased median SDE (Figure 6.2a–6.2b). Similar registration accuracy was obtained after REG<sub>2</sub><sup>3</sup>. Also, the small inter-observer delineation variation led to similar mean GTV-S registration errors of 0.7 mm (range, 0.2 mm – 2.6 mm) and 0.6 mm (range, 0.1 mm – 2.0 mm) after REG<sub>1</sub> and REG<sub>2</sub>, respectively. A typical example of segmented grayscale images after three-step multi-image registration can be found in the supplementary data available online<sup>3</sup>.

Overall pixel displacements caused by multi-image deformable registration inside the GTV (4.8 mm, 6.0 mm) were similar to displacements inside the cervix-uterus (5.5 mm, 7.0 mm) and the uterine cavity (4.7 mm, 6.3 mm) for  $REG_1$  and  $REG_2$ , respectively. Also, similar displacements inside defined structures after  $REG_1$  and  $REG_2$  were found without unrealistic pixel displacements<sup>3</sup>. Robustness evaluation showed similar cervix-uterus registration accuracy using adjacent MR images instead of corresponding MR images (Figure 6.2c–6.2d). However, larger registration errors for internal structures were obtained when using adjacent MR images.

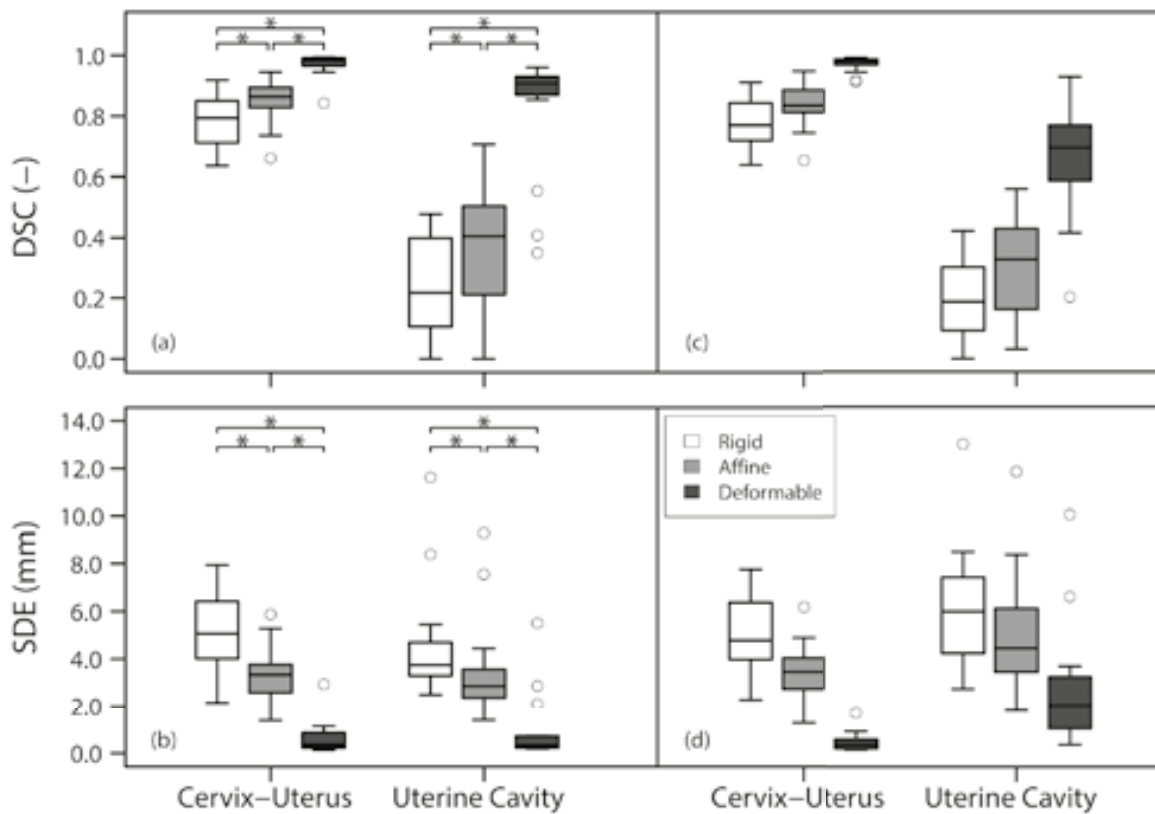


**Figure 6.2** | Box-and-whisker plots of the DSC and the SDE between the MR image and the pathology photo (a, b) and between adjacent MR images and the pathology photo (c, d) after each step in the three-step multi-image registration strategy (rigid registration, affine registration and deformable registration) for the cervix-uterus and the uterine cavity structure. The box represents the upper and lower quartiles (IQR) and the band inside the box the median value. The whisker represents the highest (lowest) value within 1.5 IQR of the upper (lower) quartile. Dots above or below the whiskers are considered outliers. Horizontal lines including asterisks indicate statistical significant difference ( $p < 0.01$ ).

After three-step multi-image registrations, an underestimation of  $GTV_{MRI}$  compared to the  $GTV_{REF}$  was determined when no margin was applied, indicated by a median  $GTV$  coverage of 59% (range, 43%–95%) for  $GTV_{MRI-1}$  after  $REG_1$  and 57% (range, 11%–98%) for  $GTV_{MRI-2}$  after  $REG_2$  (Figure 6.3). To acquire a median  $GTV$  coverage of 95%, expansions of the  $GTV_{MRI}$  within the cervix-

uterus structure of 6.0 mm and 8.0 mm were needed for  $GTV_{MRI-1}$  and  $GTV_{MRI-2}$ , respectively. Furthermore, 95% GTV coverage for 90% of the patients was obtained using margins around the  $GTV_{MRI}$  of 12.0 mm ( $REG_1$ ,  $GTV_{MRI-1}$ ) and 18.0 mm ( $REG_2$ ,  $GTV_{MRI-2}$ ) and 100% GTV coverage for all patients was acquired using a 22.0 mm margin around the  $GTV_{MRI}$  in both cases. Determination of GTV coverage using  $GTV_{MRI-1}$  ( $GTV_{MRI-2}$ ) after  $REG_2$  ( $REG_1$ ) provided similar results<sup>3</sup>. However, neither of all expansions included a margin uncertainty induced by the registration error of 1.0 mm. For the margins needed to obtain 95% GTV coverage, no significant correlation were found with time interval between MRI and surgery ( $R=0.21$ ,  $p=0.24$ ) and with GTV size ( $R=0.15$ ,  $p=0.40$ ).

Without deformation correction, i.e. after rigid registration for  $REG_1$  and  $REG_2$ , an average median GTV coverage of 54% was found when no margin was applied. Compared to the results after deformation correction, a larger margin (12.0 mm) was needed to obtain a median GTV coverage of 95% (Figure 6.3). Moreover, image alignment based on only translations and rotations led to a larger registration error (about 4.0 mm) which induced an additional uncertainty on top of the determined margin to obtain GTV coverage.

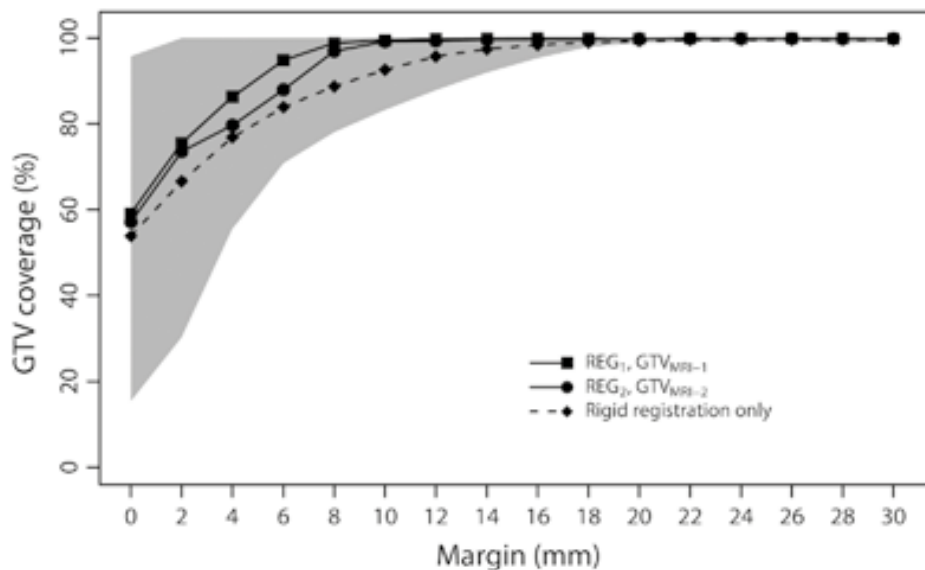


**Figure 6.3** | Median GTV coverage after three-step multi-image registration based on  $GTV_{MRI-1}$  after  $REG_1$  (squares) and based on  $GTV_{MRI-2}$  after  $REG_2$  (dots) as a function of applied margin to the  $GTV_{MRI}$  within the cervix-uterus structure. The dashed line shows the average median GTV coverage of both observations after only rigid registration and the gray region indicates the 95% confidence interval of both observations after three-step multi-image registration.

## 6.4 | Discussion

This study described a novel method to correlate pre-operatively acquired MRI and surgical specimen imaging for uterine cervical cancer patients, including large deformation corrections. Our proposed three-step multi-image registration strategy is based on boundary and internal structures and accurate correlations between MRI and pathology photos were obtained. Moreover, we corrected for possible large deformations between in-vivo and ex-vivo organ shapes by using deformable multi-image registration. In addition, the discrepancy between GTV delineations on T2-weighted MRI and pathology imaging after deformable registration was quantified by the coverage of  $GTV_{REF}$  with  $GTV_{MRI}$ . To obtain 95% GTV coverage for at least 90% of the patients, a margin of at least 12.0 mm around the  $GTV_{MRI}$  was needed. We have shown that correlations between MRI and pathology data could be obtained by deformable image registration and used for GTV validation.

Unlike methods in previously reported studies on MRI and pathology correlation for uterine cervical cancer patients [148,154], our correlation method corrected for shape deformations between both imaging data sets and therefore made the validation of GTV delineations more reliable. Without deformation corrections, less accurate correlations between MRI and pathology data were obtained and a larger margin around GTV delineations on MRI would be needed to safely cover the pathology-based GTV. Consequently, our three-step multi-image registration led to a more accurate validation of MRI-based GTV delineations compared to only rigid alignment. Moreover, the  $GTV_{MRI}$  including the margin to correct for pathology-proven macroscopic tumor extensions can be used to better define RT volumes when only the invaded part of the uterine body will be included.

Besides the boundary contour, the only corresponding landmark that could be clearly distinguished on both imaging data sets was the uterine cavity structure. To avoid registration outcome largely driven by the segmented boundary contour, a multi-image registration strategy was defined using grayscale images to also align internal structures. Using only segmented images based on boundary contours or internal structures for image registration led to a worse registration outcome compared to our method<sup>3</sup>. As a consequence, registration evaluation based on structures that were not used to optimize the registration could not be performed and registration-independent corresponding landmarks were unavailable. Therefore, registration evaluation was performed based on the cervix-uterus and the uterine cavity structures, assuming these structures represented the correlation of the entire specimen. Additionally, the GTV-S structure was defined to analyze the registration error around the GTV.

The advantage of our registration method is the use of multiple imaging pairs to optimize the final transformation using both boundary and internal structure information. Since no previous studies reported on optimized image contributions during multi-image registration, a patient-specific image pair contribution was used. Based on all patient-specific contributions, we also determined a population-based image pair contribution which can be used for ensuing patients.

This study has some limitations, mainly due to the retrospective character of this study. Only one 2D digital photo of the macroscopic intersection obtained during pathology analysis of the surgical specimen was available and we used this photo to correlate MRI and pathology data. Although 3D MRI data was available, 2D-3D image registration could not be performed reliably due to the absence of corresponding landmarks for guidance of the registration algorithm. Therefore corresponding 2D MR images were manually selected based on information of intersection directions during pathology analysis and uterine cavity visibility. Even though both images were assumed to be in the same plane, the exact direction of intersection during pathology analysis was unknown and possible rotations could have influenced the registration accuracy. Since a relatively small difference in the registration result was found due to corresponding image selection uncertainty, the impact on the determined margin was estimated to be limited and in the same order of magnitude as the difference in registration results.

Due to the absence of whole-mount sections, microscopic tumor spread could not be determined and the  $GTV_{MRI}$  was validated based on the macroscopically visible tumor on pathology photos. To safely optimize the CTV based on only the  $GTV_{MRI}$ , a future study using 3D data sets and whole-mount sections will be needed to decrease uncertainties and improve correlations in other directions (i.e. transverse, coronal). Nevertheless, the tumor extension along the axis of the uterine body is of most interest and quantification of this extension might enable a safe exclusion of the healthy part of the uterine body from RT treatment volumes. Since  $GTV_{MRI}$  expansions were performed uniformly but only within the cervix-uterus structure, the obtained margins represented discrepancies between MRI-based GTV delineations and pathology-proven GTV coverage along the axis of the uterine body.

Only anatomical T2-weighted MRI was available, because MRI was only intended to be used to determine the stage, size and location of the tumor prior to surgery. To better define the GTV and to optimize target volumes for RT purposes, quantitative MRI such as diffusion-weighted imaging or dynamic contrast-enhanced MRI can offer additional valuable information [159]. These techniques can improve tumor detection, contribute to tumor differentiating or may predict treatment response.

Since this study was performed from a RT perspective, all structures on MRI were delineated by radiation oncologists as being common practice in clinical RT. The observed small inter-observer delineation variation on MRI was in agreement with previously reported results [157]. This small variation resulted in limited impact on MRI-pathology correlation and  $GTV_{MRI}$  validation and indicated a negligible delineation bias. If appropriate tools become available, delineations on MRI can be performed automatically to eliminate the inter-observer variation. According to present RT margin concepts [147], the GTV is defined as the macroscopically visible tumor on a specific imaging modality and GTV uncertainty corrections are included in the CTV-to-PTV margin. In this study, the proposed  $GTV_{MRI}$  margin is defined to obtain GTVs that approximate macroscopically visible tumors on pathology photos. However, this margin is not directly covered by the present margin concepts. Since target volume optimization using the  $GTV_{MRI}$  margin already included

possible delineation uncertainties, a CTV-to-PTV margin without a component for delineation uncertainties is warranted.

All included patients had early-stage uterine cervical cancer (FIGO stage IB–IIA) and in general only patients with locally advanced uterine cervical cancer (FIGO stage IIB–IVA) will be treated with RT and concurrent chemotherapy. However, the validation of MRI findings using pathology data cannot be performed for patients with locally advanced tumors because these patients did not undergo surgery. Since digital photos of the median incision were only taken if the tumor was still visible macroscopically after the biopsies taken before surgery, early-stage uterine cervical cancer patients with relatively large tumors were included.

Despite the accurate observed correlations for the evaluated structures, discrepancies between  $GTV_{MRI}$  and  $GTV_{REF}$  were observed after three-step multi-image registrations. Although the exact reason for this discrepancy is unknown, it could be induced by a change in tumor size within the time between MRI acquisition and surgery due to practical workflow issues. However, the influence of this time interval on possible tumor growth is likely to be relatively small, as we found no significant correlation between observed time intervals and determined discrepancies. Furthermore, based on the observed time intervals and reported typical pre-treatment cervical tumor doubling times of 80–160 days [160] an average increase of 5% (range, 2%–10%) in the radius of tumor volumes could be expected. Given this very limited possible increase in tumor volumes within the time between MRI acquisition and surgery together with the weak correlation between observed time intervals and determined discrepancies, the influence of the time interval on obtained margins was assumed to be negligible. In addition, previous studies on MRI-pathology correlation reported similar time intervals between imaging and surgery [148,154]. Besides due to the time interval, the  $GTV_{MRI}$  could be underestimated due to the use of only one standard MRI sequence [157] or the  $GTV_{REF}$  could be overestimated due to the retrospective determination of the macroscopically visible tumor. A future prospective study using a dedicated pathology analysis and different MRI sequences will decrease these uncertainties.

## 6.5 | Conclusion

Three-step multi-image registration including deformation corrections provided accurate correlations between pre-operatively acquired MRI and surgical specimen imaging for uterine cervical cancer patients. In addition, a margin of at least 12.0 mm around MRI-based GTV delineations is needed to cover the macroscopically visible tumor extension on surgical specimen imaging. A prospective study on MRI and pathology correlation may further improve tumor definition in order to optimize RT treatment volumes and reduce radiation-induced toxicity for uterine cervical cancer patients.



# Chapter 7

Should excluding uninvaded uterine tissue  
be combined with proton therapy for  
cervical cancer?

A version of this chapter has been submitted to International  
Journal of Radiation Oncology, Biology, Physics as:

*Should excluding uninvaded uterine tissue be combined with proton therapy for  
cervical cancer?*

P. de Boer, A.J.A.J. van de Schoot, G.H. Westerveld, M. Smit, M.R. Buist, A. Bel,  
C.R.N. Rasch and L.J.A. Stalpers

## Abstract

### Purpose

In cervical cancer radiation therapy, including the entire uterus in the target volume results in large target volumes and consequently leads to high organ at risk (OAR) dose. Our aim is to quantify the dosimetric advantages of excluding the uninvaded uterine body from the target volume combined with either photon or proton therapy.

### Material & Methods

Eleven patients with locally advanced cervical cancer with a substantial (>4cm) tumor free part of the uterus towards the fundus on pre-treatment magnetic resonance imaging (MRI) were selected retrospectively. Conventional target volumes including the entire uterus and MRI-based target volumes including only the invaded part of the uterus were compared. Photon and proton plans were generated for both target volumes, resulting in four treatment plans per patient. Differences in  $V_{15Gy}$ ,  $V_{30Gy}$ ,  $V_{45Gy}$  and  $D_{mean}$  for bladder, sigmoid, rectum and small bowel were assessed. Additionally, differences in normal tissue complication probability (NTCP) were estimated for small bowel.

### Results

Compared to conventional volumes, MRI-based target volumes resulted in an average reduction of the primary internal target volume and planning target volume by 37% and by 8%, respectively. The use of MRI-based target volumes resulted in significant reductions in  $V_{15Gy}$ ,  $V_{30Gy}$ ,  $V_{45Gy}$  and  $D_{mean}$  for bladder and small bowel when applying photon therapy and were further reduced when applying proton therapy. MRI-based target volumes reduced the average NTCP for small bowel from 25% to 18% and the addition of proton therapy resulted in an average of 9%. Substantial NTCP differences (>10%) are expected in 4 patients (36%) using MRI-based target volumes and in 6 patients (55%) when adding proton therapy.

### Conclusion

MRI-based target volume definition in cervical cancer radiation therapy decreased OAR dose and acute small bowel toxicity probabilities. In the presence of smaller targets, the addition of proton therapy reduces the toxicity even more.

## 7.1 | Introduction

Chemoradiation, i.e. radiation therapy and weekly cisplatin, is the mainstay for locally advanced uterine cervical cancer. Radiation therapy typically consists of external beam radiation therapy (EBRT), followed by a brachytherapy boost. Adequate coverage of the high risk clinical target volume (CTV) in the brachytherapy boost results in a high probability of local control [161]. However, the main dose limiting factors in EBRT are acute complications such as radiation enteritis, proctitis, cystitis as well as late complications such as small bowel obstruction, perforation, fistulae and sexual dysfunction [162,163].

Large volumes of normal tissue are being irradiated during EBRT despite modern techniques such as intensity modulated radiation therapy (IMRT) or volumetric modulated arc therapy (VMAT) combined with an adaptive treatment strategy [54]. A contributing factor to late complications is the EBRT target volume, which includes the whole uterine body plus generous safety margins to compensate for interfraction position uncertainties. The obtained planning target volume (PTV) implicitly results in a substantial overlap of the high dose area with vulnerable small bowel [164-166]. In the present study, we aim to reduce these large volumes of irradiated healthy tissue and investigated two strategies.

There is no doubt that the conventional strategy of target volume definition by including the whole uterus in the CTV is indicated for patients in whom the uterine body is extensively invaded by tumor. But, particularly since the size and extension of tumors can increasingly better be visualized by magnetic resonance imaging (MRI) [167,168], it is not evident why the (whole) uterine body should be included if there is no or only limited invasion of the tumor in the uterine corpus.

Secondly, the application of proton therapy may reduce the organ at risk (OAR) dose. The characteristic Bragg peak of protons enables steep dose fall-offs around the target volume and results in limited dose to OARs [71]. However, due to these physical properties dose delivery in proton therapy is sensitive to range and position uncertainties and anatomical changes can largely influence dose delivery in proton therapy. Therefore, proton plan robustness is required together with appropriate image guidance during dose delivery.

If we assume that both strategies are applicable, the combination of proton therapy and target volume definition using MRI may result in even less collateral dose to small bowel, bladder and rectum compared to the conventional EBRT strategy. If we further correlate the potentially dosimetric advantages with existing normal tissue complication probability (NTCP) models, we will be able to estimate the reduction in small bowel toxicity after cervical cancer EBRT [141]. Therefore, the aim of this study was to quantify dosimetric advantages of proton therapy using MRI-based target volume definition in terms of DVH parameters compared to the best standard of care based on the conventional target definition strategy in photon-based EBRT. Next, we correlated these dosimetric advantages to potential reductions in small bowel toxicity probability.

## 7.2 | Material & Methods

### Patients

All patients with uterine cervical cancer receive MRI for tumor staging. As part of the clinical protocol, anatomical T2-weighted MRI is acquired using either a 1.5 Tesla MRI system (Siemens Avanto, Erlangen, Germany) or a 3.0 Tesla MRI system (Philips Ingenia, Best, the Netherlands). Patients with locally advanced cervical cancer who received curative chemoradiation underwent fludeoxyglucose (FDG) positron emitting tomography (PET)-CT imaging (Philips Gemini, Eindhoven, The Netherlands). PET-CT imaging is performed with a full bladder in radiation therapy position. Eleven women with cervical cancer who received radiation therapy between January 2014 and December 2015 and showed a substantial (>4 cm) tumor free part of the uterus towards the fundus on pre-treatment MRI were selected retrospectively. Table 7.1 presents baseline characteristics of all patients including information regarding MRI acquisition and tumor extensions.

**Table 7.1** | Baseline characteristics.

Patient		Age (years)	FIGO stage	CC tumor extension (mm)	Uterine tumor free distance † (mm)	Treatment position
1	**	34	IA2 (N1)	0	55	prone
2	*	38	IIA2 (N1)	15	51	supine
3	**	54	IIIB	32	42	prone
4	**	28	IB2	20	64	prone
5	*	47	IIB	43	59	prone
6	**	49	IIIB	62	40	supine
7	**	53	IIIB	27	45	supine
8	**	36	IIB	35	46	supine
9	**	41	IB2	28	44	supine
10	**	39	IIA2	39	58	supine
11	*	42	IB1	35	89	supine

*Abbreviations:* FIGO = International Federation of Gynecology and Obstetrics; CC = craniocaudal.

\* MRI acquired using 1.5 T MRI system (Siemens Avanto, Erlangen, Germany).

\*\* MRI acquired using 3.0 T MRI system (Philips Ingenia, Best, the Netherlands).

† Uterine tumor free distance is defined as the distance of tumor free uterine tissue cranial from the tumor.

## Structure definition

For each patient, the gross tumor volume (GTV) was delineated on the CT image after consensus between two experienced radiation oncologists. The GTV was defined as the visible tumor volume on the fused PET-CT image according to FDG-uptake and the visible tumor extend on MRI after co-registration to the CT image. Based on the delineated GTV, target volumes were defined using two different strategies: 1) the conventional definition strategy by including the entire uterus into the target volume (i.e. target volumes with the subscript ‘old’) and 2) the new definition strategy by defining the target volume based on MRI and excluding the uninvaded part of the uterus (i.e. target volumes with the subscript ‘new’).

The conventional target definition strategy recommended to define the primary clinical target volume ( $pCTV_{old}$ ) by including the GTV, the cervix, uterine corpus and upper part of the vagina [29,164,168]. The  $pCTV_{old}$  was enlarged by adding a 10 mm uniform margin to form the primary internal target volume ( $pITV_{old}$ ). In addition, the regional lymph node areas were delineated including parametric and lymph node areas around the iliac and obturator arteries/vessels ( $lnCTV$ ). The internal target volume ( $ITV_{old}$ ) was created by combining  $lnCTV$  and  $pITV_{old}$ . The  $ITV_{old}$  was expanded with an 8 mm isotropic margin to form the  $PTV_{old}$  (Figure 7.1).

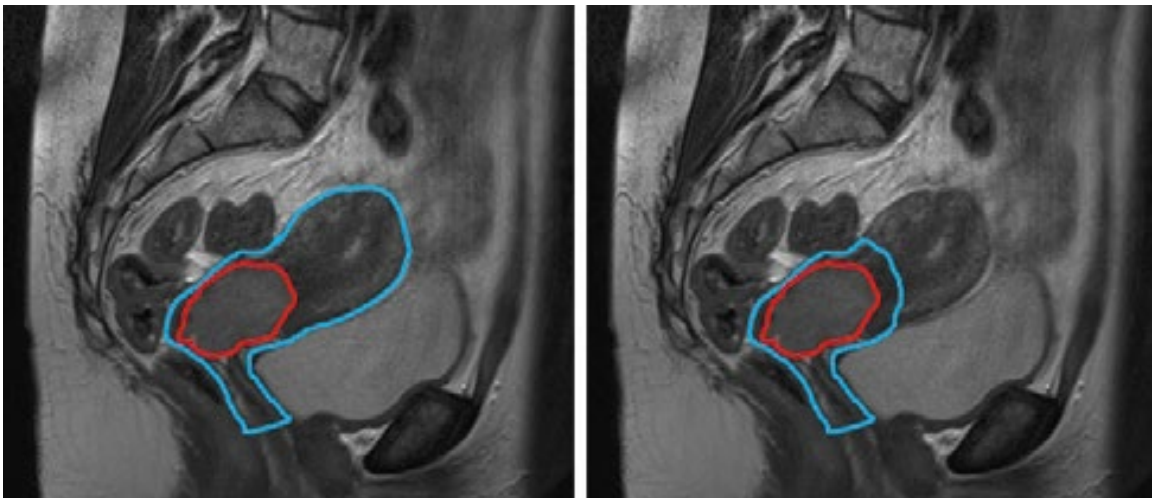


**Figure 7.1** | Sagittal view of T2-weighted MRI for patient 8 with examples of the defined volumes according to the conventional definition strategy (left) and the novel definition strategy (right). In the conventional strategy, the  $pCTV_{old}$  (blue) included besides the GTV (red) the entire uterus and upper part of the vagina. The  $pCTV_{new}$  (blue) according to the novel strategy excluded the uninvaded part of the uterus.

The new target volume definition strategy was introduced to optimize the target volume in cervical cancer, as suggested previously. Instead of including the entire uterine corpus into the target volume, a margin of 10 mm in the direction of the uterine fundus was added to the MRI-based

GTV delineation and combined with the upper part of the vagina and cervix to form the  $pCTV_{new}$  [84,167]. Again, a 10 mm isotropic margin around the  $pCTV_{new}$  defined the  $pITV_{new}$  and the  $ITV_{new}$  was defined by combining the  $lnCTV$  and  $pITV_{new}$ . The PTV was formed by expanding the  $ITV_{new}$  with an 8 mm isotropic margin. Also, on all CTs, the bowel cavity as a surrogate for small bowel, rectum, bladder, and sigmoid were delineated according to RTOG guidelines [137].

## Treatment planning

For all patients, radiation therapy plans for both target definition strategies were generated using photons (Oncontra version 4.5, Elekta AB, Stockholm, Sweden) and protons (RayStation version 4.4, RaySearch Laboratories AB, Stockholm, Sweden). All treatment plans were created based on a prescribed target dose of 46 Gy (23 x 2 Gy) and were optimized on a 3 mm uniform dose grid using the planning CT. Both photon and proton plan optimizations were started with the clinically used planning objectives template (Table 7.2) and objective values were individually optimized to minimize OAR dose while maintaining ICRU-based target coverage ( $D_{98\%} \geq 95\%$ ,  $D_{2\%} \leq 107\%$ ) [169].

Treatment planning using photons was performed based on a dual-arc VMAT (356° per arc, fixed 20° collimator angle) treatment technique. The plan optimization process aimed at planning the prescribed PTV dose of 46 Gy using a 10 MV energy with the isocenter set to the PTV center of mass.

Table 7.2 | Planning objectives for photon (proton) therapy planning.

Structure	Planning objectives
PTV (ITV)	Minimum dose 46 Gy Maximum dose 46.8 Gy
Body	Dose fall-off: 46–30 Gy over 1.0 cm
Rectum	Maximum dose 43.7 Gy Maximum 30 Gy to 70% of the volume
Bladder	Maximum dose 43.7 Gy Maximum 30 Gy to 70% of the volume
Bowel cavity	Maximum dose 43.7 Gy

*Abbreviations:* PTV = planning target volume; ITV = internal target volume.

Intensity modulated proton therapy (IMPT) plans were generated based on pencil beam scanning (spot size in air:  $\sigma=2.5\text{--}7.0$  mm (226.7–70.0 MeV)) using four fixed beams (30°, 90°, 270°, 330° (prone); 90°, 150°, 210°, 270° (supine)) [138]. In proton therapy, the ITV instead of the PTV was used for robust optimization and evaluation. Assuming a proton relative biological effectiveness of 1.1 [139], plans were generated with a prescribed ITV dose of 46 Gy-equivalent. During robust optimization, a total of 21 scenarios were included. Next to the nominal isocenter position and

the six isocenter position shifts of 8 mm in the main directions also three range errors (-3%, 0%, 3%) were included. After optimization, target coverage robustness was evaluated using 28 error scenarios, consisting of two range error (-3%, 3%) and 14 position errors of 8 mm. The position errors were simulated by isocenter position shifts in the six main directions and the eight diagonal directions of each octant in three-dimensional space [138].

## Analysis

For all patients, first target volumes according to the conventional strategy as well as the new strategy were calculated and the effect of MRI-based target volume definition was determined in terms of target volume reductions. Secondly, plan quality was verified by quantifying the conformity index (CI) and target coverage (TC). The CI was defined as the volume of the body receiving 95% of the prescribed dose (body  $V_{95\%}$ ) divided by the  $V_{95\%}$  of the target volume. The PTV was used to calculate the CI for photon plans, but for proton plans the ITV was used for CI calculation. The maximum dose received by at least 98% of the volume ( $D_{98\%}$ ) determined the TC and was reported to support the CI [170].

Differences in dose distributions corresponding to the generated treatment plans were calculated by evaluating DVH parameters for bladder, rectum, bowel cavity and sigmoid. Next to the mean dose ( $D_{\text{mean}}$ ) and maximum dose ( $D_{2\text{cc}}$ ), planned dose parameters for the volumes receiving 15 Gy ( $V_{15\text{Gy}}$ ), 30 Gy ( $V_{30\text{Gy}}$ ) and 45 Gy ( $V_{45\text{Gy}}$ ) were extracted as derivatives for volumes receiving low, intermediate and high dose, respectively. Patient-specific DVH differences with respect to the conventional definition strategy combined with photon therapy were tested pairwise for significance using a non-parametric statistical test (Wilcoxon signed-rank test).

## Toxicity

Differences in toxicity probabilities were estimated between both target definition strategies when applying photon therapy as well as proton therapy. Since NTCP models for bladder, sigmoid and rectum are only defined for dose levels above the prescribed dose of 46 Gy in cervical cancer EBRT, late toxicity probabilities cannot be determined for these OARs [171]. For small bowel, only acute toxicity models are available. Small bowel NTCP values associated with at least grade 2 acute small bowel toxicity were quantified using

$$NTCP = \frac{1}{1 + \left( \frac{V_{50}}{V_{45\text{Gy}}} \right)^k}$$

where  $V_{45\text{Gy}}$  represents the volume ( $\text{cm}^3$ ) receiving 45 Gy,  $V_{50}=410 \text{ cm}^3$  and  $k=3.2$  [141]. Improvements in NTCP between the use of photon therapy and proton therapy were calculated for each patient and correlated to  $V_{45\text{Gy}}$  of the small bowel. According to a model-based approach,

patient-specific NTCP differences were compared with the suggested 10% NTCP difference for individual patient selection who are expected to benefit from proton therapy [172].

### 7.3 | Results

For each patient, target volumes were defined according to the conventional strategy as well as our new strategy. Compared to the conventional volumes, excluding the uninvaded uterine corpus resulted in average reductions of the pITV and PTV by 37% (range, 17%–56%) and 8% (range, 3%–17%), respectively.

Photon-based VMAT plans showed consistency in CI with an average of 1.14 (range, 1.11–1.17) as well as in TC with an average of 44.2 Gy (range, 44.0 Gy – 44.5 Gy). Robustness evaluation for robustly optimized IMPT plans resulted in adequate ITV coverage ( $D_{98\%} \geq 98\%$ ;  $D_{2\%} \leq 107\%$ ) for all evaluated dose distributions. Further, nominal IMPT dose distributions showed consistency in both CI and TC, indicated by average values of 1.6 (range, 1.46–1.82) and 45.7 Gy (range, 45.5 Gy – 45.7 Gy), respectively. Figure 7.2 shows dose distribution examples for the different strategies.

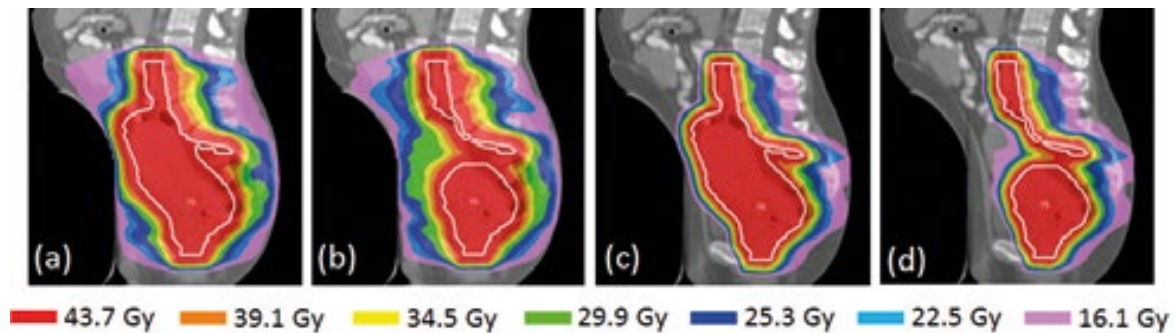


**Figure 7.2** | Sagittal view of color wash map examples of dose distributions are shown for the use of  $PTV_{old}$  (a) and  $PTV_{new}$  (b) combined with photon therapy and for the use of  $ITV_{old}$  (c) and  $ITV_{new}$  (d) combined with proton therapy. All dose distributions indicated adequate target (white contour) coverage while differences in dose to surrounding healthy tissue are observed.

For photon therapy, significant reductions in  $V_{15Gy}$ ,  $V_{30Gy}$ ,  $V_{45Gy}$  and  $D_{mean}$  for both bladder and bowel cavity were found after MRI-based target volume definition (Table 7.3, Figure 7.3). The dose to rectum and sigmoid was similar for both target definition strategies when applying photon therapy. Using conventional target volumes, the use of proton therapy instead of photon therapy was mostly pronounced in significant reductions in  $V_{15Gy}$ ,  $V_{30Gy}$ ,  $V_{45Gy}$  and  $D_{mean}$  for sigmoid and bowel cavity. Moreover, the combination of proton therapy and MRI-based target volumes resulted in additional dosimetric benefits compared to the current clinical standard, resulting in significant

reductions in bladder  $V_{15\text{Gy}}$ ,  $V_{30\text{Gy}}$ ,  $V_{45\text{Gy}}$  and  $D_{\text{mean}}$ . Compared to proton therapy using  $\text{ITV}_{\text{old}}$ , the application of proton therapy with  $\text{ITV}_{\text{new}}$  resulted in significant reductions in  $V_{30\text{Gy}}$ ,  $V_{45\text{Gy}}$  and  $D_{\text{mean}}$  for bladder, sigmoid and bowel cavity (Table 7.3).

**Table 7.3** | Comparison of the mean (standard deviation) dosimetric parameters of all patients for the dose distributions corresponding to the specific target volume and treatment modality. Statistical significant improvements ( $p < 0.05$ ) compared to current clinical practice (i.e. photon therapy,  $\text{pCTV}_{\text{old}}$ ) and proton therapy using conventional target volumes are indicated by an asterisks (\*) and a dagger (†), respectively.

	Photon therapy			Proton therapy		
	$\text{pCTV}_{\text{old}}$	$\text{pCTV}_{\text{new}}$		$\text{pCTV}_{\text{old}}$	$\text{pCTV}_{\text{new}}$	
<b>Bladder</b>						
$V_{15\text{Gy}}$ (%)	95.3 (7.8)	88.4 (10.3)	*	86.8 (7.7)	81.3 (15.2)	* *
$V_{30\text{Gy}}$ (%)	74.0 (8.4)	64.5 (10.5)	*	62.0 (10.7)	50.8 (16.0)	* †
$V_{45\text{Gy}}$ (%)	35.8 (7.2)	27.6 (6.8)	*	30.2 (11.3)	21.9 (13.8)	†
$D_{\text{mean}}$ (Gy)	37.2 (2.6)	34.0 (3.4)	*	33.0 (3.4)	29.3 (5.8)	* †
$D_{2\text{cc}}$ (Gy)	47.1 (0.6)	47.1 (0.6)		48.1 (0.9)	48.0 (0.9)	*
<b>Rectum</b>						
$V_{15\text{Gy}}$ (%)	100.0 (0.0)	100.0 (0.0)		99.7 (1.0)	99.8 (0.6)	
$V_{30\text{Gy}}$ (%)	99.7 (0.3)	99.6 (0.6)		84.3 (5.9)	81.5 (7.5)	* †
$V_{45\text{Gy}}$ (%)	47.1 (19.2)	51.7 (16.6)		40.9 (5.9)	40.3 (5.7)	
$D_{\text{mean}}$ (Gy)	43.5 (0.9)	43.5 (0.9)		39.7 (1.4)	39.2 (1.5)	* †
$D_{2\text{cc}}$ (Gy)	46.0 (0.3)	46.1 (0.4)		46.4 (0.2)	46.5 (0.2)	*
<b>Sigmoid</b>						
$V_{15\text{Gy}}$ (%)	96.0 (6.1)	92.0 (16.3)		83.7 (27.0)	82.6 (27.2)	*
$V_{30\text{Gy}}$ (%)	81.1 (27.1)	78.6 (28.3)		71.6 (25.3)	68.1 (26.3)	* †
$V_{45\text{Gy}}$ (%)	55.9 (21.7)	50.1 (23.2)	*	44.3 (18.2)	33.3 (15.6)	* †
$D_{\text{mean}}$ (Gy)	39.6 (6.8)	38.2 (8.4)	*	34.7 (10.7)	33.2 (10.9)	* †
$D_{2\text{cc}}$ (Gy)	46.9 (0.5)	46.9 (0.6)		46.9 (0.7)	46.8 (0.9)	
<b>Bowel cavity</b>						
$V_{15\text{Gy}}$ (cm <sup>3</sup> )	899.1 (287.3)	838.6 (320.7)	*	559.4 (207.0)	530.9 (212.1)	*
$V_{30\text{Gy}}$ (cm <sup>3</sup> )	501.4 (199.9)	460.3 (202.8)	*	382.3 (170.0)	337.9 (154.1)	* †
$V_{45\text{Gy}}$ (cm <sup>3</sup> )	268.0 (146.3)	226.3 (123.7)	*	227.7 (117.4)	173.4 (88.8)	* †
$D_{\text{mean}}$ (Gy)	20.7 (11.4)	16.9 (6.3)	*	12.8 (5.8)	11.8 (5.6)	* †
$D_{2\text{cc}}$ (Gy)	47.8 (0.5)	47.9 (0.5)		47.9 (0.4)	47.7 (0.4)	

*Abbreviations:* pCTV = primary clinical target volume; Gy = gray.

Figure 7.4 shows patient-specific NTCP values associated with small bowel acute toxicity for both the conventional and reduced target volumes, and for both photon therapy and proton therapy. Conventional photon therapy without the new target volume definition strategy ( $PTV_{old}$ ) resulted in an average toxicity probability of 25% (Table 7.4). Either MRI-based target volume definition or proton therapy yielded an average small bowel acute toxicity probability of 18% and the combination of both strategies resulted in an average 9% small bowel acute toxicity probability (Table 7.4).

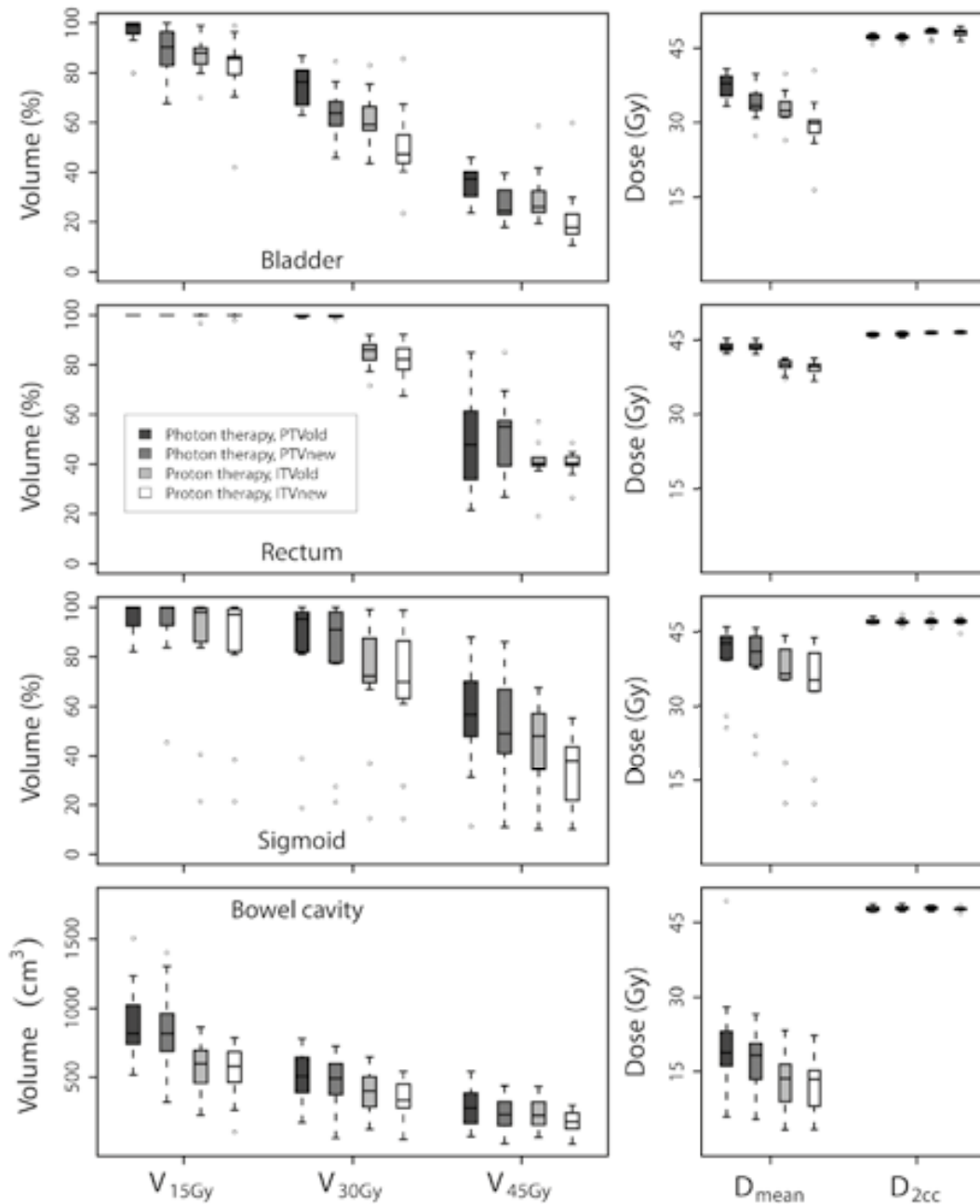


Figure 7.3 | Boxplots of DVH parameters over all planned dose distributions of all patients are shown for bladder, rectum, sigmoid and bowel cavity. Boxes represents upper and lower quartiles (IQR), the band inside the box the median value and the whiskers the highest (lowest) value within 1.5 IQR of the upper (lower) quartile.

Improvements in acute small bowel toxicity probability are mostly observed in patients with a high NTCP for standard treatment (Figure 7.4), caused by a consequently large volume of the bowel cavity receiving at least 45 Gy in current clinical practice (Figure 7.5). The proposed 10% NTCP reduction threshold as an acceptable indication for proton therapy was observed in four patients when using conventional target volumes. For these patients, the bowel cavity  $V_{45Gy}$  was at least 275 cm<sup>3</sup> in the standard treatment. If additionally the non-invaded uterine corpus was excluded from the target volume, a 10% NTCP reduction was expected in 6 out of the 11 patients of whom the bowel cavity  $V_{45Gy}$  was at least 200 cm<sup>3</sup>.

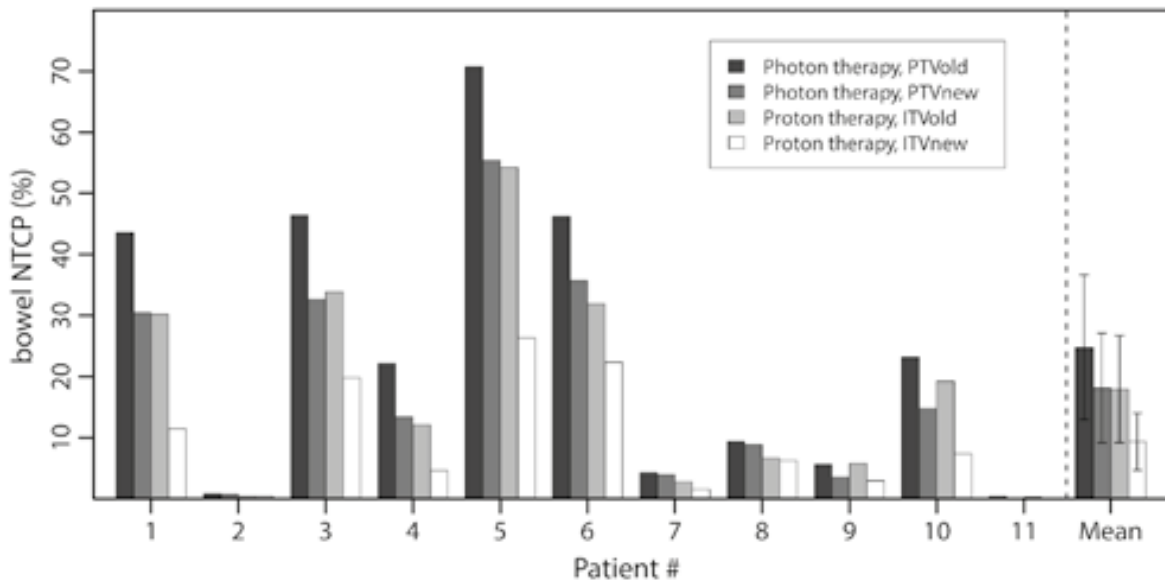
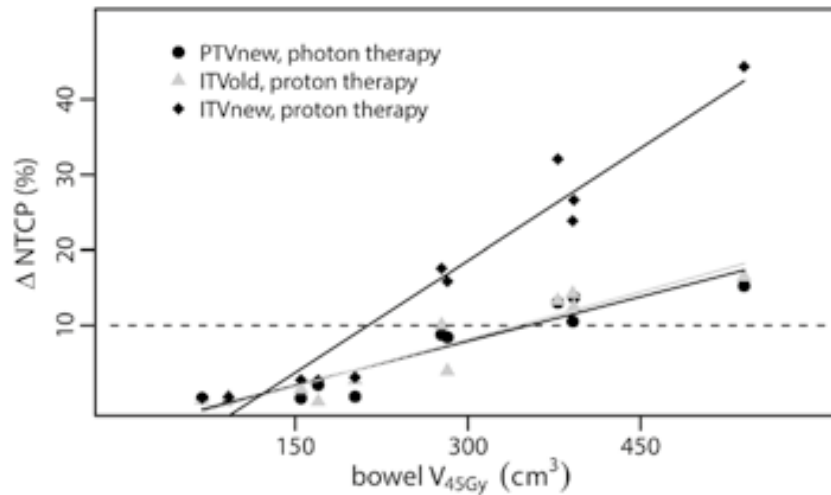


Figure 7.4 | Bar plots of the small bowel NTCP values are shown per patient according to different target volume definition strategies and different treatment modalities. The grouped bars at the right side represent mean NTCP values and the error bars indicate one standard deviation.

Table 7.4 | Comparison of the mean (range) bowel NTCP values (%) for the planned dose distributions of all patients, including the absolute NTCP differences.

	pCTV <sub>old</sub>	pCTV <sub>new</sub>	Absolute difference (%)
Photon therapy	25.0 (1.0–71.0)	18.0 (1.0–55.0)	7.0
Proton therapy	18.0 (1.0–54.0)	9.0 (1.0–26.0)	9.0
Absolute difference (%)	7.0	9.0	–

Abbreviations: pCTV = primary clinical target volume.



**Figure 7.5** | Absolute improvements in normal tissue complication probability ( $\Delta$  NTCP) compared to conventional high precision photon therapy without target volume reduction ( $PTV_{old}$ ) as a function of bowel cavity volume receiving 45 Gy in current clinical practice. Each dot represents a measurement for an individual patient and linear fits are added for visualization purposes. The dotted horizontal line indicates the 10%  $\Delta$  NTCP threshold above which proton therapy is indicated [172].

## 7.4 | Discussion

In this paper, we estimated the effect of two approaches on toxicity reduction for cervical cancer radiation therapy: 1) target definition improvement by excluding the non-invaded uterine corpus from the target volume using MRI and 2) the application of proton therapy. We found that, compared to current clinical standard EBRT, both approaches yielded an absolute NTCP reduction for acute small bowel toxicity of 7%. However, an absolute 16% reduction in acute small bowel toxicity probability may be obtained by combining MRI-based target volume definition with proton therapy. It is up to the radiation oncologist and the patient to decide on an individual basis which approach is desirable. As mentioned previously, the model-based approach suggested a 10% NTCP reduction threshold as an acceptable indication for taking proton therapy into consideration [172]. We estimated a NTCP reduction of at least 10% by proton therapy for 6 patients (55%) in whom the initial bowel cavity  $V_{45Gy}$  was above 200 cm<sup>3</sup> for MRI-based target volumes and in 4 patients (36%) above 275 cm<sup>3</sup> for the conventional target volumes. However, some aspects of both strategies for toxicity reduction in cervical cancer radiation therapy deserve some further discussion.

### MRI-based target volume definition

There is little clinical evidence about the safety of target volume reduction and about the benefit in terms of reduction of toxicity. Especially now advanced adaptive strategies combined with either

photon therapy or proton therapy are making precise dose delivery increasingly possible, methods for improved OAR sparing are warranted.

What we do know is that the uterus and the cervix is an embryological unit without a separating fascial plane, including interconnected lymphatics and the risk of cervical cancer growth into the uterine body is well known [173]. Since this infiltration was hard to detect for decades [174], guidelines continue to recommend inclusion of the uterine body within the CTV [92].

Nowadays with modern MRI techniques, uterine invasion can be assessed prior to treatment and is already widely used for brachytherapy planning [167,168]. Therefore, CTV concepts in EBRT derived from old times may possibly benefit from a modern reappraisal. If there is no sign of invasion into the uterine body, experts suggest that the uterine body can be excluded from the CTV, however, this could not be recommended due to the lack of evidence [29].

On the other hand, studies after trachelectomy have shown a higher risk of recurrences for tumors larger than 2 cm, however, these tumors typically recurred regional and not in the remaining uterine corpus [175,176]. These studies also indicate that histopathological characteristics such as lymph vascular space invasion (HR=3.2,  $P=0.03$ ) and deep stromal invasion (HR=4.5,  $P=0.005$ ) are the most important independent predicting factors for recurrence after surgery [177]. Furthermore, previous studies validated MRI-based tumor volume delineations with histopathology in cervical cancer and demonstrated the feasibility of accurate tumor definition on MRI [84,167].

Even in cervical cancer patients with FIGO stage IIB and IIIB, a local control of 96% and 86% can be achieved using image-guided adaptive brachytherapy with interstitial needles [161]. Although determined for brachytherapy, our findings suggest that the coverage of the high risk CTV, indicated by the  $D_{90\%}$ , is one of the most determining factors in successful local control for chemoradiation. The cause of recurrence in these patients is more likely due to the more challenging coverage of the tumor spread in direction of the parametria, without unacceptable exceeding OAR dose levels, rather than not reaching high dose levels in de uterine fundus.

If a large part of the uninvaded uterus can be safely excluded from the CTV, an adaptive strategy to compensate for the interfraction motion of the uterus may no longer be necessary for a subset of patients. However, target volume reduction will not necessarily results in a negligible benefit of an adaptive strategy. Substantial anatomical changes during the course of treatment may still influence dose delivery and requires an adaptive approach, especially during proton therapy. Therefore, an hybrid strategy including target volume reduction and treatment adaptations should be considered as a future solution.

## Proton therapy

Proton therapy is subject to delivery uncertainties caused by the sensitivity of protons to inter- and intra-fraction anatomical variations. To anticipate on day-to-day anatomical changes, our proton plans were robustly optimized and subsequently evaluated on robustness. Moreover, dose delivery

according to an adaptive strategy can be considered to avoid incorrect dose delivery due to large anatomical deformations [54,77].

The comparison between photon therapy and proton therapy in cervical cancer was performed previously based on the conventional target definition strategy [69,77]. Van de Schoot *et al.* [77] compared both treatment modalities combined with an adaptive strategy based on recalculated dose distributions and showed relative reductions in  $V_{15\text{Gy}}$ ,  $V_{30\text{Gy}}$  and  $V_{45\text{Gy}}$  for bladder, rectum and bowel cavity. Also, similar absolute reductions in small bowel NTCP of 7% were found. The comparison between photon therapy and proton therapy presented by Marnitz *et al.* [69] also showed similar results in favor of proton therapy. However, both model based studies compared the effect of different treatment modalities using conventional target volumes including the whole uterus.

In this study, we also estimated the additional benefit of excluding the uninvaded part of the uterine body combined with proton therapy. Since our results are solely based on planned dose distributions, the actual consequences of daily anatomical variation on DVH parameters were not taken into account. However, van de Schoot *et al.* [77] showed the feasibility of accurate dose delivery using an adaptive strategy under image guidance while maintaining the high-quality dose distributions. Given these results, it is expected that planned dose distributions presented in this study can be delivered accurately without additional deteriorations. Therefore, the NTCP reductions found in our study can be considered reliable, even when the non-invaded uterine fundus will be excluded from the CTV.

## Toxicity estimation

There is a fair consensus amongst radiation oncologists that uninvaded organs and healthy tissue should be avoided, and that new imaging techniques have become indispensable to distinguish healthy uterine tissue from tumor tissue. However, there is little clinical evidence about the safety of only including the invaded part of the uterine corpus and the associated reductions in toxicity. Late toxicity for bladder, sigmoid and rectum is mainly induced by the delivery of high doses and available NTCP models predicting these late toxicities require high dose levels. As a consequence, no NTCP differences will be observed for these OARs after cervical cancer EBRT with a prescribed dose of 46 Gy. Differences in NTCP corresponding to late toxicity are therefore not presented in this study. Nevertheless, acute toxicities already occur at lower dose levels and acute small bowel toxicity probabilities were estimated after cervical cancer EBRT.

Other available NTCP models for rectum, sigmoid, and bladder address toxicity probabilities in relation to the brachytherapy boost by using the  $D_{2cc}$  as independent variable [178,179]. However, in this study only the contribution of EBRT on toxicity probabilities is estimated without including the brachytherapy dose distribution. The accumulation of EBRT and brachytherapy dose distributions including associated toxicity probabilities will be explored in future.

## 7.5 | Conclusion

Improvements in target volume definition and proton therapy both lead to significant OAR dose reductions in cervical cancer radiation therapy as well as a significant decrease in small bowel toxicity. Moreover, the combination of both strategies resulted in an additional reduction of acute small bowel toxicity. The estimated benefit from target volume improvements combined with proton therapy is at least 10% for patients with bowel cavity  $V_{45\text{Gy}}$  above  $200\text{ cm}^3$ .



# Chapter 8

General discussion

## General discussion

The aim of adaptive radiation therapy is to achieve adequate dose delivery by compensating for interfraction anatomical variations. In cervical cancer radiation therapy, the possible large day-to-day anatomical variations require an online adaptive strategy to deliver optimized dose distributions by correcting for both systematic and random errors. In the Academic Medical Center, adaptive radiation therapy with concomitant chemotherapy has been introduced recently as the standard treatment strategy for patients with locally advanced cervical cancer.

In this thesis, we have aimed at optimizing adaptive radiation therapy in cervical cancer to improve the treatment efficiency and reduce radiation-associated toxicities. The preceding chapters addressed our solutions to optimize adaptive radiation therapy in cervical cancer. Besides improvements in daily target coverage, our solutions for photon therapy as well as proton therapy resulted in significant dose reductions to surrounding healthy tissues.

First, the clinically implemented daily plan selection adaptive strategy was described in **chapter 2** and the dosimetric consequences of this adaptive strategy compared to conventional non-adaptive radiation therapy were demonstrated. A possible solution in the process of adaptive radiation therapy optimization includes improvements on the daily plan selection methodology. Using the image segmentation method demonstrated in **chapter 3**, the daily plan selection procedure can be automated in order to decrease the decision time in the treatment room. Next to an extensive description of our (semi-)automatic bladder segmentation method on CBCT imaging, **chapter 3** also presented a description of the complete validation of the segmentation performance.

Compared to conventionally used X-rays, protons have certain distinct advantages and hold the promise of limited dose delivery to surrounding healthy tissues. Consequently, organ at risk sparing can be improved by applying adaptive proton therapy. The efficiency of proton therapy delivery was improved by selecting the optimal beam configuration in cervical cancer proton therapy. **Chapter 4** presented our solution to objectively compare beam configurations in terms of plan robustness and dose-volume histogram (DVH) parameters. The optimal beam configuration for cervical cancer proton therapy was determined and used to investigate the application of adaptive proton therapy. In **chapter 5**, the application of adaptive proton therapy in cervical cancer was described and the dosimetric advantages of adaptive proton therapy compared to photon-based adaptive radiation therapy were demonstrated.

Next to the application of proton therapy, adaptive radiation therapy in cervical cancer can be further optimized by improving the strategy of target volume definition. The conventional strategy of target definition in cervical cancer was adapted by excluding the non-invaded part of the uterine body based on exact tumor extent delineation on magnetic resonance imaging (MRI). To safely rely on MRI-based definitions, the accuracy of gross tumor volume (GTV) delineation on MRI was validated in **chapter 6**. Also, our solution on the correlation between MRI and pathology data including deformation corrections was demonstrated. Based on the accurate correlations, discrepancies between MRI-based and pathology-based tumor volumes were derived. Next, a

comparison between the conventional target definition strategy and the novel target definition strategy based on MRI was performed in terms of target coverage and OAR dose. The advantages of the novel target definition strategy were demonstrated in **chapter 7** for the application of photon therapy as well as proton therapy.

In this chapter (**chapter 8**), the results presented in this thesis are compared with other solutions in cervical cancer adaptive radiation therapy. Furthermore, future perspectives of cervical cancer treatment including evolutions in adaptive radiation therapy as well as alternative treatment options are mentioned.

## 8.1 | Adaptive radiation therapy in cervical cancer

The preferred adaptive strategy includes daily re-optimization of the dose distribution based on pre-fraction imaging, however this type of adaptation is not yet feasible due to technical and logistical limitations. Therefore, alternative strategies need to be developed to anticipate on day-to-day anatomical variations in cervical cancer.

In **chapter 2**, the clinically introduced daily plan selection adaptive strategy in cervical cancer radiation therapy was described and evaluated in detail. The adaptive strategy is based on predicting the target deformation pattern before treatment to be able to anticipate on anatomical changes during the course of radiation therapy. Since variations in target shape and position in cervical cancer are mainly caused by bladder volume differences, the target deformation model is determined by multiple pre-treatment CT imaging acquired with large bladder volume differences. Deformable image registration was applied between CT imaging acquired with extreme bladder volumes to derive the patient-specific target shape model. Corresponding to different bladder volume ranges, this full range target volume was divided in target volume subranges and associated treatment plans were generated to form the plan library. Each treatment fraction, the plan corresponding to the anatomy as observed on pre-fraction CBCT imaging is selected manually followed by dose delivery.

Compared to non-adaptive radiation therapy, the daily plan selection adaptive strategy corrected for day-to-day anatomical variations and resulted in significant improvements in target coverage. Next to the target coverage improvements, we also found a limited dose reduction for rectum and bowel and the clinical relevance of these reductions is expected to be limited. Therefore, the largest area of improvement on adaptive radiation therapy in cervical cancer was found to be the reduction in dose to healthy surrounding tissues while maintaining adequate target coverage.

### Optimization of the clinical adaptive procedure

Several aspects of the clinically applied online adaptive strategy in cervical cancer radiation therapy are open for improvements. For instance, the plan library can be personalized prior to treatment

by incorporating besides variations in bladder volume also other patient-specific variations. In addition, improvements of the patient-specific plan library can be achieved during treatment by updating the library of plans based on additional imaging. Currently, the range of target motion is predicted based on two CT images with variable bladder volumes. The prediction error can be reduced by using more than two pre-treatment CT images for model construction or the inclusion of repeat imaging (e.g. CT imaging) during the course of treatment for remodelling [56,120]. However, the introduction and evaluation of additional imaging will increase the clinical workload while the reduction in prediction error is expected to be limited.

Daily plan selection is currently performed manually based on pre-fraction CBCT imaging and the observer is assisted by fiducial markers implanted near the tumor. A fast and automatic plan selection strategy is required to reduce the decision time in the treatment room and consequently limit the effect of intrafraction anatomical changes on dose delivery [45,67,74]. Automatic image segmentation strategies are appropriate candidates to replace manual plan selection procedures. However, the performance of such methodology depends on the CBCT-based segmentation accuracy and the corresponding segmentation time. The reported correlation between bladder volume and the position of the uterus in cervical cancer patients [65,66,73,93] allowed for automatic plan selection based on bladder volume determination. The generic segmentation method presented in **chapter 3** resulted in accurate bladder segmentations on CBCT images acquired within a short period of time. However, the bladder remains a surrogate for the target position and manual verification of the automatic selection procedure based on bladder segmentation is required to avoid incorrect irradiation.

Alternative methods for online plan selection included bladder volume measurements using ultrasound [64], direct segmentation of the target volume based on MRI or CT imaging [76,180,181] and automatic segmentation of fiducial markers used for tumor demarcation [102,103,182]. However, unfortunately all proposed alternatives have limitations in clinical practice. Ultrasound measurements in the treatment room require additional in-room time and might induce additional uncertainties for dose delivery while the bladder volume is still a surrogate for the target position. Methods to directly segment the target volume for plan selection purposes are demonstrated using MRI [180,181] or CT imaging [76], however these methods are not directly suitable using CBCT imaging due to its limited soft-tissue contrast. The segmentation of implanted fiducial markers is applied previously [102,103,182], but a substantial number of fiducial markers is required to accurately determine the daily shape and position of the target volume. Moreover, migration or loss of fiducial markers during the course of treatment decrease the applicability and reliability of automatic plan selection based on fiducial marker segmentation.

## 8.2 | Proton therapy in cervical cancer

Despite the use of modern techniques, the physical properties of photon beams prevented sharp dose fall-offs around the target volume. In order to achieve less radiation-associated toxicity for cervical cancer patients after radiation therapy, the dose to healthy tissues was reduced by combining the online adaptive strategy with proton therapy. Proton therapy holds the promise to limit dose to surrounding healthy tissues [34], but the delivery of the highly conformal dose distribution is challenging due to the sensitivity of protons to range and position uncertainties induced by anatomical variations. Photon-based radiation therapy is delivered using an advanced rotational IMRT technique (i.e. VMAT) and dose delivery in proton therapy also required an optimized IMPT technique to enable a fair comparison between photon therapy and proton therapy. In order to investigate the actual benefits of adaptive proton therapy, an optimized IMPT technique allowed for a direct comparison between proton therapy and photon therapy both applied using an adaptive strategy.

### Optimization of proton delivery efficiency

We investigated beam configuration optimality in cervical cancer IMPT by comparing configuration-specific Pareto fronts. Without the arbitrariness of individual planning decisions, different beam configurations in IMPT planning were objectively compared using the set of Pareto optimal IMPT plans that reflected the optimal trade-offs between conflicting objectives. In **chapter 4**, a method to automatically approximate Pareto fronts was demonstrated in terms of plan robustness and DVH parameters. In addition, we presented a quantitative comparison and selection between beam configurations in cervical cancer IMPT.

Although the concept of Pareto optimality as an evaluative and comparative tool was previously introduced for radiation therapy purposes [128,130,131,133,183,184], for our purpose it was extended to enable IMPT beam configuration selection. Our presented method on Pareto front approximation included robustness evaluations and therefore became a time consuming procedure. Because only a large reduction in calculation time opens the possibility to a more extensive use of this method or possibly use as a clinical application, improvements in the described method are required. Alternative strategies to derive Pareto optimal solutions are currently under development and already a limited number of (sub)optimal solutions for specific purposes are implemented in commercial radiation therapy software [185].

Rotational delivery techniques in proton therapy are not yet feasible due to technical limitations, but the static field IMPT technique is an excellent alternative to deliver highly conformal dose distributions including the inherent steep dose fall-off outside the target volume. Therefore, beam configuration optimality in terms of DVH parameters and plan robustness is essential to improve the efficiency of IMPT. Although the selected beam configuration was found superior in terms of plan robustness and DVH parameters for all evaluated cervical cancer patients, this configuration

is not necessarily the solution for all patients and therefore it is recommended to derive beam configuration optimality on an individual basis. Similar to solutions presented for photon-based radiation therapy [125,126,186], the optimization of number of beams and corresponding gantry angles should be included in the plan optimization process to obtain patient-specific optimal dose distributions. Preferably, this optimization strategy also includes possible effects of prolonged delivery times [187].

The observed differences between inspected configurations imply the superiority of the four-beam configuration. In clinical practice, the limited advantages of this configuration compared to the three-beam configuration can be diminished during dose delivery. Due to the time needed for dose delivery, additional delivery uncertainties may be induced by intra-fraction anatomical changes. Therefore, a limited number of beams are preferred to preserve high-precision dose delivery in clinical practice.

### **Adaptive proton therapy in cervical cancer**

Using the selected beam configuration for cervical cancer proton therapy as described in **chapter 4**, the application of adaptive proton therapy was compared with photon-based adaptive radiation therapy in cervical cancer. Adaptive treatments for both treatment modalities were simulated using an extensive set of CT images and resulted in adequate target coverage for both treatment modalities. Compared to adaptive photon therapy, the advantages of adaptive proton therapy using the daily plan selection adaptive strategy are presented in **chapter 5**. Besides minor differences in daily target coverage, major differences in delivered dose to surrounding healthy tissues were demonstrated. Moreover, the reduction of dose to bowel and rectum resulted in decreased radiation-associated complication probabilities.

The clinical application of proton therapy relies, even more than for photon therapy, on appropriate image guidance since both inter- and intrafraction anatomical changes can severely deteriorate proton therapy dose distributions. The sensitivity of proton therapy dose distributions to anatomical variation can be decreased by introducing plan robustness with the drawback of not completely exploiting the potential benefit of proton therapy. Although robustness needs to be incorporated to a certain extent in proton plans, an adaptive strategy enabled by appropriate image guidance is necessary to ensure accurate dose delivery.

Volumetric imaging techniques are required for image guidance in proton therapy. Although in-room imaging modalities for proton therapy are confined to mobile (PET-)CT systems or gantry-mounted CBCT systems, modern proton gantries are increasingly equipped with a CBCT imaging system [188-191]. For the application of adaptive proton therapy, online imaging is necessary to perform plan selection in an accurate and fast way. Compared to CBCT imaging, in-room CT imaging acquired with a mobile system will improve the image quality with the drawback of additional in-room treatment time. As a consequence, the improvement of online imaging is of much more importance when an adaptive strategy in proton therapy is applied.

Proton therapy is often used to treat childhood cancer in order to reduce the delivered integral dose, resulting in a lower risk of secondary malignancies as well as an lower risk of radiation-associated late effects [192-194]. Also, the treatment of tumors located close to radiosensitive tissues such as central nervous system tumors and head and neck tumors are preferably treated using proton therapy [122,195]. Although cervical cancer is not one of the primary indications for proton therapy, the potential benefit of proton therapy over conventional radiation therapy is demonstrated in this thesis. Furthermore, adaptive proton therapy enables dose escalation to the primary tumor, possibly in a stereotactic fashion [196], and may be a valid alternative for patients who are not eligible for brachytherapy [124].

### 8.3 | Target definition improvements in cervical cancer

According to international guidelines, the clinical target volume (CTV) in cervical cancer radiation therapy is recommended to encompass the gross tumor volume (GTV), cervix, upper part of the vagina, lymph nodes and the entire uterus [29,92,146,164,197]. The definition of this structure in current clinical practice is usually performed using (PET-)CT imaging while MRI is often considered as an additional imaging modality to reliably assess tumor involvement in surrounding tissues. In order to improve the conventional target definition strategy, it has been suggested to exclude the non-invaded part of the uterus from the CTV by using MRI for exact GTV definition [6,29]. The inclusion of only the invaded part of the uterus in the CTV resulted in reduced target volumes and enabled high-precision radiation therapy for both photon therapy and proton therapy. In addition, target volume optimization resulted in OAR dose reductions and opens up the possibility for dose escalations in cervical cancer radiation therapy.

#### Target definition accuracy on MRI

The accuracy of GTV delineation on MRI was validated using pathology data to be able to safely exclude the non-invaded part of the uterus from the CTV. **Chapter 6** demonstrated a method to correlate in-vivo MRI and ex-vivo imaging of surgical specimens. Unlike previously reported correlations between MRI and pathology imaging in cervical cancer [148,154,167], the presented registration method also included corrections for shape deformations between both imaging sets. The presented deformable image registration method resulted in accurate correlations between MRI and pathology imaging and discrepancies between MRI-based GTV delineations and corresponding pathology proven tumor volumes were derived.

The extensive validation of MRI-based GTV definition is necessary to avoid incomplete irradiation induced by incorrect target definition. Therefore, an accurate tissue processing and registration method is required to enable the validation of MRI-based GTV delineations with pathology. In **chapter 6**, anatomical T2-weighted MRI was correlated with retrospectively selected

two-dimensional (2D) pathology images. Although the uncertainty induced by only a 2D-2D correlation was expected to be limited, the recommended three-dimensional (3D) imaging information is currently collected prospectively to improve the validation of MRI-based GTV delineations with pathology [6]. The presented deformable image registration method is expected to be easily extended in order to perform 3D-3D correlations, similar to studies on other tumor sites [152,153,198].

The use of advanced MRI techniques can offer additional information for accurate tumor detection. Instead of only anatomical T2-weighted MRI, the use of diffusion-weighted imaging (DWI) [199,200] or dynamic contrast-enhanced (DCE-)MRI [201,202] can facilitate tumor invasion detection. Furthermore, DWI and DCE-MRI might be used for tumor differentiation or treatment response prediction [203,204]. However, tumor detection using these advanced MRI techniques also needs to be validated before clinical decisions can be taken safely. The demonstrated strategy for tumor delineation validation can also be used to quantify the correctness of tumor definition using DWI or DCE-MRI.

The accuracy of GTV definition on MRI becomes more and more valuable with the increased introduction of MRI in the radiation therapy workflow. Next to pre-treatment MRI for target volume definition, additional offline MRI during the course of radiation therapy is increasingly applied for alternative treatment adaptation strategies or tumor response monitoring. For both purposes an offline evaluation of the supplementary MRI is required, but the incorporation of MRI-based decisions in the online clinical workflow will result in difficulties in terms of treatment efficiency and clinical workload. The introduction of a MRI-only radiation therapy workflow has been investigated to facilitate the inclusion of MRI-based decisions during the course of treatment next to the elimination of integral dose from CT imaging [205,206]. Radiation therapy requires high geometric precision and the MRI-only workflow allows for an accurate relation between the reference MRI and MRI findings during treatment. The introduced MRI-cobalt-60 system [207] or the scheduled introduction of the MRI-linac, a linear accelerator with an integrated MRI system [208], offers new possibilities regarding online adaptive radiation therapy possibly within a MRI-only framework.

### **Consequences of target volume definition improvements**

For both photon therapy and proton therapy, **chapter 7** demonstrated the potential benefit of excluding the non-invaded part of the uterus from the CTV in terms of target coverage and OAR dose. The GTV was defined using anatomical T2-weighted MRI and the target volume was created by adding the required radiation therapy safety margins. Compared to the use of conventional target volumes, the improved target volumes resulted in reductions of OAR dose while maintaining adequate target coverage. MRI-based target volume definition combined with the application of proton therapy resulted in even less OAR dose and substantially decreased the small bowel toxicity probability for individual patients.

The additional use of MRI for target definition enabled the GTV to be more precisely delineated in order to limit the volume of surrounding tissue that is intentionally irradiated. The direct consequence of MRI-based target volume definition is the volume reduction due to the exclusion of the non-invaded part of the uterus. As a result, the highly mobile uterine corpus is completely or partly excluded from the target volume and will diminish the interfraction anatomical variation of the target volume. Nevertheless, day-to-day anatomical variations will induce changes in target shape and position and an adaptive treatment strategy is desirable. Only a part of the patients will have limited invasion into the uterine body, resulting in a large subset of patients that will benefit from an adaptive strategy.

Even though the benefit of improvements in target volume definition was demonstrated, the actual clinical outcome and toxicity in terms of tumor control, radiation-associated side effects and quality of life need to be studied. Clinical evidence, preferably based on randomized control trials, is essential to convince radiation oncologists and patients that at least similar tumor control with minimal complications can be achieved without irradiating the whole uterus.

## 8.4 | Future perspectives

Online adaptive radiation therapy in cervical cancer is necessary for optimal dose delivery in the presence of day-to-day anatomical variations. Although actual improvements in overall survival and treatment related toxicity need to be investigated prospectively, this thesis demonstrates improvements in adaptive radiation therapy in cervical cancer. Several solutions including different treatment modalities were addressed to optimize online adaptive radiation therapy. To achieve additional advancements in treatment outcome, improvements in dose delivery precision is desired while minimizing the dose to surrounding healthy tissues. Next to the developments in radiation therapy, alternative treatment options can improve treatment outcome for patients with locally advanced cervical cancer.

### Adaptive radiation therapy

The main area of improvement in the process of adaptive radiation therapy is related to daily imaging. Current adaptive strategies in radiation therapy often rely on CBCT imaging, but the present quality of CBCT imaging limits the advancements in treatment adaptations. Although the quality of CBCT imaging is improved by optimizing reconstruction algorithms and post processing methods [55,209-212], alternative online imaging modalities with superior image quality are required to take adaptive radiation therapy to the next level. The use of in-room imaging using a CT-on-rails system offers diagnostic image quality with the drawback of increased overall treatment times and additional integral dose [213]. Furthermore, increased overall treatment times will provoke intrafraction anatomical changes. With the superior image quality of MRI compared to

(CB)CT imaging, the introduction of MRI guidance during radiation therapy opens the possibility for advanced adaptive strategies. The first commercial system for MRI-guided radiation therapy has been clinically introduced [207,214]. This system combines online MRI and cobalt-60 radiation therapy and allows for treatment adaptations including online dose calculation. However, online plan adaptation resulted in largely increased treatment times. Also, the decay of the radiation source need to be taken into account and a regular source replacement is required. In the near future, the introduction of a linear accelerator with an integrated MRI system, the MRI-linac, offers new possibilities regarding online adaptive radiation therapy [208,215]. The clinical introduction of this system opens the possibility for sophisticated adaptive strategies to be implemented including online re-optimization and dose escalation [85,216]. Due to the substantial interfraction anatomical changes, cervical cancer patients will probably benefit from adaptive radiation therapy using online MRI guidance. In the near future, cervical cancer patients will receive external beam radiation therapy including online adaptations using the MRI-linac.

Next to the improvements in photon-based radiation therapy, the treatment of cervical cancer using protons is expected to result in large advantages in treatment outcome. In the Netherlands, proton therapy facilities will become available soon and the clinical introduction of proton therapy opens the possibility for adaptive proton therapy in cervical cancer. Although cervical cancer is currently not one of the main indications for proton therapy, a selection of patients eligible for proton therapy is recommended using a model-based approach [172]. As demonstrated in this thesis, adaptive proton therapy has the potential to largely reduce radiation-induced side effects in cervical cancer. However, advanced image guidance is necessary to guarantee appropriate dose delivery in proton therapy and benefit from this treatment strategy. Moreover, the limited clinical experience on proton therapy compared to photon therapy requires a close collaboration between national and international specialists in radiation oncology to successfully introduce adaptive strategies in proton therapy. In clinical practice, the enhancement of adaptive proton therapy is hindered by the limited availability of in-room imaging (i.e. CT-on-rails imaging system or CBCT imaging system) in proton facilities. Long term developments will combine proton therapy and MRI to apply the preferred treatment modality with a promising online imaging technique [217-219]. Preferably, MRI-guided proton therapy also includes online re-optimization techniques in order to adapt cervical cancer radiation therapy instantaneously and individualize treatments by response monitoring and dose escalation.

### **Alternative treatment options**

The standard curative treatment of patients with locally advanced cervical tumors consists of radiation therapy with concomitant chemotherapy. Besides the optimization of radiation therapy techniques, improvements in treatment outcome are being investigated by advancing current treatment techniques or exploring alternative treatment options.

For instance, hyperthermia in addition to radiation therapy is the preferred choice for cervical cancer patients with a contraindication for chemotherapy. Compared to radiation therapy alone, the combination of radiation therapy with hyperthermia improves local tumor control and overall survival in patients with locally advanced cervical tumors without affecting acute or late toxicity [17,19]. These results imply possible additional improvements in treatment outcome when combining radiation therapy, chemotherapy and hyperthermia as one combined treatment strategy.

A different treatment modality for locally advanced cervical cancer is the application of immunotherapy. This therapy aims to treat and even prevent cancer by activating the immune system of the patient. The cancerous cells are killed selectively and this process is provoked by administering tumor-specific antibodies or targeting tumor-associated antigens. The systematic and targeted character of immunotherapy results in a high potential candidate for cervical cancer treatment and advancements in immunotherapy for cervical cancer are currently under investigation. Moreover, both radiation therapy and hyperthermia stimulate the release of tumor antigens which may enhance the efficacy of immunotherapy. In future, cervical cancer patients might benefit from a combined treatment consisting of radiation therapy with concomitant chemotherapy, hyperthermia and possibly immunotherapy.

## 8.5 | Conclusions

In conclusion, the results of a number of studies to optimize adaptive radiation therapy in cervical cancer have been addressed and several solutions for both photon therapy and proton therapy have been investigated. It was shown that the daily plan selection adaptive strategy in cervical cancer radiation therapy enabled corrections for interfraction anatomical changes in order to achieve maximal tumor control with minimal complications. Moreover, the simulation studies on the application of adaptive proton therapy showed the ability of high-precision dose delivery in the presence of anatomical variations and resulted in substantial improvements in organ at risk sparing. For cervical cancer patients with a limited tumor invasion into the uterus, high-precision radiation therapy may be further improved by adaptations in target volume definitions using advanced pre-treatment imaging. Target volume definition based on MRI combined with the use of proton therapy, possibly delivered using an adaptive strategy, showed large potential improvements in treatment outcome in terms of radiation-induced toxicity.



# References

- [1] The international agency for research on cancer. *www.globocan.iarc.fr*. January 2016.
- [2] The Netherlands comprehensive cancer organisation. *www.cijfersoverkanker.nl*. January 2016.
- [3] FIGO Committee on Gynecologic Oncology. FIGO staging for carcinoma of the vulva, cervix, and corpus uteri. *Int. J. Gynecol. Obstet.* 2014;125:97–98.
- [4] Greco A, Mason P, Leung AWL, *et al.* Staging of carcinoma of the uterine cervix: MRI-surgical correlation. *Clin. Radiol.* 1989;40:401–405.
- [5] Burghardt E, Hofmann HMH, Ebner F, *et al.* Magnetic resonance imaging in cervical cancer: A basis for objective classification. *Gynecol. Oncol.* 1989;33:61–67.
- [6] de Boer P, Adam JA, Buist MR, *et al.* Role of MRI in detecting involvement of the uterine internal os in uterine cervical cancer: systematic review of diagnostic test accuracy. *Eur. J. Radiol.* 2013;82:e422–e428.
- [7] Bipat S, van den Berg RA, van der Velden J, *et al.* The role of magnetic resonance imaging in determining the proximal extension of early stage cervical cancer to the internal os. *Eur. J. Radiol.* 2011;78:60–64.
- [8] Bipat S, Glas AS, van der Velden J, *et al.* Computed tomography and magnetic resonance imaging in staging of uterine cervical carcinoma: a systematic review. *Gynecol. Oncol.* 2003;91:59–66.
- [9] Kaidar-Person O, Bortnyak-Abdah R, Amit A, *et al.* The role of imaging in the management of non-metastatic cervical cancer. *Med. Oncol.* 2012;29:3389–3393.
- [10] Gaffney DK, Erickson-Wittmann BA, Jhingran A, *et al.* ACR appropriateness criteria on advanced cervical cancer expert panel on radiation oncology-gynecology. *Int. J. Radiat. Oncol. Biol. Phys.* 2011;81:609–614.
- [11] Singh AK, Grigsby PW, Dehdashti F, *et al.* FDG-PET lymph node staging and survival of patients with FIGO stage IIIB cervical carcinoma. *Int. J. Radiat. Oncol. Biol. Phys.* 2003;56:489–493.
- [12] Gien LT, Covens A. Fertility-sparing options for early stage cervical cancer. *Gynecol. Oncol.* 2010;117:350–357.
- [13] Henderson MA, Burmeister BH, Ainslie J, *et al.* Adjuvant lymph-node field radiotherapy versus observation only in patients with melanoma at high risk of further lymph-node field relapse after lymphadenectomy (ANZMTG 01.02/TROG 02.01): 6-year follow-up of a phase 3, randomised controlled trial. *Lancet Oncol.* 2015;16:1049–1060.
- [14] Rose PG, Bundy BN, Watkins EB, *et al.* Concurrent cisplatin-based radiotherapy and chemotherapy for locally advanced cervical cancer. *N. Engl. J. Med.* 1999;340:1144–1153.
- [15] Peters WA, Liu PY, Barrett RJ, *et al.* Concurrent chemotherapy and pelvic radiation therapy compared with pelvic radiation therapy alone as adjuvant therapy after radical surgery in high-risk early-stage cancer of the cervix. *J. Clin. Oncol.* 2000;18:1606–1613.
- [16] Whitney CW, Sause W, Bundy BN, *et al.* Randomized comparison of fluorouracil plus cisplatin versus hydroxyurea as an adjunct to radiation therapy in stage IIB-IVA carcinoma of the cervix with negative para-aortic lymph nodes: a Gynecologic Oncology Group and Southwest Oncology Group study. *J. Clin. Oncol.* 1999;17:1339–1348.
- [17] van der Zee J, González González D, van Rhoon GC, *et al.* Comparison of radiotherapy alone with radiotherapy plus hyperthermia in locally advanced pelvic tumours: a prospective, randomised, multicentre trial. *Lancet.* 2000;355:1119–1125.
- [18] Franckena M, Stalpers LJA, Koper PCM, *et al.* Long-term improvement in treatment outcome after radiotherapy and hyperthermia in locoregionally advanced cervix cancer: an update of the Dutch Deep Hyperthermia Trial. *Int. J. Radiat. Oncol. Biol. Phys.* 2008;70:1176–1182.
- [19] Lutgens L, van der Zee J, Pijls-Johannesma M, *et al.* Combined use of hyperthermia and radiation therapy for treating locally advanced cervical carcinoma. *Cochrane Libr. Syst. Rev.* 2010;1:CD006377.
- [20] Al-Mansour Z, Verschraegen C. Locally advanced cervical cancer: what is the standard of care? *Curr. Opin. Oncol.* 2010;22:503–512.
- [21] Hellebust TP, Kirisits C, Berger D, *et al.* Recommendations from Gynaecological (GYN) GEC-ESTRO Working Group: Considerations and pitfalls in commissioning and applicator reconstruction in 3D image-based treatment planning of cervix cancer brachytherapy. *Radiother. Oncol.* 2010;96:153–160.

- [22] Wang X, Liu R, Ma B, *et al.* High dose rate versus low dose rate intracavity brachytherapy for locally advanced uterine cervix cancer. *Cochrane Database Syst. Rev.* 2010;7:CD007563.
- [23] Rath GK, Sharma DN, Julka PK, *et al.* Pulsed-dose-rate intracavitary brachytherapy for cervical carcinoma: the AIIMS experience. *Am. J. Clin. Oncol.* 2010;33:238–241.
- [24] Engelsman M, Schwarz M, Dong L. Physics controversies in proton therapy. *Semin. Radiat. Oncol.* 2013;23:88–96.
- [25] Siddiqui F, Shi C, Papanikolaou N, *et al.* Image-guidance protocol comparison: Supine and prone set-up accuracy for pelvic radiation therapy. *Acta Oncol.* 2008;47:1344–1350.
- [26] Wiesendanger-Wittmer EM, Sijtsema NM, Muijs CT, *et al.* Systematic review of the role of a belly board device in radiotherapy delivery in patients with pelvic malignancies. *Radiother. Oncol.* 2012;102:325–334.
- [27] Stromberger C, Kom Y, Kawgan-Kagan M, *et al.* Intensity-modulated radiotherapy in patients with cervical cancer. An intra-individual comparison of prone and supine positioning. *Radiat. Oncol.* 2010;5:63.
- [28] Martin J, Fitzpatrick K, Horan G, *et al.* Treatment with a belly-board device significantly reduces the volume of small bowel irradiated and results in low acute toxicity in adjuvant radiotherapy for gynecologic cancer: results of a prospective study. *Radiother. Oncol.* 2005;74:267–274.
- [29] Lim K, Small W, Portelance L, *et al.* Consensus guidelines for delineation of clinical target volume for intensity-modulated pelvic radiotherapy for the definitive treatment of cervix cancer. *Int. J. Radiat. Oncol. Biol. Phys.* 2011;79:348–355.
- [30] Fotina I, Winkler P, Künzler T, *et al.* Advanced kernel methods vs. Monte Carlo-based dose calculation for high energy photon beams. *Radiother. Oncol.* 2009;93:645–653.
- [31] Krieger T, Sauer OA. Monte Carlo- versus pencil-beam-/collapsed-cone- dose calculation in a heterogeneous multi-layer phantom. *Phys. Med. Biol.* 2005;50:859–868.
- [32] Cozzi L, Dinshaw KA, Shrivastava SK, *et al.* A treatment planning study comparing volumetric arc modulation with RapidArc and fixed field IMRT for cervix uteri radiotherapy. *Radiother. Oncol.* 2008;89:180–191.
- [33] Lomax A. Intensity modulation methods for proton radiotherapy. *Phys. Med. Biol.* 1999;44:185–205.
- [34] Johansson B, Ridderheim M, Glimelius B. The potential of proton beam radiation therapy in prostate cancer, other urological cancers and gynaecological cancers. *Acta Oncol.* 2005;44:890–895.
- [35] Georg D, Georg P, Hillbrand M, *et al.* Assessment of improved organ at risk sparing for advanced cervix carcinoma utilizing precision radiotherapy techniques. *Strahlenther. Onkol.* 2008;184:586–591.
- [36] van Herk M. Different styles of image-guided radiotherapy. *Semin. Radiat. Oncol.* 2007;17:258–267.
- [37] Dawson LA, Jaffray DA. Advances in image-guided radiation therapy. *J. Clin. Oncol.* 2007;25:938–946.
- [38] Mao W, Hsu A, Riaz N, *et al.* Image-guided radiotherapy in near real time with intensity-modulated radiotherapy megavoltage treatment beam imaging. *Int. J. Radiat. Oncol. Biol. Phys.* 2009;75:603–610.
- [39] Herman MG, Pisansky TM, Kruse JJ, *et al.* Technical aspects of daily online positioning of the prostate for three-dimensional conformal radiotherapy using an electronic portal imaging device. *Int. J. Radiat. Oncol. Biol. Phys.* 2003;57:1131–1140.
- [40] Dávila Fajardo R, Lekkerkerker SJ, van der Horst A, *et al.* EUS-guided fiducial markers placement with a 22-gauge needle for image-guided radiation therapy in pancreatic cancer. *Gastrointest. Endosc.* 2014;79:851–855.
- [41] Chai X, van Herk M, van de Kamer JB, *et al.* Behavior of lipiodol markers during image guided radiotherapy of bladder cancer. *Int. J. Radiat. Oncol. Biol. Phys.* 2010;77:309–314.
- [42] Machiels M, van Hooft J, Jin P, *et al.* Endoscopy/EUS-guided fiducial marker placement in patients with esophageal cancer: a comparative analysis of 3 types of markers. *Gastrointest. Endosc.* 2015;82:641–649.
- [43] Jin P, Hulshof MCCM, de Jong R, *et al.* Quantification of respiration-induced esophageal tumor motion using fiducial markers and four-dimensional computed tomography. *Radiother. Oncol.* 2016;118:492–497.
- [44] Kaatee RSJP, Olofsen MJJ, Verstraate MJB, *et al.* Detection of organ movement in cervix cancer patients using a fluoroscopic electronic portal imaging device and radiopaque markers. *Int. J. Radiat. Oncol. Biol. Phys.* 2002;54:576–583.
- [45] Hariopotornkul NH, Nath SK, Scanderbeg D, *et al.* Evaluation of intra- and inter-fraction movement of the cervix during intensity modulated radiation therapy. *Radiother. Oncol.* 2011;98:347–351.

- [46] Langerak T, Mens JW, Quint S, *et al.* Cervix motion in 50 cervical cancer patients assessed by daily cone beam computed tomographic imaging of a new type of marker. *Int. J. Radiat. Oncol. Biol. Phys.* 2015;93:532–539.
- [47] Yan D, Vicini F, Wong J, *et al.* Adaptive radiation therapy. *Phys. Med. Biol.* 1997;42:123–132.
- [48] Yan D, Ziaja E, Jaffray D, *et al.* The use of adaptive radiation therapy to reduce setup error: a prospective clinical study. *Int. J. Radiat. Oncol. Biol. Phys.* 1998;41:715–720.
- [49] Nuver TT, Hoogeman MS, Remeijer P, *et al.* An adaptive off-line procedure for radiotherapy of prostate cancer. *Int. J. Radiat. Oncol. Biol. Phys.* 2007;67:1559–1567.
- [50] de Boer HCJ, Heijmen BJM. A protocol for the reduction of systematic patient setup errors with minimal portal imaging workload. *Int. J. Radiat. Oncol. Biol. Phys.* 2001;50:1350–1365.
- [51] Bel A, van Herk M, Bartelink H, *et al.* A verification procedure to improve patient set-up accuracy using portal images. *Radiother. Oncol.* 1993;29:253–260.
- [52] Wright P, Muren LP, Høyer M, *et al.* Evaluation of adaptive radiotherapy of bladder cancer by image-based tumour control probability modelling. *Acta Oncol.* 2010;49:1045–1051.
- [53] Vestergaard A, Søndergaard J, Petersen JB, *et al.* A comparison of three different adaptive strategies in image-guided radiotherapy of bladder cancer. *Acta Oncol.* 2010;49:1069–1076.
- [54] Ahmad R, Bondar L, Voet P, *et al.* A margin-of-the-day online adaptive intensity-modulated radiotherapy strategy for cervical cancer provides superior treatment accuracy compared to clinically recommended margins: a dosimetric evaluation. *Acta Oncol.* 2013;52:1430–1436.
- [55] Søvik A, Rødal J, Skogmo HK, *et al.* Adaptive radiotherapy based on contrast enhanced cone beam CT imaging. *Acta Oncol.* 2010;49:972–977.
- [56] Stewart J, Lim K, Kelly V, *et al.* Automated weekly replanning for intensity-modulated radiotherapy of cervix cancer. *Int. J. Radiat. Oncol. Biol. Phys.* 2010;78:350–358.
- [57] Thörnqvist S, Hysing LB, Zolnay AG, *et al.* Adaptive radiotherapy in locally advanced prostate cancer using a statistical deformable motion model. *Acta Oncol.* 2013;52:1423–1429.
- [58] Lutkenhaus LJ, Visser J, de Jong R, *et al.* Evaluation of delivered dose for a clinical daily adaptive plan selection strategy for bladder cancer radiotherapy. *Radiother. Oncol.* 2015;116:51–56.
- [59] Heijkoop ST, Langerak TR, Quint S, *et al.* Clinical implementation of an online adaptive plan-of-the-day protocol for nonrigid motion management in locally advanced cervical cancer IMRT. *Int. J. Radiat. Oncol. Biol. Phys.* 2014;90:673–679.
- [60] Meijer GJ, van der Toorn P-P, Bal M, *et al.* High precision bladder cancer irradiation by integrating a library planning procedure of 6 prospectively generated SIB IMRT plans with image guidance using lipiodol markers. *Radiother. Oncol.* 2012;105:174–179.
- [61] Vestergaard A, Kallehauge JF, Petersen JBB, *et al.* An adaptive radiotherapy planning strategy for bladder cancer using deformation vector fields. *Radiother. Oncol.* 2014;112:371–375.
- [62] Nijkamp J, Marijnen C, van Herk M, *et al.* Adaptive radiotherapy for long course neo-adjuvant treatment of rectal cancer. *Radiother. Oncol.* 2012;103:353–359.
- [63] Gill S, Pham D, Dang K, *et al.* Plan of the day selection for online image-guided adaptive post-prostatectomy radiotherapy. *Radiother. Oncol.* 2013;107:165–170.
- [64] Ahmad R, Hoogeman MS, Quint S, *et al.* Inter-fraction bladder filling variations and time trends for cervical cancer patients assessed with a portable 3-dimensional ultrasound bladder scanner. *Radiother. Oncol.* 2008;89:172–179.
- [65] Bondar L, Hoogeman M, Mens JW, *et al.* Toward an individualized target motion management for IMRT of cervical cancer based on model-predicted cervix-uterus shape and position. *Radiother. Oncol.* 2011;99:240–245.
- [66] Ahmad R, Hoogeman MS, Bondar M, *et al.* Increasing treatment accuracy for cervical cancer patients using correlations between bladder-filling change and cervix-uterus displacements: proof of principle. *Radiother. Oncol.* 2011;98:340–346.
- [67] Kerkhof EM, van der Put RW, Raaymakers BW, *et al.* Intrafraction motion in patients with cervical cancer: The benefit of soft tissue registration using MRI. *Radiother. Oncol.* 2009;93:115–121.

- [68] Kerkhof EM, Raaymakers BW, van der Heide UA, *et al.* Online MRI guidance for healthy tissue sparing in patients with cervical cancer: an IMRT planning study. *Radiother. Oncol.* 2008;88:241–249.
- [69] Marnitz S, Wlodarczyk W, Neumann O, *et al.* Which technique for radiation is most beneficial for patients with locally advanced cervical cancer? Intensity modulated proton therapy versus intensity modulated photon treatment, helical tomotherapy and volumetric arc therapy for primary radiation – an intraindividual comparison. *Radiat. Oncol.* 2015;10:91.
- [70] Milby AB, Both S, Ingram M, *et al.* Dosimetric comparison of combined intensity-modulated radiotherapy (IMRT) and proton therapy versus IMRT alone for pelvic and para-aortic radiotherapy in gynecologic malignancies. *Int. J. Radiat. Oncol. Biol. Phys.* 2012;82:e477–e484.
- [71] Song WY, Huh SN, Liang Y, *et al.* Dosimetric comparison study between intensity modulated radiation therapy and threedimensional conformal proton therapy for pelvic bone marrow sparing in the treatment of cervical cancer. *J. Appl. Clin. Med. Phys.* 2010;11:3255.
- [72] Eifel PJ, Winter K, Morris M, *et al.* Pelvic irradiation with concurrent chemotherapy versus pelvic and para-aortic irradiation for high-risk cervical cancer: an update of Radiation Therapy Oncology Group trial (RTOG) 90-01. *J. Clin. Oncol.* 2004;22:872–880.
- [73] Jadon R, Pembroke CA, Hanna CL, *et al.* A systematic review of organ motion and image-guided strategies in external beam radiotherapy for cervical cancer. *Clin. Oncol.* 2014;26:185–196.
- [74] Heijkoop ST, Langerak TR, Quint S, *et al.* Quantification of intra-fraction changes during radiotherapy of cervical cancer assessed with pre- and post-fraction Cone Beam CT scans. *Radiother. Oncol.* 2015;117:536–541.
- [75] van de Schoot AJAJ, Schooneveldt G, Wognum S, *et al.* Generic method for automatic bladder segmentation on cone beam CT using a patient-specific bladder shape model. *Med. Phys.* 2014;41:031707.
- [76] Bondar ML, Hoogeman M, Schillemans W, *et al.* Intra-patient semi-automated segmentation of the cervix-uterus in CT-images for adaptive radiotherapy of cervical cancer. *Phys. Med. Biol.* 2013;58:5317–5332.
- [77] van de Schoot AJAJ, de Boer P, Crama KF, *et al.* Dosimetric advantages of proton therapy compared with photon therapy using an adaptive strategy in cervical cancer. *Acta Oncol.* 2016; doi:10.3109/0284186X.2016.1139179.
- [78] Bondar L, Hoogeman MS, Vásquez Osorio EM, *et al.* A symmetric nonrigid registration method to handle large organ deformations in cervical cancer patients. *Med. Phys.* 2010;37:3760–3772.
- [79] Veiga C, McClelland J, Moinuddin S, *et al.* Toward adaptive radiotherapy for head and neck patients: Feasibility study on using CT-to-CBCT deformable registration for “dose of the day” calculations. *Med. Phys.* 2014;41:031703.
- [80] Stanley N, Glide-Hurst C, Kim J, *et al.* Using patient-specific phantoms to evaluate deformable image registration algorithms for adaptive radiation therapy. *J. Appl. Clin. Med. Phys.* 2013;14:4363.
- [81] Onozato Y, Kadoya N, Fujita Y, *et al.* Evaluation of on-board kV cone beam computed tomography based dose calculation with deformable image registration using hounsfield unit modifications. *Int. J. Radiat. Oncol. Biol. Phys.* 2014;89:416–423.
- [82] Oh S, Stewart J, Moseley J, *et al.* Hybrid adaptive radiotherapy with on-line MRI in cervix cancer IMRT. *Radiother. Oncol.* 2014;110:323–328.
- [83] Bondar ML, Hoogeman MS, Mens JW, *et al.* Individualized nonadaptive and online-adaptive intensity-modulated radiotherapy treatment strategies for cervical cancer patients based on pretreatment acquired variable bladder filling computed tomography scans. *Int. J. Radiat. Oncol. Biol. Phys.* 2012;83:1617–1623.
- [84] van de Schoot AJAJ, de Boer P, Buist MR, *et al.* Quantification of delineation errors of the gross tumor volume on magnetic resonance imaging in uterine cervical cancer using pathology data and deformation correction. *Acta Oncol.* 2014;54:224–231.
- [85] Kontaxis C, Bol GH, Lagendijk JJW, *et al.* A new methodology for inter- and intrafraction plan adaptation for the MR-linac. *Phys. Med. Biol.* 2015;60:7485–7497.
- [86] Jaffray DA, Siewerdsen JH, Wong JW, *et al.* Flat-panel cone-beam computed tomography for image-guided radiation therapy. *Int. J. Radiat. Oncol. Biol. Phys.* 2002;53:1337–1349.
- [87] Oelfke U, Tücking T, Nill S, *et al.* Linac-integrated kV-cone beam CT: technical features and first applications. *Med. Dosim.* 2006;31:62–70.

- [88] Muren LP, Smaaland R, Dahl O. Conformal radiotherapy of urinary bladder cancer. *Radiother. Oncol.* 2004;73:387–398.
- [89] Tyagi N, Lewis JH, Yashar CM, *et al.* Daily online cone beam computed tomography to assess interfractional motion in patients with intact cervical cancer. *Int. J. Radiat. Oncol. Biol. Phys.* 2011;80:273–280.
- [90] Peng C, Ahunbay E, Chen G, *et al.* Characterizing interfraction variations and their dosimetric effects in prostate cancer radiotherapy. *Int. J. Radiat. Oncol. Biol. Phys.* 2011;79:909–914.
- [91] Nijkamp J, de Jong R, Sonke J-J, *et al.* Target volume shape variation during irradiation of rectal cancer patients in supine position: comparison with prone position. *Radiother. Oncol.* 2009;93:285–292.
- [92] Taylor A, Powell MEB. An assessment of interfractional uterine and cervical motion: implications for radiotherapy target volume definition in gynaecological cancer. *Radiother. Oncol.* 2008;88:250–257.
- [93] Buchali A, Koswig S, Dinges S, *et al.* Impact of the filling status of the bladder and rectum on their integral dose distribution and the movement of the uterus in the treatment planning of gynaecological cancer. *Radiother. Oncol.* 1999;52:29–34.
- [94] Thongphiew D, Wu QJ, Lee WR, *et al.* Comparison of online IGRT techniques for prostate IMRT treatment: Adaptive vs repositioning correction. *Med. Phys.* 2009;36:1651.
- [95] Lim K, Kelly V, Stewart J, *et al.* Pelvic radiotherapy for cancer of the cervix: is what you plan actually what you deliver? *Int. J. Radiat. Oncol. Biol. Phys.* 2009;74:304–312.
- [96] Pos FJ, Hulshof M, Lebesque J, *et al.* Adaptive radiotherapy for invasive bladder cancer: a feasibility study. *Int. J. Radiat. Oncol. Biol. Phys.* 2006;64:862–868.
- [97] Li T, Thongphiew D, Zhu X, *et al.* Adaptive prostate IGRT combining online re-optimization and re-positioning: a feasibility study. *Phys. Med. Biol.* 2011;56:1243–1258.
- [98] Burrige N, Amer A, Marchant T, *et al.* Online adaptive radiotherapy of the bladder: small bowel irradiated-volume reduction. *Int. J. Radiat. Oncol. Biol. Phys.* 2006;66:892–897.
- [99] Foroudi F, Wong J, Kron T, *et al.* Online adaptive radiotherapy for muscle-invasive bladder cancer: results of a pilot study. *Int. J. Radiat. Oncol. Biol. Phys.* 2011;81:765–771.
- [100] Weiss E, Wu J, Sleeman W, *et al.* Clinical evaluation of soft tissue organ boundary visualization on cone-beam computed tomographic imaging. *Int. J. Radiat. Oncol. Biol. Phys.* 2010;78:929–936.
- [101] Stippel G, van Rooijen DC, Crezee J, *et al.* Automatic delineation of body contours on cone-beam CT images using a delineation booster. *Phys. Med. Biol.* 2012;57:N225–N236.
- [102] Poulsen PR, Fledelius W, Keall PJ, *et al.* A method for robust segmentation of arbitrarily shaped radiopaque structures in cone-beam CT projections. *Med. Phys.* 2011;38:2151.
- [103] Fledelius W, Worm E, Elstrøm U V, *et al.* Robust automatic segmentation of multiple implanted cylindrical gold fiducial markers in cone-beam CT projections. *Med. Phys.* 2011;38:6351–6361.
- [104] Yan D, Jaffray DA, Wong JW. A model to accumulate fractionated dose in a deforming organ. *Int. J. Radiat. Oncol. Biol. Phys.* 1999;44:665–675.
- [105] Jaffray DA, Lindsay PE, Brock KK, *et al.* Accurate accumulation of dose for improved understanding of radiation effects in normal tissue. *Int. J. Radiat. Oncol. Biol. Phys.* 2010;76:S135–S139.
- [106] Chai X, van Herk M, Betgen A, *et al.* Automatic bladder segmentation on CBCT for multiple plan ART of bladder cancer using a patient-specific bladder model. *Phys. Med. Biol.* 2012;57:3945–3962.
- [107] Chai X, van Herk M, Betgen A, *et al.* Semiautomatic bladder segmentation on CBCT using a population-based model for multiple-plan ART of bladder cancer. *Phys. Med. Biol.* 2012;57:N525–N541.
- [108] Taubin G. A signal processing approach to fair surface design. *Proc. 22nd Annu. Conf. Comput. Graph. Interact. Tech.* 1995:351–358.
- [109] Brechbühler C, Gerig G, Kübler O. Parametrization of closed surfaces for 3-D shape description. *Comput. Vis. Image Underst.* 1995;61:154–170.
- [110] Söhn M, Birkner M, Yan D, *et al.* Modelling individual geometric variation based on dominant eigenmodes of organ deformation: implementation and evaluation. *Phys. Med. Biol.* 2005;50:5893–5908.

- [111] Nelder JA, Mead R. A simplex method for function minimization. *Comput. J.* 1965;7:308–13.
- [112] Lütgendorf-Caucig C, Fotina I, Stock M, *et al.* Feasibility of CBCT-based target and normal structure delineation in prostate cancer radiotherapy: multi-observer and image multi-modality study. *Radiother. Oncol.* 2011;98:154–161.
- [113] Foroudi F, Haworth A, Pangehel A, *et al.* Inter-observer variability of clinical target volume delineation for bladder cancer using CT and cone beam CT. *J. Med. Imaging Radiat. Oncol.* 2009;53:100–106.
- [114] de Crevoisier R, Melancon AD, Kuban D a, *et al.* Changes in the pelvic anatomy after an IMRT treatment fraction of prostate cancer. *Int. J. Radiat. Oncol. Biol. Phys.* 2007;68:1529–1536.
- [115] Wognum S, Bondar L, Zolnay AG, *et al.* Control over structure-specific flexibility improves anatomical accuracy for point-based deformable registration in bladder cancer radiotherapy. *Med. Phys.* 2013;40:021702.
- [116] Meijer GJ, Rasch CRN, Remeijer P, *et al.* Three-dimensional analysis of delineation errors, setup errors, and organ motion during radiotherapy of bladder cancer. *Int. J. Radiat. Oncol. Biol. Phys.* 2003;55:1277–1287.
- [117] Simmat I, Georg P, Georg D, *et al.* Assessment of accuracy and efficiency of atlas-based autosegmentation for prostate radiotherapy in a variety of clinical conditions. *Strahlenther. Onkol.* 2012;188:807–815.
- [118] Logsdon MD, Eifel PJ. Figo IIIB squamous cell carcinoma of the cervix: an analysis of prognostic factors emphasizing the balance between external beam and intracavitary radiation therapy. *Int. J. Radiat. Oncol. Biol. Phys.* 1999;43:763–775.
- [119] Portelance L, Chao KS, Grigsby PW, *et al.* Intensity-modulated radiation therapy (IMRT) reduces small bowel, rectum, and bladder doses in patients with cervical cancer receiving pelvic and para-aortic irradiation. *Int. J. Radiat. Oncol. Biol. Phys.* 2001;51:261–266.
- [120] van de Bunt L, van der Heide UA, Ketelaars M, *et al.* Conventional, conformal, and intensity-modulated radiation therapy treatment planning of external beam radiotherapy for cervical cancer: The impact of tumor regression. *Int. J. Radiat. Oncol. Biol. Phys.* 2006;64:189–196.
- [121] Vale CL, Tierney JF, Davidson SE, *et al.* Substantial improvement in UK cervical cancer survival with chemoradiotherapy: results of a Royal College of Radiologists' audit. *Clin. Oncol.* 2010;22:590–601.
- [122] Kraan AC, van de Water S, Teguh DN, *et al.* Dose uncertainties in IMPT for oropharyngeal cancer in the presence of anatomical, range, and setup errors. *Int. J. Radiat. Oncol. Biol. Phys.* 2013;87:888–896.
- [123] Georg D, Kirisits C, Hillbrand M, *et al.* Image-guided radiotherapy for cervix cancer: high-tech external beam therapy versus high-tech brachytherapy. *Int. J. Radiat. Oncol. Biol. Phys.* 2008;71:1272–1278.
- [124] Clivio A, Kluge A, Cozzi L, *et al.* Intensity modulated proton beam radiation for brachytherapy in patients with cervical carcinoma. *Int. J. Radiat. Oncol. Biol. Phys.* 2013;87:897–903.
- [125] Breedveld S, Storchi PRM, Voet PWJ, *et al.* iCycle: Integrated, multicriterial beam angle, and profile optimization for generation of coplanar and noncoplanar IMRT plans. *Med. Phys.* 2012;39:951–963.
- [126] Meedt G, Alber M, Nüsslin F. Non-coplanar beam direction optimization for intensity-modulated radiotherapy. *Phys. Med. Biol.* 2003;48:2999–3019.
- [127] Wang X, Zhang X, Dong L, *et al.* Effectiveness of noncoplanar IMRT planning using a parallelized multiresolution beam angle optimization method for paranasal sinus carcinoma. *Int. J. Radiat. Oncol. Biol. Phys.* 2005;63:594–601.
- [128] Ottosson RO, Engstrom PE, Sjöström D, *et al.* The feasibility of using Pareto fronts for comparison of treatment planning systems and delivery techniques. *Acta Oncol.* 2009;48:233–237.
- [129] Fredriksson A, Forsgren A, Hårdemark B. Minimax optimization for handling range and setup uncertainties in proton therapy. *Med. Phys.* 2011;38:1672–1684.
- [130] van Kesteren Z, Janssen TM, Damen E, *et al.* The dosimetric impact of leaf interdigitation and leaf width on VMAT treatment planning in Pinnacle: comparing Pareto fronts. *Phys. Med. Biol.* 2012;57:2943–2952.
- [131] Janssen T, van Kesteren Z, Franssen G, *et al.* Pareto fronts in clinical practice for pinnacle. *Int. J. Radiat. Oncol. Biol. Phys.* 2013;85:873–880.
- [132] Li H, Zhang X, Park P, *et al.* Robust optimization in intensity-modulated proton therapy to account for anatomy changes in lung cancer patients. *Radiother. Oncol.* 2015;114:367–372.

- [133] Ottosson RO, Karlsson A, Behrens CF. Pareto front analysis of 6 and 15 MV dynamic IMRT for lung cancer using pencil beam, AAA and Monte Carlo. *Phys. Med. Biol.* 2010;55:4521–4533.
- [134] Bosman PAN. The anticipated mean shift and cluster registration in mixture-based EDAs for multi-objective optimization. *Proc. 12th Annu. Conf. Genet. Evol. Comput.* 2010:351–358.
- [135] Bosman PAN. On gradients and hybrid evolutionary algorithms for real-valued multi-objective optimization. *IEEE Trans. Evol. Comput.* 2012;16:51–69.
- [136] Paganetti H. Range uncertainties in proton therapy and the role of Monte Carlo simulations. *Phys. Med. Biol.* 2012;57:R99–R117.
- [137] Gay HA, Barthold HJ, O'Meara E, *et al.* Pelvic normal tissue contouring guidelines for radiation therapy: a Radiation Therapy Oncology Group consensus panel atlas. *Int. J. Radiat. Oncol. Biol. Phys.* 2012;83:e353–e362.
- [138] van de Schoot AJAJ, Visser J, van Kesteren Z, *et al.* Beam configuration selection for robust intensity-modulated proton therapy in cervical cancer using Pareto front comparison. *Phys. Med. Biol.* 2016;61:1780–1794.
- [139] Paganetti H, Niemierko A, Ancukiewicz M, *et al.* Relative biological effectiveness (RBE) values for proton beam therapy. *Int. J. Radiat. Oncol. Biol. Phys.* 2002;53:407–421.
- [140] Stenmark MH, Conlon ASC, Johnson S, *et al.* Dose to the inferior rectum is strongly associated with patient reported bowel quality of life after radiation therapy for prostate cancer. *Radiother. Oncol.* 2014;110:291–297.
- [141] Roeske JC, Bonta D, Mell LK, *et al.* A dosimetric analysis of acute gastrointestinal toxicity in women receiving intensity-modulated whole-pelvic radiation therapy. *Radiother. Oncol.* 2003;69:201–207.
- [142] Weistrand O, Svensson S. The ANACONDA algorithm for deformable image registration in radiotherapy. *Med. Phys.* 2015;42:40–53.
- [143] van Rooijen DC, van Wieringen N, Stippel G, *et al.* Dose-guided radiotherapy: potential benefit of online dose recalculation for stereotactic lung irradiation in patients with non-small-cell lung cancer. *Int. J. Radiat. Oncol. Biol. Phys.* 2012;83:e557–e562.
- [144] Wognum S, Heethuis SE, Rosario T, *et al.* Validation of deformable image registration algorithms on CT images of ex vivo porcine bladders with fiducial markers. *Med. Phys.* 2014;41:071916.
- [145] Haie-Meder C, Pötter R, Van Limbergen E, *et al.* Recommendations from Gynaecological (GYN) GEC-ESTRO Working Group (I): concepts and terms in 3D image based 3D treatment planning in cervix cancer brachytherapy with emphasis on MRI assessment of GTV and CTV. *Radiother. Oncol.* 2005;74:235–245.
- [146] Tanderup K, Georg D, Pötter R, *et al.* Adaptive management of cervical cancer radiotherapy. *Semin. Radiat. Oncol.* 2010;20:121–129.
- [147] van Herk M. Errors and margins in radiotherapy. *Semin. Radiat. Oncol.* 2004;14:52–64.
- [148] Mitchell DG, Snyder B, Coakley F, *et al.* Early invasive cervical cancer: tumor delineation by magnetic resonance imaging, computed tomography, and clinical examination, verified by pathologic results, in the ACRIN 6651/GOG 183 Intergroup Study. *J. Clin. Oncol.* 2006;24:5687–5694.
- [149] Subak LL, Hricak H, Powell CB, *et al.* Cervical carcinoma: computed tomography and magnetic resonance imaging for preoperative staging. *Obstet. Gynecol.* 1995;86:43–50.
- [150] Barillot I, Reynaud-Bougnoix A. The use of MRI in planning radiotherapy for gynaecological tumours. *Cancer Imaging.* 2006;6:100–106.
- [151] Park H, Piert MR, Khan A, *et al.* Registration methodology for histological sections and in vivo imaging of human prostate. *Acad. Radiol.* 2008;15:1027–1039.
- [152] Groenendaal G, Moman MR, Korporaal JG, *et al.* Validation of functional imaging with pathology for tumor delineation in the prostate. *Radiother. Oncol.* 2010;94:145–150.
- [153] Caldas-Magalhaes J, Kasperts N, Kooij N, *et al.* Validation of imaging with pathology in laryngeal cancer: accuracy of the registration methodology. *Int. J. Radiat. Oncol. Biol. Phys.* 2012;82:e289–e298.
- [154] deSouza NM, Scoones D, Krausz T, *et al.* High-resolution MR imaging of stage I cervical neoplasia with a dedicated transvaginal coil: MR features and correlation of imaging and pathologic findings. *AJR. Am. J. Roentgenol.* 1996;166:553–559.

- [155] Zhang Y, Hu J, Li J, *et al.* Comparison of imaging-based gross tumor volume and pathological volume determined by whole-mount serial sections in primary cervical cancer. *Onco. Targets. Ther.* 2013;6:917–923.
- [156] Klein S, Staring M, Murphy K, *et al.* Elastix: a toolbox for intensity-based medical image registration. *IEEE Trans. Med. Imaging.* 2010;29:196–205.
- [157] Dimopoulos JCA, De Vos V, Berger D, *et al.* Inter-observer comparison of target delineation for MRI-assisted cervical cancer brachytherapy: application of the GYN GEC-ESTRO recommendations. *Radiother. Oncol.* 2009;91:166–172.
- [158] Mazaheri Y, Bokacheva L, Kroon D-J, *et al.* Semi-automatic deformable registration of prostate MR images to pathological slices. *J. Magn. Reson. imaging.* 2010;32:1149–1157.
- [159] Sala E, Rockall A, Rangarajan D, *et al.* The role of dynamic contrast-enhanced and diffusion weighted magnetic resonance imaging in the female pelvis. *Eur. J. Radiol.* 2010;76:367–385.
- [160] Wyatt RM, Beddoe AH, Dale RG. The effects of delays in radiotherapy treatment on tumour control. *Phys. Med. Biol.* 2003;48:139–155.
- [161] Pötter R, Georg P, Dimopoulos JCA, *et al.* Clinical outcome of protocol based image (MRI) guided adaptive brachytherapy combined with 3D conformal radiotherapy with or without chemotherapy in patients with locally advanced cervical cancer. *Radiother. Oncol.* 2011;100:116–123.
- [162] Castelnau-Marchand P, Chargari C, Maroun P, *et al.* Clinical outcomes of definitive chemoradiation followed by intracavitary pulsed-dose rate image-guided adaptive brachytherapy in locally advanced cervical cancer. *Gynecol. Oncol.* 2015;139:288–294.
- [163] Kavanagh BD, Pan CC, Dawson LA, *et al.* Radiation dose-volume effects in the stomach and small bowel. *Int. J. Radiat. Oncol. Biol. Phys.* 2010;76:101–107.
- [164] Taylor A, Rockall AG, Reznik RH, *et al.* Mapping pelvic lymph nodes: guidelines for delineation in intensity-modulated radiotherapy. *Int. J. Radiat. Oncol. Biol. Phys.* 2005;63:1604–1612.
- [165] van de Bunt L, Jürgenliemk-Schulz IM, de Kort GAP, *et al.* Motion and deformation of the target volumes during IMRT for cervical cancer: what margins do we need? *Radiother. Oncol.* 2008;88:233–240.
- [166] Collen C, Engels B, Duchateau M, *et al.* Volumetric imaging by megavoltage computed tomography for assessment of internal organ motion during radiotherapy for cervical cancer. *Int. J. Radiat. Oncol. Biol. Phys.* 2010;77:1590–1595.
- [167] de Boer P, Bleeker MCG, Spijkerboer AM, *et al.* Craniocaudal tumour extension in uterine cervical cancer on MRI compared to histopathology. *Eur. J. Radiol. Open.* 2015;2:111–117.
- [168] Pötter R, Haie-Meder C, van Limbergen E, *et al.* Recommendations from gynaecological (GYN) GEC ESTRO working group (II): Concepts and terms in 3D image-based treatment planning in cervix cancer brachytherapy — 3D dose volume parameters and aspects of 3D image-based anatomy, radiation physics, radiobiology. *Radiother. Oncol.* 2006;78:67–77.
- [169] International commission on radiation units and measurements. *ICRU report 83: prescribing, recording, and reporting photon-beam intensity-modulated radiation therapy (IMRT)*. Vol. 10. Oxford, UK: Oxford University Press; 2010.
- [170] Feuvret L, Noël G, Mazeron J-J, *et al.* Conformity index: a review. *Int. J. Radiat. Oncol. Biol. Phys.* 2006;64:333–342.
- [171] Marks LB, Yorke ED, Jackson A, *et al.* Use of normal tissue complication probability models in the clinic. *Int. J. Radiat. Oncol. Biol. Phys.* 2010;76:S10–S19.
- [172] Langendijk JA, Lambin P, de Ruyscher D, *et al.* Selection of patients for radiotherapy with protons aiming at reduction of side effects: The model-based approach. *Radiother. Oncol.* 2013;107:267–273.
- [173] Höckel M, Horn L-C, Fritsch H. Association between the mesenchymal compartment of uterovaginal organogenesis and local tumour spread in stage IB–IIB cervical carcinoma: a prospective study. *Lancet Oncol.* 2005;6:751–756.
- [174] Kim H, Kim W, Lee M, *et al.* Tumor volume and uterine body invasion assessed by MRI for prediction of outcome in cervical carcinoma treated with concurrent chemotherapy and radiotherapy. *Jpn. J. Clin. Oncol.* 2007;37:858–866.

- [175] Plante M, Gregoire J, Renaud M-C, *et al.* The vaginal radical trachelectomy: An update of a series of 125 cases and 106 pregnancies. *Gynecol. Oncol.* 2011;121:290–297.
- [176] Nishio H, Fujii T, Kameyama K, *et al.* Abdominal radical trachelectomy as a fertility-sparing procedure in women with early-stage cervical cancer in a series of 61 women. *Gynecol. Oncol.* 2009;115:51–55.
- [177] Diaz JP, Sonoda Y, Leitao MM, *et al.* Oncologic outcome of fertility-sparing radical trachelectomy versus radical hysterectomy for stage IB1 cervical carcinoma. *Gynecol. Oncol.* 2008;111:255–260.
- [178] Georg P, Pötter R, Georg D, *et al.* Dose effect relationship for late side effects of the rectum and urinary bladder in magnetic resonance image-guided adaptive cervix cancer brachytherapy. *Int. J. Radiat. Oncol. Biol. Phys.* 2012;82:653–657.
- [179] Mazon R, Petit C, Rivin E, *et al.* 45 or 50 Gy, which is the optimal radiotherapy pelvic dose in locally advanced cervical cancer in the perspective of reaching magnetic resonance image-guided adaptive brachytherapy planning aims? *Clin. Oncol.* 2016;28:171–177.
- [180] Lu C, Chelikani S, Papademetris X, *et al.* An integrated approach to segmentation and nonrigid registration for application in image-guided pelvic radiotherapy. *Med. Image Anal.* 2011;15:772–785.
- [181] Lu C, Chelikani S, Jaffray D a, *et al.* Simultaneous nonrigid registration, segmentation, and tumor detection in MRI guided cervical cancer radiation therapy. *IEEE Trans. Med. Imaging.* 2012;31:1213–1227.
- [182] Fledelius W, Worm E, Høyer M, *et al.* Real-time segmentation of multiple implanted cylindrical liver markers in kilovoltage and megavoltage x-ray images. *Phys. Med. Biol.* 2014;59:2787–2800.
- [183] de Kerf G, van Gestel D, Mommaerts L, *et al.* Evaluation of the optimal combinations of modulation factor and pitch for Helical TomoTherapy plans made with TomoEdge using Pareto optimal fronts. *Radiat. Oncol.* 2015;10:191.
- [184] Lechner W, Kragl G, Georg D. Evaluation of treatment plan quality of IMRT and VMAT with and without flattening filter using Pareto optimal fronts. *Radiother. Oncol.* 2013;109:437–441.
- [185] Wala J, Craft D, Paly J, *et al.* Maximizing dosimetric benefits of IMRT in the treatment of localized prostate cancer through multicriteria optimization planning. *Med. Dosim.* 2013;38:298–303.
- [186] Djajaputra D, Wu Q, Wu Y, *et al.* Algorithm and performance of a clinical IMRT beam-angle optimization system. *Phys. Med. Biol.* 2003;48:3191–3212.
- [187] Tang S, Deville C, Tochner Z, *et al.* Impact of intrafraction and residual interfraction effect on prostate proton pencil beam scanning. *Int. J. Radiat. Oncol. Biol. Phys.* 2014;90:1186–1194.
- [188] Zhu X, Espana S, Daartz J, *et al.* Monitoring proton radiation therapy with in-room PET imaging. *Phys. Med. Biol.* 2011;56:4041–4057.
- [189] Mori S, Zenklusen S, Knopf AC. Current status and future prospects of multi-dimensional image-guided particle therapy. *Radiol. Phys. Technol.* 2013;6:249–272.
- [190] Cheung JP, Park PC, Court LE, *et al.* A novel dose-based positioning method for CT image-guided proton therapy. *Med. Phys.* 2013;40:051714.
- [191] Mendenhall NP, Hoppe BS, Nichols RC, *et al.* Five-year outcomes from 3 prospective trials of image-guided proton therapy for prostate cancer. *Int. J. Radiat. Oncol. Biol. Phys.* 2014;88:596–602.
- [192] van Dijk IWEM, Oldenburger F, Cardous-Ubbink MC, *et al.* Evaluation of late adverse events in long-term wilms' tumor survivor. *Int. J. Radiat. Oncol. Biol. Phys.* 2010;78:370–378.
- [193] van Dijk IWEM, Cardous-Ubbink MC, van der Pal HJH, *et al.* Dose-effect relationships for adverse events after cranial radiation therapy in long-term childhood cancer survivors. *Int. J. Radiat. Oncol. Biol. Phys.* 2013;85:768–775.
- [194] Hall EJ. Intensity-modulated radiation therapy, protons, and the risk of second cancers. *Int. J. Radiat. Oncol. Biol. Phys.* 2006;65:1–7.
- [195] Mizumoto M, Tsuboi K, Igaki H, *et al.* Phase I/II trial of hyperfractionated concomitant boost proton radiotherapy for supratentorial glioblastoma multiforme. *Int. J. Radiat. Oncol. Biol. Phys.* 2010;77:98–105.
- [196] Higginson DS, Morris DE, Jones EL, *et al.* Stereotactic body radiotherapy (SBRT): Technological innovation and application in gynecologic oncology. *Gynecol. Oncol.* 2011;120:404–412.

- [197] Taylor A, Rockall AG, Powell MEB. An atlas of the pelvic lymph node regions to aid radiotherapy target volume definition. *Clin. Oncol.* 2007;19:542–550.
- [198] Groenendaal G, Borren A, Moman MR, *et al.* Pathologic validation of a model based on diffusion-weighted imaging and dynamic contrast-enhanced magnetic resonance imaging for tumor delineation in the prostate peripheral zone. *Int. J. Radiat. Oncol. Biol. Phys.* 2012;82:e537–e544.
- [199] Gladwish AP, Han K, Foltz WD. Variation in apparent diffusion coefficient measurements among women with locally advanced cervical cancer. *Radiother. Oncol.* 2015;117:532–535.
- [200] McVeigh PZ, Syed AM, Milosevic M, *et al.* Diffusion-weighted MRI in cervical cancer. *Eur. J. Radiol.* 2008;18:1058–1064.
- [201] Lund KV, Simonsen TG, Hompland T, *et al.* Short-term pretreatment DCE-MRI in prediction of outcome in locally advanced cervical cancer. *Radiother. Oncol.* 2015;115:379–385.
- [202] Kallehauge JF, Tanderup K, Duan C, *et al.* Tracer kinetic model selection for dynamic contrast-enhanced magnetic resonance imaging of locally advanced cervical cancer. *Acta Oncol.* 2014;53:1064–1072.
- [203] Fu Z-Z, Peng Y, Cao L-Y, *et al.* Value of apparent diffusion coefficient (ADC) in assessing radiotherapy and chemotherapy success in cervical cancer. *Magn. Reson. Imaging.* 2015;33:516–524.
- [204] Hameeduddin A, Sahdev A. Diffusion-weighted imaging and dynamic contrast-enhanced MRI in assessing response and recurrent disease in gynaecological malignancies. *Cancer Imaging.* 2015;15:3.
- [205] Lee YK, Bollet M, Charles-Edwards G, *et al.* Radiotherapy treatment planning of prostate cancer using magnetic resonance imaging alone. *Radiother. Oncol.* 2003;66:203–216.
- [206] Siversson C, Nordström F, Nilsson T, *et al.* MRI only prostate radiotherapy planning using the statistical decomposition algorithm. *Med. Phys.* 2015;42:6090–6097.
- [207] Mutic S, Dempsey JF. The ViewRay system: magnetic resonance-guided and controlled radiotherapy. *Semin. Radiat. Oncol.* 2014;24:196–199.
- [208] Raaymakers BW, Lagendijk JJW, Overweg J, *et al.* Integrating a 1.5 T MRI scanner with a 6 MV accelerator: proof of concept. *Phys. Med. Biol.* 2009;54:N229–N237.
- [209] Ali I, Ahmad S, Alsbou N, *et al.* Correction of image artifacts from treatment couch in cone-beam CT from kV on-board imaging. *J. Xray. Sci. Technol.* 2011;19:321–332.
- [210] Han X, Pearson E, Pelizzari C, *et al.* Algorithm-enabled exploration of image-quality potential of cone-beam CT in image-guided radiation therapy. *Phys. Med. Biol.* 2015;60:4601–4633.
- [211] Yan H, Cervino L, Jia X, *et al.* A comprehensive study on the relationship between the image quality and imaging dose in low-dose cone beam CT. *Phys. Med. Biol.* 2012;57:2063–2080.
- [212] Tian Z, Jia X, Yuan K, *et al.* Low-dose CT reconstruction via edge-preserving total variation regularization. *Phys. Med. Biol.* 2011;56:5949–5967.
- [213] Li X, Quan EM, Li Y, *et al.* A fully automated method for CT-on-rails-guided online adaptive planning for prostate cancer intensity modulated radiation therapy. *Int. J. Radiat. Oncol. Biol. Phys.* 2013;86:835–841.
- [214] Wooten HO, Green O, Yang M, *et al.* Quality of intensity modulated radiation therapy treatment plans using a <sup>60</sup>Co magnetic resonance image guidance radiation therapy system. *Int. J. Radiat. Oncol. Biol. Phys.* 2015;92:771–778.
- [215] Lagendijk JJW, Raaymakers BW, van Vulpen M. The magnetic resonance imaging-linac system. *Semin. Radiat. Oncol.* 2014;24:207–209.
- [216] Bol GH, Lagendijk JJW, Raaymakers BW. Virtual couch shift (VCS): accounting for patient translation and rotation by online IMRT re-optimization. *Phys. Med. Biol.* 2013;58:2989–3000.
- [217] Raaymakers BW, Raaijmakers AJE, Lagendijk JJW. Feasibility of MRI guided proton therapy: magnetic field dose effects. *Phys. Med. Biol.* 2008;53:5615–5622.
- [218] Crijs SPM, Raaymakers BW, Lagendijk JJW. Real-time correction of magnetic field inhomogeneity-induced image distortions for MRI-guided conventional and proton radiotherapy. *Phys. Med. Biol.* 2011;56:289–297.
- [219] Hartman J, Kontaxis C, Bol GH, *et al.* Dosimetric feasibility of intensity modulated proton therapy in a transverse magnetic field of 1.5 T. *Phys. Med. Biol.* 2015;60:5955–5969.

# Summary

Cervical cancer is the fourth most common cancer in women worldwide and the sixth most common cancer type among women in the Netherlands. Radiation therapy with concomitant chemotherapy is the primary treatment for patients with locally advanced cervical tumors and consists of external beam radiation therapy followed by brachytherapy. External beam radiation therapy is the most common form of radiation therapy in which the tumor is irradiated from outside the body, generally performed using a linear accelerator (Figure 1.3). Prior to radiation therapy, computed tomography (CT) imaging is performed with the patient in treatment position and the CT image is used for target definition and radiation therapy planning. The calculated dose distribution is delivered in multiple fractions on consecutive days to maximize the effect of radiation on tumor cells while minimizing the damage to surrounding healthy tissues. Each treatment day, the patient is positioned on the treatment table under image guidance similar to the position during pre-treatment CT imaging. However, the shape and position of the target volume can vary largely between treatment days due to anatomical changes. These day-to-day anatomical variations are mainly induced by differences in bladder volume. Despite drinking protocols and the use of generous safety margins, interfraction anatomical changes result in insufficient target volume irradiation and might limit the efficiency of radiation therapy. The introduction of pre-fraction cone-beam (CBCT) imaging enabled three-dimensional soft-tissue visualization and allowed for treatment adaptations. Adaptive radiation therapy aims to achieve adequate dose delivery in the presence of patient-specific interfraction anatomical variations by adapting the dose delivery during the course of treatment.

In the Academic Medical Center, an adaptive strategy is introduced for curative radiation therapy in cervical cancer. The implemented adaptive strategy based on daily plan selection from a pre-treatment generated library of plans is described in detail in **chapter 2**. Instead of only one CT image, prior to treatment two CT images are acquired with large bladder volume differences to determine the extreme target positions. The possible intermediate target positions are derived by interpolating between both extreme target positions and multiple plans corresponding to different target positions are generated to form the plan library. Each treatment day, the plan corresponding to the target position as observed on pre-fraction CBCT imaging is selected. Next to the detailed description of the strategy, the daily plan selection adaptive strategy is evaluated in terms of target coverage and organ at risk (OAR) sparing. Compared to conventional non-adaptive radiation therapy, daily plan selection compensated for anatomical changes and consequently improved daily target coverage significantly. Daily plan selection also significantly reduced the dose to rectum and bowel, however the clinical relevance of these reductions is expected to be limited. Therefore, the largest area of improvement on adaptive radiation therapy in cervical cancer was found to be the reduction in OAR dose while maintaining adequate target coverage.

The implemented adaptive strategy improved cervical cancer radiation therapy, but each treatment day the adaptive plan is selected manually based on pre-fraction CBCT imaging. The decision time in the treatment room can be decreased using a fast and accurate automatic plan selection strategy. The correlation between bladder volume and the position of the target volume makes automatic bladder segmentation an appropriate candidate for automatic plan selection during adaptive radiation therapy in cervical cancer. The proposed method for automatic bladder segmentation on CBCT imaging is extensively described in **chapter 3**. Using a patient-specific bladder shape model based on two bladder structures with extreme volumes, the presented method automatically produced accurate bladder segmentations in a relatively short time. Additionally, incorrect segmentation results can be adapted locally by quick manual corrections. Next to the detailed description of the segmentation method, the performance of bladder segmentation is validated by comparing the segmentation results with manual bladder delineations. The accurate agreement between manual delineations and automatic segmentations is indicated by the Dice similarity coefficient (DSC) and the surface distance error (SDE). The mean DSC (SDE) of 0.82 (0.33 cm) after fully automatic segmentation was improved to 0.87 (0.25 cm) when allowing additional manual adaptations. The mean difference in bladder volume between automatic segmentation and manual delineation was 12 ml. This difference was decreased to 4 ml when applying semi-automatic segmentations. In conclusion, the presented method is suitable for online bladder segmentation on CBCT imaging and can be used for automatic plan selection in cervical cancer adaptive radiation therapy.

Improvements in cervical cancer radiation therapy are required to further decrease radiation-associated toxicities. Therefore, the application of adaptive proton therapy is investigated in order to reduce dose to healthy surrounding tissues. Although the characteristic Bragg peak implies certain distinct advantages over conventionally used X-rays, the delivery of highly conformal dose distributions is challenging due to the sensitivity of protons to range and position uncertainties. As a consequence, proton plans are required to be robust against these possible uncertainties. Next to the inclusion of plan robustness, optimization of dose delivery in intensity-modulated proton therapy (IMPT) is required to enable a fair comparison between photon therapy and proton therapy.

In **chapter 4**, the efficiency of proton therapy in cervical cancer is improved by deriving beam configuration optimality in cervical cancer IMPT. Optimal trade-offs between conflicting objectives can be reflected by the Pareto front. Therefore, the effect of different beam configurations is investigated on plan robustness and dose-volume histogram (DVH) parameters by comparing Pareto fronts. The developed method iteratively approximated the Pareto front and resulted in three-dimensional Pareto fronts based on 200 automatically generated IMPT plans. Differences between configuration-specific Pareto fronts were quantified and the two-beam configuration was completely dominated by the three-beam configuration and the four-beam configuration. Moreover, the four-beam configuration was found to be superior for all analyzed patients in terms of robustness, target coverage and OAR sparing. Compared to the three-beam configuration, the median target coverage increased on average by 0.2 Gy when using the four-beam configuration

and the median improvements in DVH parameters for rectum and bladder were on average 3.6% and 1.3%, respectively. In conclusion, the demonstrated method relied on an objective comparison between beam configurations and resulted in the selection of the configuration using four beams in cervical cancer IMPT.

The previously selected beam configuration was used in **chapter 5** to determine the dosimetric advantages of adaptive proton therapy compared to adaptive photon therapy in cervical cancer. Based on daily plan selection, adaptive treatments for both photon therapy and proton therapy were simulated by using weekly CT images for adaptive plan selection and dose distribution recalculation. The dose to 98% of the target volume was at least 95% of the prescribed dose in 96% and 92% of the recalculated fractions for adaptive photon therapy and adaptive proton therapy, respectively. Compared to adaptive photon therapy, adaptive proton therapy maintains adequate target coverage while significant dose reductions can be achieved for bladder, small bowel and rectum. Additionally, the observed improvements in dose to rectum and small bowel indicated reductions in expected toxicity for both organs.

Adaptive radiation therapy in cervical cancer can be further improved by revising the conventional target definition strategy. According to international guidelines, the target volume in cervical cancer radiation therapy is recommended to also include the entire uterine body. By excluding the non-invaded part of the uterine body after exact tumor definition using magnetic resonance imaging (MRI), an additional reduction in radiation-associated toxicity probabilities can be achieved. However, the accuracy of tumor delineation on MRI needs to be determined to safely rely on MRI-based target volume definitions.

In **chapter 6**, the accuracy of gross tumor volume (GTV) delineation on MRI is validated using pathology data. A novel method is presented to correlate pre-operatively acquired MRI and pathology photos after macroscopic intersection in cervical cancer. The developed three-step multi-image registration strategy is based on boundary structures as well as internal structures and included corrections for possible large deformations. The application of this image registration strategy resulted in accurate correlations between MRI and pathology data. The inclusion of the deformable image registration step corrected for possible large deformations between in-vivo and ex-vivo organ shapes and resulted in a median DSC and SDE of 0.98 and 0.4 mm and 0.90 and 0.4 mm for the boundary structure and internal structures, respectively. Subsequently, the discrepancy between GTV delineations on MRI and the delineated tumor volume on pathology imaging was quantified after accurate correlations. This quantification resulted in a general underestimation of the MRI-based GTVs. Therefore, a margin around the MRI-based GTV delineation is required to safely cover the macroscopically visible tumor extension.

In **chapter 7**, the dosimetric consequences of MRI-based target volume definition are determined. For photon therapy as well as proton therapy, treatment plans were generated based on defined target volumes using the conventional strategy (i.e. including the entire uterine body) and the new strategy (i.e. including only the invaded part of the uterine body). Compared to the use of conventional target volumes, target volume definition based on MRI resulted in reductions of OAR

dose while maintaining adequate target coverage when applying photon-based radiation therapy. Target volume definition using MRI combined with the application of proton therapy resulted in even less OAR dose and decreased small bowel toxicity probability substantially for individual patients. Furthermore, the proposed 10% toxicity probability reduction threshold as acceptable indication for taking proton therapy into consideration was observed in four out of the eleven patients (36%). If the non-invaded part of the uterine body is also excluded from the target volume, a toxicity probability difference of at least 10% was found in six out of the eleven patients (55%). The toxicity probability reductions based on target volume definition using MRI are promising and the addition of proton therapy is even more promising in cervical cancer radiation therapy.

In **chapter 8**, the solutions for the optimization of adaptive radiation therapy in cervical cancer presented in this thesis are summarized. For both photon therapy and proton therapy, the daily plan selection adaptive strategy in cervical cancer radiation therapy enabled corrections for interfraction anatomical changes in order to achieve maximal tumor control. Daily plan selection can be automated using the presented bladder segmentation method on CBCT imaging. Compared to adaptive photon therapy, high-precision dose delivery based on adaptive proton therapy resulted in substantial improvements in dose to healthy tissues. Moreover, improvements in target volume definition using advanced pre-treatment imaging combined with proton therapy showed large potential advantages in treatment outcome in terms of radiation-induced toxicity. Furthermore, future directions in cervical cancer radiation therapy are described including the application of MRI-guided radiation therapy and the clinical introduction of proton therapy in the Netherlands. Also, alternative treatment options in cervical cancer are addressed. In future, cervical cancer patients might benefit from a combined treatment consisting of adaptive radiation therapy with concurrent chemotherapy, hyperthermia and possibly immunotherapy.

# Nederlandse samenvatting

Baarmoederhalskanker is de vierde meest voorkomende vorm van kanker bij vrouwen wereldwijd en onder vrouwen in Nederland is baarmoederhalskanker de zesde meest voorkomende vorm van kanker. De primaire behandeling voor patiënten met een grote maar niet uitgezaaide tumor in de baarmoederhals bestaat uit radiotherapie in combinatie met chemotherapie.

Radiotherapie bij patiënten met baarmoederhalskanker bestaat uit uitwendige radiotherapie gevolgd door inwendige radiotherapie oftewel brachytherapie. Tijdens een behandeling met radiotherapie wordt gebruik gemaakt van ioniserende straling. Deze straling zorgt voor schade aan het weefsel, maar maakt geen onderscheid tussen tumorcellen en gezonde cellen, waardoor ook deze worden beschadigd. In tegenstelling tot tumorcellen zijn gezonde cellen in staat om deze schade te herstellen op basis van goed functionerende herstelmechanismen. Uitwendige radiotherapie is de meest voorkomende vorm van radiotherapie waarbij de tumor wordt bestraald van buiten het lichaam. Deze vorm van bestraling wordt meestal toegepast met behulp van een lineaire versneller (Figuur 1.3) waarbij de patiënt op de behandeltafel ligt en de versneller om de patiënt kan draaien.

Voorafgaand aan radiotherapie wordt een CT (*computed tomography*) scan van de patiënt in behandelpositie gemaakt. Deze CT scan wordt vervolgens gebruikt voor het definiëren van het doelgebied, het definiëren van omliggende stralingsgevoelige organen en het berekenen van een bestralingsplan. Op basis van de anatomie zichtbaar op de CT scan wordt bepaald vanuit welke richtingen de bestralingsbundels op de tumor gericht worden. Tevens wordt de stralingsintensiteit per gekozen bundel geoptimaliseerd met als doel een zo hoog mogelijke stralingsdosis aan de tumor te geven terwijl de dosis in het gezond omliggend weefsel geminimaliseerd wordt. De berekende dosisverdeling wordt vervolgens opgesplitst in een aantal bestralingsfracties en patiënten worden gedurende enkele opeenvolgende weken dagelijks bestraald. Een gefractioneerde behandeling is erop gericht om het effect van straling op tumor cellen te maximaliseren terwijl gezonde cellen in staat zijn zich te herstellen tussen bestralings-fracties.

Voorafgaand aan iedere bestralingsfractie wordt de patiënt gepositioneerd op de behandeltafel zoals tijdens de eerder gemaakte CT scan. Lineaire versnellers zijn tegenwoordig uitgerust met een CBCT (*cone-beam CT*) systeem waarmee de positie van de patiënt geverifieerd kan worden vlak voor de feitelijke bestraling. Deze CBCT scan wordt vergeleken met de eerder gemaakte CT scan door middel van beeldregistratie en op basis van deze vergelijking kan de positie van de patiënt voorafgaand aan een bestralingsfractie nog worden bijgesteld. Echter, de vorm en positie van het doelgebied kan flink variëren van behandeldag tot behandeldag, voornamelijk door een verschil in blaasvolume. Ondanks drinkinstructies en het gebruik van veiligheidsmarges rondom het doelgebied resulteren deze anatomische veranderingen in een soms onvolledige bestraling van het doelgebied waardoor de effectiviteit van radiotherapie afneemt. De introductie van een CBCT scan maakt het echter mogelijk om de anatomie van de patiënt te visualiseren voorafgaand aan iedere

bestralingsfractie. Op basis van deze CBCT scan kan vervolgens de bestraling worden aangepast aan de dagelijkse anatomische situatie. Dit wordt adaptieve radiotherapie genoemd.

In het Academisch Medisch Centrum is recent een strategie geïntroduceerd om adaptieve radiotherapie toe te passen bij patiënten met baarmoederhalskanker. Deze adaptieve methode is gebaseerd op het dagelijks selecteren van een geschikt bestralingsplan uit een vooraf gecreëerde set van bestralingsplannen. In **hoofdstuk 2** wordt deze adaptieve methode beschreven. Voorafgaand aan de behandeling worden twee CT scans gemaakt met verschillende blaasvullingen, één met een volle blaas en één met een lege blaas, om de uiterste posities van het doelgebied in kaart te brengen. Mogelijke tussenliggende posities van het doelgebied worden bepaald door middel van interpolatie en vervolgens wordt voor iedere positie van het doelgebied een bestralingsplan gemaakt. Voorafgaand aan iedere bestralingsfractie wordt het plan gekozen dat correspondeert met de positie van het doelgebied zoals zichtbaar op de CBCT scan. De geïntroduceerde adaptieve methode is geëvalueerd waarbij de resultaten vergeleken zijn met conventionele niet-adaptieve radiotherapie. Het dagelijks selecteren van een geschikt bestralingsplan resulteert in het significant beter bestralen van het doelgebied. Daarnaast resulteert het anticiperen op anatomische veranderingen in een dosisreductie voor de endeldarm en de dunne darm. Adaptieve radiotherapie voor patiënten met baarmoederhalskanker kan verder verbeterd worden door de dosis richting gezond weefsel te reduceren en daarmee de kans op complicaties te verkleinen.

De geïntroduceerde adaptieve strategie kan gebruikt worden om te corrigeren voor anatomische veranderingen door het dagelijks selecteren van een geschikt plan. Iedere dag wordt handmatig een geschikt bestralingsplan gekozen op basis van een CBCT scan. Deze tijdrovende handeling met de patiënt inmiddels op de behandeltafel kan versneld gebeuren wanneer het geschikte bestralingsplan snel, nauwkeurig en automatisch gekozen wordt. De sterke correlatie tussen het blaasvolume en de positie van het doelgebied maakt het automatisch segmenteren van de blaas een geschikte manier om het juiste bestralingsplan automatisch te selecteren. **Hoofdstuk 3** beschrijft een methode om automatisch de blaas te segmenteren op een CBCT scan. Op basis van de volle en de lege blaasstructuur wordt een patiënt-specifiek model gemaakt dat de vorm van de blaas beschrijft. Dit model wordt vervolgens gebruikt om de blaas in een korte tijd automatisch en nauwkeurig te segmenteren op een CBCT scan. Daarnaast bestaat de mogelijkheid om handmatig eventuele onjuiste segmentaties aan te passen.

Deze blaas segmentatie methode is gevalideerd door de resultaten te vergelijken met blaas structuren handmatig ingetekend door een ervaren waarnemer. De overeenkomst tussen beide structuren is gekwantificeerd door middel van de DSC (*Dice similarity coefficient*) en de SDE (*surface distance error*). Een gemiddelde DSC van 0,82 (0,0: geen overeenkomst; 1,0: identiek) na een volledig automatische segmentatie is toegenomen tot 0,87 na het toestaan van enkele manuele correcties. Een gemiddelde SDE van 0,33 cm na automatische segmentatie is gereduceerd tot 0,25 cm na enkele manuele aanpassingen. Daarnaast resulteerde automatische segmentatie in een gemiddeld verschil in blaasvolume van 12 ml in vergelijking met het volume van de ingetekende blaas structuren. Dit verschil werd gereduceerd tot 4 ml na enkele manuele correcties. Deze

methode is daarmee geschikt voor een nauwkeurige segmentatie van de blaas op een CBCT scan en kan gebruikt worden voor het automatisch selecteren van het juiste bestralingsplan tijdens adaptieve radiotherapie voor patiënten met baarmoederhalskanker.

Door de methode van adaptieve radiotherapie voor patiënten met baarmoederhals-kanker te optimaliseren kunnen complicaties als gevolg van de bestraling verminderd worden. Eén mogelijkheid om de afgegeven dosis aan gezond weefsel te reduceren is door gebruik te maken van protonentherapie. In vergelijking met conventionele fotonentherapie heeft het gebruik van protonentherapie een aantal duidelijke voordelen, maar een behandeling met protonen is tevens uitdagend doordat protonen heel gevoelig zijn voor anatomische veranderingen. Een kleine verandering in anatomie of een minimale verschuiving van de patiënt kan tijdens protontherapie al leiden tot inadequate radiotherapie. Om dit te ondervangen dienen bestralingsplannen voor protonentherapie robuust te zijn ten aanzien van eventuele onzekerheden, waardoor bij een kleine verandering de gewenste dosisafgifte gewaarborgd blijft. Een eerlijke vergelijking tussen fotonentherapie en protonentherapie vereist optimale bestralings-plannen voor beide modaliteiten.

Om de effectiviteit van protonentherapie te verbeteren wordt in **hoofdstuk 4** een methode beschreven waarmee de optimale bundelconfiguratie wordt bepaald voor protonentherapie bij patiënten met baarmoederhalskanker. De bundelconfiguratie omvat het aantal bestralingsbundels en de bijbehorende invalshoek en is in protonentherapie sterk afhankelijk van de locatie van de tumor. In dit hoofdstuk wordt allereerst een methode geïntroduceerd om voor een gegeven bundelconfiguratie automatisch 200 bestralingsplannen te genereren. Uit deze 200 plannen wordt vervolgens de set van optimale bestralingsplannen gedestilleerd op basis van zowel de robuustheid van deze bestralingsplannen als de belangrijkste dosisparameters. De set van optimale bestralingsplannen op basis van deze conflicterende dosis parameters wordt het Pareto front genoemd. Voor drie verschillende bundelconfiguraties wordt het Pareto front bepaald, namelijk voor configuraties bestaande uit twee bundels, drie bundels en vier bundels. De gegenereerde Pareto fronten worden vervolgens vergeleken om een geschikte bundelconfiguratie te selecteren. Deze methode resulteert in een objectieve vergelijking tussen de verschillende bundelconfiguraties en leidde vervolgens tot het selecteren van de optimale configuratie bestaande uit vier bundels voor protonentherapie bij patiënten met baarmoederhalskanker.

**Hoofdstuk 5** beschrijft de dosimetrische voordelen van protonentherapie ten opzichte van fotonentherapie. Op basis van de eerder beschreven adaptieve strategie waarbij dagelijks het geschikte plan wordt gekozen zijn behandelingen gesimuleerd voor zowel fotonentherapie als protonentherapie. Voor protonentherapie is hierbij gebruik gemaakt van de geselecteerde bundelconfiguratie uit het vorige hoofdstuk. Met behulp van wekelijks verkregen CT scans is de afgegeven dosis berekend voor beide bestralings-modaliteiten. Deze wekelijkse CT scans bevatten anatomische variatie waardoor de gesimuleerde behandelingen een goede benadering van de werkelijkheid is. De adaptieve strategie leidde voor beide modaliteiten tot het adequate bestralen van het doelgebied. Het toepassen van adaptieve protonentherapie kan bovendien leiden tot een significante vermindering van de dosis richting gezond weefsel, te weten de blaas, de dunne darm

en de endeldarm. Deze dosisreductie wijst tevens op een sterke vermindering van de mogelijke complicaties voor endeldarm en dunne darm na adaptieve protonentherapie voor patiënten met baarmoederhalskanker.

Radiotherapie voor patiënten met baarmoederhalskanker kan mogelijk verder verbeterd worden door de conventionele manier van definiëren van het doelgebied te herzien. Internationale richtlijnen adviseren om naast de baarmoederhals ook de gehele baarmoeder als doelgebied te beschouwen, waardoor een groot doelvolumen ontstaat. Mogelijkerwijs kunnen complicaties als gevolg van bestraling verminderd worden door op basis van MRI (*magnetic resonance imaging*) het deel van de baarmoeder zonder ingroei van tumor niet als doelgebied te beschouwen. Om te onderzoeken of dit op een veilige manier te doen is doordat we kunnen vertrouwen op de tumordefinitie gebaseerd op MRI, is de nauwkeurigheid van tumordefinitie op basis van MRI bepaald.

In **hoofdstuk 6** wordt de nauwkeurigheid van tumordefinitie op basis van MRI gevalideerd met behulp van foto's van de baarmoeder nadat deze chirurgisch verwijderd is. Hiervoor is een methode geïntroduceerd om de baarmoeder afgebeeld op MRI voorafgaand aan een chirurgische ingreep te correleren aan een afbeelding van de operatief verwijderde baarmoeder. Deze methode bestaat uit drie achtereenvolgende stappen om beide afbeeldingen nauwkeurig te vergelijken en bevat bovendien een manier om te corrigeren voor mogelijke grote vervormingen van het orgaan. Het toepassen van deze methode resulteerde in een goede correlatie tussen de baarmoeder afgebeeld op MRI en foto's nadat deze chirurgisch verwijderd is. Deze correlatie resulteerde voor de volledige baarmoederstructuur in een mediaan voor de DSC en de SDE van 0,98 en 0,4 mm, respectievelijk. Voor de interne structuren van de baarmoeder werd een mediaan voor de DSC en de SDE gevonden van 0,90 en 0,4 mm, respectievelijk. Gebaseerd op deze goede correlatie is het tumorvolume gedefinieerd op basis van MRI vergeleken met het tumorvolume zichtbaar op de afbeelding van het chirurgische preparaat. Uit deze vergelijking bleek een algemene onderschatting van het op MRI gebaseerde tumorvolume. Hierdoor is een veiligheidsmarge rondom het MRI-gebaseerde tumor volume noodzakelijk om op een veilige manier het doelgebied te reduceren voor patiënten met baarmoederhalskanker.

De consequenties van MRI-gebaseerde tumor volumes met betrekking tot de afgegeven dosis worden in **hoofdstuk 7** bepaald. Voor zowel fotonentherapie als protonentherapie zijn bestralingsplannen gemaakt op basis van doelgebieden gedefinieerd op twee verschillende manieren. Naast het conventionele doelgebied waarbij de gehele baarmoeder is geïnccludeerd wordt ook het verkleinde doelgebied gebruikt dat op basis van MRI gedefinieerd is en waarbij het deel van de baarmoeder zonder ingroei van tumor buiten beschouwing gelaten wordt. Vergeleken met het gebruik van conventionele doelgebieden resulteert het gebruik van verkleinde doelgebieden in een dosisreductie voor gezond weefsel bij fotonentherapie. De combinatie van een gereduceerd doelgebied en protonentherapie resulteerde in nog minder dosis voor gezond weefsel. Tevens wordt de kans op dunne darmcomplicaties verkleind voor individuele patiënten.

Om in aanmerking te komen voor protonentherapie is in Nederland een richtlijn voorgesteld waarbij een minimale afname van 10% in complicatiekans als drempel genomen wordt. Op basis van deze richtlijn zouden vier van de elf patiënten in deze studie in aanmerking komen voor protonentherapie wanneer gebruik gemaakt wordt van conventionele doelgebieden. Wanneer het gezonde deel van de baarmoeder niet als doelgebied beschouwd wordt zouden zelfs zes van de elf patiënten in aanmerking komen voor protonentherapie. De reductie in de complicatiekans wanneer het doelgebied gedefinieerd wordt op basis van MRI is veelbelovend en de toevoeging van protonentherapie versterkt deze verwachtingen.

In **hoofdstuk 8** worden de gepresenteerde oplossingen voor het optimaliseren van adaptieve radiotherapie bediscussieerd. De klinische introductie van adaptieve radiotherapie voor patiënten met baarmoederhalskanker zorgt voor een verbetering in het bestralen van de tumor. Daarnaast kan het adaptieve plan automatisch geselecteerd worden op basis van een automatische segmentatie van de blaas. Adaptieve radiotherapie voor patiënten met baarmoederhalskanker kan verder verbeterd worden door een mogelijke klinische introductie van adaptieve protonentherapie in de nabije toekomst. Naast het gericht bestralen van de tumor kan door het toepassen van protonentherapie de afgegeven dosis aan omliggende stralingsgevoelige organen sterk verminderd worden. Verder kan de definitie van het doelgebied verbeterd worden wanneer gebruik gemaakt wordt van betere beeldvormingstechnieken zoals MRI. Op basis van MRI kan het doelgebied uiterst nauwkeurig bepaald worden met een afname van het doelgebied tot gevolg waardoor mogelijke complicaties na radiotherapie verder zullen afnemen.

De gepresenteerde oplossingen zijn in perspectief geplaatst door ze te vergelijken met andere manieren om radiotherapie voor baarmoederhalskanker te verbeteren. Daarnaast worden mogelijke oplossingen uit de nabije toekomst besproken waarbij de introductie van MRI-gestuurde radiotherapie en de klinische introductie van protonentherapie in Nederland beschouwd worden als twee belangrijke pijlers. Ook worden alternatieve behandelmogelijkheden besproken waar patiënten met baarmoederhalskanker in de toekomst een mogelijk voordeel van hebben. Een gecombineerde behandeling bestaande uit adaptieve radiotherapie met gelijktijdige chemotherapie, hyperthermie en mogelijk ook immuuntherapie leidt in de toekomst mogelijk tot een verdere verbetering van de behandeling van baarmoederhalskanker.



# Addendum

List of abbreviations

List of publications

PhD portfolio

Curriculum vitae

Infographic

Dankwoord



# List of abbreviations

2D	Two Dimensional
3D	Three Dimensional
ART	Adaptive Radiation Therapy
CBCT	Cone Beam Computed Tomography
CI	Conformity Index
CPU	Central Processing Unit
CT	Computed Tomography
CTV	Clinical Target Volume
$D_{98\%}$	Dose received by at least 98% of the volume
DCE	Dynamic Contrast Enhanced
DNA	Deoxyribonucleic Acid
DSC	Dice Similarity Coefficient
DVH	Dose Volume Histogram
DWI	Diffusion Weighted Imaging
EBRT	External Beam Radiation Therapy
EPID	Electronic Portal Imaging Devices
FDG	Fludeoxyglucose
FIGO	International Federation of Gynecology and Obstetrics
GB	Giga Byte
GHz	Giga Hertz
GPU	Graphics Processing Unit
GTV	Gross Tumor Volume
Gy	Gray
HDR	High-Dose Rate
HPV	Human Papilloma Virus
HU	Hounsfield Unit
ICRU	International Commission on Radiation Units & Measurements
IGAPT	Image Guided Adaptive Proton Therapy
IGART	Image Guided Adaptive Radiation Therapy
IGRT	Image Guided Radiation Therapy
IMPT	Intensity Modulated Proton Therapy
IMRT	Intensity Modulated Radiation Therapy
IQR	Inter Quartile Range
ITV	Internal Target Volume
kV	Kilo Volt
LDR	Low-Dose Rate

List of abbreviations

MLC	Multi Leaf Collimator
MRI	Magnetic Resonance Imaging
MU	Monitor Unit
MV	Mega Volt
NTCP	Normal Tissue Complication Probability
OAR	Organ At Risk
PCA	Principal Component Analysis
pCTV	primary Clinical Target Volume
PDR	Pulsed-Dose Rate
pITV	primary Internal Target Volume
PT	Proton Therapy
PTV	Planning Target Volume
RAM	Random Access Memory
RT	Radiation Therapy
RTOG	Radiation Therapy Oncology Group
RTT	Radiation Therapy Technologist
SD	Standard Deviation
SDE	Surface Distance Error
TC	Target Coverage
$V_{95\%}$	Volume receiving at least 95% of the prescribed dose
VMAT	Volumetric Modulated Arc Therapy

# List of publications

## Published scientific articles

### **Generic method for automatic bladder segmentation on cone beam CT using a patient-specific bladder shape model**

A.J.A.J. van de Schoot, G. Schooneveldt, S. Wognum, M.S. Hoogeman, X. Chai, L.J.A. Stalpers, C.R.N. Rasch and A. Bel

*Medical Physics* 2014; 41(3): 031707.

### **Quantification of delineation errors of the gross tumor volume on magnetic resonance imaging in uterine cervical cancer using pathology data and deformation correction**

A.J.A.J. van de Schoot, P. de Boer, M.R. Buist, J. Stoker, M.C.G. Bleeker, L.J.A. Stalpers, C.R.N. Rasch and A. Bel

*Acta Oncologica* 2015; 54(2): 224–231.

### **Beam configuration selection for robust intensity-modulated proton therapy in cervical cancer using Pareto front comparison**

A.J.A.J. van de Schoot, J. Visser, Z. van Kesteren, T.M. Janssen, C.R.N. Rasch and A. Bel

*Physics in Medicine and Biology* 2016; 61(4): 1780–1794.

### **Dosimetric advantages of proton therapy compared with photon therapy using an adaptive strategy in cervical cancer**

A.J.A.J. van de Schoot, P. de Boer, K.F. Crama, J. Visser, L.J.A. Stalpers, C.R.N. Rasch and A. Bel

*Acta Oncologica* 2016; doi:10.3109/0284186X.2016.1139179.

### **Craniocaudal tumour extension in uterine cervical cancer on MRI compared to histopathology**

P. de Boer, M.C.G. Bleeker, A.M. Spijkerboer, A.J.A.J. van de Schoot, S. Bipat, M.R. Buist, C.R.N. Rasch, J. Stoker and L.J.A. Stalpers

*European Journal of Radiology Open* 2015; 2: 111–117.

## Submitted scientific articles

### **Dosimetric advantages of a clinical daily adaptive plan selection strategy compared with a non-adaptive strategy in cervical cancer radiation therapy**

A.J.A.J. van de Schoot, P. de Boer, J. Visser, L.J.A. Stalpers, C.R.N. Rasch and A. Bel

*Acta Oncologica* 2016; submitted.

**Dose coverage calculation using a statistical shape model – applied to cervical cancer radiotherapy**

D. Tilly, A.J.A.J. van de Schoot, E. Grusell, A. Bel and A. Ahnesjö  
*Physics in Medicine and Biology* 2016; submitted.

**Should excluding uninvaded uterine tissue be combined with proton therapy for cervical cancer?**

P. de Boer, A.J.A.J. van de Schoot, G.H. Westerveld, M. Smit, M.R. Buist, A. Bel, C.R.N. Rasch and L.J.A. Stalpers  
*International Journal of Radiation Oncology Biology Physics* 2016; submitted.

**Proceedings and abstracts**

**Automatic bladder segmentation on CBCT for plan selection during cervical ART – [oral]**

A.J.A.J. van de Schoot, G. Schooneveldt, S. Wognum, M.S. Hoogeman, X. Chai, L.J.A. Stalpers, C.R.N. Rasch and A. Bel  
*AAPM 55<sup>th</sup> annual meeting, August 4 – 8, 2013, Indianapolis, Indiana, United States of America*

**Correlation between ex vivo surgical specimen and pre-operative MR imaging for cervical cancer patients – [oral]**

A.J.A.J. van de Schoot, P. de Boer, L.J.A. Stalpers, C.R.N. Rasch and A. Bel  
*ESTRO 33, April 4 – 8, 2014, Vienna, Austria*

**Beam set-up selection using Pareto fronts for robust proton therapy planning in cervical cancer – [poster]**

A.J.A.J. van de Schoot, J. Visser, Z. van Kesteren, T.M. Janssen, C.R.N. Rasch and A. Bel  
*3<sup>rd</sup> ESTRO FORUM, April 24 – 28, 2015, Barcelona, Spain*

**Dosimetric benefit of adaptive proton therapy compared to adaptive photon therapy in cervical cancer – [oral]**

A.J.A.J. van de Schoot, P. de Boer, K.F. Crama, J. Visser, L.J.A. Stalpers, C.R.N. Rasch and A. Bel  
*ESTRO 35, April 29 – May 3, 2016, Turin, Italy*

**Measuring uterine cervical cancer on MRI correlated to pathological assessment; the PREPAC-study – [poster]**

P. de Boer, A.J.A.J. van de Schoot, S. Bipat, M.R. Buist, M.C.G. Bleeker, J. Stoker, L.J.A. Stalpers and C.R.N. Rasch  
*ESTRO 33, April 4 – 8, 2014, Vienna, Austria*

**Robust photon versus robust proton therapy planning with a library of plans for cervical cancer – [oral]**

K.F. Crama, A.J.A.J. van de Schoot, J. Visser and A. Bel

*ESTRO 35, April 29 – May 3, 2016, Turin, Italy*

**Dose coverage calculation based on a statistical shape model for cervical cancer radiation therapy – [oral]**

D. Tilly, A.J.A.J. van de Schoot, A. Bel and A. Ahnesjö

*ICCR 2016, June 27 – 30, 2016, London, United Kingdom*



# PhD portfolio

Name PhD student: Agustinus Jacobus Antonius Joannes van de Schoot  
AMC department: Radiation Oncology  
Research school: AMC Graduate School for Medical Sciences  
PhD period: January 2012 – July 2016  
Promotor: Prof. dr. C.R.N. Rasch  
Copromotores: Dr. A. Bel  
Prof. dr. L.J.A. Stalpers

1 ECTS = 28 hours

<b>PhD training</b>	<b>Year</b>	<b>Workload (ECTS)</b>
<b>General courses</b>		
<i>AMC Graduate School for Medical Sciences</i>		
Oral presentation in English	2012	0.8
Reference manager course	2012	0.3
Scientific writing for publication in English	2012	1.5
Practical Biostatistics	2013	1.1
Statistical Computing in R	2013	0.4
UNIX course	2014	0.3
Educational Skills Training	2014	0.3
<b>Specific courses</b>		
Introduction to treatment planning in Oncentra (Veenendaal, the Netherlands)	2012	0.4
<i>ESTRO school</i>		
Physics for clinical radiotherapy (Ghent, Belgium)	2012	1.5
Current advancements in treatment planning and optimization (Vienna, Austria)	2014	0.4
Basic treatment planning (Budapest, Hungary)	2014	1.5
4D Treatment planning and delivery (Barcelona, Spain)	2015	0.4

**Seminars, workshops and master classes***Weekly department seminars*

Multidisciplinary meeting, department of Radiation Oncology, AMC	2012 – 2016
Physics meeting, department of Radiation Oncology, AMC	2012 – 2016
Research meeting, department of Radiation Oncology, AMC	2012 – 2016

*Other seminars*

Amsterdam regional radiotherapy lectures (AMC, VUmc, NKI-AvL)	2012 – 2016
Spinoza lectures, AMC	2012 – 2016
Ruysch lectures, AMC	2012 – 2016

**International conferences**

AAPM 55 <sup>th</sup> annual meeting & exhibition, Indianapolis, Indiana, USA	2013
ESTRO 33, Vienna, Austria	2014
3 <sup>rd</sup> ESTRO FORUM, Barcelona, Spain	2015
ESTRO 35, Turin, Italy	2016

**Symposia & meetings***Oncology Graduate School Amsterdam (OOA)*

Annual graduate student retreat, Ermelo, the Netherlands	2012
Annual graduate student retreat, Renesse, the Netherlands	2013
Annual graduate student retreat, Renesse, the Netherlands	2014

*Scientific meetings on radiation therapy physics*

Research day, VUmc, Amsterdam, the Netherlands	2012
Research day, AMC, Amsterdam, the Netherlands	2012
Research day, EUMC, Rotterdam, the Netherlands	2013
Research day, UMCU, Utrecht, the Netherlands	2013
Research day, UMCU, Utrecht, the Netherlands	2014
Research day, AMC, Amsterdam, the Netherlands	2014
Research day, UMCU, Utrecht, the Netherlands	2015

Nucletron User Meeting, the Hague, the Netherlands	2012
Annual meeting of the Center of Gynecological Oncology Amsterdam, Amsterdam, the Netherlands	2014

**Presentations**

<i>Methodology to correlate pathology and MR imaging data for cervical cancer patients using non-rigid registration</i> – poster presentation at OOA retreat 2012, Ermelo, the Netherlands	2012	0.5
<i>Automatic delineation of bladder contours on CBCT</i> – oral presentation at physics meeting, department of Radiation Oncology, AMC, the Netherlands	2013	
<i>Generic method for automatic bladder segmentation on CBCT using a patient-specific bladder shape model</i> – oral presentation at physics meeting, department of Radiation Oncology, AMC, the Netherlands	2013	
<i>Automatic bladder segmentation on CBCT for plan selection during cervical ART</i> – oral presentation at AAPM 55 <sup>th</sup> annual meeting, Indianapolis, Indiana, USA	2013	0.5
<i>Automatic bladder segmentation on CBCT for plan selection during cervical ART</i> – oral presentation at OOA retreat 2013, Renesse, the Netherlands	2013	0.5
<i>Generic method for automatic bladder segmentation on CBCT using a patient-specific bladder shape model</i> – oral presentation at multidisciplinary meeting, department of Radiation Oncology, AMC, the Netherlands	2013	
<i>Correlation between ex vivo surgical specimen and pre-operative MR imaging for cervical cancer patients</i> – oral presentation at ESTRO 33, Vienna, Austria	2014	0.5
<i>Image guided radiotherapy of cervical cancer</i> – oral presentation at the annual meeting of the Center of Gynecological Oncology Amsterdam, NKI-AvL, Amsterdam, the Netherlands	2014	0.5
<i>Validation of tumor delineations on MRI for cervical cancer radiotherapy</i> – oral presentation at OOA retreat 2014, Renesse, the Netherlands	2014	0.5
<i>Beam configuration selection for robust intensity-modulated proton therapy in cervical cancer using Pareto front comparison</i> – oral presentation at physics meeting, department of Radiation Oncology, AMC, the Netherlands	2015	
<i>Beam set-up selection using Pareto fronts for robust proton therapy planning in cervical cancer</i> – poster discussion at 3 <sup>rd</sup> ESTRO FORUM, Barcelona, Spain	2015	0.5

<i>Beam configuration selection for robust intensity-modulated proton therapy in cervical cancer using Pareto front comparison</i> – oral presentation at the research day on radiation therapy physics, UMCU, Utrecht, the Netherlands	2015	0.5
<i>Dosimetric advantages of proton therapy compared with photon therapy using an adaptive strategy in cervical cancer</i> – oral presentation at multidisciplinary meeting, department of Radiation Oncology, AMC, the Netherlands	2015	
<i>Dosimetric benefit of adaptive proton therapy compared to adaptive photon therapy in cervical cancer</i> –oral presentation at ESTRO 35, Turin, Italy	2016	0.5

## Teaching

### Supervising

K.F. Crama – Master student Radiation Oncology at the Inholland University of Applied Sciences, Haarlem, the Netherlands	2014 – 2015	4
C. Bloklander – Bachelor student <i>Medische Beeldvorming en Radiotherapeutische Technieken</i> at Inholland Hogeschool, Haarlem, the Netherlands	2015	3
R. van Veen – Master student Technical Medicine at the University of Twente, Enschede, the Netherlands	2015	3

# Curriculum vitae

## EN

Agustinus (Stijn) Jacobus Antonius Joannes van de Schoot was born on November 22, 1985, in Boxtel (the Netherlands) and he was raised in Oirschot. He graduated from pre-university secondary education at the Jacob-Roelandslyceum in Boxtel in 2005. In the same year, he started the bachelor program Biomedical Engineering at the Eindhoven University of Technology. In 2008, Stijn started the master program Medical Engineering at the Eindhoven University of Technology in close collaboration with Maastricht University and Maastricht University Medical Center. As part of his master education, he carried out a research internship at the department of Physical Sciences at the Peter MacCallum Cancer Center in Melbourne, Australia. Stijn obtained his MSc degree in 2011 after his one-year graduation research project at the department of Radiation Oncology of the University Medical Center Utrecht. In 2012, he started his PhD research at the department of Radiation Oncology of the Academic Medical Center, University of Amsterdam on adaptive radiation therapy in cervical cancer. The conducted research resulted in this dissertation entitled *Optimization of adaptive radiation therapy in cervical cancer – solutions for photon and proton therapy*. Since May 2016 Stijn is working on a Postdoc project at the department of Radiation Oncology of the Netherlands Cancer Institute – Antoni van Leeuwenhoek Hospital in Amsterdam.

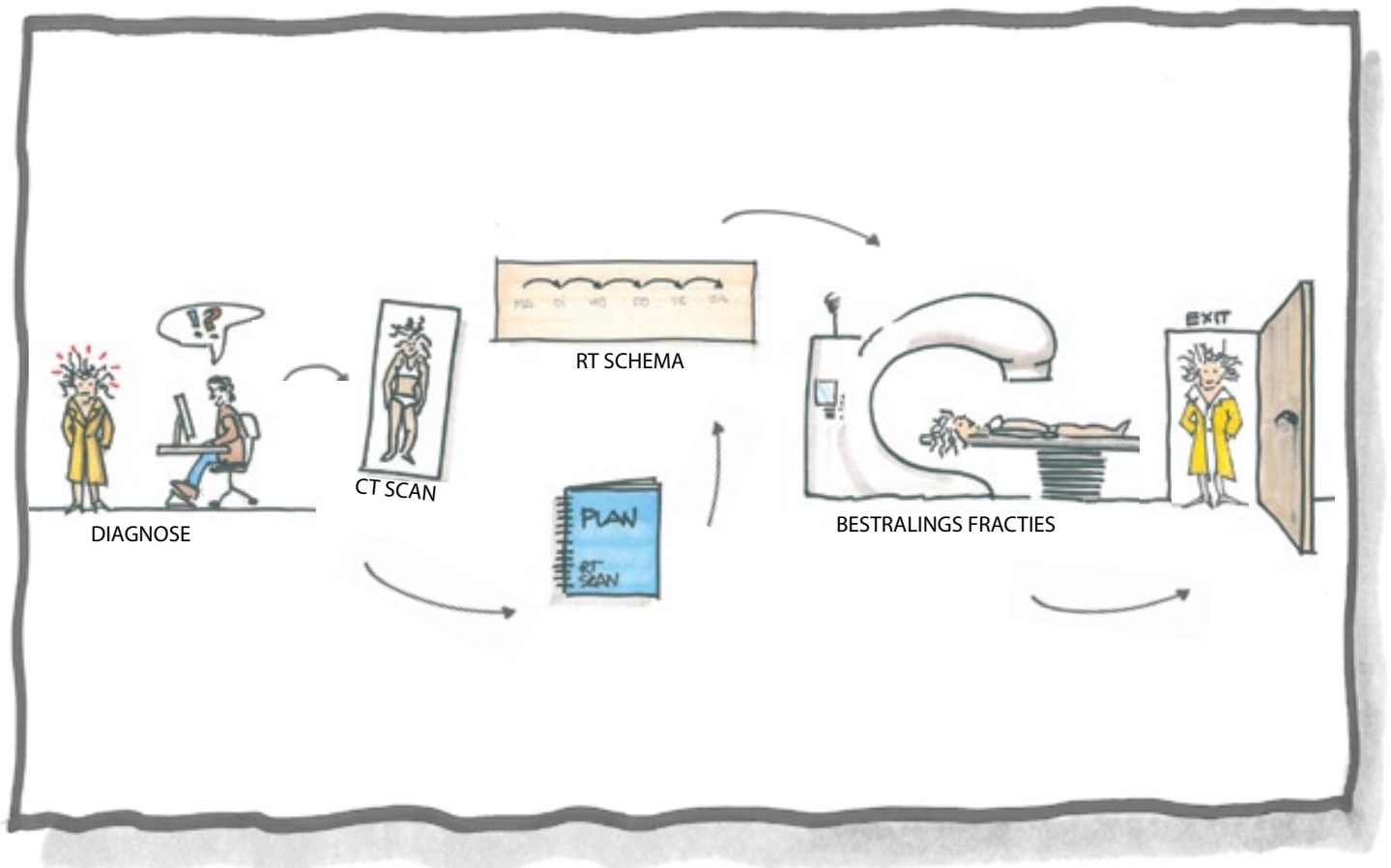
## NL

Agustinus (Stijn) Jacobus Antonius Joannes van de Schoot werd geboren op 22 november 1985 te Boxtel (Nederland) en groeide op in Oirschot. Hij behaalde zijn vwo-diploma in 2005 aan het Jacob-Roelandslyceum te Boxtel. In hetzelfde jaar startte hij met de bacheloropleiding Biomedische Technologie aan de Technische Universiteit Eindhoven. In 2008 begon Stijn met de masteropleiding Medische Technologie aan de Technische Universiteit Eindhoven in samenwerking met de Universiteit van Maastricht en het Maastricht Universitair Medisch Centrum. Als onderdeel van zijn masteropleiding verrichtte hij een onderzoeksstage op de afdeling Physical Sciences van het Peter MacCallum Cancer Center te Melbourne, Australië. Stijn behaalde zijn masterdiploma in 2011 na het afronden van zijn eenjarig afstudeeronderzoek op de afdeling Radiotherapie van het Universitair Medisch Centrum Utrecht. In 2012 begon hij aan zijn promotieonderzoek op de afdeling Radiotherapie van het Academisch Medisch Centrum, Universiteit van Amsterdam betreffende adaptieve radiotherapie bij baarmoederhals tumoren. Het verrichtte onderzoek resulteerde in dit proefschrift getiteld *Optimization of adaptive radiation therapy in cervical cancer – solutions for photon and proton therapy*. Vanaf mei 2016 is Stijn als Postdoc werkzaam op de afdeling Radiotherapie van het Nederlands Kanker Instituut – Antoni van Leeuwenhoek ziekenhuis te Amsterdam.

# H1

## Radiotherapie bij baarmoederhalskanker

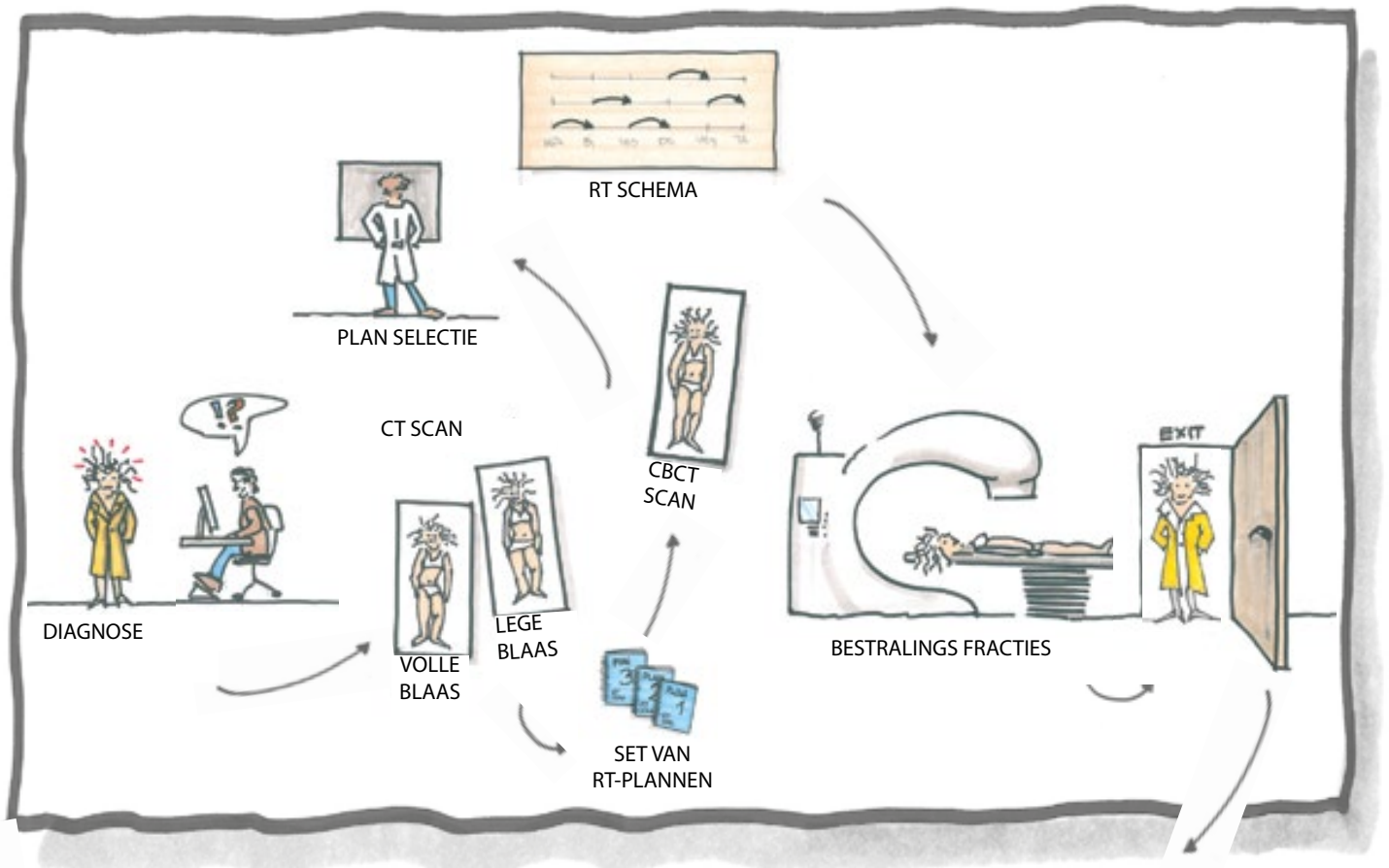
NIET ADAPTIEVE SITUATIE



# H2

## Adaptieve radiotherapie

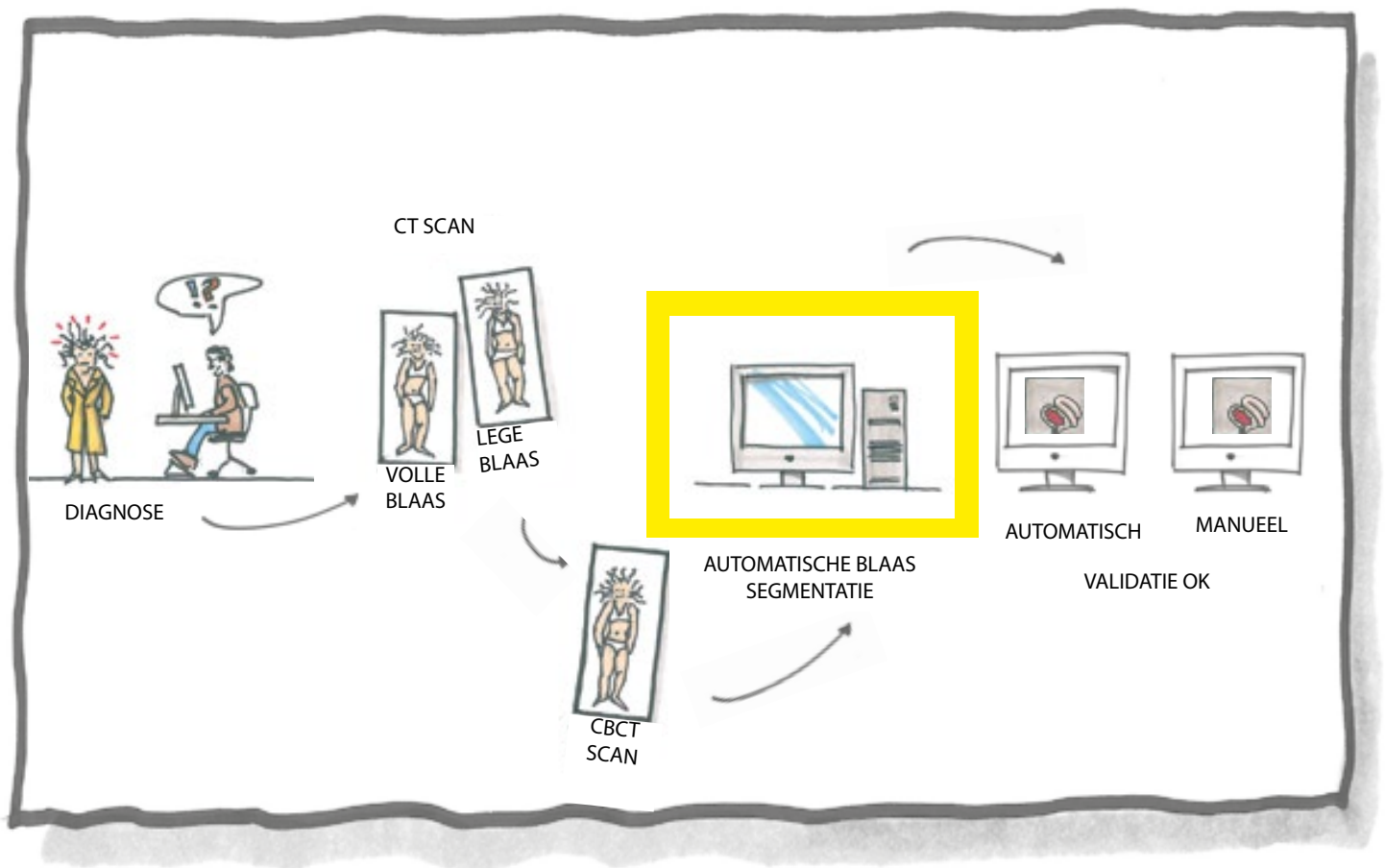
### DOSIMETRISCHE VERGELIJKING



DOSIMETRISCHE VERGELIJKING: BETER BESTRALEN VAN TUMOR IN ADAPTIEVE SITUATIE

# H3

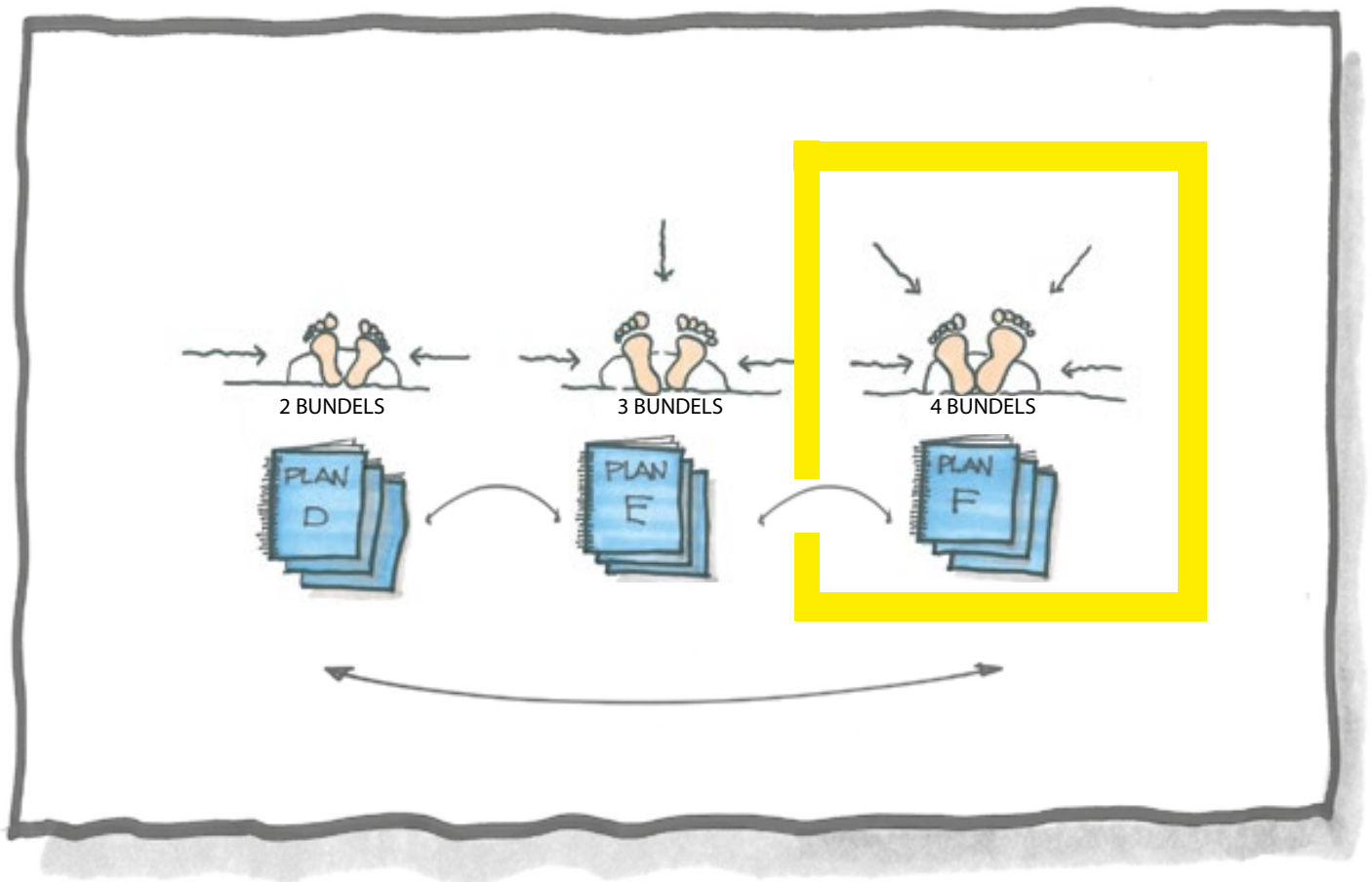
## Automatische blaassegmentatie



# H4

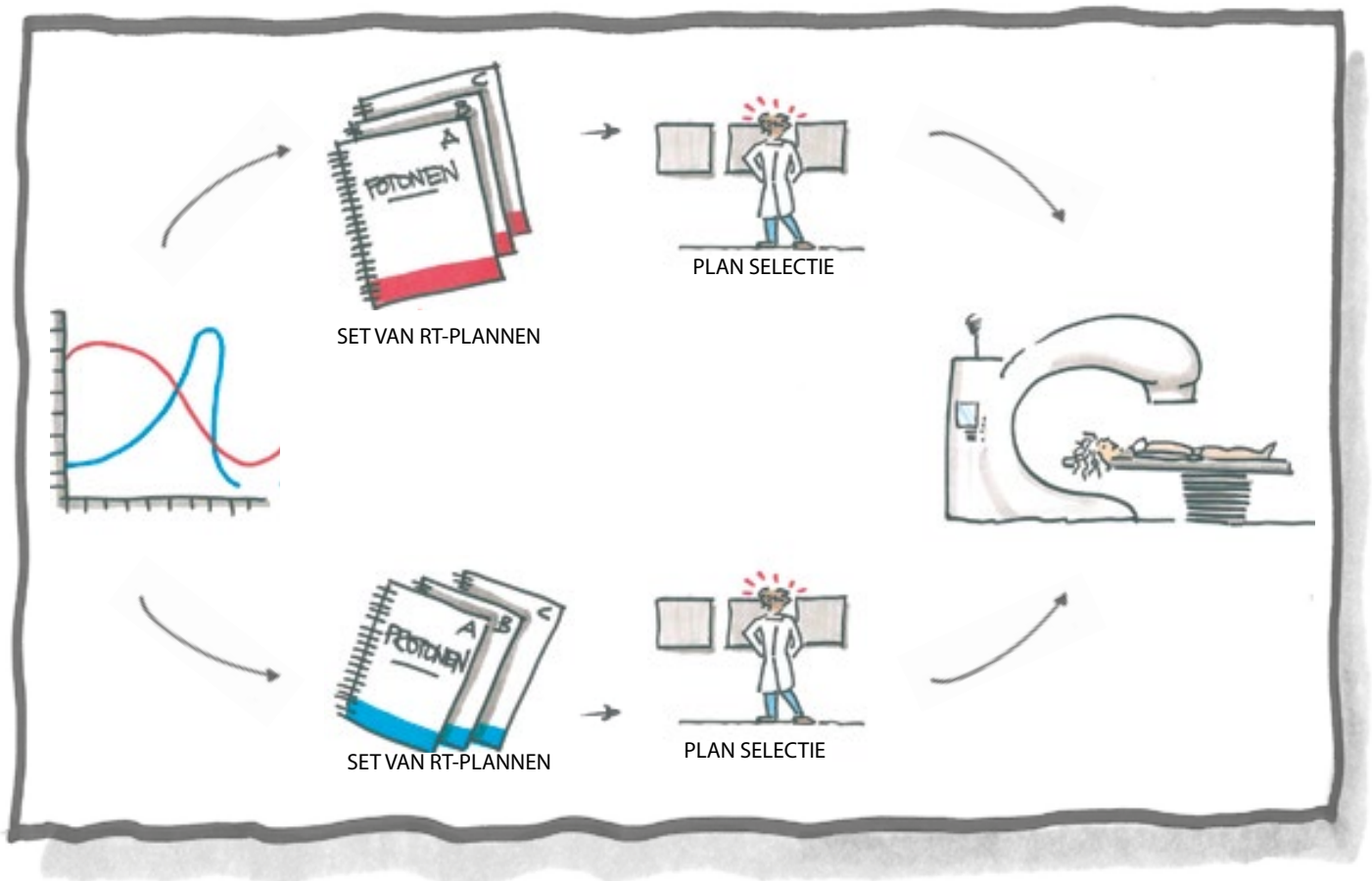
## Bundel configuratie voor protonentherapie

SELECTIE CONFIGURATIE D, E of F



# H5

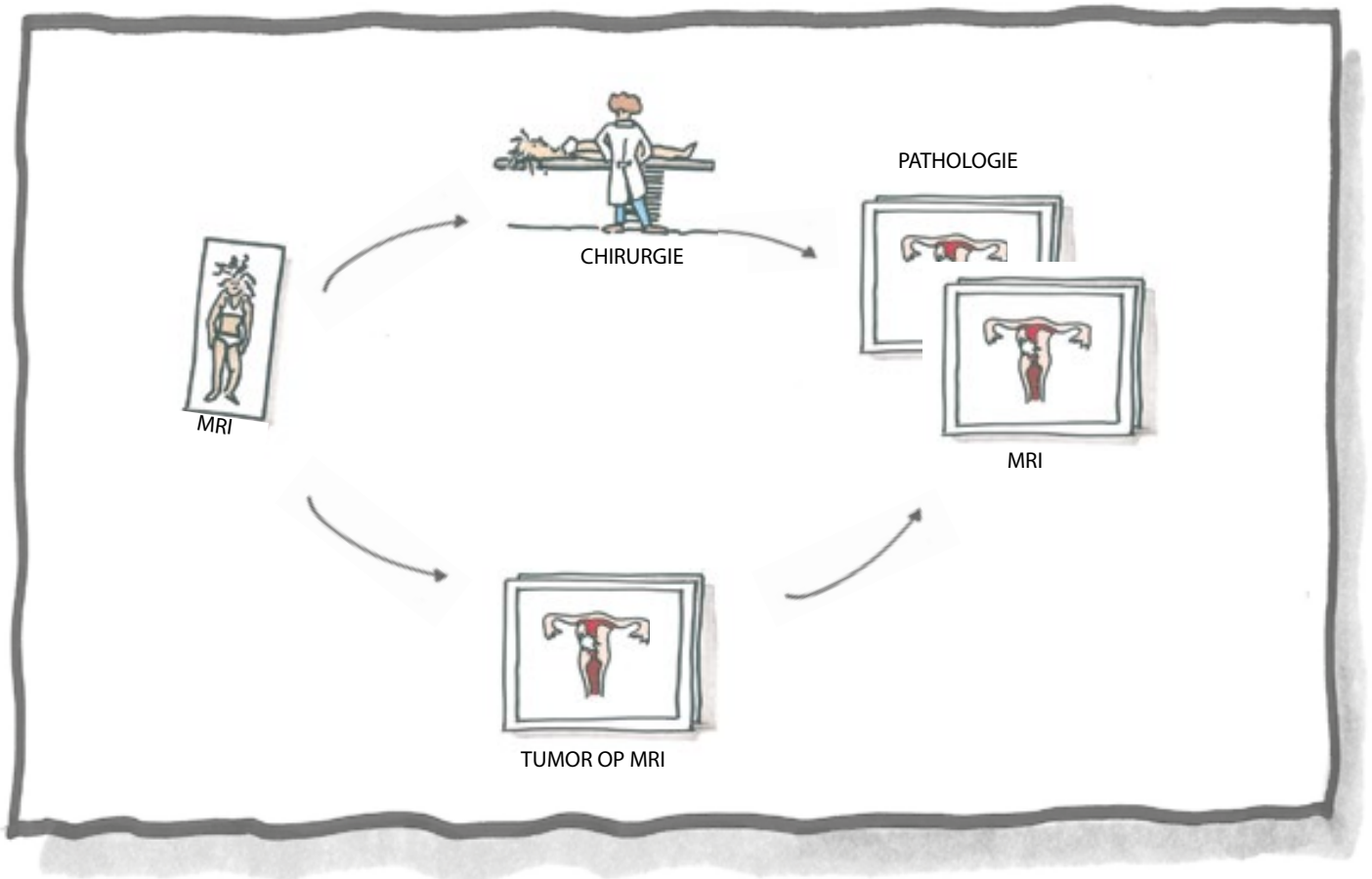
## Adaptieve radiotherapie: fotonen vs. protonen



CONCLUSIE: BIJ PROTONEN MINDER DOSIS VOOR GEZOND WEEFSEL

# H6

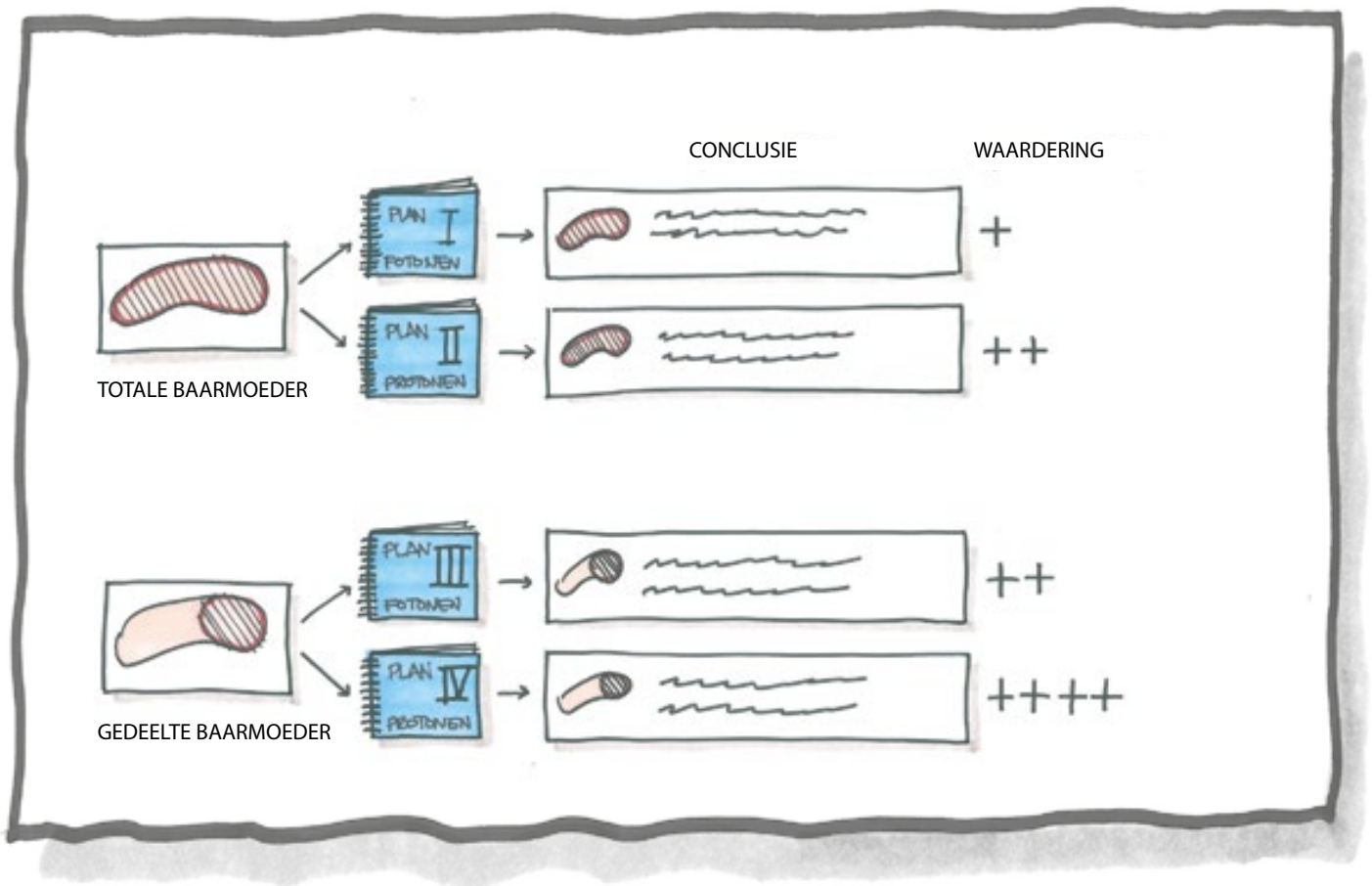
## Tumor definitie op MRI: validatie



CONCLUSIE: ONDERSCHATTING VAN TUMORVOLUME OP MRI

# H7

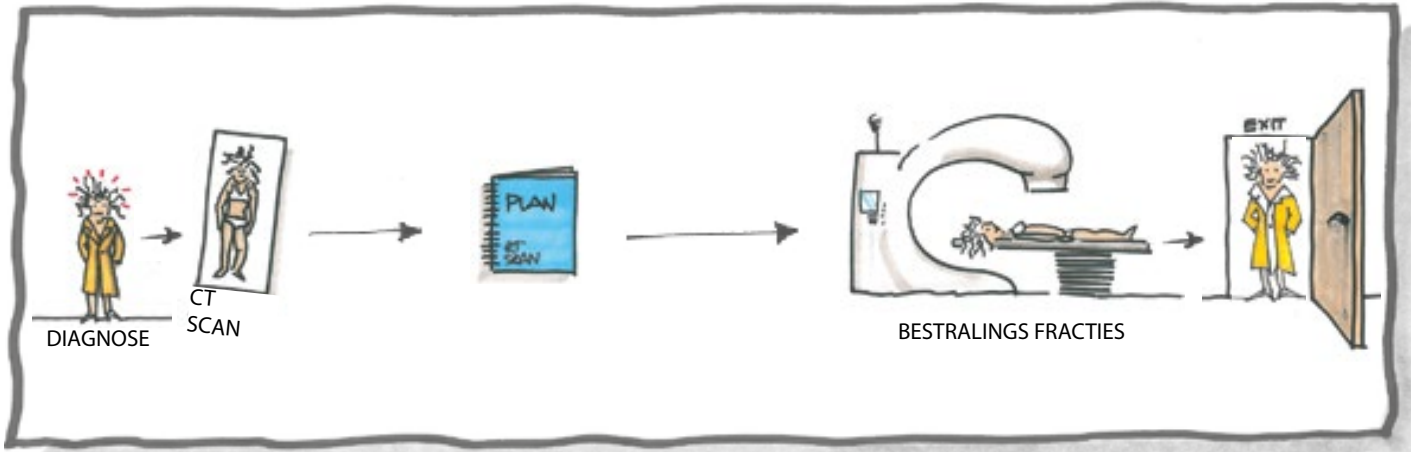
## Tumordefinitie MRI



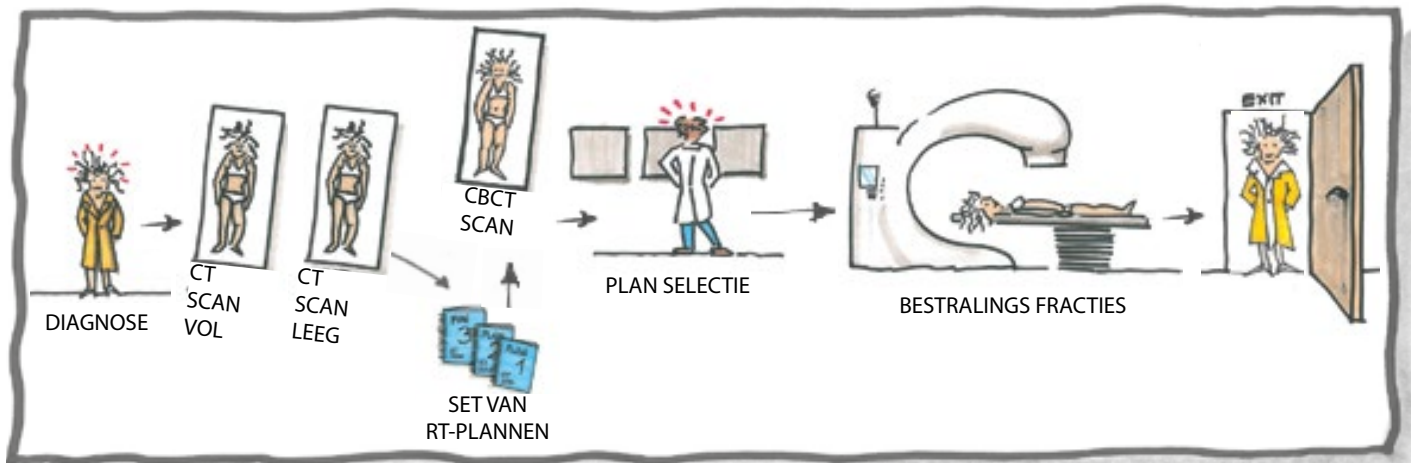
# H8

## Conclusie

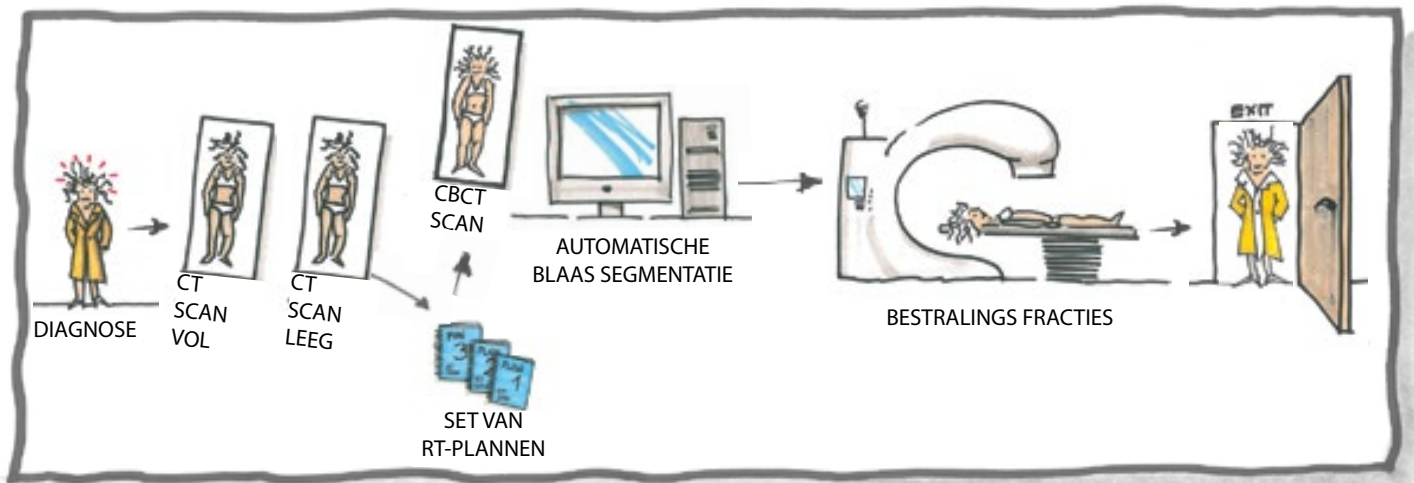
### Niet adaptieve radiotherapie



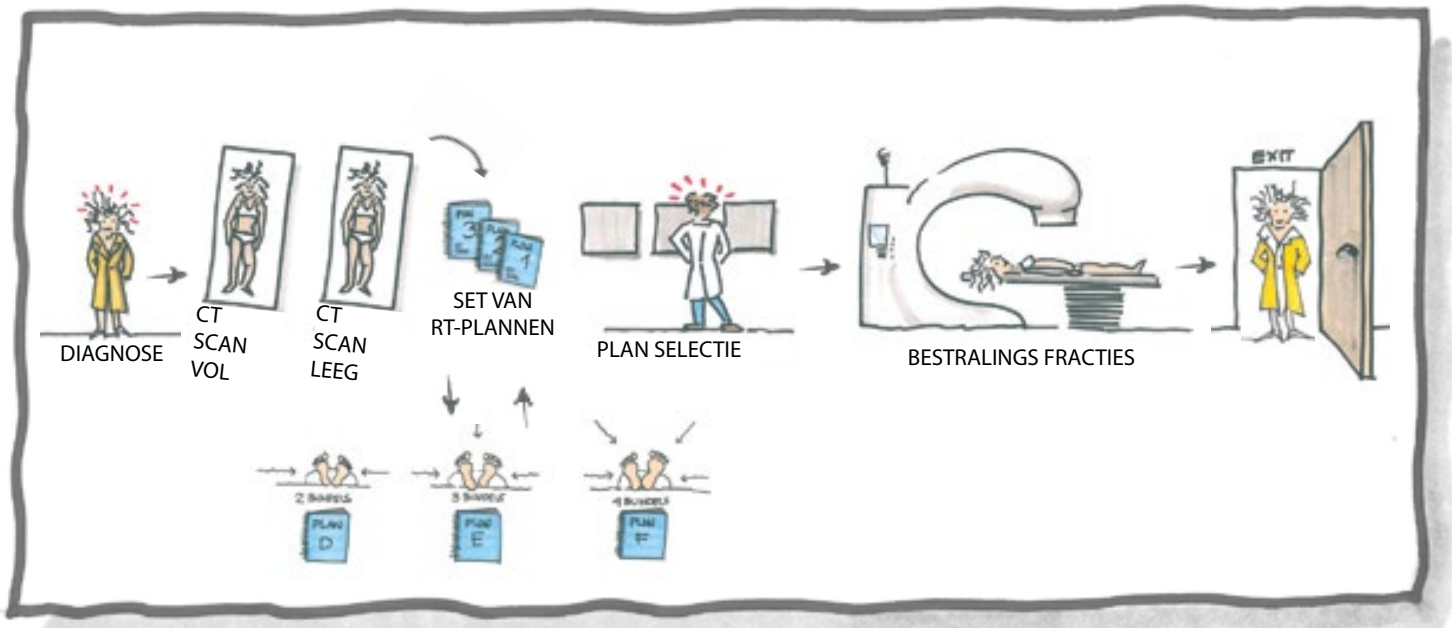
### Adaptieve radiotherapie



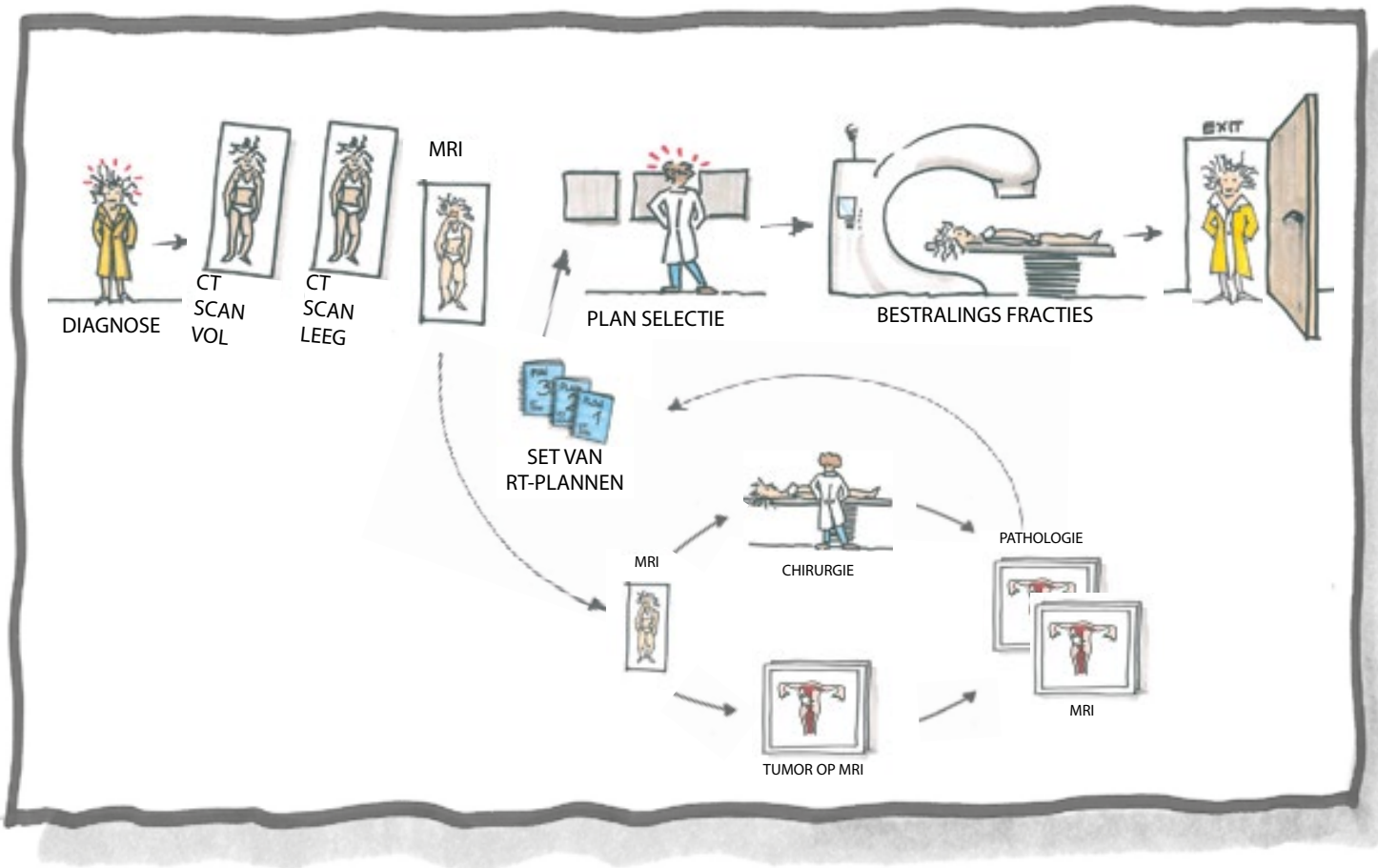
### Automatische plan selectie



### Adaptieve protonentherapie



### Tumordefinitie met behulp van MRI



# Dankwoord

Het promotietraject bestaande uit vier jaar onderzoek is voorbij gevlogen met dit proefschrift als resultaat. Hoewel mijn naam op de omslag pronkt, zijn er veel mensen die hebben bijgedragen aan de totstandkoming van dit proefschrift. Op deze plek wil ik iedereen bedanken die direct dan wel indirect, bewust of onbewust, een bijdrage heeft geleverd aan dit proefschrift.

**Coen**, dank voor je vertrouwen en de kans die je me geboden hebt om dit onderzoek te verrichten. Tijdens bijeenkomsten was je altijd geïnteresseerd in de voortgang en zette me regelmatig aan het denken over mogelijke verbeteringen en/of toevoegingen. Daarnaast heeft je kritische blik zeker een positieve bijdrage gehad in de totstandkoming van dit proefschrift.

**Arjan**, als copromotor en dagelijks begeleider wist je me op een uiterst prettige manier door het promotietraject te leiden. Tijdens onze wekelijkse bijeenkomsten luisterde je, stelde kritische vragen, gaf nieuwe inzichten en motiveerde me waardoor ik iedere week met nieuwe energie en ideeën je kamer uit stapte. Ook buiten deze bijeenkomsten om stond je deur altijd open. Ik waardeer het enorm dat ik altijd even binnen kon stappen voor inhoudelijke én minder inhoudelijke zaken. Hartelijk dank voor de tijd en energie die je de afgelopen jaren hebt geïnvesteerd in het onderzoek en in mijn persoonlijke ontwikkeling. Ik kijk met erg veel plezier terug op onze samenwerking.

**Lukas**, dank voor de fijne samenwerking. Ondanks je drukke programma wist je zeer regelmatig tijd vrij te maken voor bijeenkomsten of om weer eens een manuscript te beoordelen. Niet zelden was jij het die het belang van de patiënt benadrukte. Dat je deur altijd open stond voor een korte vraag of een inhoudelijke discussie heb ik als zeer prettig ervaren. Je enthousiasme is erg aanstekelijk en met enige regelmaat wist je mij en anderen te verblijden met een anekdote of een goed verhaal. Sommige anekdotes zal ik dan ook niet snel vergeten!

**Alle coauteurs** wil ik bedanken voor de succesvolle samenwerking en de zeer waardevolle bijdrage aan dit proefschrift. Ik waardeer het enorm dat jullie me geholpen hebben, ondanks ieders (over)volle agenda. Daarnaast waren de op- en/of aanmerkingen op de verschillende manuscripten heel nuttig!

Tevens wil ik **alle collega-onderzoekers** bedanken voor de inhoudelijke discussies en het delen van promotieproblematiek, maar zeker ook voor de gezelligheid en het vieren van successen. Mede door de fijne sfeer binnen de onderzoeksgroep zijn de afgelopen jaren voorbij gevlogen en kijk ik met veel plezier terug op deze periode. Zonder anderen tekort te doen wil ik een paar collega-onderzoekers expliciet bedanken:

**Lotte**, we zijn tegelijk aan het promotie-avontuur begonnen én zijn het gehele traject kamergenoten geweest. Onze onderzoeken hadden veel raakvlakken en niet zelden konden we elkaar helpen met inhoudelijke problemen, zonder elkaar voor de voeten te lopen. Daarnaast was er ook altijd ruimte om persoonlijke ervaringen en actualiteiten te delen. Deze gesprekken resulteerde regelmatig in het organiseren van een borrel, activiteit of sportpoule. Ik had niet gedacht dat onze tourpoule het startschot zou zijn voor afdelingsbrede tour- en WK-poules. Bedankt voor de fijne tijd als kamergenoot en heel veel plezier en succes toegewenst in je verdere carrière!

**Eelco**, ook wij zijn bijna vier jaar kamergenoten geweest en ik bewaar goede herinneringen aan deze periode. Naast inhoudelijke problematiek bespraken we regelmatig minder inhoudelijke en persoonlijke zaken, vaak onder het genot van een kop koffie. Aan het eind van de dag werd die kop koffie met enige regelmaat vervangen door een biertje om de écht belangrijke zaken door te nemen. Daarnaast heb ik veel plezier beleefd aan de activiteiten buiten het werk om. Fijn dat je mijn paranimf wil zijn!

**Peter**, we zijn tegelijk begonnen aan een gezamenlijk project en vanaf dag één hebben we veel samengewerkt. Jouw klinische blik en mijn fysieke benadering bleek een succesvolle combinatie. Ondanks je drukke programma (opleiding tot radiotherapeut-oncoloog en promotieonderzoek) wist je regelmatig tijd vrij te maken voor mijn onderzoek. Bedankt voor al het werk dat je hebt gedaan voor dit proefschrift. Je gedrevenheid en werklust gaan er zeker voor zorgen dat ook jij je promotieonderzoek tot een goed einde weet te brengen!

Verder wil ik de **gehele fysica groep** (onderzoekers, klinisch fysici (in opleiding), klinisch fysisch medewerkers, ICT'ers en technici) bedanken voor de fijne samenwerking en voor de goede sfeer en gezelligheid, zowel op de werkvloer als tijdens activiteiten buiten de afdeling.

Daarnaast wil ik **alle collega's van de afdeling Radiotherapie** bedanken die op één of andere manier een bijdrage hebben geleverd aan het tot stand komen van mijn proefschrift. Bedankt voor de fijne sfeer op de afdeling, ik vond het zeer prettig om deel uit te mogen maken van dit team!

**Hans**, bedankt dat je tijd vrijgemaakt hebt om mijn proefschrift te doorgronden en mijn bevindingen vervolgens begrijpelijk te illustreren, met de infographic als resultaat.

Tot slot wil ik mijn **vrienden** en **familie** bedanken voor de getoonde interesse in mijn promotieonderzoek en de steun die ik heb mogen ontvangen, in welke vorm dan ook.

Tevens wil ik mijn **vrienden** bedanken voor de vele gezellige momenten die zonder twijfel een positieve bijdrage hebben geleverd aan dit proefschrift. Ik hoop dat we in de toekomst nog vele gezellige en memorabele momenten mogen beleven.

Mijn **ouders** wil ik ook graag hartelijk danken voor de steun die ik altijd heb mogen ontvangen, zowel vóór als tijdens mijn promotietraject. De afgelopen jaren hebben jullie me mijn eigen weg laten zoeken, maar toonden jullie altijd interesse. Hoewel ik soms moeilijk kon uitleggen wat ik precies deed probeerden jullie het altijd te blijven volgen. Jullie steun was ontzettend waardevol.

**Florien**, dank je wel voor je onvoorwaardelijke steun. Jouw bijdrage is van onschatbare waarde geweest waarvoor ik je ontzettend dankbaar ben!









